Final Report: A multiscale analysis on the moisture effect of dynamics responses of granular matters

FINAL TECHNICAL REPORT

WaiChing Sun

April 15, 2016

US ARMY RESEARCH OFFICE

CONTRACT NO. W911NF-14-1-0658

Contents

List of Figures

Forward

This final report details the research conducted by the Columbia University research group supported by the Earth Materials and Processes Program under the contract number W911NF1410658. During the period 1/1/2015 to 9/1/2015, three graduate research assistants Yang Liu (now postdoctoral associate at MIT), Mr. Kun Kang, and Mr SeonHong Na and the PI have utilized the support to conduct research for fluid-infiltrating granular and geological materials. Dr. Simon Salager and his PhD student Dr. Ghonwa Khaddour from Joseph Fourier University at Grenoble France, have also provided important micro-CT images of a Hostun sand specimen taken undergoing drained triaxial compression test through a no-cost collaboration. The research presented in this report is a team effort of the aforementioned individuals.

The 9-month support from the STIR grant has directly lead to 10 journal publications published in a number of highly respected peer-review journals, in the field of computational mechanics (e.g. Computer Methods in Applied Mechanics and Engineering, International Journal of Numerical Methods in Engineering) geomechanics and geotechnical engineerin (e.g. Journal of Geophysical Research, Geotechnique Letters) and engineering mechanics (e.g.Journal of Applied Mechanics, Journal of Engineering Mechanics) published from January 2015 to April 2016. This report provides a brief account of the major accomplishments, which includes the introduction of the tensorial Bishop's coefficient, the formulation of a multiscale model that connects DEM model with finite element analysis, the application of microCT images to calibrate material parameters for granular materials idealized as higher-order continua and a stabilized large deformation model that captures the fluid-solid interaction of granular materials under non-isothermal condition. In the next few chapters, we will provide a statement of the problems the research team studied (Chapter 1), a summary of major research accomplishments and the potential impact of the research and the relevant to the Army research (Chapter 2) and future work and extensions (Chapter 3). A selection of published results are highlighted in Chapters 4-6.

The PI and the research team are grateful for receiving the crucial support from the Earth Material and Process Program under the directorship of Dr. Julia Barzyk to start the new research team at Columbia. The accomplishment mentioned above cannot be made possible without this support.

Chapter 1

Statement of the Problems Studied

The reason we can build sand sculpture is due to the presence of liquid bridges and water clusters among particles that are otherwise cohesion-less. These liquid bridges may form, coalescence and break, and the evolution of their geometrical features and sizes are dictated by the amount of suction, wettability of the solid, but also how the granular particles move against each other. From a micromechanical perspective, liquid bridge and the solid grains are two interacting networks that transmits force and moment. As a result, when subjected to external loadings, granular assemblies with a a very small volume fraction of water can behave profoundly different than the dry counterpart. Understanding how solid particles and pore fluid interacts is important for a number of engineering applications, including landslides, vehicle mobility and seismic signature of earth materials.

Previous theoretical studies and experimental programs have mainly focused on two different approaches. The first is to consider the fluid-solid interface explicitly and model the flow of fluid and motion of particles on a detailed grain-to-grain basis [Scholtès et al., 2009, Wang and Sun, 2015]. Another approach is to idealize the wetted and fully saturated granular materials as two-phase mixture and apply continuum mechanics theory to resolve the hydro-mechanical coupling effect with continuum-based numerical methods, such as finite element and finite volume model. [Lewis et al., 1986, Borja and Alarcón, 1995a, Markert et al., 2010, Kolditz et al., 2012, Sun et al., 2013f]. Nevertheless, the connection between the grain-scale phenomena and the field-scale behaviors of the wetted granular materials is rarely captured quantitatively. Establishing such a connection may yield a unified framework for these two distinctive concepts often being used separately by physicists and geotechnical engineers. The objective of this STIR research is to layout the groundwork to build such a connection via a combination of theoretical, experimental and computational studies.

The first objective of this project is to understand the connection between the macroscopic effective stress theory commonly used in field-scale prediction and the topological evolution of liquid bridge via grain-scale simulations. In particular, we explicitly modeled grain-to-grain interaction with discrete element method, while introducing solution from Young-Laplace equation to captures the grain-air-water interaction mechanism at grain-scale. A linear normal contact model is used to model the normal contact, while the tangential response is governed by Coulomb friction law. This mechanical discrete element model is coupled with a capillary model in which solutions of Young-Laplace equation are used to compute the force exerted on the particles by liquid bridges. From a microscopic perspective, the menisci may form a force chain network similar to the force chain of grain-to-grain contact network. As the grain assemblies are subjected to external loadings, liquid bridges may form or rupture due to the motion of particles and thus change the topology of the menisci network. Since rupture and formation of liquid bridges are governed by the distance between particles, grain size distribution plays an important role on the evolution of menisci network. To study how suction effect varies with grain size distribution, we conduct suction controlled experience on two grain assemblies, one composed of particles of similar sizes and another one composed of a mixture of large particles and fines. The partial Cauchy stresses are homogenized from both the solid grains and menscii networks. Simulation results from suction-controlled compression tests at a variety of suction level are analyzed (cf. Wang and Sun [2015]).

The second objective of this project is to propose a new multiscale hydro-mechanical model that (1) provides the physical underpinning from discrete element simulations, (2) resolves the problems associated with the phenomenological nature of drag force, and (3) improves the efficiency of large-scale problems. Our strategy is to first focus on a sub-class of problems in which the solid skeleton is composed of particulate assemblies in solid state (rather than granular flow) and the porous space is fully saturated with a single type of pore fluid

in laminar regime. As in the previous work for particle-fluid system [Curtis and Van Wachem, 2004, Robinson et al., 2014], we also adopt the assumption that a weak separation of scale exists between the motion of solid particles and that of the pore fluid. Our major departure is the way we employ this weak separation of the pore fluid to establish hydro-mechanical coupling across length scales. Instead of using the phenomenological drag force model to establish coupling, we use the effective stress principle to partition the macroscopic total stress as the sum of effective stress, which comes from microscopic DEM simulation, and the fluid contribution, which comes from the Biot's coefficient inferred from DEM assemblies and the pore pressure updated from a total Lagrangian poromechanics finite element solver (cf. Wang and Sun [2016b,a]).

As many engineering and military applications often involves geological materials undergoing large deformation under the non-isothermal condition, we also introduce, for the first time, a large deformation thermo-hydro-mechanics theory, and develop the corresponding stabilized finite element model suitable for equal-order discretized displacement, pore pressure and temperature. The resultant system of equation is solved fully implicitly and monolithically to preserve the Mandel-Cryer effect when the multiphysical coupling is strong. The necessary condition for numerical stability for thermo-hydro-mechanics problem and the corresponding combined inf-sup condition are derived. A new stabilization procedure is established based on the combined inf-sup condition (cf. Sun [2015b]).

All these research objectives identified in the original proposal has been fulfilled in this project. Furthermore, as the research progresses, we also identify a number of opportunities to further understand the multi-scale connection of the grain-scale and macroscopic behaviors. For instance, we have explored how one may use grain-scale model to identify the optimal mateiral parameters for constitutive models when access to experimental data is extremely limited (cf. Liu et al. [2016]), how to quantify the evolution of anisotropy of fabrics, stress and permeability when the granular material is subjected to shear loads (cf. Kuhn et al. [2015])., and the inherent length scale introduced from the multiphysical coupling process when wave propagates inside porous media under non-isothermal condition (cf. Na and Sun [2016]).

Chapter 2

Summary of the research accomplishment

We present in this section a brief summary of the research accomplishment obtained in this project, which addresses the objectives identified in the previous section. Complete list of publication, presentation and conference proceeding resulted from this STIR grant support is provided separately in the final report. The major findings described in this chapter has been all accepted in peer-review journals, i.e., Sun [2015b], Wang and Sun [2015, 2016a,b], Liu et al. [2015, 2016], Kuhn et al. [2015], Guo et al. [2016], Zheng et al. [2016], Na and Sun [2016].

1. The introduction of a tensorial Bishop's coefficient to address the apparent cohesion and induced shear strength provided by the liquid bridges at the pendular regime (details can be found in the following publications: Wang and Sun [2015], Kuhn et al. [2015]):

   (a) We introduce a new effective stress theory for unsaturated granular materials at the pendular regime in which the liquid constituent can take both volmetric and deviatoric loadings. This is a more realistic approach than the classical unsaturated effective stress theory, as liquid bridges exist in the pore space do exhibit shear strength and interact with the particles at the grain scale at the pendular regime.

   (b) Upon the introduction of the tensorial Bishop's coefficient, we use DEM to simulate deformation of a granular assemblies subjected to triaxial compression tests. The liquid bridge is modeled via the Yong-Laplace equation that is coupled with the discrete element simulations.

   (c) The simulation results suggest that not only the retention behavior of wetted granular matters is hysteresis, but the anisotropy of the liquid bridge fabrics is also highly path-dependent. While the traditional phenomenological models tend to model all path-dependent behavior in the constitutive law of the solid skeleton, the research has shown that both the path-dependence of the solid skeleton formed by the particles and the liquid bridges are due to different reasons (breakage and formation of liquid brdiges vs. granular re-arrangement) and hence must be considered separately.

   (d) We also found that the topology of both the liquid bridges and the grain contacts evolve very differently for poorly and well graded granular assemblies. In the numerical simulations, granular materials mixed with powder exhibits profoundly higher shear strength.

   (e) To objectively measure and quantify the degree of anisotropy of fabric, we also introduce thirteen measures of fabric and arranged them into four different categories, the particle bodies, the particle surfaces, the grain contacts and voids. Results from the DEM simulations show that anisotropy becomes more apparent when shear, but they lags changes in the bulk stress and tends to continuously evolves even when approaching the critical state, especially if the particles of the assemblies exhibit high aspect ratio.

2. The development of discrete-to-continuum coupling method for dry and water-infiltrating granular materials in geometrical linear and nonlinear regimes (cf. Liu et al. [2015], Wang and Sun [2016b], Guo et al. [2016]).

   (a) We establish a nonlocal DEM-FEM coupling scheme for dry granular materials. Using a corotational framework and an fully explicit time integrator, the mulutiscale model uses dynamic relaxation to achieve quasi-static status both at the RVE level and at the global system of equations.

Verification has been done to ensure the correctness of the numerical methods. Comparison with benchmark DEM simulations indicate that the DEM-FEM model is able to replicate the comparable porosity profile and shear band thickness observed in detailed large-scale discrete element simulations, within a fraction of CPU time. This is the first research that provides the remedy to address the lack of physical length scale issue in DEM-FEM model.

(b) An attempt to replace phenomenological constitutive law with grain-scale DEM simulations in a continuum-based finite element simulations was performed. In this particular example, a thick-walled hollow cylinder tests in dry sand. With a sufficiently fine mesh, the DEM-FEM simulations are able to replicate the curved anti-symmetric shear band observed in the cavity problem. More importantly, the dual-scale simulation is able to establish a connection of the force chain evolution and the formation of curved shear band during the drilling process.

(c) For the first time, we introduce a dual-scale effective stress principle in which the total stress of a solid-fluid mixture is partitioned into two parts, the homogenized effective stress from the solid skeleton and the continuum pore fluid. This definition provides the starting points to establish a DEM-FEM model in which the macroscopic finite element simulations are carried out without any need of introducing any constitutive model other than contact laws for grain-to-grain contacts.

(d) Unlike the previous DEM-FEM simulation which is either limited to geometrical linear regime or only applicable to completely dry granular materials, the new proposed model employs a mixed finite element and finite strain poroplasticity framework to capture the hydro-mechanical coupling effect in the geometrically nonlinear regime. To the best of the PI's knowledge, this is the first time such a model has been successfully established.

(e) By establishing the linkage between granular kinematics to the macroscopic hydro0mechanical responses, the research team is able to use simulations to directly access the fabric anisotropy of the granular materials in a field-scale simulations. In particular, the research team determines that the onset of the so-called anistoropic crtical state proposed by Li and Dafalias [2011] often occur only inside the shear band and is associated with the strain localization phenomena.

(f) THe DEM-FEM model is also extended to incorporate higher-order kinematics. The new idea here is to conduct second-order homogenization to compute stress and couple stress from discrete element. In this new theory, micro-rotation of the particles are considered in the macroscopic simulations and additional governing equation for the balance of angular momentum is added such that the higher-order kinematics of the granular assemblies are considered. The upshot of this new method is that it does not require the a-prior knowledge of the exact length scale of the assemblies a prior or the usage of it to compute nonlocal strain. Instead, the new DEM-FEM model requires no additional information, but can predict the onset of strain localziation and other length-scale dependent responses while upholding mesh independence.

3. Material parameter identification of multiscale models with conventional experiments and micro-CT images (cf. Wang and Sun [2016a], Liu et al. [2016]).

(a) For the first time, we establish an inverse problem in which material parameters of a micropolar hypoplasticity is determined from a combination of macroscopic constitutive responses and meso-scale void ratio distribution obtained from micro-CT images obtained during a drained triaxial compression tests.

(b) Using different types of objective functions, information obtained from experiments are converged into constraints and finding the material parameters that best curve-fit the experimental measures are equivalent to finding the set of material parameters that minimizes a functional.

(c) We test how different views of measuring the compatibility between the experimental observation and numerical predictions encoded in the objective function affects the forward prediction ability of the calibrated numerical models.

(d) The simulations calibrated with micro-CT images and macroscopic constitutive responses exhibit similar macroscopic responses, however, only the micro-CT image calibrated simulations yield the correct bifurcation modes. This is an important discovery. The combined numerical-laboratory experiments prove that using the macroscopic constitutive responses to calibrate multiscale and microscopic models, such as discrete element models, is insufficient.

(e) In the case where meso-scale information is completely absence, and experimental data are extremely difficult to obtain, we introduce a new calibration method called extended digital database to calibrate macroscopic model. The idea is to use the limited available experimental data to first calibrate a high-fidelity model, then using the simulated responses inferred from the high-fidelity model as supplement to resolve the under-constraint issue due to the lack of experimental data.

4. Thermo-hydro-mechanical coupling effects of fluid-infiltrating porous media (cf. [Sun, 2015b, Na and Sun, 2016]).

   (a) A large deformation thermo-hydro-mechanics continuum theory for porous media under the non-isothermal condition is formulated. Unlike previous theoretical development and modeling effects in which the thermo-mechanical coupling effects are neglected, the new formulation considered the heat generated due to the plastic dilatancy at finite strain.

   (b) From a numerical standpoint, the research team has also a major breakthrough in which they proved that the previous unsuccessful attempt to model the thermo-hydro-mechanical coupling effects and the spurious pore pressure and temperature oscillations observed in the numerical solutions are related to the so-called lack of two-fold inf-sup condition.

   (c) By identify this numerical deficiency, a remedy stabilization procedure is proposed. This stabilization procedure has proven to be able to successfully generate numerical stable results that are important to predict thermal-softening responses of porous media.

   (d) On a related note, the research team has also studied the wave propagation in a thermo-sensitive porous medium. By conducting stability and dispersion analysis, we discover that while the rate dependence introduced by the thermal and hydraulic diffusion processes did introduce a physical length scale, this physical length scale may vanish and is therefore not sufficient to regularize the boundary value problems representing the thermo-hydro-mechanical processes. This is important, as there is confusion in the literature about the role of thermo-hydraulic flow on the onset and propagation of deformation band. Our analytical solution indicates that while thermal and hydraulic conductivities do affect the thickness of the deformation bands, these diffusion processes do not necessarily regularizes the thermoal-hydro-mechancial models.

Chapter 3

Impact of the research and relevant to Army

We strongly believe that the research developed in this project has led to important advancements in the understanding of the path-dependent, hysteresis solid-fluid interaction process of granular materials partially or fully saturated with water, while simultaneously address and overcome major challenges involved in modeling, calibrating, replicating and predicting these multi-physical processes that were previously unresolved. Through multiscale coupling, the numerical techniques provide a fundamentally new approach to link grain-scale simulations directly to field-scale problems, via first-order and second-order homogenization. These results obtained from the STIR project improve the modeling and computational capabilities of the state-of-the-art techniques, especially on predicting surface processes that involves soil failures, strain localization, and formation of deformation bands, which are all relevant to Army.

These results have also been presented in more than 10 publications, as well as in many conference contributions, keynote and invited lectures, in professional meeting, universities and government agencies. A complete list of publications prepared in this project is presented. Recognition to the research developed in this project has come in different forms in the United States and across the globe. In particular, the PI has received the Dresden Fellowship from Technische Universität Dresden, Germany for his work on computational modeling on wetted granular materials in 2016, and invited to be deliver department seminars at Harvard (Harvard Applied Mechanics Colloquia), Brown, Columbia, UT Austin (Claude R. Hocott Lecture), Sandia National Laboratories, Los Alamos National Laboratory, University of Perugia, Italy and University of Hong Kong in 2015. During the period of the performance of this project, the PI has awarded the ARO Young Investigator award in 2015 and was invited to deliver keynote lectures at International Plasticity conference and US Army TARDEC.

We would like to mention also the strong educational component of the research developed in this project. In particular, the research grant has partially supported two graduate students, Miss Yang Liu (PhD graduated August 2016, now postdoctoral scholar at MIT) and Mr Kun Wang (PhD expected Spring 2018). The PhD students have won prestigious recognition from the training provided by the STIR grant. In particular, Yang Liu has won the best poster award over more than 100 mini-symposia at US Congress of Computational Mechanics, San Diego. PhD student SeonHong Na has won travel scholarship to attend Engineering Mechanics Institute conference at Stanford University and to deal.ii workshop at Texas A& M University, while PhD student Kun Wang has won travel scholarship to attend Society of Engineering Science Meeting at Texas A&M University.

In addition, the research proposal also provides opportunities for Mr SeonHong Na, a Fulbright Fellow and PhD student of the PI, to participate in theoretical and computational research on granular materials. Many of the major findings have been published in peer-reviewed journals. The research also lead to a new international collaboration with the Joseph Fourier University who are one of the leading group in X-ray tomographic imaging techniques for granular materials problem.

Chapter 4

Future work and extension

The theory, computer models and analyses developed in this project are currently being extended and generalized for understanding the wetted granular materials across different degree of saturation regimes and thermal conditions. In particular, we note that the groundwork laid by this project for pendular regime opens door for the development of a new unified theoretical and computational framework that enables one single multiscale model to capture the interactions among liquid bridges, water cluster, air bubble and solid grains across **all** degree of saturation regimes.

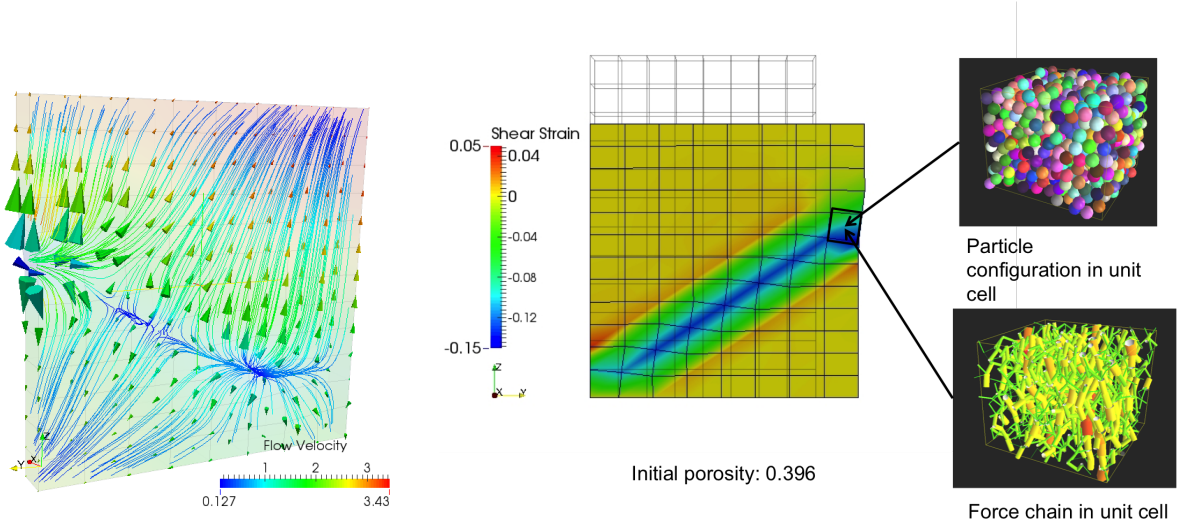

(a) Macroscopic flow streamline induced by deformation

(b) Macro- and mico-scale deformed configurations

Figure 4.1: *Preliminary results of an undrained triaxial compression test of a fully saturated granular specimen simulated via multiscale discrete-continuum coupling model developed by the PI.*

Our major plan for future work is to launch a new research program that fully integrates advanced X-ray imaging techniques, theoretical and computational modeling of discrete-continuum coupling models, and topology and microstructural analysis using graph theory to predict the hydro-mechanical behavior of wetted granular matters across all saturation regimes. In particular, the research team will derive rigorously validated multiscale methods that combine the strength of microstructured based granular mechanics and the higher-order continuum based poromechanics. We will develop two discrete-continuum coupling schemes, one based on total stress, another one based on the effective stress principle. The total stress coupling scheme is more computationally costly but conceptually simple. This model employs total Lagrangian mesh and a macroscopic mixed finite element as a vehicle to carry fully coupled direct simulation of particle-fluid systems at each unit cell. For each incremental time step, the macroscopic finite element will provide the unit cell hydraulic and mechanical boundary conditions. In each unit cell, a coupled DEM-LBM will be carry out and the total stress of the porous media will be upscaled back to the Gauss point of each finite element to enforce the balance principles at the macroscopic continuum level. Figure 4.1 shows the preliminary results obtained from this direct approach, where a water-saturated granular assembly is subjected to a bi-axial loading.

On the other hand, the effective stress coupling scheme will exploit the effect stress principle to partition stress stemming from grain contact and those from fluid-solid interfaces at grain-scale. By assuming the validity of effective stress principle, which has recently been a subject of ongoing debate (e.g. De Buhan and Dormieux [1996], Chateau and Dormieux [2002], Khalili et al. [2004]), the microscopic fluid-solid interaction will be modeled in a staggered scheme. Like the first approach, the finite element model will provide updates to the unit cell. However, the main departure here is that the DEM simulation in this alternative approach will be used to provide prediction of **effective stress**, while the two-phase simulations will be used to obtain the macroscopic water and air infiltrating vectors at each time step. In both cases, the interaction of pore fluid and solid grain is captured at continuum scale via a mixed finite element formulation. As a result, there is no need to incorporate phenomenological law to model the path dependent retention behavior at the macroscopic continuum level, as shown in 4.2.

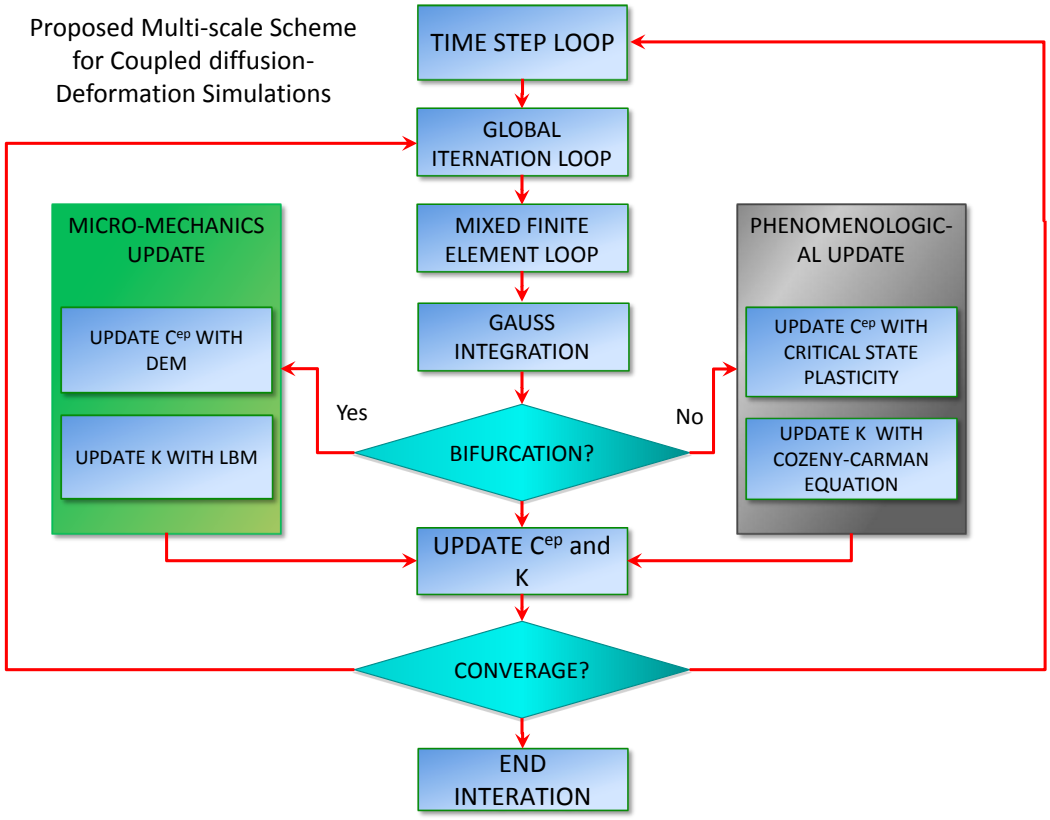

Figure 4.2: *Multiscale LBM-DEM-FEM model that upscaling liquid-grain interactions at pore-scale to field scale continuum simulations. Length scale is preserved by modeling granular assemblies as three-dimensional non-local continua.*

The two multiscale approaches will be used to reconstruct triaxial compression tests under both drained and undrained condition. X-ray CT scanning will be performed at selected time step. An ID tracking approach will be used to keep track of kinematics of each individual grain, liquid bridge and cluster [Khaddour et al., 2013]. A comparison of the results obtained from the two methods will be systematically compared with both the microscopic kinematic data and the macroscopic stress-strain curves. This combined experimental and computational exercise can provide important data and evidence to either validate or point out the limitation of the effective stress principle. Given the fact that the effective stress principle is the cornerstone of poromechanics theory that are widely used from a wide spectrum of applications (e.g. bio-medical engineering, food industry, reservoir mechanics, geotechnical engineering and geophysics), the results of this study, if successful, will have far-reaching impacts across multiple science discipline.

To accurately capture the length scale of deformation bands without artificial calibrations, we will derive a multiscale coupling scheme that links between grain-scale simulations with higher-order continuum simulation. Previously, the PI has attempted to use the staggered nonlocal operator to define a nonlocal strain over a sampling volume for dry granular material. Results have shown that the shear band thickness obtained from the nonlocal coupling DEM-FEM simulations does not exhibit mesh dependence – a significant improvement over previous efforts such as Guo and Zhao [2014], Nguyen et al. [2014], Liu et al. [2015], Wang and Sun [2016b]. Nevertheless, in order to insert the correct length scale in the post-bifurcation regime, calibrations of the length

scale with the observed thickness of deformation band are required. This calibration step is not trivial for wet granular matters as the shear band thickness is influenced by the multi-physical coupling effect between the liquid bridges and solid particles [Zhang et al., 1999a, Na and Sun, 2016]. In this research, we will derive a new method to link Cosserat unsaturated continuum model with discrete element simulations. This adoption of Cosserat material model naturally includes grain rotation from discrete element simulations. Since grain-scale simulations are coupled through the continuum models but not directly linked in space, the multiscale model can obtain the necessary small-scale information without exhausting computational resource through a divide-and-conquer approach. As a result, the proposed multiscale model can overcome the computational barrier to simulate large-scale wet granular problems that are more directly relevant to field scale applications, such as landslide and soil collapse. With this new capability to simulate large-scale system while retaining microstructural information at Gauss points where RVE are located, significant insight on how granular and menisci systems collectively interact can be obtained via techniques from graph theory [Satake, 1993, 2004, Tordesillas et al., 2010].

The resultant multiscale model will serve as a key step to unveil the following important scientific questions:

- Whether the effective stress principle can be fully validated via a multiscale framework?
- What is the proper "scaling law" for the stress anistropy induced by the liquid bridge and cluster and grain contact fabrics?
- How does the capillary hysteresis evolve under different stress path?
- How does the suction-induced anisotropy affects the path-dependent responses of granular materials at different spatial and temporal scales?
- How does the shape, grain size distribution of particles affect water retention behavior?
- How does the existence of pore fluid menisci and surface tension influence the onset and propagation of strain localization?

All of these important questions have not been completely understood by using either stand-alone discrete or continuum models separately in previous work. Therefore, establishing a single unified model that can capture the discrete-continuum transition across the entire spectrum of saturation regimes is an enormous contribution for both the fundamental science of wetted granular matters and engineering practices that involves earth surface processes.

These plans are being supported by the Young Investigator Program Award from the Earth Materials and Process Program of the Army Research Office, with the starting date of September 1st, 2015. This important continued support is gratefully acknowledged. We strongly believe that the combination of all these results will lead to more powerful novel computational tools and deepen understanding of the connections of hydro-mechanical processes across length scales. These elements will provide a sound theoretical basis necessary for the analysis of complex practical problems of interest to the Army.

Chapter 5

Key findings on liquid bridges and the induced strength anistropy

5.1 Introduction

Many near-surface granular materials, such as sand, silt, seafloor sediment, are infiltrated by water and air due to rainfall, ground water level changes, or external loadings that promote fluid transport. This moisture content may transform the mechanical responses of grains that are otherwise cohesion-less and thus reshape the earth surface features. For instance, adding small water in cohesion-less dry sand may create enough surface tensions among grains to transform dry sand into an ideal raw material for sculptures. The moisture content may also change the frictional coefficient of granular materials – a fact exploited by Ancient Egyptians to facilitate the sliding of heavy objects as evidenced by the wall painting from 1880 B.C. in the tomb of Djehutihotep [Fall et al., 2014]. In 1490, Leonadro de Vinici began his investigation on capillary phenomena. His study on capillary has been continued with the work of Laplace, Young, Gauss, Rayleigh, and numerous others in mathematics, physics, mechanics and engineering disciplines [Koiso and Palmer, 2007]. Figure 5.1 depicts the

SATURATION DEGREE [%]	SATURATION REGIME		MEAN FORCES
0 %	Dry	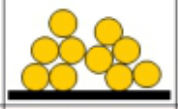	Gravity, contact
0% - 5%	Pendular	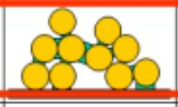	Gravity, contact, capillary
5% - 35%	Funicular	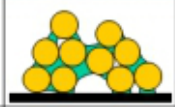	Gravity, contact, capillary
35%-90%	Capillary		Gravity, contact, capillary, [drag]
90%-100%	Saturated	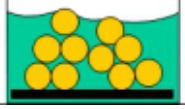	Gravity, contact, [drag]

Figure 5.1: *Saturation regimes of soils (adopted fromNewitt and Conway-Jones [1958]). The hydro-mechanical responses of wetted granular matter in the pendular regime is the focus of this study.*

fluid-particle interactions at various degree of saturation. At nearly saturated condition, capillary effect is nearly isotropic. However, at the funicular and pendular regimes where water may form liquid clusters and bridges, anisotropy of the capillary effect can be significant. The surface tension and the presence of menisci may have important implications on mechanical responses of granular matters. In the pendular regime where degree of saturation is low, the intermolecular forces exerted on the solid-fluid interface may be strong enough such that

the liquid may stick and form a pendular birdge in-between solid grains instead of flow in the pores. While a liquid bridge may introduce attractive force among grains, the relative movement of the grains connected by the liquid bridges may cause it to spread, stretch and rupture.

At the macroscopic level, the forces due to interaction between solid grains and liquid bridges are often collectively taken into account as an **isotropic** suction or capillary stress exerted on a continuum mixture composed of solid, air and liquid [Bishop, 1960, Bishop and Blight, 1963]. This isotropic capillary pressure is often incorporated into hydro-mechanical finite element models via an extension of effective stress theory. Equipped with appropriate plasticity models that replicate the suction-dependent constitutive responses (e.g. the basic Barcelona model [Wheeler et al., 2002]) and retention behaviors, this macroscopic approach has enjoyed a great success in modeling unsaturated porous media, especially when the degree of saturation is sufficiently high [Lewis and Schrefler, 1998, Zienkiewicz et al., 1999a, Borja and Koliji, 2009, Sheng et al., 2004]. Nevertheless, recent experimental and theoretical studies have demonstrated that capillary stress is in fact **anisotropic** in pendular regime Lu and Likos [2004], Scholtès et al. [2009]. This anisotropy evolves as liquid bridges form or rupture in the deforming granular material [Richefeu et al., 2006, Scholtès et al., 2009, Wan et al., 2014]. Since the migration of water inside the wetted granular matters also affects the size and shape of the liquid bridges, this anistropic suction effect is expected to be hysteretic and depends strongly on air and water diffusion. As a result, moisture content may significant alter how wave propagates in unsaturated granular matters. Nevertheless, the exact mechanism that leads to this evolving anisotropic effect has not been fully understood [Wan et al., 2014].

This study is aimed to use discrete element simulations to improve our understanding on the grain-air-water interaction mechanism at grain-scale and how the micro-mechanical interaction induces macroscopic stress anisotropy. In particular, a linear normal contact model is used to model the normal contact, while the tangential response is governed by Coulomb friction law. This mechanical discrete element model is coupled with a capillary model in which solutions of Young-Laplace equation are used to compute the force exerted on the particles by liquid bridges. From a microscopic perspective, the menisci may form a force chain network similar to the force chain of grain-to-grain contact network. As the grain assemblies are subjected to external loadings, liquid bridges may form or rupture due to the motion of particles and thus change the topology of the menisci network. Since rupture and formation of liquid bridges are governed by the distance between particles, grain size distribution plays an important role on the evolution of menisci network. To study how suction effect varies with grain size distribution, we conduct suction controlled experience on two grain assemblies, one composed of particles of similar sizes and another one composed of a mixture of large particles and fines. The partial Cauchy stresses are homogenized from both the solid grains and menscii networks. Simulation results from suction-controlled compression tests at a variety of suction level are analyzed.

As for notations and symbols, bold-faced letters denote tensors; the symbol '$\cdot$' denotes a single contraction of adjacent indices of two tensors (e.g. $\boldsymbol{a} \cdot \boldsymbol{b} = a_i b_i$ or $\boldsymbol{c} \cdot \boldsymbol{d} = c_{ij} d_{jk}$); the symbol ':' denotes a double contraction of adjacent indices of tensor of rank two or higher (e.g. $\boldsymbol{C} : \boldsymbol{\epsilon^e} = C_{ijkl} \epsilon^e_{kl}$); the symbol '$\otimes$' denotes a juxtaposition of two vectors (e.g. $\boldsymbol{a} \otimes \boldsymbol{b} = a_i b_j$) or two symmetric second order tensors (e.g. $(\boldsymbol{\alpha} \otimes \boldsymbol{\beta}) = \alpha_{ij} \beta_{kl}$).

5.2 Generalized Bishop's coefficient tensor

In geotechnical engineering and geomechanics practice, air-water-particle interaction is rarely modeled explicitly. Rather, macroscopic homogenized theory, such as Biot's poroelasticity theory or mixture theory are often used to model the collective responses of the air, water and solid constituents at macroscopic scale. In this situation, Cauchy stress (or other appropriate stress measures) is partitioned into three parts, i.e., the effective stress and the pore water and air pressures. Such a macroscopic treatment is often referred as effective stress principle. The effective stress principle is originally proposed for saturated porous media in 1936 [Terzaghi, 1996, De Boer, 1996, Sun, 2013, Sun et al., 2013e,b]. The Terzaghi's effective stress principle may be stated in the form of two propositions:

1. Effective stress is the exclusive cause for the change of volume and shear strength of a soil.
2. The effective stress of a soil is defined as the different between the total applied stress and the pore fluid pressure.

Extension of effective stress principle to unsaturated porous media has been proposed by Bishop [1960]. The Bishop's effective stress, which is listed in (5.1), is commonly accepted by the geomechanics research community, although the validity of the total stress partition between suction and effective stress is subjected to

long-term debate and sometimes misunderstood as indicated by Jennings and Burland [1962], Laloui and Nuth [2009].

$$\sigma'_{ij} = \sigma_{ij} - p_a\delta_{ij} + \chi s\delta_{ij} \tag{5.1}$$

with σ_{ij} being the total stress tensor, $s = p_a - p_w$ the difference between the pore air pressure p_a and the pore water pressure p_w, i.e., capillary pressure, and χ the Bishop's coefficient which is related to the degree of saturation S_r [Bishop, 1960]. The major upshot of the usage of Bishop's effective stress is that it enables a simple transition to the Terzaghi's effective stress by imposing $\chi = S_r = 1$ when the porous medium becomes fully saturated, and $\chi = S_r = 0$ when the porous medium is dry. The Bishop's coefficient is considered to be a scalar due to the underlying assumption that the capillary effect is isotropic. However, this assumption is not valid according to experiments conducted on wetted granular matters in the pendular regime in which the anistropic nature of the capillary effects cannot be neglected [Lu et al., 2007, Manahiloh and Muhunthan, 2012, Fall et al., 2014]. A possible explanation of the anisotropic effect is that the anisotropy is stemmed from micro-structural attributes. In particular, since the orientation of the force chains formed by both the granular contacts and pore water menisci are both not isotropic, the macroscopic capillary stress, which is a function of force and branch vectors, is also not necessarily isotropic. Furthermore, since the spatial distributions of granular contacts and pore water menisci are evolving when the wetted granular assemblies subjected to external loadings, this anisotropic effect is likely to evolve according to the load history, as evidenced by experimental data obtained from CT images, [Alonso et al., 2010, Hicher and Chang, 2007, Hashemi et al., 2013, Higo et al., 2013]. Moreover, Richefeu et al. [2006], Soulie et al. [2006] and Scholtès et al. [2009] conducted discrete element simulations to investigate contact and liquid bridge fabric. They showed that liquid bridge fabric is both anisotropic and path dependent when subjected to shear loading. This anisotropy may lead to the anisotropy of macroscopic effective and capillary stress tensors (obtained from homogenizing grain-to-grain and grain-water-grain contact force and branch vectors) being anisotropic. In this study, our objective is to quantify the interplay between the microscopic force chain orientation and macroscopic anisotropy of effective and capillary stresses. In particular, the macroscopic stress is obtained via homogenization of force and branch vectors [Sun et al., 2013c, Iwashita and Oda, 2000, Cambou et al., 2009], i.e.,

$$\sigma_{ij} = \sigma_{ij}^{\text{contact}} + \sigma_{ij}^{\text{capillary}} + p_a\delta_{ij}, \tag{5.2}$$

$$\sigma_{ij}^{\text{contact}} = \sigma_{ij}^{'} = \frac{1}{V}\sum_{gc=1}^{N_{gc}} F_{\text{contact},i}^{gc} l_j^{gc}, \tag{5.3}$$

$$\sigma_{ij}^{\text{capillary}} = \frac{1}{V}\sum_{n=1}^{N_n} F_{\text{capillary},i}^{n} l_j^{n} \tag{5.4}$$

where gc stands for grain contact and n stands for liquid bridge neck. l^{gc} and l^n represent the vectors connecting centers of two grains corresponding to the solid contact and liquid meniscus respectively.Since microstructural attributes of both force and branch vectors depend on orientations of particle contacts, the capillary stress $\sigma_{ij}^{\text{capillary}}$, which is the sum of dyadic products of capillary forces and branch vectors as defined in (5.2), is usually not isotropic even though the macroscopic suction remains isotropic. As a result, we introduce a tensorial form of Bishop coefficient to replace the isotropic term $\chi s\delta_{ij}$ in (5.1) by the tensorial form $\chi_{ij}s$.

$$\sigma'_{ij} = \sigma_{ij} - p_a\delta_{ij} + \chi_{ij}s \tag{5.5}$$

Comparison of (5.5) and (5.2) leads to:

$$\sigma_{ij}^{\text{capillary}} = -\chi_{ij}s = -\chi_{ij}(p_a - p_w) \tag{5.6}$$

Like the isotropic classical counterpart in Laloui and Nuth [2009], this generalized Bishop's coefficient tensor χ_{ij} is generally not a constant parameter but depends on the microstructural attributes, such as force chain topology and pore size distribution. This features will be analyzed in the following sections in which suction-controlled triaxial loadings are prescribed in wetted granular assemblies. We account for these changes by micromechanical studies of contact normal and menisci orientation as well as interparticle distance. Our goal is to investigate how the degree of anisotropy of χ_{ij} evolves differently in wetted granular matters of different grain size distribution. The influence of fines content and suction pressure on the principal values and directions of χ_{ij} will also be examined.

5.3 DEM models

The behavior of wet granular media under external loads has been studied both by experimental and numerical approaches [Bishop and Blight, 1963, Fall et al., 2014, Laloui and Nuth, 2009, Wheeler et al., 2002]. As the overall behavior of the specimen is strongly related to the interaction between individual particles and liquid bridges, understanding on the microscopic forces, grain structures and water distribution is a key step toward understanding the macrscopic behavior of unsaturated porous media. While recent advancement on tomographic imaging techniques may potentially open door to study the connection between micro-structures and macroscopic responses, applying this technique to wetted granular matters remains a technical challenging task Hashemi et al. [2013]. Meanwhile, macroscopic continuum models based on either mixture theory or extensions of Biot's poroelasticity theory have been often used to capture mechanical behaviors of wetted granular matters. In macroscopic continuum models, the air-water-solid interactions are not modeled explicitly. Rather, they are collectively considered as a continuum mixture with each constituent (solid, water and air) occupying a fraction of volume at each macroscopic material points [Borja and Koliji, 2009, Laloui and Nuth, 2009, Salager et al., 2006, Sun et al., 2011c,a].

An alternative to this continuum approach is to explicitly model the interactions among particles, liquid bridges and air in the wetted granular assemblies. This discrete mechanics approach, often referred as distinct or discrete element method (DEM), is first introduced by Cundall and Strack [1979]. In DEM, motion of particles are governed by Newton's second law and their positions and velocities are computed by an explicit finite difference integration scheme. In this study, we use an open source discrete element code, YADE (Yet Another Dynamic Engine) to model the friction-cohesive mechanical behavior of wetted granular matters at the pendular regime [Šmilauer et al., 2010]. The linkage between micro-scale and macro-scale properties is established by the homogenization techniques, where macroscopic strain and stress tensors of a representative elementary volume are derived from the positions of particles and liquid bridges, as well as the normal, tangential forces exerted on them [Kruyt and Rothenburg, 1996]. The capillary physics was introduced into the model by solving the Young-Laplace equation. Various numerical simulations have been conducted to examine the evolution of mechanical and hydraulic properties of unsaturated granulates. To simplify the problem, we assume that the degree of saturation remains low enough during the numerical simulations such that water only exists in the form of liquid bridges between the surface of grain pairs. As a result, inter-particle normal force is combined effect of grain-to-grain normal contact force and capillary force developed in liquid bridges. Such hypothesis is usually valid at low water content and the corresponding unsaturated state is called the pendular regime. The triaxial compression tests were performed on numerical samples and the effect of partial saturation on macro and micro behaviors is studied.

5.3.1 Contact friction model

The classic frictional-normal contact law for cohensionless particles is adopted in the DEM simulation to model the granular contact between two particles. The contact force between two particles is generated when the two overlap with each other and follows the Hooke's law. Two stiffness can be defined: K_n and K_t in the normal $\boldsymbol{n}$ and tangential direction $\boldsymbol{t}$ of the contact plane respectively, as shown in Figure 5.2. Incremental

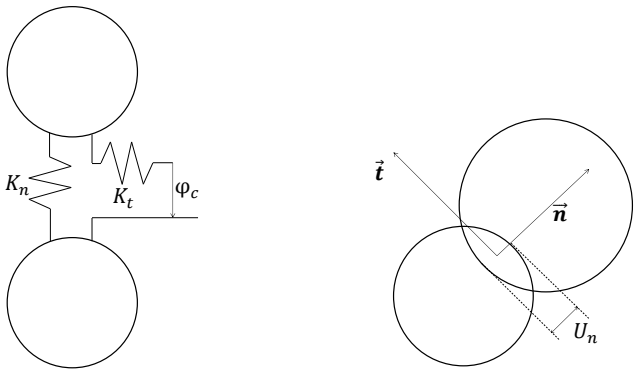

Figure 5.2: *Contact friction model.*

changes in the normal force $d\boldsymbol{F}_n$ and the tangential force $d\boldsymbol{F}_t$ are thus expressed as:

$$d\boldsymbol{F}_n = K_n dU_n \boldsymbol{n} \tag{5.7}$$

$$d\boldsymbol{F}_t = -K_t d\boldsymbol{U}_t \tag{5.8}$$

where dU_n is the incremental normal overlap distance and $d\boldsymbol{U}_t$ is the incremental tangential relative displacement vector.

The tangential force is limited by a maximum value of $||\boldsymbol{F}_t^{max}|| = -\mu||\boldsymbol{F}_n||$ according to the Coulomb friction law, where μ is the Coulomb friction coefficient. It is related to the inter-particle friction angle ϕ_c by $\mu = \tan(\phi_c)$.

More complex model such as Hertz-Mindlin could also be used [Sun et al., 2013c], yet studies suggested that there are no significant improvements compared to the linear model and that the calculation time increases significantly Di Renzo and Di Maio [2004].

5.3.2 Capillary model

Many DEM liquid bridge models have been developed to introduce attractive capillary forces between grains in pendular regime, and some of them are based on solving the Young-Laplace equation. For example, some researchers approximate the form of liquid bridge by torus and derive the water volume and capillary force from the suction pressure $\Delta p = p_{air} - p_{water}$, but the capability of treating poly-disperse assemblies is limited [Jiang et al., 2004]. There are also models which explicitly express the capillary force in terms of geometric parameters of liquid bridge, but in those cases the suction pressure becomes an additional unknown [Soulie et al., 2006]. In this study, we employ the capillary model implemented in the DEM code YADE to simulate the capillary effect at grain-scale. This model, originally introduced by Scholtès et al. [2009], differs from the above approaches in the sense that the suction pressure Δp is assumed uniform in space and serves as the control parameter for unsaturated sample tests. The distribution of liquid bridges in the samples is hence close to homogeneous. The menisci volumes and capillary forces are directly computed from Δp and grain-pair geometry by interpolating discrete numerical solutions of the Young-Laplace equation. We briefly outline the capillary model in this section and interested readers please refer to [Scholtès et al., 2009] for further information.

The geometry and parameters of the liquid bridge model are illustrated by Figure 5.3. The complex profile of the menisci is described by the curve function $y(x)$ in the coordinate system of 5.3. The two principal radii of the local surface curvature are given by $r_1(x) = y(x)\sqrt{1 + y'^2(x)}$ and $r_2(x) = \frac{(1+y'^2(x))^{3/2}}{y''(x)}$. The curvature of the liquid bridge C is defined by $\frac{1}{C} = \frac{1}{r_1} + \frac{1}{r_2}$. R_1 and R_2 are sphere radii, ζ_1 and ζ_2 are the filling angles, θ is the wetting angle, x_{c1} and x_{c2} are the x-coordinates of the solid-liquid-air interface, and D is the intergranular distance.

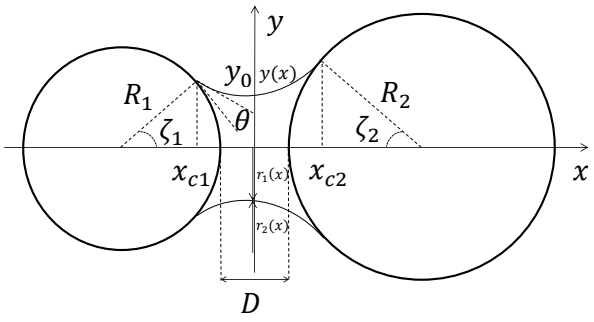

Figure 5.3: *Liquid bridge model*

The liquid bridge model is governed by a system of four nonlinear equations. Firstly, the curvature of the liquid bridge C can be related to the suction pressure $\Delta p = p_{air} - p_{water}$ and the surface tension γ through the Young-Laplace equation:

$$\Delta p = s = \frac{\gamma}{C} \tag{5.9}$$

The non-linear differential equation for the menisci profile $y(x)$ therefore writes:

$$\frac{\Delta p}{\gamma}(1 + y'^2(x))^{3/2} + \frac{1 + y'^2(x)}{y(x)} - y''(x) = 0 \tag{5.10}$$

The attractive capillary force exerted by the liquid bridge can be estimated at the profile neck y_0 based on the "gorge method" [Hotta et al., 1974]:

$$F_{\text{capillary}} = 2\pi y_0 \gamma + \pi y_0^2 \Delta p \tag{5.11}$$

The corresponding volume of liquid bridge between two spheres is computed by:

$$V = \pi \int_{x_{c1}}^{x_{c2}} y^2(x)dx - \frac{1}{3}\pi R_1^3(1-\cos(\zeta_1))^2(2+\cos(\zeta_1)) - \frac{1}{3}\pi R_2^3(1-\cos(\zeta_2))^2(2+\cos(\zeta_2)) \tag{5.12}$$

and the intergranular distance D:

$$D = R_2(1-\cos(\zeta_2)) + x_{c2} + R_1(1-\cos(\zeta_1)) - x_{c1} \tag{5.13}$$

The solution scheme of the above system of equations (5.10) - (5.13) incorporated in YADE leads to a suction-controlled model where the capillary force and volume of a liquid bridge can be determined by the imposed macroscopic suction pressure Δp for a given pair of spheres of radius R_1, R_2 and their inter-granular distance D. The formation of liquid bridge is assumed to occur once the two grains come into contact. The critical inter-granular distance beyond which the liquid bridge ruptures is not explicitly given, but corresponds to the distance value from which the Young-Laplace equation no longer provides a stable liquid bridge [Lian et al., 1993]. The distribution of liquid bridges evolves with the updated sample configuration and the overall degree of saturation is directly computed by the total volume of menisci. In this study, the surface tension is set to be 0.073 N/m and the contact angle θ is equal to 0 in the program.

The current model presents some simplifications and limitations. All particles in the granular assemblies are assumed spherical, and surface roughness and gravity are negligible [Toker et al., 2014]. The degree of saturation is restricted to low values ($Sr < 12\%$) so that overlappings of neighboring inter-particle liquid bridges are assumed negligible. The interparticle friction angle is assumed constant and does not vary with the degree of saturation. The model also does not incorporate the redistribution law of water when the menisci breaks.

5.4 DEM experiment results

5.4.1 Evolution of Bishop's coefficient during suction-controlled triaxial tests

We firstly investigate the evolution of the Bishop's effective stress coefficient χ during a triaxial compression test on a specimen of equal-sized spheres. The diameter of the grains is set to a small value of 0.1 mm (fine sand). A box made of six rigid frictionless walls is constructed, inside which a DEM assembly is prepared by a sphere packing generation algorithm available in YADE and contains about 11,000 particles. The material parameters are chosen to be the same as the previous DEM experiments in [Scholtès et al., 2009] (YoungâĂŹs modules E=50 MPa, ratio of tangential and normal stiffness $\alpha = \frac{k_t}{k_n} = 0.5$, and friction angle $\varphi_c = 30$ degree). The deforming of the DEM sample is carried out by moving the walls according to the prescribed loading processes. The suction pressure in the numerical test is maintained constant (10 kPa), corresponding to a suction-controlled triaxial test on unsaturated soil. This first simulation consists of three stages. An isotropic compression takes place under a confining pressure of 10 kPa. The quasi-static compression is carried out along the Y axis until 15% axial strain at which the sample is near its critical state, while the lateral borders (X, Z axis) always offer the 10 kPa confining pressure. The deformed sample is then subjected to an extensive loading path along the Y axis back to its origin zero-strain configuration, in order to see if the evolution of the BishopâĂŹs coefficient will follow the same curve in the opposite direction. The state path of the numerical test is shown in Fig.5.4 in the space of the shear stress $q = \sigma_1 - \sigma_3$, the average effective stress $p' = \frac{1}{3}(\sigma_1' + \sigma_2' + \sigma_3')$ and the porosity Φ, where the subscripts 1,2,3 denote the major, intermediate and minor principal directions in the compression test respectively. Note that we conserve this assignment although at the late phase of the reverse test the major and minor principal directions will switch between them ($\sigma_1 < \sigma_3$), thus allowing the shear stress to be negative and the ratio of the principal values to be smaller than 1.

The simulated hydro-mechanical responses such as the shear stress and the porosity (Fig.5.5) resemble those in classical triaxial compression and extension tests on sand [Shapiro, 2000]. In the compression test, as expected, the pre-consolidated sample shows an initial contractancy and then dilates with a decreasing slope until a critical porosity or degree of saturation is reached. During the extension test, the sample is firstly compressed and then dilated. However, the paths it follows does not coincide with the previous curves in

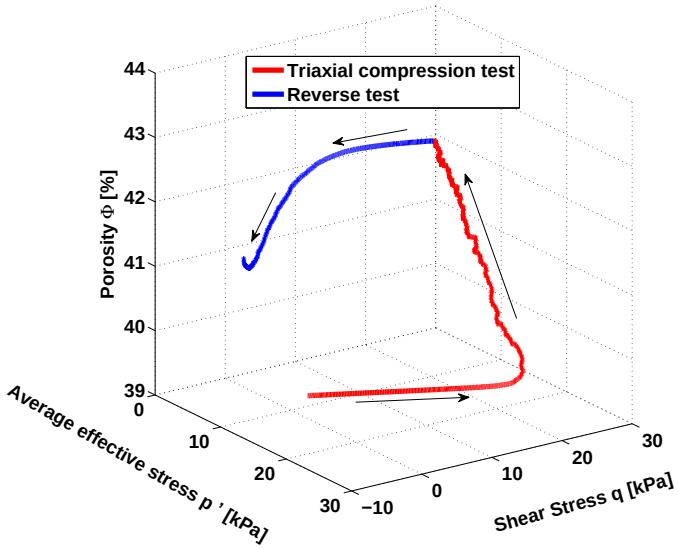

Figure 5.4: *State path of the triaxial compression test and the reverse test. The arrows point at the loading direction.*

compression test, although the only change in experiment conditions is the reverse of the axial loading direction. This can be foreseen based on the plastic nature of granular materials: the deformation of granular media induces a permanent change in the contact fabric because the internal contact and liquid bridge forces between grains are not capable of restoring the initial configuration. Under the external restoring load, the total major principal stress σ_1 quickly drops to the controlled lateral stress σ_3 at 14.2% strain (with initial isotropically confined sample as reference)and the principal directions alter thereafter. The switch between the contractancy and dilatancy occurs at 4% strain as indicated by the porosity Φ, the degree of saturation S_r and the coordination number K. We distinguish the coordination number of grain contact forces and the coordination number of liquid bridge forces and present their evolution in Fig. 6. The number of grain contacts immediately decreases when the deviatoric loading begins, and the evolution of number of liquid bridges lags behind, since meniscus could persist when a grain pair initially in contact is separated by a distance smaller than the model's rupture distance.

During the compression test as shown by the red curves in Fig.5.5, both the major principal component χ_1 and the minor component χ_3 of χ briefly increase and then decrease smoothly. The fact that χ_3 decreases more rapidly than χ_1 clearly reveals the anisotropic nature of the Bishop's effective stress coefficient. The measure of the anisotropy $\frac{\chi_1}{\chi_3}$ also follows closely the same pattern, suggesting a relation between the density of the sample and the anisotropy of the capillary stress tensor.

As for the extension test shown by the blue curves in Fig.5.5, χ_1 and χ_3 exhibit different behavior: χ_1 rises to a peak value at 12.5% strain and the the latter decreases neglecting the continuous reduction of Φ and the augmentation of S_r; χ_3 persistently increases although both Φ and S_r attain their extrema and evolves in opposite direction. The resulting evolvement ratio $\frac{\chi_1}{\chi_3}$ consists of two straight lines of different slopes (Fig.5.5 (f) guide lines) divided at the 12.5% strain where χ_1 reaches its peak.

The relation between χ and S_r is illustrated in Fig.5.7. Unlike the former totally different paths in the spaces such as (q, p', Φ), (q, ϵ) and (Φ, ϵ), the opposite loading initially reverses χ_1, χ_3 and $\frac{\chi_1}{\chi_3}$ approximately along the same paths as those in the compression test. The paths all bifurcate around $S_r = 3.58\%$ (Fig.5.7 guide lines), corresponding to the peak of χ_1 at 12.5 % strain. The Bishop's coefficient becomes more and more isotropic as its two principal components approach each other and an unstable isotropic state is attained when S_r reaches its extremum at 4% strain. Afterwards, the principal directions of χ alter and the degree of anisotropy rises again.

A micromechanical analysis method has been developed and exploited to investigate the internal structure of liquid bridges of wet granular media. The method separates the distribution of the menisci orientation and the distribution of the mean capillary force intensity by writing the capillary stress in the following form [Scholtès et al., 2009]:

$$\sigma^{\text{capillary}} = \frac{1}{V}\int_V < \mathbf{F}_{\text{capillary}} \cdot \mathbf{l} >_{\mathbf{n}} P_{\text{meniscus}}(\mathbf{n})\mathbf{n} \otimes \mathbf{n} dV \tag{5.14}$$

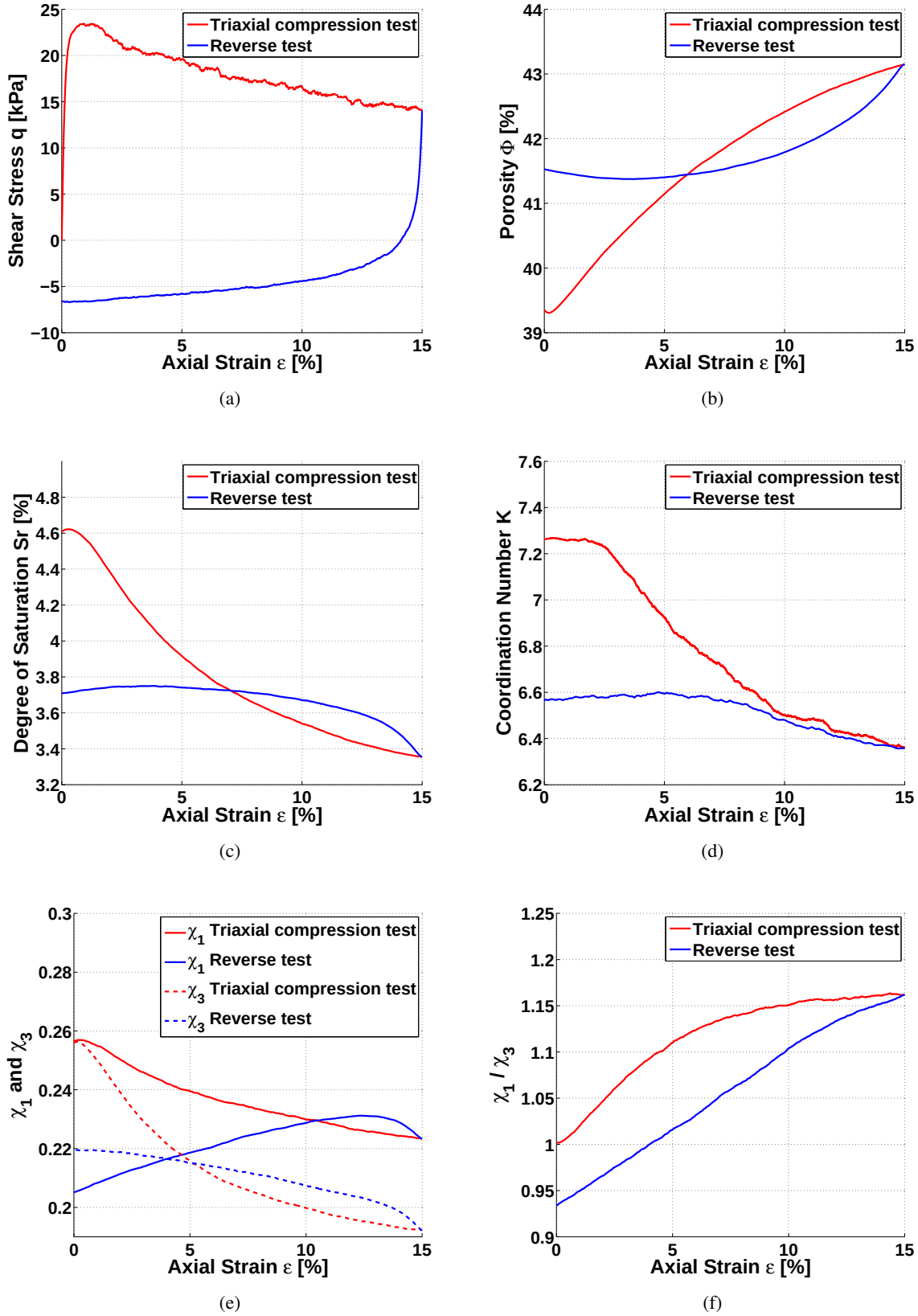

Figure 5.5: *Evolution of the (a) shear stress, (b) porosity, (c) degree of saturation, (d) coordination number, (e) major and minor principle values of the Bishop's coefficient and (f) their ratio along the triaxial compression test (red line, from left to right) and the reverse extension test (blue line, from right to left).*

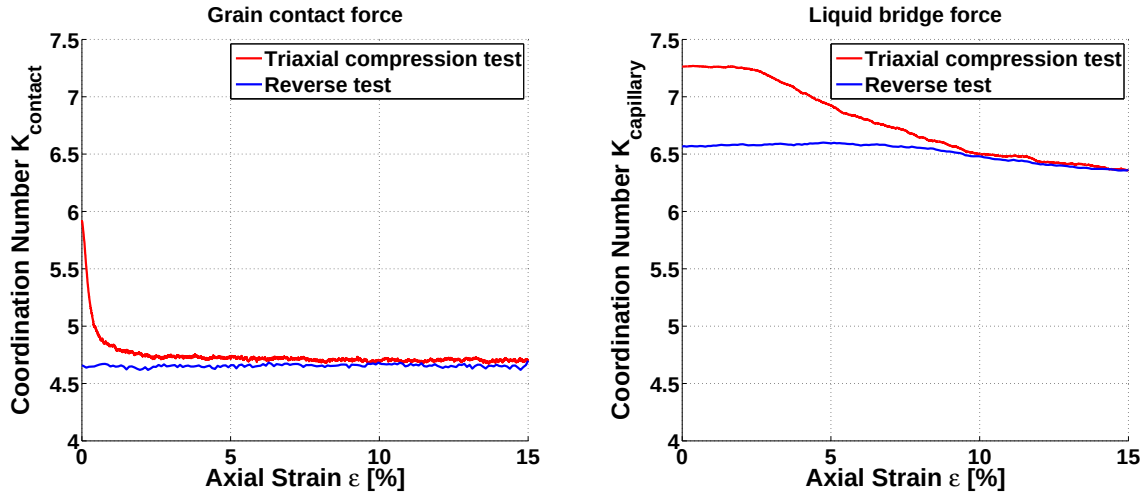

(a) (b)

Figure 5.6: *Evolution of the (a) coordination number of grain contact forces and (b) coordination number of liquid bridge forces along the triaxial compression test (red line, from left to right) and the reverse extension test (blue line, from right to left).*

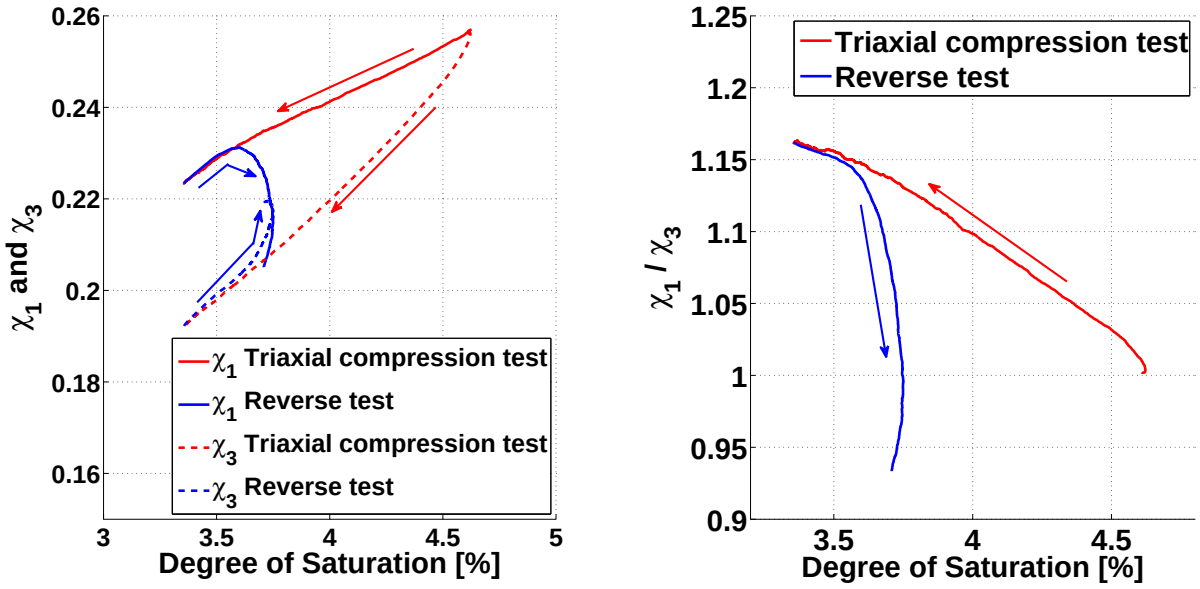

(a) (b)

Figure 5.7: *Major and minor principle values χ_1 and χ_3 of the Bishop's coefficient (a) and their ratio (b) vs. degree of saturation. At the late phase of the reverse test the major and minor principal directions switch between them, yet the subscripts 1 and 3 still refer to the same principal directions as before, allowing the ratio to be smaller than 1.*

where $\mathbf{n}$ refers to the unit vector of azimuthal direction emanated from the center of granular sample, $P_{\text{meniscus}}(\mathbf{n})$ is the probability of a meniscus having the orientation $\mathbf{n}$ and $< \mathbf{F}_{\text{capillary}} \cdot \mathbf{l} >_{\mathbf{n}}$ is the mean value of the dot product of the capillary force and the branch vector along the direction $\mathbf{n}$.

Figure 5.1 recapitulates the rose diagram within the YZ plane of the distribution of $P(\mathbf{n})$ and $< \mathbf{F} \cdot \mathbf{l} >_{\mathbf{n}}$ for both contacts and liquid bridges, setting the compression axis Y as the 0 degree reference. $P_{\text{contact}}(\mathbf{n})$ increases quickly in the Y direction and reduces in the lateral direction, in accordance with the external loading. $P_{\text{meniscus}}(\mathbf{n})$, however, has its own fabric and align with the Y axis very smoothly, since liquid bridges can still connect two separated grains within a rupture distance. On the other hand, both $< \mathbf{F}_{\text{contact}} \cdot \mathbf{l} >_{\mathbf{n}}$ and $< \mathbf{F}_{\text{capillary}} \cdot \mathbf{l} >_{\mathbf{n}}$ reach abruptly their maximum anisotropic patterns and then gradually reduce to smaller area when the whole sample becomes loose.

With regard to the subsequent extension test, Figure **??** illustrates the internal structure evolution when the

strain 0%	1%	5%
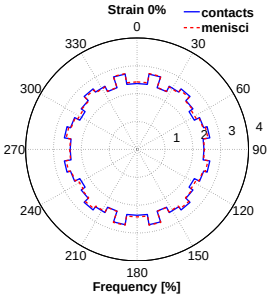	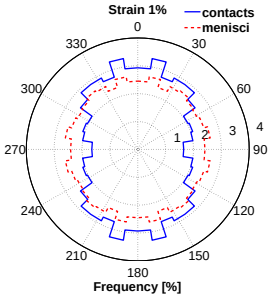	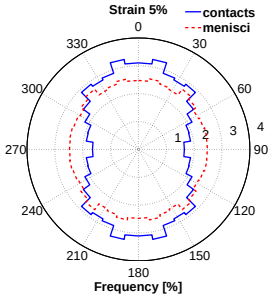
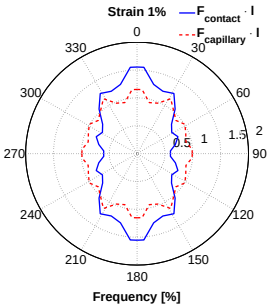	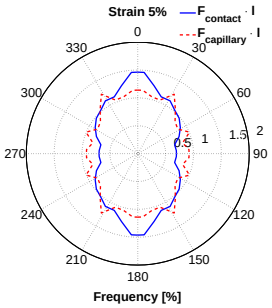	

Table 5.1: *Distribution of contact and menisci normal $P_{contact}(\boldsymbol{n})$, $P_{meniscus}(\boldsymbol{n})$ and average force intensity $< \boldsymbol{F}_{contact} \cdot \boldsymbol{l} >_{\boldsymbol{n}}$, $< \boldsymbol{F}_{capillary} \cdot \boldsymbol{l} >_{\boldsymbol{n}}$ during the suction controlled triaxial compression test.*

active border moves in the opposite direction. The elevation of χ_1 at the beginning appears to be dominated by the fact that more liquid bridges are oriented around the Y axis. This trend stops at 12.5% strain and $P_{\text{meniscus}}(\mathbf{n})$ starts to increase in the perpendicular direction. According to the capillary model introduced in section 5.3.2, the magnitude of the capillary force decreases as the inter-granular distance increases. The $< \mathbf{F} \cdot \mathbf{l} >_{\mathbf{n}}$ diagrams thus indicate that the inter-particle distances along Y axis are slowly enlarged and the distances along Z direction are reduced. Both evolution of $P_{\text{meniscus}}(\mathbf{n})$ and $< \mathbf{F} \cdot \mathbf{l} >_{\mathbf{n}}$ result in the decrease of the major principal component of the capillary stress $\sigma_1^{\text{capillary}}$ and χ_1 drops gradually as shown in Fig. 5.5 and 5.7.

The above micromechanical analysis emphasizes that the distribution of liquid bridge orientation and intergranular distance have important roles on the anisotropy of the Bishop's effective stress coefficient χ. The fabric of menisci orientation and that of intergranular distance are generally different and their evolution under external loads depends on the previous configuration of the granular structure or the loading history. The main source of the discrepancy between contact and capillary stress anisotropies is the different role capillary interactions play in grain assemblies. Unlike solid contact between grains, liquid bridges are capable of connecting closely separated neighboring particles and provide attractive capillary forces.

Additional simulations analogous to the previous tests were later performed to study the effect of suction pressure SU on the evolution of χ during the extension test. The curves shown in Fig.5.8 confirm that the formerly observed evolution trends of χ_1, χ_3 and $\frac{\chi_1}{\chi_3}$ also present for SU=20 kPa and SU=50 kPa. However, both the strains at which χ_1 reaches its peak and χ_1 and χ_3 intersect shift to right. Furthermore, the degree of anisotropy increases with SU.

5.4.2 Effect of fines content on Bishop's coefficient

It has been commonly accepted that the internal structure of granular materials will be modified upon addition of fine particles. For example, small amounts of silt particles introduced into sand could make the sand structure less stable, thus increase the compressibility of the mixture [Lade and Yamamuro, 1997]. The behavior of this granular mixture under external loads strongly depends on its internal force-chain, through which interaction forces are transferred and endured [Thevanayagam, 1998]. Some fines may be inactive in the force transmission as they sit in voids of the soil skeleton constructed by coarse grains, while others can sustain forces as they are trapped in the contact regions between the larger grains. When more fines are added, the contact between fine grains may become predominant inside the sample. An illustration of different mixture

strain 15%	12.5%	10%
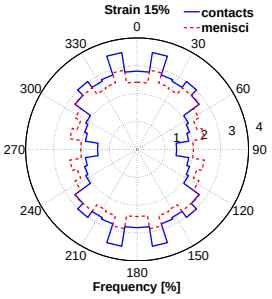	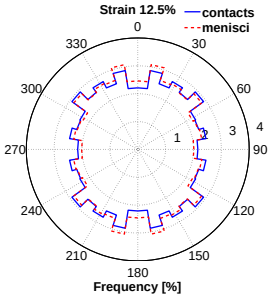	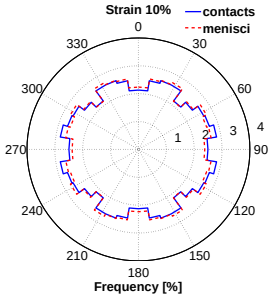
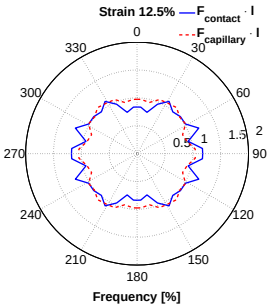	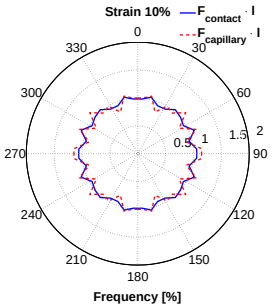	

Table 5.2: *Distribution of contact and menisci normal $P_{contact}(\boldsymbol{n})$, $P_{meniscus}(\boldsymbol{n})$ and average force intensity $< \boldsymbol{F}_{contact} \cdot \boldsymbol{l} >_{\boldsymbol{n}}$, $< \boldsymbol{F}_{capillary} \cdot \boldsymbol{l} >_{\boldsymbol{n}}$ during the suction-controlled triaxial extension test.*

configurations is shown in Fig.5.9.

In our DEM simulations on investigating the effect of fines content on Bishop's coefficient χ, we prepared a series of numerical samples composed of large particles and different amounts of fines. The same sphere packing generation algorithm as in Section 4.1 is employed. Firstly, for each sample, 5,000 large grains of 0.1 mm diameter are randomly distributed inside a cubic box made of six rigid frictionless walls with no overlaps in between. All samples have the same initial configuration of coarse grains. Then, fine grains of 0.04 mm diameter are randomly inserted into the void of these coarse grain networks. In the resulting mixtures, the ratios of the number of coarse grains and fine grains $n_{\text{coarse}} : n_{\text{fine}}$ are equal to 1:7, 1:8, 1:9 and 1:10, respectively. Each sample is consolidated closely to the same porosity of 0.342 under 10 kPa confining pressure by setting the friction angle to as small as 0.5 degree. It is then reset to 30 degree for compression test along Y axis.

As presented in Fig. 5.10, $n_{\text{coarse}} : n_{\text{fine}} = 1 : 7$ and $n_{\text{coarse}} : n_{\text{fine}} = 1 : 8$ samples have nearly the same peak shear stresses as the coarse sample, but possess higher residual shear stresses. The peaks in other samples are slightly reduced, suggesting that the skeleton of coarse grains is rendered less stable by high amounts of fines. The dilantacy for all mixtures is largely increased as expected.

When different amount of fines are added into the sample of large grains, the major principal component of the Bishop's coefficient χ_1 as well as the major/minor principle value ratio $\frac{\chi_1}{\chi_3}$ decreases significantly, as observed in Fig. 5.11. Since the initial grain assemblies composed of particles of different sizes do not necessarily yield isotropic grain structures, the principal components χ_1 and χ_3 may not coincide at 0% strain. For each coarse-fine grains sample in our simulations, the major principal direction corresponds to the lateral directions (X, Z axis) at the beginning of the deviatoric loading. As the axial strain (along Y axis) is applied gradually, the axial component of Bishop's coefficient surpasses the lateral components and thus the axial direction becomes the major principal direction. The strain at which the principal directions alter depends on the fines content. The ratio $\frac{\chi_1}{\chi_3}$ is reduced in all mixtures by about 6.8 percent. This observation reveals that the mechanical response of grain assemblies with fines is more isotropic.

Fig. 5.12 provides the relationships between the Bishop's coefficient and the degree of saturation. The increased retention of water, reduction of component values and decreased anisotropy could be clearly observed. These phenomena make χ closer to the $\chi = S_r$ line, corresponding to the assumption that the coefficient is equal to the degree of saturation [Laloui and Nuth, 2009].

In order to gain a notion on how the internal structures of the coarse-fine mixtures are influenced by deviatoric loading and presence of fines, we distinguished the contacts between two coarse grains, two fines and

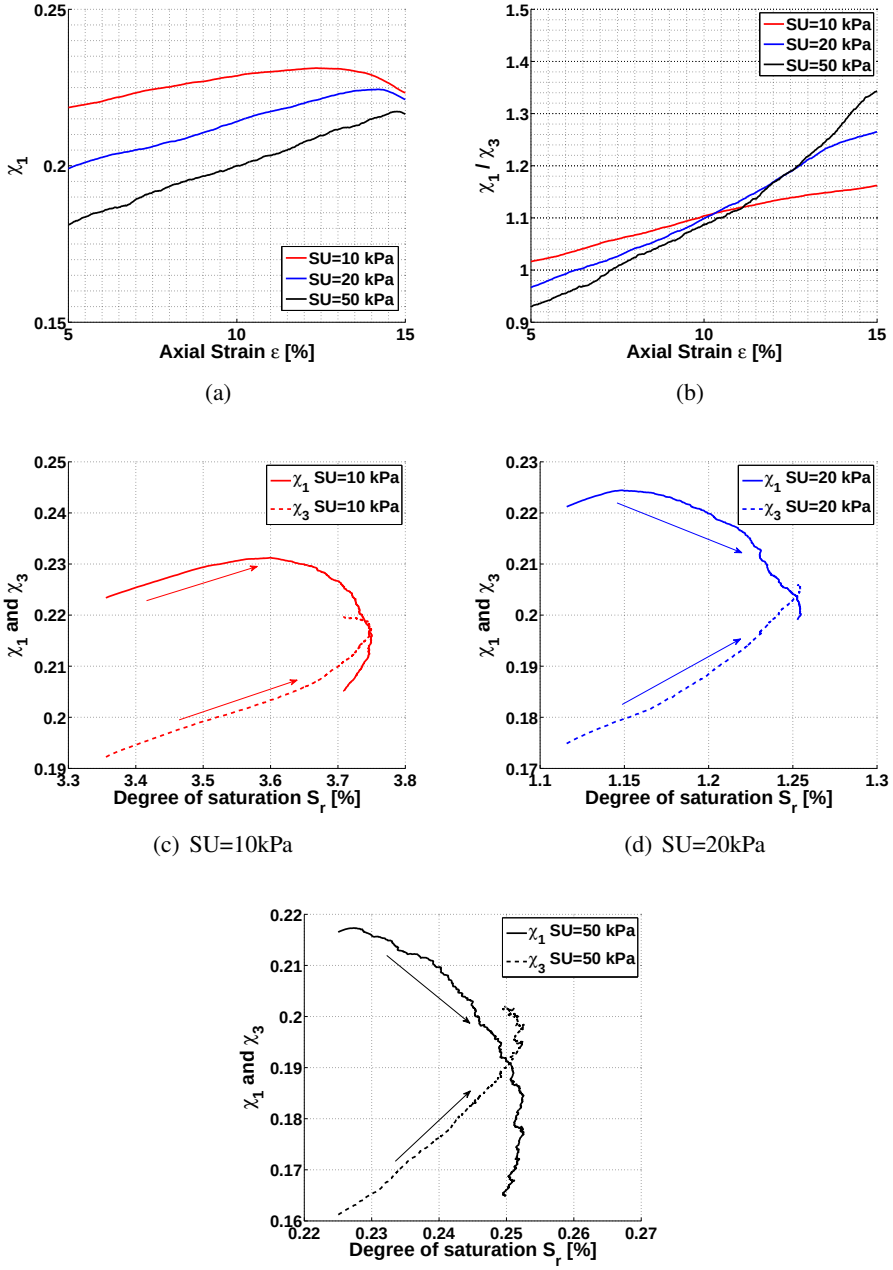

Figure 5.8: *Evolution of Bishop's coefficient during extension test (from 15% to 5%).* χ_1 *(top left) and* $\frac{\chi_1}{\chi_3}$ *(top right) versus axial strain.* χ_1 *and* χ_3 *versus degree of saturation* S_r *(bottom) under suction of 10 kpa (c), 20 kpa (d), and 50 kpa (e). The arrows point at the loading direction. The initial isotropic configuration is set to be the reference.*

coarse-fine grains couple, then monitored the evolution of their potion during triaxial compression tests. The same counts were performed for liquid bridges. The results are shown in Fig.5.13. It is common behavior that the coarse-coarse contacts and coarse-fine contacts decrease as the samples are slowly compressed along Y axis, while the portion of fine-fine contacts augment. Liquid bridges have the similar trends but the changes are more subtle. Besides, we could see that the coarse-fine interactions dominate in $n_{\text{coarse}} : n_{\text{fine}} = 1 : 7$ sample. When the fines content is varied to $n_{\text{coarse}} : n_{\text{fine}} = 1 : 8$, the coarse-fine and fine-fine occupy approximately the same level of portion. With further increase in fines content, fine-fine interactions predominate over coarse-fine interactions, indicating that the skeleton constituted of fine grains starts to take over the responsibility of reacting to external loads.

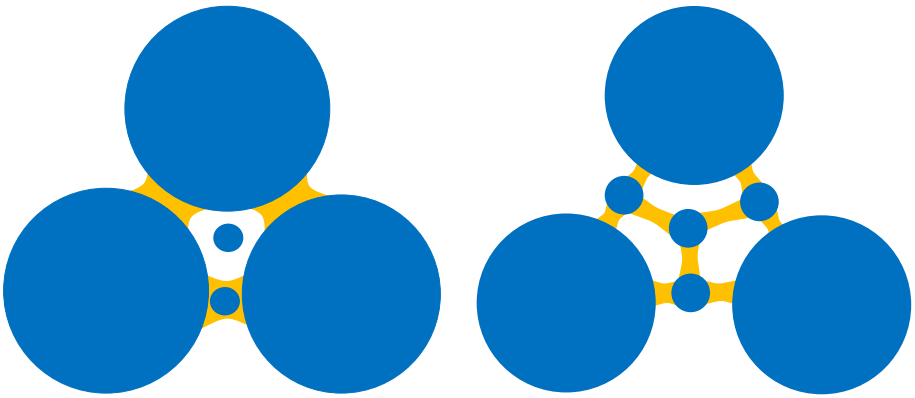

(a) (b)

Figure 5.9: *Inter-granular soil mix classification. Case (a): network dominated by coarse grain interactions with fine particles confined within void or between grains. Case (b): network dominated by fine grain interactions. The inter-granular distances are enlarged to show the network of liquid bridges.*

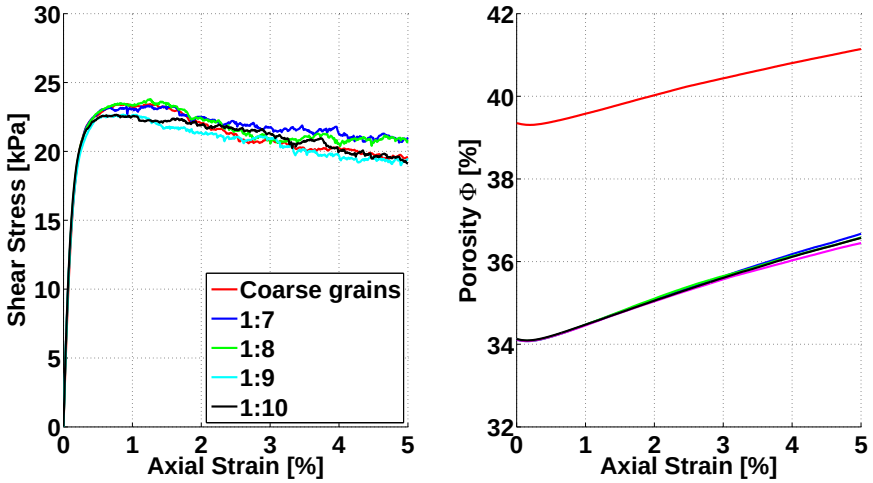

Figure 5.10: *Shear stress (left) and porosity (right) versus axial strain curves with SU= 10kPa under constant confining stress 10 kPa. The samples are prepared with different ratios of the number of coarse grains and fine grains* $n_{coarse} : n_{fine}$

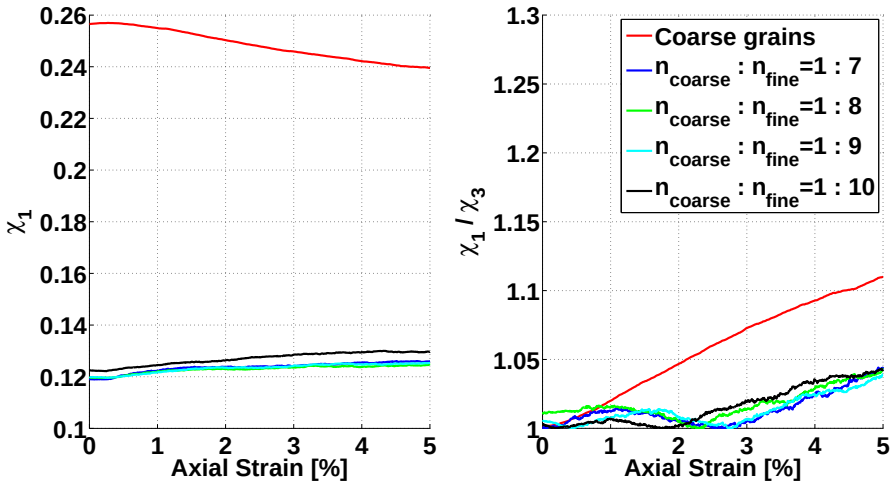

Figure 5.11: χ_1 *(left) and* $\frac{\chi_1}{\chi_3}$ *(right) versus axial strain for samples of different amount ratios of coarse grains and fine grains* $n_{coarse} : n_{fine}$

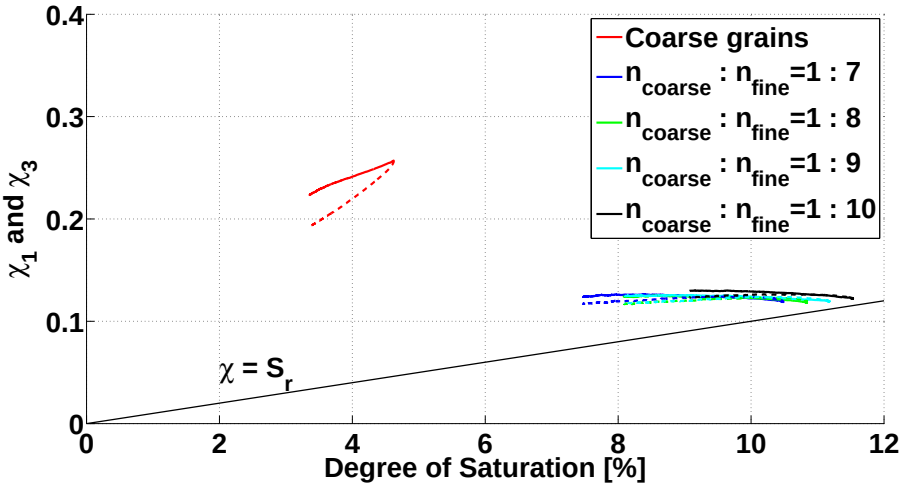

Figure 5.12: χ_1 *(solid lines) and* χ_3 *(dashed lines) versus degree of saturation* S_r *for samples of different amount ratios of coarse grains and fine grains* $n_{coarse} : n_{fine}$

5.4.3 Effect of suction pressure on χ for coarse sample and coarse-fine mixture

In this section we perform triaxial compression tests with different suction pressure SU on samples of equal-sized coarse grains of diameter 0.1 mm (A) and the mixture of coarse and fine grains (B). Firstly, 5,000 large grains are distributed randomly inside a cubic box with no overlaps in between, whose configuration is identical in A and B. Then, for sample B, fine grains of 0.04 mm diameter are inserted into the void as many as possible. The resulting mixture has a coarse/fine grains number ratio of 1:7.3 and a volume ratio of 1:0.4672. Both samples are isotropically consolidated under confining pressure of 10 kPa before the deviatoric loading.The initial porosity of sample A and B are 0.394 and 0.341, respectively.

Fig.5.14 presents the stress-strain relationships and porosity versus axial strain curves under different suction pressure of 10 kPa, 20 kPa, 50 kPa. Both A (left column)and B (right column) show peak shear stresses and exhibit strain-softening behavior, as well as the initial contractancy and following dilatancy. The curves suggest that adding fines into the coarse grains increases the peak shear stress and also the dilatancy under the same SU. In addition, fines make the suction pressure effect more significant, based on the observation that the discrepancies of the stress and porosity curves between different pressure are enlarged for sample B.

Fig. 17 presents the evolution of principal components of Bishop's coefficient and their ratio. For sample A, the principal values curves under different SU display the similar behavior as the study in Section 3.1. Both χ_1 and χ_3 decrease as the SU increases. For sample B, however, the evolution of the principal values is changed, since the initial internal structure constituted by coarse grains is modified by fines. Under 10 kPa suction pressure, the components significantly reduce 54 percent at 0% strain compared to A, and the component in lateral direction is larger than the axial component at the first time. The principal directions switch later at about 2% strain. The differences of χ_1 and χ_3 between the cubic shape at 0% strain and the deformed shape at 5% strain are also decreased. The same reduction also appears for SU=20k Pa, where the magnitudes maintain the same. On the other hand, for SU=50k Pa, the initial values of χ_1 and χ_3 increased about 58%. The curves of χ_1/χ_3 in Fig.5.16 indicate that the degree of anisotropy increases with SU for each sample. Comparison between A and B shows that χ becomes more isotropic when fines are added in between large particles. The ratio χ_1/χ_3 drops by 6.3%, 10.5% and 7.7% for SU=10 kPa, 20 kPa and 50 kPa respectively. This phenomenon may be attributed to the fact that the number of water bridges between two large grains is remarkably raised. Fine particles could fill the void between coarse grains and offer more proximate intergranular regions, thus capture much more water. Moreover, the contact normals between fines inside the inter-space of large grains are diversified and thus making the directions of trapped menisci more random. In this case the coarse grains are submerged in media of fines and smaller water bridges that are closer to saturated water than the discrete water bridges in sample A. Therefore, sample B exhibits less anisotropy on Bishop's coefficient than sample A.

Fig.5.16 describes the relationship between the Bishop's coefficient and S_r under different suction pressure. All the curves shift towards right for sample B, confirming that more water is retained. For SU=10 kPa, the combination of this phenomena and the reduction of χ_1 and χ_3 values makes χ closer to the $\chi = S_r$ line.

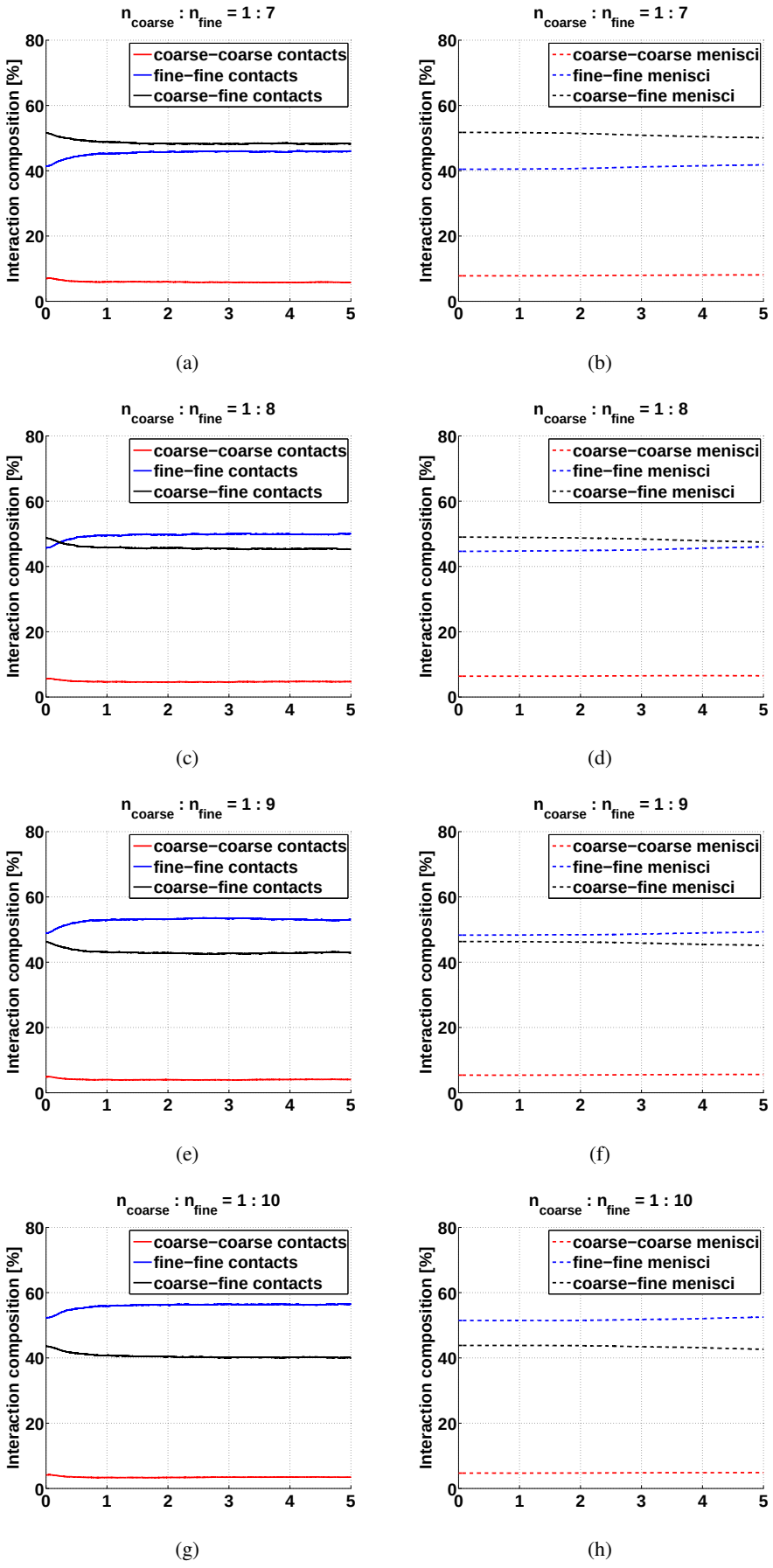

Figure 5.13: *Evolution of interaction compositions versus axial strain for samples of different amount ratios of coarse grains and fine grains* $n_{coarse} : n_{fine}$

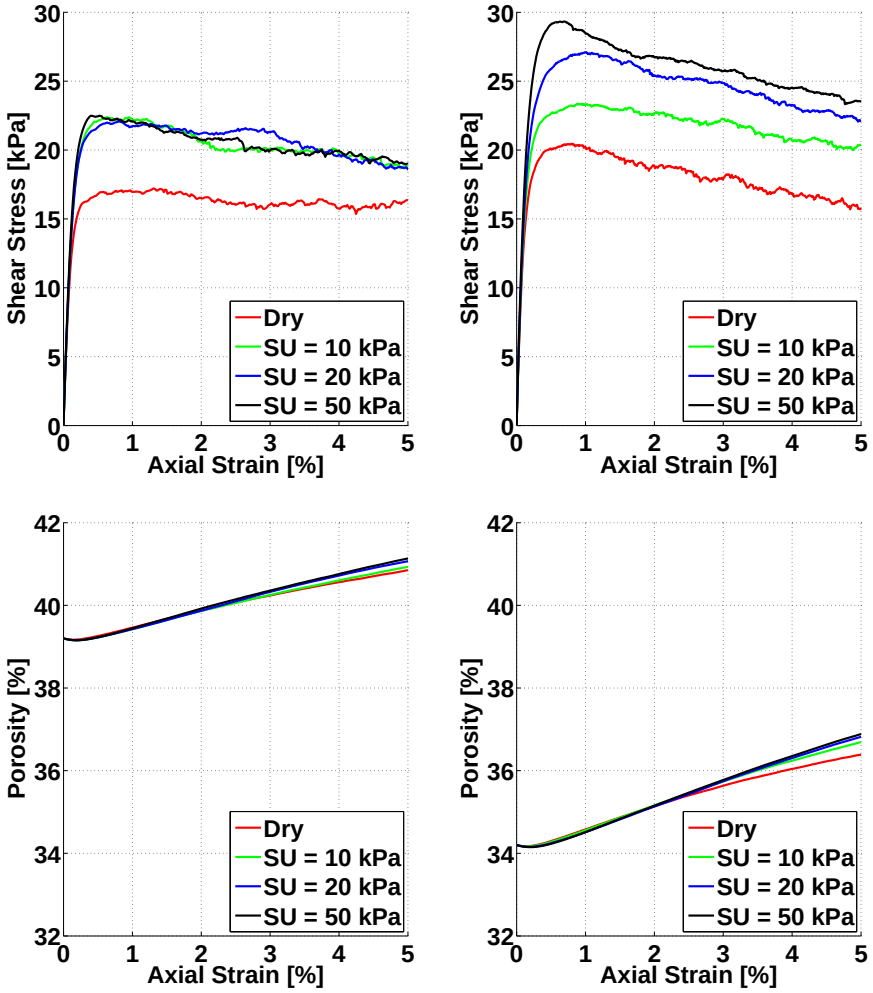

Figure 5.14: *Shear stress and porosity versus axial strain curves with different suctions (SU) under constant confining stress 10 kPa. Left column: sample of coarse grains . Right column: mixture of coarse and fine grains*

5.5 Conclusions

In this work, we introduce a tensorial Bishop coefficient χ to characterize the anistropic responses of wetted granular materials. Using solutions from the Young-Laplace equation, we conduct discrete element simulations to analyze how the formation and rupture of liquid bridges affects the principal values and directions of the tensorial Bioshop coefficient for two grain assemblies undergoing triaxial compression and extension loading paths. The results suggest that the anisotropy of χ is inherently path dependent and also related to suction pressure. A statistic analysis of interaction normal distribution offers micro-scale investigation of the effect of contact and menisci fabric evolution on Bishop's coefficient. Another group of simulations were performed on samples of coarse grains whose internal skeleton was modified by insertion of different amounts of fine grains. These samples of various fines contents were subjected to triaxial compression loading. Results suggest a dependence of Bishop's coefficient on the type of interaction that dominates the skeleton. Comparing results for both coarse sample and mixtures, we concluded that the addition of fines captures more water and renders the liquid bridges distribution less discontinuous and less anisotropic. On the other hand, the tests under different suction pressure confirmed that a sample with high SU retains less volume of water, thus has a more discrete menisci distribution and show more anisotropy on Bishop's coefficient.

This paper focuses on the study of unsaturated granular matter in pendular regime. To extend this study to higher degree of saturation, the Young-Laplace equation could no longer be used. The usage of CFD or two-phase flow interacting with DEM is more appropriate and will be in the scope of future studies. The current models also does not consider some factors such as surface roughness, hysteresis of contact angle and the coalescence and redistribution of liquid bridges. The study within this paper bases on the idealized numerical model and does not fully replicate the real behaviour of unsaturated soils. An ongoing research is performed to improve the numerical model by comparing with experimental results.

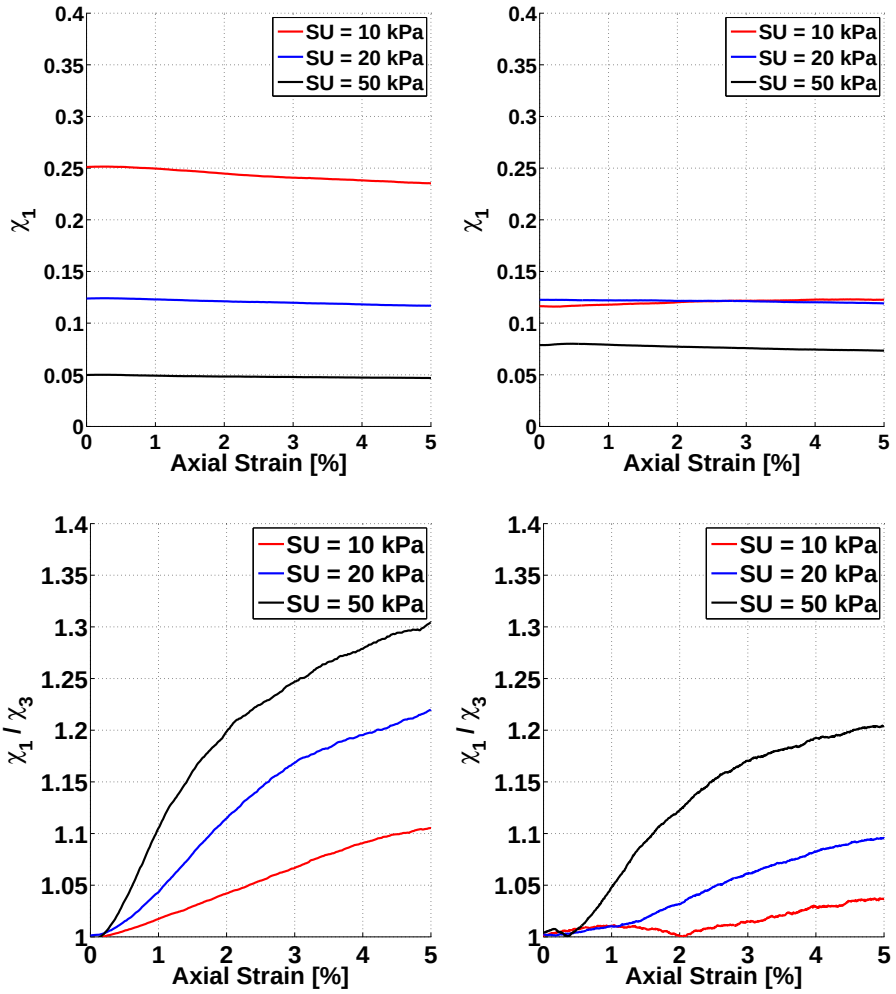

Figure 5.15: χ_1 *and* $\frac{\chi_1}{\chi_3}$ *versus axial strain for sample of coarse grains (left column) and mixture of coarse and fine grains (right column)*

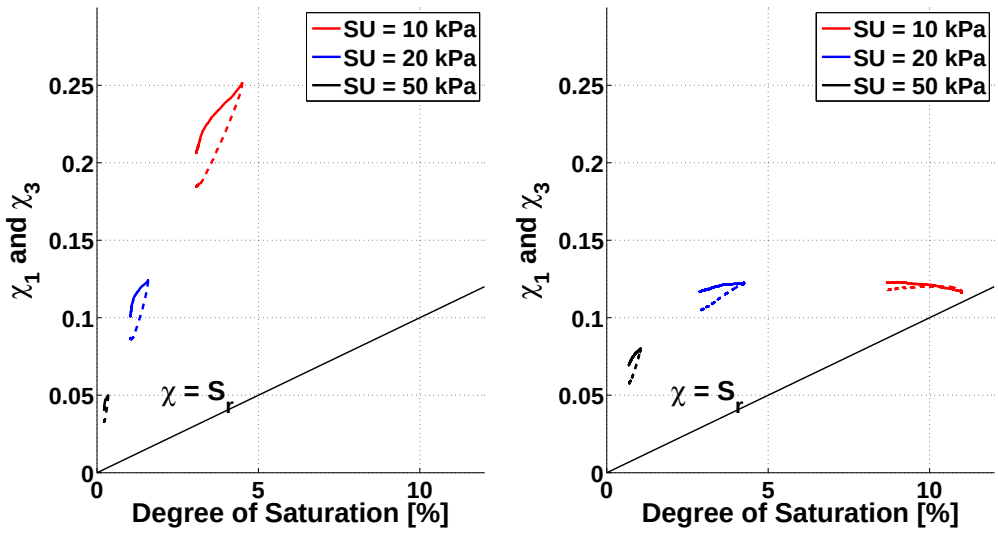

Figure 5.16: χ_1 *(solid lines) and* χ_3 *(dashed lines) versus degree of saturation* S_r *for sample of coarse grains (left column) and mixture of coarse and fine grains (right column)*

Chapter 6

Key Findings on multiscale granular physics

6.1 Introduction

A two-phase fluid-infiltrating porous solid is made of a solid matrix and a pore space saturated by fluid. When subjected to external loading, the mechanical responses of the porous solid strongly depend on whether and how pore fluid diffuse inside the pore space. The classical approach to model the fluid-solid interaction in a porous solid is to consider it as a mixture continuum in the macroscopic scale. At each continuum material point, a fraction of volume is occupied by one or multiple types of fluid, while the rest of volume is occupied by the solid constituent. A governing equation can then be derived from balance principles of the mixture [Terzaghi et al., 1943, Biot, 1941b, Truesdell and Toupin, 1960, Bowen, 1980, 1982]. One key ingredient for the success of this continuum approach is the effective stress principle, which postulates that the external loading imposed on porous solid is partially carried by the solid skeleton and partially supported by the fluid [Terzaghi, 1936, Biot, 1941b, Nur and Byerlee, 1971b, Rice and Cleary, 1976a]. By assuming that the total stress is a linear combination of the effective stress of the solid skeleton and the pore pressure of interstitial fluid, analytical and numerical solutions can be sought once a proper set of constitutive laws is identified to relate effective stress with strain and internal variables, and Darcy's velocity with pore pressure can be identified even though effective stress cannot be measured directly [Terzaghi et al., 1943, Schofield and Wroth, 1968, Wood, 1990, Manzari and Dafalias, 1997, Pestana and Whittle, 1999, Ling et al., 2002]. In recent years, the advancement of computational resources has led to the development of numerous finite element models that employ the effective stress principle [Prevost, 1982, Simon et al., 1986, Borja and Alarcón, 1995b, Armero, 1999, Sun et al., 2013e, Sun, 2015a]. Nevertheless, modeling the complex path-dependent responses for geomaterials remains a big challenge [Dafalias and Manzari, 2004]. This difficulty is partly due to the need to incorporate a large amount of internal variables and material parameters, which makes the calibration more difficult. Another difficulty is due to the weak underpinning of the phenomenological approach to replicate anisotropy caused by changes of micro-structures and fabric [Li and Dafalias, 2015].

A conceptually simple but computational expensive remedy to resolve this issue is to explicitly model the microscopic fluid-solid interaction. In fact, this approach has been widely used to study sedimentation problems. Previous work, such as Han et al. [2007], Mansouri et al. [2009], Goniva et al. [2010], Han and Cundall [2013], Robinson et al. [2014], Berger et al. [2015], has obtained various degree of successes in simulating fluidized granular beds by establishing information exchange mechanism among discrete element model and fluid solvers. For a subset of two-phase problems in which the length scale of interest is larger than the grain diameter and the fluid flow is laminar, the pore-scale interstitial fluid motion is often not resolved but instead modeled via a locally averaged Navier-Stokes equations (LANS) that couples with DEM via a parametric drag force [Curtis and Van Wachem, 2004, Robinson et al., 2014]. By assuming that a weak separation of scale is valid, this meso-scale approach essentially couples the large scale Navier-Stokes fluid motion with grain-scale DEM model that captures the granular flow nature via interface force. While this method is found to be very efficient for mixing problem, coupling the macroscopic flow at meso-scale via force-based interaction is not without limitations. First, the simulated hydro-mechanical coupling effect is highly sensitive to the fluid drag force model chosen to replicate the particle-fluid interaction. This can lead to complications for calibration and material identification, as the expressions of these fluid drag forces are often empirically correlated by the local porosity, Reynolds number and other factors such as the diameter of the particles, [Zhu et al., 2007]. Furthermore, the meso-scale fluid-particle simulations still require significant computational resources when a large number of particles are involved.

The purpose of this study is to propose a new multiscale hydro-mechanical model that (1) provides the physical underpinning from discrete element simulations, (2) resolves the problems associated with the phenomenological nature of drag force, and (3) improves the efficiency of large-scale problems. Our target is a sub-class of problems in which the solid skeleton is composed of particulate assemblies in solid state (rather than granular flow) and the porous space is fully saturated with a single type of pore fluid in laminar regime. As in the previous work for particle-fluid system [Curtis and Van Wachem, 2004, Robinson et al., 2014], we also adopt the assumption that a weak separation of scale exists between the motion of solid particles and that of the pore fluid. Our major departure is the way we employ this weak separation of the pore fluid to establish hydro-mechanical coupling across length scales. Instead of using the phenomenological drag force model to establish coupling, we use the effective stress principle to partition the macroscopic total stress as the sum of effective stress, which comes from microscopic DEM simulation, and the fluid contribution, which comes from the Biot's coefficient inferred from DEM assemblies and the pore pressure updated from a total Lagrangian poromechanics finite element solver.

The coupled transient problem requires a time integration scheme to advance numerical solution from known solid displacement $\boldsymbol{u}_n$ and pore-fluid pressure p_n^f at time t_n to unknowns $\boldsymbol{u}_{n+1}$ and p_{n+1}^f at the next time step $t_{n+1} = t_n + \Delta t$. Explicit integration scheme has been employed in multiscale dynamic analysis of soils [Onate and Rojek, 2004]. This method is simple in the sense that it advances solutions without solving system of equations. However, it often requires small time steps in order to achieve numerical stability, and when coupling with DEM solver, the condition is even more stringent. Another approach, the implicit scheme, has the possibility of attaining unconditional stability, but the linearization of variational equations, equation solving and iterations require much computational cost per time step. To make a trade-off, Hughes et al. [1979] and Prevost [1983] suggest the usage of an implicit-explicit predictor/multicorrector scheme in nonlinear hydro-mechanical transient problem. Our main contribution in this study is the extension of this method to multiscale coupling problems. We suggest a distinct treatment of the elastic and plastic component of material stiffness homogenized from DEM microstructures. Accordingly, an information exchange scheme is established between the FEM and DEM solvers.

The rest of this paper is organized as follows. In section 2, we first describe the homogenization theory for saturated porous media serving as the framework for micro-macro transitions. Then, the discrete-continuum coupling model in the finite deformation range is presented in Section 3. The details of the multiscale semi-implicit method are provided in Section 4, with an emphasis placed on how the material properties homogenized from DEM are employed in the semi-implicit FEM-mixed-DEM solution scheme. Selected problems in geomechanics are simulated via the proposed method to study its performance and their results are presented in Section 5. Finally, concluding remarks are given in Section 6.

As for notations and symbols, bold-faced letters denote tensors; the symbol '$\cdot$' denotes a single contraction of adjacent indices of two tensors (e.g. $\boldsymbol{a} \cdot \boldsymbol{b} = a_i b_i$ or $\boldsymbol{c} \cdot \boldsymbol{d} = c_{ij} d_{jk}$); the symbol ':' denotes a double contraction of adjacent indices of tensor of rank two or higher (e.g. $\boldsymbol{C} : \boldsymbol{\epsilon^e} = C_{ijkl}\epsilon^e_{kl}$); the symbol '$\otimes$' denotes a juxtaposition of two vectors (e.g. $\boldsymbol{a} \otimes \boldsymbol{b} = a_i b_j$) or two symmetric second order tensors (e.g. $(\boldsymbol{\alpha} \otimes \boldsymbol{\beta}) = \alpha_{ij}\beta_{kl}$). As for sign conventions, we consider the direction of the tensile stress and dilative pressure as positive. We impose a superscript $(\cdot)^{\text{DEM}}$ on a variable to emphasize that such variable is inferred from DEM.

6.2 Homogenization theory for porous media

In this section, we describe the homogenization theory we adopt to establish the DEM-mixed-FEM coupling model for fully saturated porous media. Previous work for dry granular materials, such as Miehe and Dettmar [2004], Miehe et al. [2010], Nitka et al. [2011], Guo and Zhao [2014], has demonstrated that a hierarchical discrete-continuum coupling model can be established by using grain-scale simulations to provide Gauss point stress update for finite element simulations in a fully implicit scheme. Nevertheless, the extension of this idea for partially or fully saturated porous media has not been explored, to the best knowledge of the authors.

In this work, we hypothesize that the pore-fluid flow inside the pores is in the laminar regime and is dominated by viscous forces such that Darcy's law is valid at the representative elementary volume level [Sun et al., 2011c,a, 2013c]. Provided that this assumption is valid, we define the pore pressure field only at the macroscopic level and neglect local fluctuation of the pore pressure at the pore- and grain-scale.

On the other hand, we abandon the usage of macroscopic constitutive law to replicate the constitutive responses of the solid constituent. Instead, we apply the effective stress principle [Terzaghi et al., 1943, Gray et al., 2009, 2013] and thus allow the change of the macroscopic effective stress as a direct consequence of the

compression, deformation and shear resistance of the solid constituent inferred from grain-scale simulations. As a result, the effective stress can be obtained from homogenizing the forces and branch vectors of the force network formed by the solid particles or aggregates, while the total stress becomes a partition of the homogenized effective stress from the microscopic granular assemblies, and the pore pressure from the macroscopic mixture continuum.

6.2.1 Dual-scale effective stress principle

In this study, we make assumptions that (1) a separation of scale exists and that (2) a representative volume element (RVE) can be clearly defined. Strictly speaking, the assumption (2) is true if the unit cell has a periodic microstructure or when the volume is sufficiently large such that it possesses statistically homogeneous and ergodic properties [Gitman et al., 2007].

With the aforementioned assumptions in mind, we consider a homogenized macroscopic solid skeleton continuum $\mathcal{B}^s \subset \mathbb{R}^3$ whose displacement field is C^0 continuous. Each position of the macroscopic solid body in the reference configuration, i.e., $\boldsymbol{X} = \boldsymbol{X}^s \in \mathcal{B}_0^s$, is associated with a micro-structure of the RVE size. Let us denote the trajectories of the macroscopic solid skeleton and the fluid constituent in the saturated two-phase porous medium from the reference configuration to the current solid configuration as,

$$\boldsymbol{x} = \boldsymbol{\varphi}^s(\boldsymbol{X}, t) \;\; ; \;\; \boldsymbol{x} = \boldsymbol{\varphi}^f(\boldsymbol{X}^f, t) \tag{6.1}$$

Unless the porous medium is locally undrained, the solid and fluid constituents are not bundled to move along the same trajectory, i.e., $\boldsymbol{\varphi}^s(\cdot, t) \neq \boldsymbol{\varphi}^f(\cdot, t)$. If we choose to follow the macroscopic solid skeleton trajectory to formulate the macroscopic balance principles, then the control volumes are attached to solid skeleton only, and the pore fluid motion is described by relative movement between the fluid constituent and the solid matrix, as shown in Fig. 6.1. The deformation gradient of the macroscopic solid constituent $\boldsymbol{F}$ can therefore be written as,

$$\boldsymbol{F} = \frac{\partial \boldsymbol{\varphi}(\boldsymbol{X}^s, t)}{\partial \boldsymbol{X}^s} = \frac{\partial \boldsymbol{\varphi}(\boldsymbol{X}, t)}{\partial \boldsymbol{X}} = \frac{\partial \boldsymbol{x}}{\partial \boldsymbol{X}} \tag{6.2}$$

in which we omit the superscript s when quantities are referred to solid phase. Now, following [Miehe and

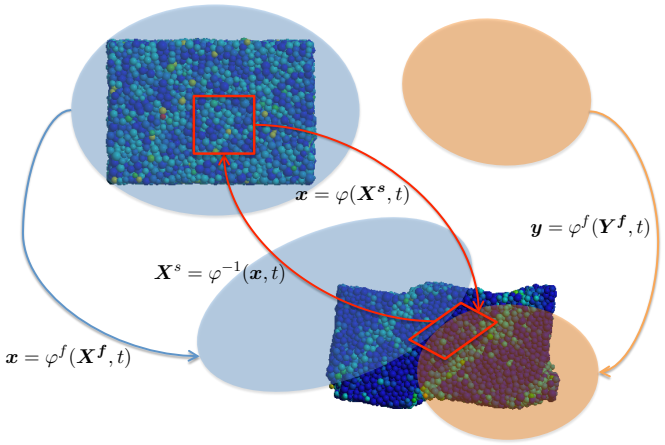

Figure 6.1: *Trajectories of the solid and fluid constituents $\boldsymbol{\varphi}^s = \boldsymbol{\varphi}$ and $\boldsymbol{\varphi}^f$. The motion $\boldsymbol{\varphi}$ conserves all the mass of the solid constituent, while the fluid may enter or leave the body of the solid constituent. Figure reproduced from [Sun et al., 2013e]*

.

Dettmar, 2004], we associate each point in the current configuration $\boldsymbol{x}$ with an aggregate of N particles inside the representative volume $\mathcal{V}$. Furthermore, we introduce a local coordinate system for the RVE in which the position vector $\boldsymbol{y} \in \mathbb{R}^3$ becomes $\boldsymbol{0}$ at the geometric centroid of the RVE. The locations of the centroids of the N particles expressed using the local coordinate system read, i.e.,

$$\boldsymbol{y}_p \in \mathcal{V}, \;\; p = 1, 2, ...N. \tag{6.3}$$

where $\boldsymbol{y}_p$ is the local position vector of the center of the p-th particle in the microstructure and $\boldsymbol{x} + \boldsymbol{y}_p$ is the same position expressed in the macroscopic current coordinate system. Particles inside the RVE may make contacts to each other. The local position vector of each contact between each particle-pair $\boldsymbol{y}_c$ can be written as,

$$\boldsymbol{y}_c \in \mathcal{V}, \quad c = 1, 2, ...N_c. \tag{6.4}$$

Both the positions of the particles $\boldsymbol{y}_p$ and that of the contacts $\boldsymbol{y}_c$ are governed by contact law and the equilibrium equations. Previous works, such as Curtis and Van Wachem [2004], El Shamy and Zeghal [2005], Han and Cundall [2011], Galindo-Torres et al. [2013], Robinson et al. [2014], Cui et al. [2014], have found success in explicitly modeling the pore-scale grain-fluid interaction. Nevertheless, such grain-fluid interaction simulations do impose a very high computational demand due to the fact that the fluid flow typically requires at least an order more of degree of freedoms to resolve the flow in the void space among particles. However, for seepage flow that is within the laminar regime where Darcy's law applies, the new insight obtained from the costly simulations will be limited. As a result, this discrete-continuum coupling model does not explicitly model the pore-scale solid-fluid interaction. Instead, we rely on the hypothesis that effective stress principle is valid for the specific boundary value problems we considered. In particular, we make the following assumptions:

- The void space is always fully saturated with one type of fluid and there is no capillary effect that leads to apparent cohesion of the solid skeleton.
- The flow in the void space remains Darcian at the macroscopic level.
- All particles in the granular assemblies are in contact with the neighboring particles.
- Fluidization, suffusion and erosion do not occur.
- Grain crushing does not occur.
- There is no mass exchange between the fluid and solid constituents.

As a result, we may express the total macroscopic Cauchy stress as a function of homogenized Cauchy effective stress inferred from DEM and the macroscopic pore pressure obtained from the mixed finite element, i.e.

$$\boldsymbol{\sigma}(\boldsymbol{x}, t) = < \boldsymbol{\sigma}'(\boldsymbol{x}, t) >_{\text{RVE}} - B(\boldsymbol{x}, t) p^f(\boldsymbol{x}, \boldsymbol{t}) \boldsymbol{I} \tag{6.5}$$

where

$$< \boldsymbol{\sigma}'(\boldsymbol{x}, t) >_{\text{RVE}} = \frac{1}{2\text{V}_{\text{RVE}}} \sum_{c}^{Nc} (\boldsymbol{f}^c \otimes \boldsymbol{l}^c + \boldsymbol{l}^c \otimes \boldsymbol{f}^c) \tag{6.6}$$

$\boldsymbol{f}^c$ is the contact force and $\boldsymbol{l}^c$ is the branch vector, the vector that connects the centroids of two grains forming the contact [Christoffersen et al., 1981, Bagi, 1996, Sun et al., 2013c], at the grain contact $\boldsymbol{x} + \boldsymbol{y}_c \in \mathbb{R}^3$. V_{RVE} is the volume of the RVE and N_c is the total number of particles in the RVE. Meanwhile, the Biot's coefficient B reads,

$$B(\boldsymbol{x}, \boldsymbol{t}) = 1 - \frac{K_T^{\text{DEM}}(\boldsymbol{x}, t)}{K_s} \tag{6.7}$$

with $K_T^{\text{DEM}}(\boldsymbol{x}, t)$ and K_s being the effective tangential bulk modulus of the solid matrix inferred from DEM, and the bulk modulus of the solid grain respectively [Nur and Byerlee, 1971b, Simon et al., 1986]. Notice that, in the geotechnical engineering and geomechanics literature, such as Ng [2006], Kuhn et al. [2014], it is common to impose incompressible volumetric constraint on dry DEM assembly to simulate undrained condition at meso-scale. This treatment can be considered as a special case of (8.9) when the bulk modulus of the solid grain is significantly higher than that of the skeleton such that the Biot's coefficient is approximately equal to one.

6.2.2 Micro-macro-transition for solid skeleton

In this study, we consider the class of two-phase porous media of which the solid skeleton is composed of particles. These particles can be cohesion-less or cohesive, but the assemblies they formed are assumed to be of particulate nature and hence suitable for DEM simulations. [Cundall and Strack, 1979].

In our implementation, the DEM simulations are conducted via YADE (Yet Another Dynamic Engine [Šmilauer et al., 2010]), an open source code base for discontinua. These grain-scale DEM simulations are used

as a replacement to the macroscopic constitutive laws that relate strain measure with effective stress measure for each RVE associated with a Gauss point in the macroscopic mixed finite element. In particular, a velocity gradient is prescribed to move the frame of the unit cell and the DEM will seek for the static equilibrium state via dynamics relaxation method. After static equilibrium is achieved, the internal forces and branch vectors are used to compute the homogenized effective Cauchy stress via the micro-macro transition theory [Miehe and Dettmar, 2004, Miehe et al., 2010, Wellmann et al., 2008]. For completeness, we provide a brief overview of DEM, the procedure for generation of RVEs and the study on the size of RVEs in Appendix A,B and C.

The Hill-Mandel micro-heterogeneity condition demands that the power at the microscopic scale must be equal to the the rate of work done measured by the macroscopic effective stress and strain rate measures. For the solid constituent of the two-phase porous media, this condition can be expressed in terms of any power-conjugate effective stress and strain rate pair , such as $(\boldsymbol{P}', \dot{\boldsymbol{F}})$ and $(\boldsymbol{S}', \dot{\boldsymbol{E}})$ and $(\boldsymbol{\sigma}', \boldsymbol{D})$ [Borja and Alarcón, 1995b, Armero, 1999]. For instance, the condition can be written in terms of the effective stress and rate of deformation of the solid skeleton, i.e.,

$$< \boldsymbol{\sigma}' >_{\text{RVE}} : < \boldsymbol{D} >_{\text{RVE}} = < \boldsymbol{\sigma}' : \boldsymbol{D} >_{\text{RVE}} \tag{6.8}$$

where $\boldsymbol{D}$ is the rate of deformation, i.e., the symmetric part of the velocity gradient tensor,

$$< \boldsymbol{D} >_{\text{RVE}} = \frac{1}{2}(< \boldsymbol{L} >_{\text{RVE}} + < \boldsymbol{L}^{\text{T}} >_{\text{RVE}}) \;\; ; \;\; \boldsymbol{L} = \boldsymbol{\nabla}^{\boldsymbol{x}} \boldsymbol{v} \tag{6.9}$$

and $< \boldsymbol{\sigma}' >_{\text{RVE}}$ is defined previously in (6.6). Previous studies, such as, Miehe and Dettmar [2004], Wellmann et al. [2008], Miehe et al. [2010], Fish [2013], have established that the linear deformation, periodic, and uniform traction are three boundary conditions that satisfy the Hill-Mandel micro-heterogeneity condition. In our implementation, we apply the periodic boundary condition to obtain the effective stress measure, because the periodic boundary condition may yield responses that are softer than those obtained from the linear deformation BC but stiffer than those obtained from the uniform traction BC. In particular, the periodic boundary condition enforces two constraints: (1) the periodicity of the deformation, i.e.,

$$[[\boldsymbol{y}_b]] = < \boldsymbol{F} >_{\text{RVE}} [[\boldsymbol{Y}_b]] \;\text{ and }\; [[\boldsymbol{R}_b]] = \boldsymbol{0} \tag{6.10}$$

where $[[\cdot]]$ denotes the jump across boundaries, $\boldsymbol{y}_b$ and $\boldsymbol{Y}_b$ represent the position vectors of the particles at the boundary of the reference and current configurations, $R_b \in SO(3)$ represents the rotation tensor of particles at the boundary, and (2) the anti-periodicity of the force $\boldsymbol{f}_b$ and moment on the boundary of the RVE, i.e.,

$$[[\boldsymbol{f}_b]] = \boldsymbol{0} \;\text{ and }\; [[(\boldsymbol{y}_c - \boldsymbol{y}_b) \times \boldsymbol{f}_b]] = \boldsymbol{0} \tag{6.11}$$

In YADE, the DEM code we employed for grain-scale simulations, the deformation of an RVE is driven by a periodic cell box in which the macroscopic velocity gradient of the unit cell $< \boldsymbol{L} >_{\text{RVE}}$ can both be measured and prescribed.

6.3 Multiscale DEM-mixed-FEM hydro-mechanical model

The differential equations governing the isothermal saturated porous media in large deformation are derived based on the mixture theory, in which solid matrix and pore fluid are treated together as a multiphase continuum [Prevost, 1982, Borja and Alarcón, 1995b, Armero, 1999, Coussy, 2004b, Sun et al., 2013e, Martinez et al., 2013]. The solid and fluid constituents may simultaneously occupy fractions of the volume of the same material point. The physical quantities of the mixture, such as density and total stress, are spatially homogenized from its components. For example, the averaged density of the fluid saturated soil mixture is defined as:

$$\rho = \rho^s + \rho^f = (1 - \phi)\rho_s + \phi\rho_f \tag{6.12}$$

where ρ^α is the partial mass density of the α constituent and ρ_α is the intrinsic mass density of the α constituent, with ϕ being the porosity.

6.3.1 Balance of linear momentum

For the balance of linear momentum law in finite strain, we adopt the total Lagrangian formulation and choose the total second Piola-Kirchhoff stress (PK2) $\boldsymbol{S}$ as the stress measure. The inertial effect is neglected. The equation takes the form:

$$\nabla^{\boldsymbol{X}} \cdot (\boldsymbol{F}\boldsymbol{S}) + J(\rho^s + \rho^f)\boldsymbol{g} = \boldsymbol{0} \tag{6.13}$$

where the Jacobian $J = \det(\boldsymbol{F})$. The principle of effective stress postulates that the total Cauchy stress $\boldsymbol{\sigma}$ can be decomposed into an effective stress due to the solid skeleton deformation and an isotropic pore pressure (p^f) stress. The effective stress principle in terms of PK2 writes:

$$\boldsymbol{S} = \boldsymbol{S'}^{\text{DEM}} - J\boldsymbol{F}^{-1}B^{\text{DEM}}p^f\boldsymbol{I}\boldsymbol{F}^{-T} \tag{6.14}$$

where

$$\boldsymbol{S'}^{\text{DEM}} = J\boldsymbol{F}^{-1}\boldsymbol{\sigma'}^{\text{DEM}}\boldsymbol{F}^{-T} = J\boldsymbol{F}^{-1}\big(\frac{1}{\text{V}_{\text{RVE}}}\sum_{i}^{Nc}\boldsymbol{f}\otimes\boldsymbol{l}\big)\boldsymbol{F}^{-T} \tag{6.15}$$

Thus the balance of linear momentum becomes:

$$\nabla^{\boldsymbol{X}}\cdot(\boldsymbol{F}\boldsymbol{S'}^{\text{DEM}} - JB^{\text{DEM}}p^f\boldsymbol{F}^{-T}) + J(\rho^s+\rho^f)\boldsymbol{g} = \boldsymbol{0} \tag{6.16}$$

6.3.2 Balance of fluid mass

The simplified u-p formulation in finite strain requires another equation illustrating the balance of mass for pore fluid constituent:

$$\frac{D\rho^f}{Dt} = -\nabla^{\boldsymbol{X}}\cdot(J\boldsymbol{F}^{-\mathbf{1}}[\phi^{\text{DEM}}\rho_f(\boldsymbol{v}^{\boldsymbol{f}}-\boldsymbol{v})]) \tag{6.17}$$

We make isothermal and barotropic assumptions and suppose that $p^f << K_s$ and that $\frac{DB^{\text{DEM}}}{Dt} \sim 0$. After simplifications [Sun et al., 2013e], the balance of mass becomes:

$$\frac{B^{\text{DEM}}}{J}\frac{DJ}{Dt} + \frac{1}{M^{\text{DEM}}}\frac{Dp^f}{Dt} + \nabla^{\boldsymbol{X}}\cdot(\frac{1}{\rho_f}(J\boldsymbol{F}^{-\mathbf{1}}[\phi^{\text{DEM}}\rho_f(\boldsymbol{v}^{\boldsymbol{f}}-\boldsymbol{v})])) = 0 \tag{6.18}$$

where

$$M^{\text{DEM}} = \frac{K_sK_f}{K_f(B^{\text{DEM}}-\phi^{\text{DEM}}) + K_s\phi^{\text{DEM}}} \tag{6.19}$$

is the Biot's modulus [Nur and Byerlee, 1971b], with K_f being the bulk modulus of pore fluid.

In this paper, Darcy's constitutive law relating the relative flow and the pore pressure is employed, neglecting the inertial effect:

$$\boldsymbol{Q} = \boldsymbol{K}^{\text{DEM}}\cdot(-\nabla^{\boldsymbol{X}}p^f + \rho_f\boldsymbol{F}^{\text{T}}\cdot\boldsymbol{g}) \tag{6.20}$$

where the pull-back permeability tensor $\boldsymbol{K}^{\text{DEM}}$ is defined as

$$\boldsymbol{K}^{\text{DEM}} = J\boldsymbol{F}^{-1}\cdot\boldsymbol{k}^{\text{DEM}}\cdot\boldsymbol{F}^{\text{-T}} \tag{6.21}$$

Assume that the effective permeability tensor $\boldsymbol{k}^{\text{DEM}}$ is isotropic, i.e.,

$$\boldsymbol{k}^{\text{DEM}} = k^{\text{DEM}}\boldsymbol{I} \tag{6.22}$$

where k^{DEM} is the scalar effective permeability in unit of $\frac{m^2}{Pa\cdot s}$. It is updated from porosity of DEM RVEs according to the Kozeny-Carmen equation.

6.3.3 Weak form

To construct the macroscopic hydro-mechanical boundary-value problem, consider a reference domain $\mathcal{B}$ with its boundary $\partial\mathcal{B}$ composed of Dirichlet boundaries (solid displacement $\partial\mathcal{B}_{\boldsymbol{u}}$, pore pressure $\partial\mathcal{B}_p$) and Von Neumann boundaries (solid traction $\partial\mathcal{B}_{\boldsymbol{t}}$, fluid flux $\partial\mathcal{B}_q$) satisfying

$$\begin{cases} \partial\mathcal{B} = \overline{\partial\mathcal{B}_{\boldsymbol{u}}\cup\partial\mathcal{B}_{\boldsymbol{t}}} = \overline{\partial\mathcal{B}_p\cup\partial\mathcal{B}_q} \\ \emptyset = \partial\mathcal{B}_{\boldsymbol{u}}\cap\partial\mathcal{B}_{\boldsymbol{t}} = \partial\mathcal{B}_p\cap\partial\mathcal{B}_q \end{cases} \tag{6.23}$$

The prescribed boundary conditions are

$$\begin{cases} \boldsymbol{u} = \overline{\boldsymbol{u}} \text{ on } \partial\mathcal{B}_{\boldsymbol{u}} \\ \boldsymbol{P}\cdot\boldsymbol{N} = (\boldsymbol{F}\cdot\boldsymbol{S})\cdot\boldsymbol{N} = \overline{\boldsymbol{t}} \text{ on } \partial\mathcal{B}_{\boldsymbol{t}} \\ p^f = \overline{p} \text{ on } \partial\mathcal{B}_p \\ -\boldsymbol{N}\cdot\boldsymbol{Q} = \overline{Q} \text{ on } \partial\mathcal{B}_{\boldsymbol{Q}} \end{cases} \tag{6.24}$$

where $\boldsymbol{N}$ is outward unit normal on undeformed surface $\partial\mathcal{B}$.

For model closure, the initial conditions are imposed as

$$p^f = p_0^f, \;\; \boldsymbol{u} = \boldsymbol{u_0} \;\text{ at }\; t = t_0 \tag{6.25}$$

Following the standard procedures of the variational formulation, we obtain finally the weak form of the balance of linear momentum and mass

$$\begin{aligned} G \quad &: \quad V_{\boldsymbol{u}} \times V_p \times V_\eta \to \mathbb{R} \\ G(\boldsymbol{u}, p^f, \boldsymbol{\eta}) \quad &= \quad \int_{\mathcal{B}} \nabla^{\boldsymbol{X}} \boldsymbol{\eta} : (\boldsymbol{F} \cdot \boldsymbol{S'}^{\text{DEM}} - JBp^f \boldsymbol{F}^{\text{-T}}) \, \text{dV} - \int_{\mathcal{B}} J(\rho^f + \rho^s)\boldsymbol{\eta} \cdot \boldsymbol{g} \text{dV} \\ &\quad - \int_{\partial\mathcal{B}_t} \boldsymbol{\eta} \cdot \bar{\boldsymbol{t}} \, \text{d}\Gamma = 0 \end{aligned} \tag{6.26}$$

$$\begin{aligned} H \quad &: \quad V_{\boldsymbol{u}} \times V_p \times V_\psi \to \mathbb{R} \\ H(\boldsymbol{u}, p^f, \psi) \quad &= \quad \int_{\mathcal{B}} \psi \frac{B^{\text{DEM}}}{J} \dot{J} \, \text{dV} + \int_{\mathcal{B}} \psi \frac{1}{M^{\text{DEM}}} \dot{p^f} \, \text{dV} \\ &\quad - \int_{\mathcal{B}} \nabla^{\boldsymbol{X}} \psi \cdot [\boldsymbol{K}^{\text{DEM}} \cdot (-\nabla^{\boldsymbol{X}} p^f + \rho_f \boldsymbol{F}^{\text{T}} \cdot \boldsymbol{g})] \, \text{dV} \\ &\quad - \int_{\partial B_Q} \psi \overline{\boldsymbol{Q}} \, \text{d}\Gamma = 0 \end{aligned} \tag{6.27}$$

The first integral of $H(\boldsymbol{u}, p^f, \psi)$ can be related to the solid velocity field $\dot{\boldsymbol{u}}$ using the equations $\dot{J} = J \nabla^{\boldsymbol{x}} \cdot \dot{\boldsymbol{u}}$ and $\nabla^{\boldsymbol{x}} \cdot \dot{\boldsymbol{u}} = \nabla^{\boldsymbol{X}} \dot{\boldsymbol{u}} : \boldsymbol{F}^{\text{-T}}$ [Borja and Alarcón, 1995b]:

$$\int_{\mathcal{B}} \psi \frac{B^{\text{DEM}}}{J} \dot{J} \, \text{dV} = \int_{\mathcal{B}} \psi B^{\text{DEM}} \nabla^{\boldsymbol{x}} \cdot \dot{\boldsymbol{u}} \, \text{dV} = \int_{\mathcal{B}} \psi B^{\text{DEM}} \boldsymbol{F}^{\text{-T}} : \nabla^{\boldsymbol{X}} \dot{\boldsymbol{u}} \, \text{dV} \tag{6.28}$$

The displacement and pore pressure trial spaces for the weak form are defined as

$$V_{\boldsymbol{u}} = \{\boldsymbol{u} : \mathcal{B} \to \mathbb{R}^3 | \boldsymbol{u} \in [H^1(\mathcal{B})]^3, \boldsymbol{u}|_{\partial B_{\boldsymbol{u}}} = \overline{\boldsymbol{u}}\} \tag{6.29}$$

$$V_p = \{p^f : \mathcal{B} \to \mathbb{R} | p^f \in H^1(\mathcal{B}), p^f|_{\partial B_p} = \overline{p}\} \tag{6.30}$$

and the corresponding admissible spaces of variations are defined as

$$V_{\boldsymbol{\eta}} = \{\boldsymbol{\eta} : \mathcal{B} \to \mathbb{R}^3 | \boldsymbol{\eta} \in [H^1(\mathcal{B})]^3, \boldsymbol{\eta}|_{\partial B_{\boldsymbol{u}}} = \boldsymbol{0}\} \tag{6.31}$$

$$V_\psi = \{\psi : \mathcal{B} \to \mathbb{R} | \psi \in H^1(\mathcal{B}), \psi|_{\partial B_p} = 0\} \tag{6.32}$$

H^1 denotes the Sobolev space of degree one, which is the space of square integrable function whose weak derivative up to order 1 are also square integrable (cf. Hughes [1987], Brenner and Scott [2008]).

6.3.4 Finite element spatial discretization

The spatially discretized equations can be derived following the standard Galerkin procedure. Shape functions $\boldsymbol{N_u}(\boldsymbol{X})$ and $\boldsymbol{N_p}(\boldsymbol{X})$ are used for approximation of solid motion $\boldsymbol{u}$, $\dot{\boldsymbol{u}}$ and pore pressure p^f, $\dot{p^f}$, respectively:

$$\begin{cases} \boldsymbol{u} = \boldsymbol{N_u} \bar{\boldsymbol{u}}, \;\; \dot{\boldsymbol{u}} = \boldsymbol{N_u} \dot{\bar{\boldsymbol{u}}}, \;\; \boldsymbol{\eta} = \boldsymbol{N_u} \bar{\boldsymbol{\eta}} \\ p^f = \boldsymbol{N_p} \bar{\boldsymbol{p}^f}, \;\; \dot{p^f} = \boldsymbol{N_p} \dot{\bar{\boldsymbol{p}}}^{\boldsymbol{f}}, \;\; \psi = \boldsymbol{N_p} \bar{\psi} \end{cases} \tag{6.33}$$

with $\bar{\boldsymbol{u}}$ being the nodal solid displacement vector, $\bar{\boldsymbol{p}}^{\boldsymbol{f}}$ being the nodal pore pressure vector, $\dot{\bar{\boldsymbol{u}}}$, $\dot{\bar{\boldsymbol{p}}}^{\boldsymbol{f}}$ being their time derivatives, and $\bar{\boldsymbol{\eta}}$, $\bar{\psi}$ being their variations.

The adopted eight-node hexahedral element interpolates the displacement and pore pressure field with the same order. As a result, this combination does not inherently satisfy the inf-sup condition [White and Borja,

2008b, Sun et al., 2013e, Sun, 2015a]. Therefore a stabilization procedure is necessary. In this study, the fluid pressure Laplacian scheme is applied. This scheme consists of adding the following stabilization term to the balance of mass equation (8.64) :

$$\int_{\mathcal{B}} \nabla^{\boldsymbol{X}} \psi \, \alpha_{stab} \, \nabla^{\boldsymbol{X}} \dot{p^f} \mathrm{dV} \tag{6.34}$$

with α_{stab} a scale factor depending on element size and material properties of the porous media. For detailed formulations, please refer to [Truty and Zimmermann, 2006b, Sun et al., 2013e].

We obtain the finite element equations for balance of linear momentum and balance of mass as:

$$\begin{cases} G(\boldsymbol{u}, p^f, \boldsymbol{\eta}) = 0 \\ H(\boldsymbol{u}, p^f, \psi) = 0 \end{cases} \Longrightarrow \begin{cases} \boldsymbol{F^s_{int}}(\bar{\boldsymbol{u}}) - \boldsymbol{K^{up}} \bar{\boldsymbol{p}}^{\boldsymbol{f}} - \boldsymbol{G^1} = \boldsymbol{F^1_{ext}} \\ \boldsymbol{C_1} \dot{\bar{\boldsymbol{u}}} + (\boldsymbol{C_2} + \boldsymbol{C_{stab}}) \dot{\bar{\boldsymbol{p}}}^{\boldsymbol{f}} + \boldsymbol{K^p} \bar{\boldsymbol{p}}^{\boldsymbol{f}} - \boldsymbol{G^2} = \boldsymbol{F^2_{ext}} \end{cases} \tag{6.35}$$

with expressions for each term:

$$\begin{cases} \boldsymbol{F^s_{int}}(\bar{\boldsymbol{u}}) = \displaystyle\int_{\mathcal{B}} (\nabla^{\boldsymbol{X}} \boldsymbol{N_u})^{\mathrm{T}} : (\boldsymbol{F} \cdot \boldsymbol{S'}^{\mathrm{DEM}}) \mathrm{dV} \\ \boldsymbol{K^{up}} = \displaystyle\int_{\mathcal{B}} J B^{\mathrm{DEM}} (\nabla^{\boldsymbol{X}} \boldsymbol{N_u})^{\mathrm{T}} : \boldsymbol{F}^{\text{-T}} \cdot \boldsymbol{N_p} \mathrm{dV} \\ \boldsymbol{C_1} = \displaystyle\int_{\mathcal{B}} B^{\mathrm{DEM}} \boldsymbol{N_p}^{\mathrm{T}} \boldsymbol{F}^{\text{-T}} : (\nabla^{\boldsymbol{X}} \boldsymbol{N_u}) \mathrm{dV} \\ \boldsymbol{C_2} = \displaystyle\int_{\mathcal{B}} \frac{1}{M^{\mathrm{DEM}}} \boldsymbol{N_p}^{\mathrm{T}} \boldsymbol{N_p} \mathrm{dV} \\ \boldsymbol{C_{stab}} = \displaystyle\int_{\mathcal{B}} (\nabla^{\boldsymbol{X}} \boldsymbol{N_p})^{\mathrm{T}} \alpha_{stab} (\nabla^{\boldsymbol{X}} \boldsymbol{N_p}) \mathrm{dV} \\ \boldsymbol{K^p} = \displaystyle\int_{\mathcal{B}} (\nabla^{\boldsymbol{X}} \boldsymbol{N_p})^{\mathrm{T}} (J \boldsymbol{F}^{-1} \cdot \boldsymbol{k}^{\mathrm{DEM}} \cdot \boldsymbol{F}^{\text{-T}}) (\nabla^{\boldsymbol{X}} \boldsymbol{N_p}) \mathrm{dV} \\ \boldsymbol{G^1} = \displaystyle\int_{\mathcal{B}} J(\rho^f + \rho^s) \boldsymbol{N_u}^{\mathrm{T}} \boldsymbol{g} \mathrm{dV} \\ \boldsymbol{G^2} = \displaystyle\int_{\mathcal{B}} (\nabla^{\boldsymbol{X}} \boldsymbol{N_p})^{\mathrm{T}} (J \boldsymbol{F}^{-1} \cdot \boldsymbol{k}^{\mathrm{DEM}} \cdot \boldsymbol{F}^{\text{-T}}) \rho_f \boldsymbol{F}^{\mathrm{T}} \cdot \boldsymbol{g} \mathrm{dV} \\ \boldsymbol{F^1_{ext}} = \displaystyle\int_{\partial \mathcal{B}_t} \boldsymbol{N_u}^{\mathrm{T}} \bar{\boldsymbol{t}} \mathrm{d\Gamma} \\ \boldsymbol{F^2_{ext}} = \displaystyle\int_{\partial B_Q} \boldsymbol{N_p}^{\mathrm{T}} \overline{\boldsymbol{Q}} \mathrm{d\Gamma} \end{cases} \tag{6.36}$$

The non-linear equation system (6.35) can be rewritten in a compact form:

$$\boldsymbol{M^*} \cdot \boldsymbol{v} + \boldsymbol{F^{int}}(\boldsymbol{d}) - \boldsymbol{G}(\boldsymbol{d}) = \boldsymbol{F^{ext}} \tag{6.37}$$

where $\boldsymbol{M^*} = \begin{bmatrix} \boldsymbol{0} & \boldsymbol{0} \\ \boldsymbol{C_1} & (\boldsymbol{C_2} + \boldsymbol{C_{stab}}) \end{bmatrix}$, $\boldsymbol{v} = \begin{Bmatrix} \dot{\bar{\boldsymbol{u}}} \\ \dot{\bar{\boldsymbol{p}}}^{\boldsymbol{f}} \end{Bmatrix}$, $\boldsymbol{F^{int}} = \begin{Bmatrix} \boldsymbol{F^s_{int}}(\bar{\boldsymbol{u}}) - \boldsymbol{K^{up}} \bar{\boldsymbol{p}}^{\boldsymbol{f}} \\ \boldsymbol{K^p} \bar{\boldsymbol{p}}^{\boldsymbol{f}} \end{Bmatrix}$, $\boldsymbol{d} = \begin{Bmatrix} \bar{\boldsymbol{u}} \\ \bar{\boldsymbol{p}}^{\boldsymbol{f}} \end{Bmatrix}$, $\boldsymbol{G} = \begin{Bmatrix} \boldsymbol{G^1} \\ \boldsymbol{G^2} \end{Bmatrix}$ and $\boldsymbol{F^{ext}} = \begin{Bmatrix} \boldsymbol{F^1_{ext}} \\ \boldsymbol{F^2_{ext}} \end{Bmatrix}$.

6.3.5 Consistent linearization

The semi-implicit solution scheme requires the expression of the tangential stiffness of the implicit contribution. Thus, we perform the consistent linearization of the weak forms (8.63) and (8.64) in the reference configuration [Borja et al., 1998b, Sanavia et al., 2002]. For the balance of linear momentum equation, the

consistent linearization reads,

$$\begin{aligned}\delta G(\boldsymbol{u},p^f,\boldsymbol{\eta}) = &\overbrace{\int_{\mathcal{B}} (\boldsymbol{F}^{\mathrm{T}}\cdot\nabla^{\boldsymbol{X}}\boldsymbol{\eta}) : (\boldsymbol{C}^{SE})^{\mathrm{DEM}} : \boldsymbol{\delta E}\,\mathrm{dV}}^{\bar{\boldsymbol{\eta}}^{\mathrm{T}}\boldsymbol{K}^{\boldsymbol{s}}\boldsymbol{\delta}\bar{\boldsymbol{u}}} + \overbrace{\int_{\mathcal{B}} \boldsymbol{S'}^{\mathrm{DEM}} : (\nabla^{\boldsymbol{X}}\boldsymbol{\delta u})^{\mathrm{T}}\cdot\nabla^{\boldsymbol{X}}\boldsymbol{\eta}\,\mathrm{dV}}^{\bar{\boldsymbol{\eta}}^{\mathrm{T}}\boldsymbol{K}^{\boldsymbol{geo}}_{\boldsymbol{S'}}\boldsymbol{\delta}\bar{\boldsymbol{u}}} \\ &- \overbrace{\int_{\mathcal{B}} \nabla^{\boldsymbol{X}}\boldsymbol{\eta} : \delta(JB^{\mathrm{DEM}}\boldsymbol{F}^{\text{-T}})p^f\,\mathrm{dV}}^{\bar{\boldsymbol{\eta}}^{\mathrm{T}}\boldsymbol{K}^{\boldsymbol{geo}}_{\boldsymbol{p^f}}\boldsymbol{\delta}\bar{\boldsymbol{u}}} - \overbrace{\int_{\mathcal{B}} JB^{\mathrm{DEM}}\nabla^{\boldsymbol{X}}\boldsymbol{\eta} : \boldsymbol{F}^{\text{-T}}\delta p^f\,\mathrm{dV}}^{\bar{\boldsymbol{\eta}}^{\mathrm{T}}\boldsymbol{K}^{\boldsymbol{up}}\delta\bar{\boldsymbol{p}}^{\boldsymbol{f}}} \\ &- \overbrace{\int_{\mathcal{B}} \rho_f\nabla^{\boldsymbol{X}}\cdot(J\boldsymbol{F}^{\text{-1}}\cdot\boldsymbol{\delta u})\boldsymbol{\eta}\cdot\boldsymbol{g}\,\mathrm{dV}}^{\bar{\boldsymbol{\eta}}^{\mathrm{T}}\delta\boldsymbol{G}^{\boldsymbol{1}}} - \overbrace{\int_{\partial\mathcal{B}_t}\boldsymbol{\eta}\cdot\boldsymbol{\delta}\bar{\boldsymbol{t}}\,\mathrm{d\Gamma}}^{\bar{\boldsymbol{\eta}}^{\mathrm{T}}\delta\boldsymbol{F}^{\boldsymbol{1}}_{\boldsymbol{ext}}} = 0\end{aligned} \tag{6.38}$$

where $C^{SE}_{IJKL} = \frac{\partial S'_{IJ}}{\partial E_{KL}}$ is the material tangential stiffness. $\delta\boldsymbol{E}$ is the variation of the Green-Lagrange strain tensor and $\delta\boldsymbol{E} = \frac{1}{2}[(\nabla^{\boldsymbol{X}}\delta\boldsymbol{u})^{\mathrm{T}}\boldsymbol{F} + \boldsymbol{F}^{\mathrm{T}}(\nabla^{\boldsymbol{X}}\delta\boldsymbol{u})]$. $\boldsymbol{K}^{\boldsymbol{geo}}_{\boldsymbol{S'}}$ and $\boldsymbol{K}^{\boldsymbol{geo}}_{\boldsymbol{p^f}}$ are the initial stress and initial pore pressure contributions to the geometrical stiffness. For the balance of mass equation, the corresponding linearization term reads,

$$\begin{aligned}\delta H(\boldsymbol{u},p^f,\psi) = &\overbrace{\int_{\mathcal{B}}\psi\delta(B^{\mathrm{DEM}}\boldsymbol{F}^{\text{-T}}) : \nabla^{\boldsymbol{X}}\dot{\boldsymbol{u}}\,\mathrm{dV}}^{\bar{\boldsymbol{\psi}}^{\mathrm{T}}\delta\boldsymbol{C_1}\dot{\bar{\boldsymbol{u}}}} + \overbrace{\int_{\mathcal{B}}\psi B^{\mathrm{DEM}}\boldsymbol{F}^{\text{-T}} : \nabla^{\boldsymbol{X}}\boldsymbol{\delta}\dot{\boldsymbol{u}}\,\mathrm{dV}}^{\bar{\boldsymbol{\psi}}^{\mathrm{T}}\boldsymbol{C_1}\boldsymbol{\delta}\dot{\bar{\boldsymbol{u}}}} \\ &+ \overbrace{\int_{\mathcal{B}}\psi\delta(\frac{1}{M^{\mathrm{DEM}}})\dot{p^f}\,\mathrm{dV}}^{\bar{\boldsymbol{\psi}}^{\mathrm{T}}\delta\boldsymbol{C_2}\dot{\bar{\boldsymbol{p}}}^{\boldsymbol{f}}} + \overbrace{\int_{\mathcal{B}}\psi\frac{1}{M^{\mathrm{DEM}}}\delta\dot{p^f}\,\mathrm{dV}}^{\bar{\boldsymbol{\psi}}^{\mathrm{T}}\boldsymbol{C_2}\boldsymbol{\delta}\dot{\bar{\boldsymbol{p}}}^{\boldsymbol{f}}} + \overbrace{\int_{\mathcal{B}}\nabla^{\boldsymbol{X}}\psi\,\alpha_{stab}\,\nabla^{\boldsymbol{X}}\delta\dot{p^f}\mathrm{dV}}^{\bar{\boldsymbol{\psi}}^{\mathrm{T}}\boldsymbol{C}_{\boldsymbol{stab}}\boldsymbol{\delta}\dot{\bar{\boldsymbol{p}}}^{\boldsymbol{f}}} \\ &+ \overbrace{\int_{\mathcal{B}}\nabla^{\boldsymbol{X}}\psi\cdot\boldsymbol{K}^{\mathrm{DEM}}\cdot\nabla^{\boldsymbol{X}}\delta p^f\,\mathrm{dV}}^{\bar{\boldsymbol{\psi}}^{\mathrm{T}}\boldsymbol{K}^{\boldsymbol{p}}\boldsymbol{\delta}\bar{\boldsymbol{p}}^{\boldsymbol{f}}} + \overbrace{\int_{\mathcal{B}}\nabla^{\boldsymbol{X}}\psi\cdot\delta\boldsymbol{K}^{\mathrm{DEM}}\cdot\nabla^{\boldsymbol{X}}p^f\,\mathrm{dV}}^{\bar{\boldsymbol{\psi}}^{\mathrm{T}}\boldsymbol{K}^{\boldsymbol{p}}_{\boldsymbol{1}}\boldsymbol{\delta}\bar{\boldsymbol{u}}} \\ &- \overbrace{\int_{\mathcal{B}}\nabla^{\boldsymbol{X}}\psi\cdot\delta(\boldsymbol{K}^{\mathrm{DEM}}\cdot\rho_f\boldsymbol{F}^{\mathrm{T}})\cdot\boldsymbol{g}\,\mathrm{dV}}^{\bar{\boldsymbol{\psi}}^{\mathrm{T}}\delta\boldsymbol{G^2}} - \overbrace{\int_{\partial B_Q}\psi\boldsymbol{\delta}\overline{\boldsymbol{Q}}\,\mathrm{d\Gamma}}^{\bar{\boldsymbol{\psi}}^{\mathrm{T}}\delta\boldsymbol{F}^{\boldsymbol{2}}_{\boldsymbol{ext}}} = 0\end{aligned} \tag{6.39}$$

where $\boldsymbol{K}^{\boldsymbol{p}}_{\boldsymbol{1}}$ is the geometrical term related to the permeability k.

The proposed semi-implicit scheme splits $G(\boldsymbol{u},p^f,\boldsymbol{\eta})$ and $H(\boldsymbol{u},p^f,\psi)$ into implicitly treated parts and explicitly treated parts, thus only a subset of the linearization terms in (6.38) and (6.39) will be used. The implicit-explicit split will be explained in the next section.

6.4 Semi-implicit multiscale time integrator

While both implicit and explicit time integrators have been used in DEM-FEM coupling models for dry granular materials [Miehe and Dettmar, 2004, Guo and Zhao, 2014, Liu et al., 2015], the extension of these algorithms to multiphysics hydro-mechanical problem is not straightforward. The key difference is that the pore-fluid diffusion is transient and hence the initial boundary value problem is elliptic.

While it is possible to add the inertial terms and update the macroscopic displacement and pore pressure explicitly via a dynamics relaxation procedure, this strategy is impractical due to the small critical time step size of the explicit scheme as pointed out by Prevost [1983]. Another possible approach is to solve the macroscopic problem in a fully implicit, unconditionally stable scheme. The drawback of this approach is that it requires additional CPU time to compute the elasto-plastic tangential stiffness from DEM. Unlike a conventional constitutive model (in which an analytical expression of the tangential stiffness is often available and hence easy to implement), the tangential stiffness inferred from DEM must be obtained numerically via perturbation methods [Guo and Zhao, 2014, Brothers et al., 2014]. For three-dimensional simulations, this means that additional 36 to 81 simulations are required to obtain the tangential stiffness, depending on which energy-conjugate stress-strain pair is used in the formulation. This is a sizable burden given the fact that a converged update may require tens of iterations.

To avoid this additional computational cost, we adopt the implicit-explicit predictor/multicorrector scheme originally proposed in Hughes et al. [1979] and Prevost [1983] and apply it to the finite strain DEM-mixed-FEM model. In Prevost [1983], the internal force is split into two components, one treated implicitly and another treated explicitly. We adopt this idea here by treating the elasto-plastic force from DEM explicitly, and the other internal forces implicitly, in a fashion similar to the unconditionally stable Yanenko operator splitting (i.e. $\mathcal{L} = \mathcal{L}_{exp} + \mathcal{L}_{imp}$, c.f. Yanenko [1971]).

The implicit time integration based on the generalized trapezoidal rule consists of satisfying the equation (6.37) at time t_{n+1}:

$$\boldsymbol{M}^*_{n+1} \cdot \boldsymbol{v}_{n+1} + \boldsymbol{F}^{int}(\boldsymbol{d}_{n+1}) - \boldsymbol{G}(\boldsymbol{d}_{n+1}) = \boldsymbol{F}^{ext}_{n+1} \tag{6.40}$$

with the solution

$$\boldsymbol{d}_{n+1} = \tilde{\boldsymbol{d}} + \alpha \Delta t \boldsymbol{v}_{n+1} \tag{6.41}$$

where

$$\tilde{\boldsymbol{d}} = \boldsymbol{d}_n + (1-\alpha)\Delta t \boldsymbol{v}_n. \tag{6.42}$$

The notation is as follows: the subscripts n and $n+1$ denote that the variables are evaluated at time t_n and t_{n+1}, respectively; Δt is the time step; α is the integration parameter. The quantity $\tilde{\boldsymbol{d}}$ is referred to as the predicted solution.

Similar to the scheme of Prevost [1983], the semi-implicit predictor-corrector scheme is performed by evaluating a portion of the left hand side forces of (6.40) explicitly using the predicted solution $\tilde{\boldsymbol{d}}$ and $\boldsymbol{v}_n$, and treating the remaining portion implicitly with the solution $\boldsymbol{d}_{n+1}$ and $\boldsymbol{v}_{n+1}$:

$$\boldsymbol{F}_{\text{IMP}}(\boldsymbol{v}_{n+1}, \boldsymbol{d}_{n+1}) + \boldsymbol{F}_{\text{EXP}}(\boldsymbol{v}_n, \tilde{\boldsymbol{d}}) = \boldsymbol{F}^{ext}_{n+1} \tag{6.43}$$

where

$$\begin{cases} \boldsymbol{F}_{\text{IMP}} = \{\boldsymbol{M}^* \cdot \boldsymbol{v}\}^{\text{implicit}}_{n+1} + \left\{\boldsymbol{F}^{int}(\boldsymbol{d}_{n+1})\right\}^{\text{implicit}} \\ \boldsymbol{F}_{\text{EXP}} = \{\boldsymbol{M}^* \cdot \boldsymbol{v}\}^{\text{explicit}}_{n} + \left\{\boldsymbol{F}^{int}(\tilde{\boldsymbol{d}})\right\}^{\text{explicit}} - \boldsymbol{G}(\tilde{\boldsymbol{d}}) \end{cases} \tag{6.44}$$

To obtain the macroscopic displacement and pore pressure at time t_{n+1} from the non-linear equation system (6.43), Newton-Raphson iteration method is employed. Let us denote the corrected solutions as $\boldsymbol{d}^j_{n+1}$ and $\boldsymbol{v}^j_{n+1}$, at the time step $n+1$ and jth iteration, i.e.,

$$\boldsymbol{d}^j_{n+1} = \tilde{\boldsymbol{d}} + \alpha \Delta t \boldsymbol{v}^j_{n+1} \tag{6.45}$$

with $\boldsymbol{v}^0_{n+1} = \boldsymbol{0}$. The relationship of their increments is thus:

$$\Delta \boldsymbol{d}^j_{n+1} = \alpha \Delta t \Delta \boldsymbol{v}^j_{n+1} \tag{6.46}$$

The equation (6.43) in terms of these iterative solutions is written as:

$$\boldsymbol{F}_{\text{IMP}}(\boldsymbol{v}^{j+1}_{n+1}, \boldsymbol{d}^{j+1}_{n+1}) + \boldsymbol{F}_{\text{EXP}}(\boldsymbol{v}^{j}_{n+1}, \boldsymbol{d}^{j}_{n+1}) = \boldsymbol{F}^{ext}_{n+1} \tag{6.47}$$

The consistent linearization of the implicit part $\boldsymbol{F}_{\text{IMP}}$ is required to solve (6.47). The resulting tangential stiffness matrix depends on what force terms are included in $\{\boldsymbol{M}^* \cdot \boldsymbol{v}\}^{\text{implicit}}$ and $\left\{\boldsymbol{F}^{int}\right\}^{\text{implicit}}$.

For the implicit-explicit split of the nonlinear rate of change term $\boldsymbol{M}^* \cdot \boldsymbol{v}$, note that, from (6.38) and (6.39), its variation contains two components:

$$\frac{\partial(\boldsymbol{M}^* \cdot \boldsymbol{v})}{\partial \boldsymbol{v}} \cdot \boldsymbol{\delta v} = (\boldsymbol{M}^* + \frac{\partial \boldsymbol{M}^*}{\partial \boldsymbol{v}} \cdot \boldsymbol{v}) \cdot \boldsymbol{\delta v} \tag{6.48}$$

In the proposed scheme, the rate of change term is split in a way that only $\boldsymbol{M}^*$ is treated implicitly:

$$\frac{\partial(\boldsymbol{M}^* \cdot \boldsymbol{v})}{\partial \boldsymbol{v}} = \left\{\frac{\partial \boldsymbol{M}^* \cdot \boldsymbol{v}}{\partial \boldsymbol{v}}\right\}^{\text{implicit}} + \left\{\frac{\partial \boldsymbol{M}^* \cdot \boldsymbol{v}}{\partial \boldsymbol{v}}\right\}^{\text{explicit}} \; ; \; \begin{cases} \left\{\frac{\partial \boldsymbol{M}^* \cdot \boldsymbol{v}}{\partial \boldsymbol{v}}\right\}^{\text{implicit}} = \boldsymbol{M}^* \\ \left\{\frac{\partial \boldsymbol{M}^* \cdot \boldsymbol{v}}{\partial \boldsymbol{v}}\right\}^{\text{explicit}} = \frac{\partial \boldsymbol{M}^*}{\partial \boldsymbol{v}} \cdot \boldsymbol{v} \end{cases} \tag{6.49}$$

From the above implicit-explicit split, the first order linearization form of $\boldsymbol{F}_{\text{IMP}}$ in (6.47) reads:

$$\begin{aligned}\boldsymbol{F}_{\text{IMP}}(\boldsymbol{v}_{n+1}^{j+1}, \boldsymbol{d}_{n+1}^{j+1}) &\simeq \boldsymbol{F}_{\text{IMP}}(\boldsymbol{v}_{n+1}^{j}, \boldsymbol{d}_{n+1}^{j}) + \boldsymbol{M}^{*} \cdot \Delta \boldsymbol{v}_{n+1}^{j+1} + \boldsymbol{K}_{\boldsymbol{T}}^{\text{implicit}} \cdot \Delta \boldsymbol{d}_{n+1}^{j+1} \\ &\simeq \boldsymbol{F}_{\text{IMP}}(\boldsymbol{v}_{n+1}^{j}, \boldsymbol{d}_{n+1}^{j}) + \underbrace{[\boldsymbol{M}^{*} + \alpha \Delta t \boldsymbol{K}_{\boldsymbol{T}}^{\text{implicit}}]}_{\boldsymbol{M}^{**}} \cdot \Delta \boldsymbol{v}_{n+1}^{j+1}\end{aligned} \tag{6.50}$$

where

$$\boldsymbol{K}_{\boldsymbol{T}}{}^{\text{implicit}} \cdot \Delta \boldsymbol{d}_{n+1}^{j+1} = \frac{d}{d\beta} \left\{ \boldsymbol{F}^{\boldsymbol{int}}(\boldsymbol{d}_{n+1}^{j} + \beta \Delta \boldsymbol{d}_{n+1}^{j+1}) \right\}^{\text{implicit}} |_{\beta=0} \tag{6.51}$$

is the directional derivative of $\left\{ \boldsymbol{F}^{\boldsymbol{int}} \right\}^{\text{implicit}}$ at $\boldsymbol{d}_{n+1}^{j}$ in the direction of $\Delta \boldsymbol{d}_{n+1}^{j+1}$.

For construction of $\boldsymbol{K}_{\boldsymbol{T}}{}^{\text{implicit}}$, firstly, a complete linearization of the internal force $\boldsymbol{F}^{\boldsymbol{int}}$ results in the following form of tangential stiffness matrix, according to (6.38) and (6.39):

$$\boldsymbol{K}_{\boldsymbol{T}} = \frac{\partial \boldsymbol{F}^{\boldsymbol{int}}}{\partial \boldsymbol{d}} = \begin{bmatrix} (\underbrace{\boldsymbol{K}^{\boldsymbol{e}} - \boldsymbol{K}^{\boldsymbol{ep}}}_{\boldsymbol{K}^{\boldsymbol{s}}} + \boldsymbol{K}^{\boldsymbol{geo}}) & -\boldsymbol{K}^{\boldsymbol{up}} \\ \boldsymbol{K}_{\boldsymbol{1}}^{\boldsymbol{p}} & \boldsymbol{K}^{\boldsymbol{p}} \end{bmatrix} \tag{6.52}$$

where $\boldsymbol{K}^{\boldsymbol{e}}$ is the elastic contribution and $\boldsymbol{K}^{\boldsymbol{ep}}$ is the non-linear elastic-plastic contribution to the material tangential stiffness $\boldsymbol{K}^{\boldsymbol{s}}$. $\boldsymbol{K}^{\boldsymbol{geo}}$ represents the sum of the geometrical stiffness $\boldsymbol{K}_{\boldsymbol{S'}}^{\boldsymbol{geo}}$ and $\boldsymbol{K}_{\boldsymbol{p^f}}^{\boldsymbol{geo}}$.

Since computation of the homogenized $\boldsymbol{K}^{\boldsymbol{s}}$ from DEM RVEs produces considerable computational cost, in the proposed multiscale solution scheme, we choose to treat $\boldsymbol{K}^{\boldsymbol{e}}$ implicitly and $\boldsymbol{K}^{\boldsymbol{ep}}$ explicitly. $\boldsymbol{K}^{\boldsymbol{e}}$ is thus evaluated at the initial time step using the elastic properties (bulk modulus K_{bulk}^{DEM} and shear modulus G_{shear}^{DEM}) homogenized from the initial RVEs. $\boldsymbol{K}^{\boldsymbol{up}}$ and $\boldsymbol{K}^{\boldsymbol{p}}$ are included in the implicit part of the tangential stiffness matrix. The geometrical terms $\boldsymbol{K}^{\boldsymbol{geo}}$ and $\boldsymbol{K}_{\boldsymbol{1}}^{\boldsymbol{p}}$ are treated explicitly. With these considerations and (6.52), the resulting operator split writes:

$$\begin{cases} \boldsymbol{K}_{\boldsymbol{T}} = \boldsymbol{K}_{\boldsymbol{T}}{}^{\text{implicit}} + \boldsymbol{K}_{\boldsymbol{T}}{}^{\text{explicit}} \\ \boldsymbol{K}_{\boldsymbol{T}}{}^{\text{implicit}} = \dfrac{\partial \left\{ \boldsymbol{F}^{\boldsymbol{int}} \right\}^{\text{implicit}}}{\partial \boldsymbol{d}} = \begin{bmatrix} \boldsymbol{K}^{\boldsymbol{e}} & -\boldsymbol{K}^{\boldsymbol{up}} \\ \boldsymbol{0} & \boldsymbol{K}^{\boldsymbol{p}} \end{bmatrix} \\ \boldsymbol{K}_{\boldsymbol{T}}{}^{\text{explicit}} = \begin{bmatrix} -\boldsymbol{K}^{\boldsymbol{ep}} + \boldsymbol{K}^{\boldsymbol{geo}} & \boldsymbol{0} \\ \boldsymbol{K}_{\boldsymbol{1}}^{\boldsymbol{p}} & \boldsymbol{0} \end{bmatrix} \end{cases} \tag{6.53}$$

From equations (6.44), (6.47), (6.49), (6.50) and (6.53), we obtain equation (6.54), which represents the iteration equation of the semi-implicit predictor-multicorrector scheme:

$$\boldsymbol{M}^{**} \cdot \Delta \boldsymbol{v}_{n+1}^{j+1} = \Delta \boldsymbol{F}_{n+1}^{j} = \boldsymbol{F}_{n+1}^{\boldsymbol{ext}} - \boldsymbol{M}^{*} \cdot \boldsymbol{v}_{n+1}^{j} - \boldsymbol{F}^{\boldsymbol{int}}(\boldsymbol{d}_{n+1}^{j}) - \boldsymbol{G}(\boldsymbol{d}_{n+1}^{j}) \tag{6.54}$$

where the internal force $\boldsymbol{F}^{\boldsymbol{int}}(\boldsymbol{d}_{n+1}^{j})$ has two contributions: the PK2 effective stresses which are homogenized from DEM RVEs and the macroscopic internal force from FEM, i.e.,

$$\boldsymbol{F}^{\boldsymbol{int}}(\boldsymbol{d}_{n+1}^{j}) = \left\{ \begin{matrix} \boldsymbol{f}^{\boldsymbol{int}}(\boldsymbol{u}_{n+1}^{j}) \\ \boldsymbol{0} \end{matrix} \right\}^{\text{DEM}} + \left\{ \boldsymbol{F}^{\boldsymbol{int}}(\boldsymbol{d}_{n+1}^{j}) \right\}^{\text{FEM}} \tag{6.55}$$

ϕ^{DEM}, B^{DEM}, M^{DEM} and k^{DEM} are homogenized at each time step to construct the tangential matrix $\boldsymbol{M}^{**}$. The convergence is achieved when $\frac{||\Delta \boldsymbol{F}_{n+1}^{j}||}{||\Delta \boldsymbol{F}_{n+1}^{0}||} \leq$ TOL [Prevost, 1983]. In the numerical examples TOL is equal to 10^{-4} . The matrix forms of the finite strain multiscale u-p formulation are provided in the Appendix. To recapitulate and illustrate the multiscale semi-implicit scheme, we present a flowchart as shown in Fig.6.2.

6.5 Numerical Examples

The objective of this section is to demonstrate the versatility and accuracy of the proposed method in both the small and finite deformation ranges. The numerical examples in this section are the representative problems commonly encountered in geotechnical engineering. The first example is the Terzaghi's problem, which serves as a benchmark to verify the implementation of the numerical schemes proposed in this paper. This example

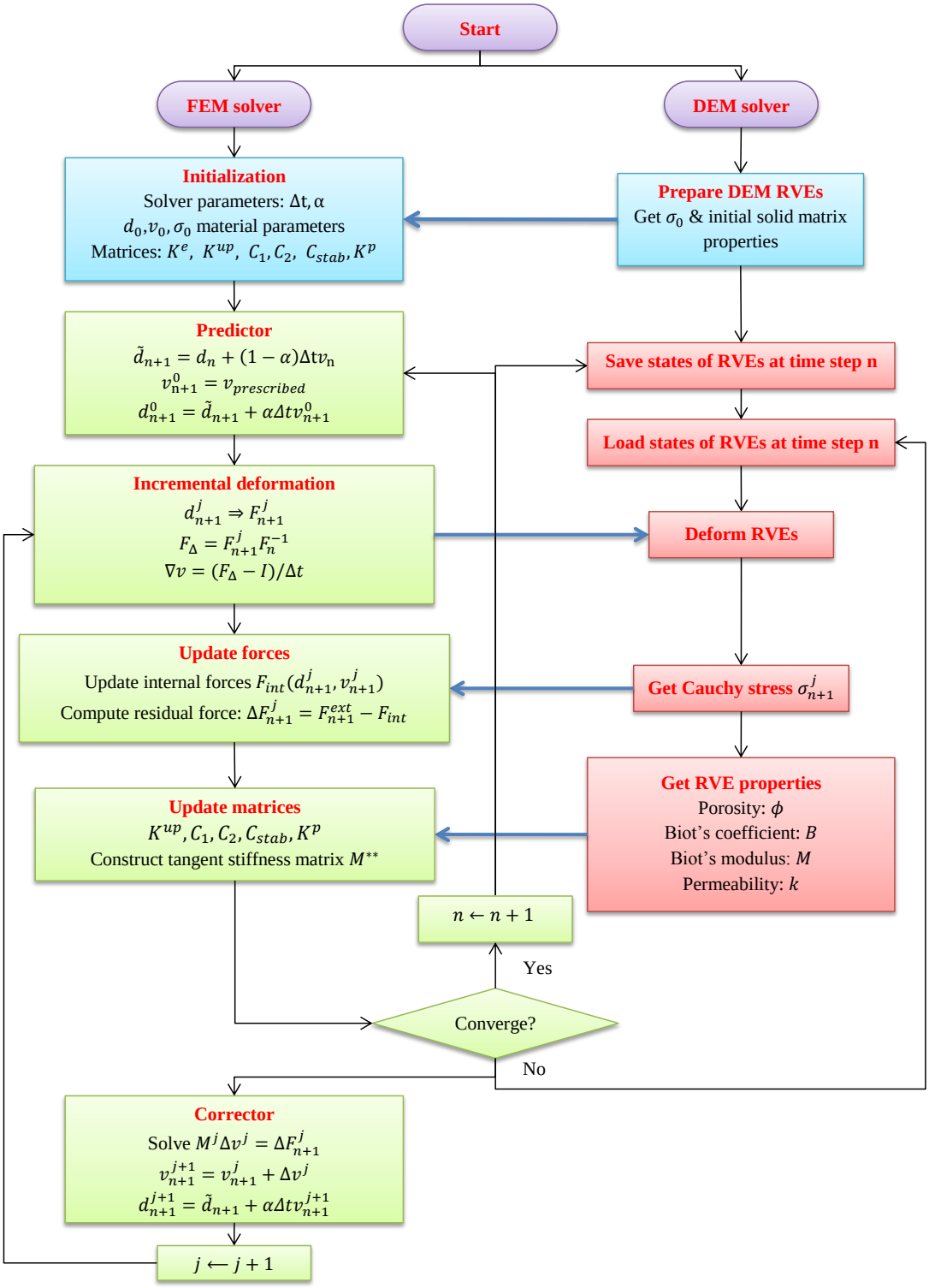

Figure 6.2: *Flowchart of the multiscale semi-implicit scheme. Blue blocks represent initialization steps of the solution scheme ; Green blocks refer to FEM solver steps and red blocks refer to DEM solver steps; Blue arrows indicate the information flow between the two solvers.*

is followed by a globally undrained shear test which examines how granular motion altered by fluid seepage within a soil specimen affects the macroscopic responses. In the third example, we simulate the responses of a cylindrical DEM-FEM model with drained condition subjected to triaxial compression loading with both quarter- and full domains and found that the quarter simulation may suppress the non-symmetric bifurcation mode that leads to shear band. The analysis on fabric tensor also reveals that the fabric and deviatoric stress

Parameter	Value
Solid matrix bulk modulus	40 MPa
Solid matrix shear modulus	40 MPa
Fluid bulk modulus	22 GPa
Permeability	$1 \times 10^{-9}\ m^2/(Pa \cdot s)$
Solid density	2700 kg/m^3
Fluid density	1000 kg/m^3
Porosity	0.375

Table 6.1: *Material parameters in Terzaghi's problem*

tensors are almost co-axial inside the shear band, but they are not co-axial in the host matrix. The last example is a slope stability problem in which only a portion of domain, i.e. the slip surface is modeled by the DEM-FEM model and compared with the prediction done via SLOPE/W. The result shows that the multiscale analysis may lead a more conservative prediction than the classical Bishop's method.

6.5.1 Verification with Terzaghi's one-dimensional consolidation

We verify our semi-implicit DEM-mixed-FEM scheme in both infinitesimal strain and finite strain regimes with the Terzaghi's 1D consolidation problem. This benchmark problem serves two purposes. First, we want to ensure that the semi-implicit FE algorithm converges to the analytical solution in the geometrically linear regime. Second, we want to assess whether the geometrical effort is properly incorporated in the numerical scheme in the finite deformation range. The Terzaghi's problem is well known and exact solution is available [Terzaghi et al., 1943]. While numerical solution of Terzaghi's problem does not provide much new insight beyond the established results, comparing the numerical solution with the analytical counterpart is nevertheless an important step in the verification procedure. In particular, this comparison ensures that the implementation of the model accurately represents the conceptual description and specification, as pointed out by Jeremić et al. [2008].

The model consists of a soil column of 10 m deep discretized by 10 3D hexahedral finite elements of size 1 m each along the column. The bottom surface is fixed and undrained, while the top boundary is drained and subjected to pressure of 1 MPa (small strain condition) and 10 MPa (large strain condition). The lateral surfaces are all impermeable and allow only vertical displacements. The material parameters assumed in this example are recapitulated in Table 6.1. Firstly the simulation is performed under consolidation pressure of 1 MPa from 0 s to 500 s with time step of 1 s. The comparison between the analytical solution and the numerical solution shown in Fig. 6.3 verifies the correctness of the u-p semi-implicit scheme and the effectiveness of the fluid pressure Laplacian stabilization scheme.

To illustrate the influence of geometrical non-linearity and varied permeability on the consolidation behavior, the soil column is subjected to a pressure of 10 MPa, resulting in a final vertical strain of about 8%. The pressure and displacement evolution computed by different formulations are shown in Fig. 6.4. The finite strain scheme with constant permeability and the small strain scheme yield the same results until a compression of about 5 % vertical strain (at 250 s). Thereafter, due to the additional geometric nonlinear terms, the finite strain scheme gives smaller displacement and pressure compared to small strain, indicating that geometrical non-linearity becomes significant. When the permeability is permitted to decrease along with the reduced porosity during consolidation according to the Kozeny-Carman relation, the soil column requires more time to reach the final steady state, yet the final values remain the same as finite strain with constant permeability. The above observations are consistent with previous numerical studies [Li et al., 2004, Regueiro and Ebrahimi, 2010] .

6.5.2 Globally undrained shear test of dense and loose assemblies

For the second example we employ our multiscale scheme to perform shear tests on both dense and loose granular assemblies. The macroscopic geometry and boundary conditions are illustrated on a sample discretized by coarse mesh ($1\times5\times5$ in X,Y,Z directions) as Fig. 6.5. We also use a medium fine mesh ($1\times8\times8$) and a fine mesh ($1\times10\times10$) to investigate the mesh dependency issue of the proposed scheme. All results in this section are computed from the fine mesh model, if not specified. The nodes on the bottom boundary are fixed in all directions and those on the upper boundary are translated identically towards the positive y axis at a constant rate. They are maintained at a constant vertical stress $\sigma_z = 100kPa$ by a horizontal rigid layer (not shown). This constraint is imposed in the model by the Lagrange multiplier method. The lateral surfaces are constrained

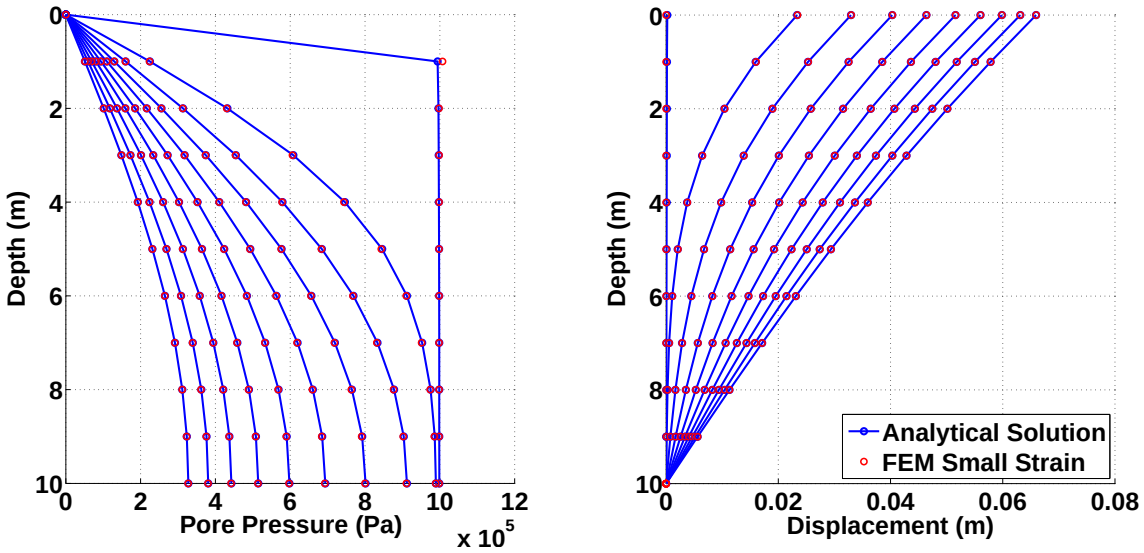

(a) (b)

Figure 6.3: *Response of saturated soil column under 1 MPa consolidation pressure from 0 s to 500 s (50 s between adjacent lines), verification of small strain formulation with analytical solutions (a) Pore pressure (b) Vertical displacement*

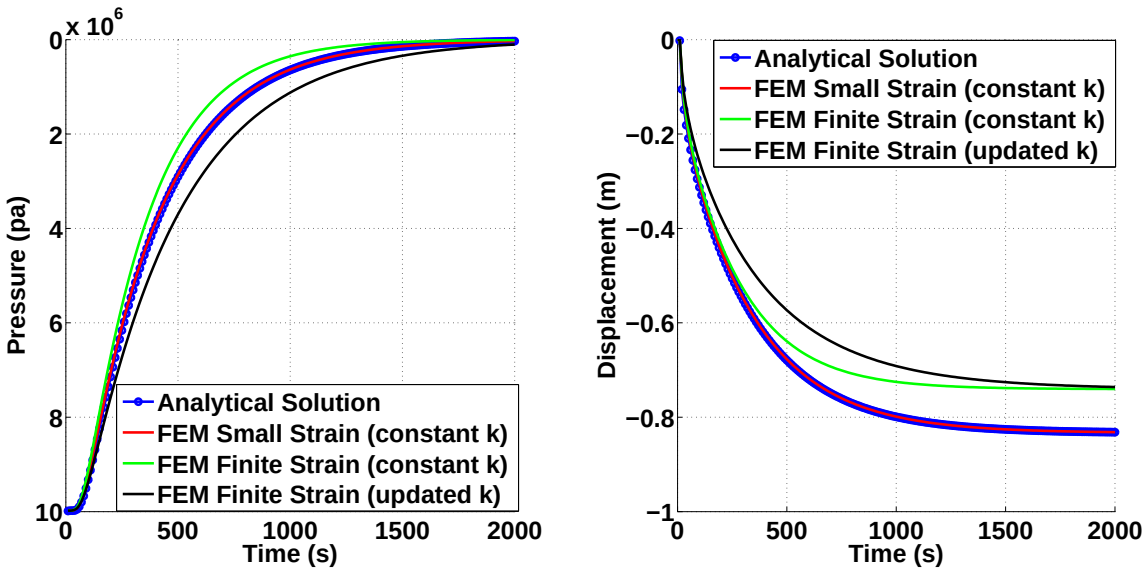

(a) (b)

Figure 6.4: *Response of saturated soil column under 10 MPa consolidation pressure. Comparison of analytical solution, numerical result from formulations of small strain, large strain with constant permeability k (in m/s) and large strain with k updated by the Kozeny-Carman equation. (a) Pore pressure evolution at bottom surface (b) Vertical displacement evolution at top surface*

by frictionless rigid walls (not shown). All surfaces are impervious. The gravitational effect is not considered in this study. For coupled microscopic DEM models, periodic unit cells composed of uniform spheres are prepared by an isotropic compression engine in YADE up to $\sigma_{iso} = 100kPa$ with initial porosity of 0.375 and 0.427 for dense and loose assemblies respectively, and then are assigned identically to all the integration points of the FEM model before shearing.

The finite strain formulation is first adopted to study the hydro-mechanical coupling effect during the shearing of the dense and loose samples with undrained boundaries. The material parameters used in the simulations allowing hydraulic diffusion within the specimen are presented in Table 6.2. They are categorized into micromechanical material parameters used in DEM solver, poro and poro-plasticity parameters derived from

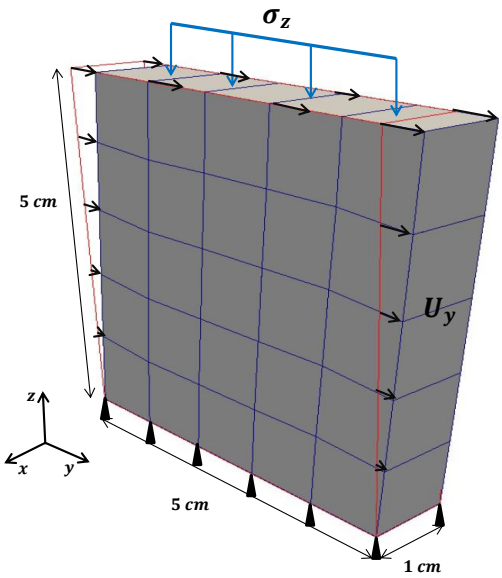

Figure 6.5: *Geometry and boundary conditions for globally undrained shear test*

DEM RVEs and macroscopic properties set in FEM. Note that the permeability k is updated with porosity of RVEs using the Kozeny-Carman relation during the simulation. To prevent local seepage of water within the samples, the permeability k is set to 0 $m^2/(Pa \cdot s)$.

Fig. 6.6 represents the global shear stress and volumetric strain behavior of shear simulations with and without local seepage of water. The strain-hardening behavior of undrained dense granular assemblies (left column) and strain-softening behavior of undrained loose granular assemblies (right column) are recovered [Yoshimine et al., 1998]. In both assemblies, when local seepage is prohibited, the shear stress immediately rises when the shearing begins and the saturated porous media behaves stiffer than the samples with local seepage. Note that the sudden drop in Fig. 6.6(b) is due to the unstable solid matrix of loosely confined DEM unit cell. The volumetric strain of the dense sample with seepage monotonically increases. This phenomenon is attributed to the rearrangement of solid matrix as the grains tend to rise over adjacent grains when they are driven by shear forces. In absence of local diffusion, the dense sample experiences a reduction of volume instead, suggesting that the compression of overall solid matrix predominates the above phenomenon. As for loose samples, however, the volumetric behavior is opposite. When local diffusion of water is prohibited, the pore collapse and densification of local regions within specimen could occur, resulting in a compression at early stage of shearing before the dilatancy phenomenon. The curve of no-local-seepage case shows that the dilatancy phenomenon prevails all along the shearing. In all cases, the volume changes are beneath 0.12%, confirming that the samples are indeed sheared under globally undrained condition.

We examine the mesh dependency by three aforementioned mesh densities adopted in simulations of dense assembly with local seepage. The effect is presented via plots of global $\sigma_{yz} - \gamma_{yz}$ and $\varepsilon_v - \gamma_{yz}$ responses as Fig. 6.7. For stress response, discrepancy between medium and fine meshes is not significant, but coarse mesh apparently yields stiffer solution after 2% shear strain and the maximum deviation is about 7.6% with respect to the fine mesh solution. The differences between ε_v curves are less significant and do not exceed 4% of the fine mesh solution. Thus, our choice of the fine mesh to conduct numerical experiments is acceptable.

We next display the difference between finite and small strain multiscale schemes for simulations of dense granular sample in both local diffusion conditions in Fig. 6.8. According to the global shear responses, the small strain and finite strain yield consistent solutions within 2% shear strain. Then the discrepancy gradually emerges and the introduction of geometrical non-linearity renders the sample stiffer. This observation is the same as the conclusion in the previous Terzaghi's problem section. Finite strain solutions exhibit less volume changes in both cases. Moreover, geometrical non-linear term even alters the dilatancy behavior: the sample is computed to be compressed when no local seepage of water is allowed, while the small strain solution conserves the dilatant trend.

	Parameter	Value
Microscopic property in DEM	Solid grain normal stiffness k_n	$2.2 \times 10^6\ N/m$
	Solid grain tangential stiffness k_s	$1.9 \times 10^6\ N/m$
	Solid grain friction angle β	30°
	Solid grain bulk modulus K_s	0.33 GPa
Macroscopic property inferred from DEM	Porosity ϕ	dense: 0.375, loose: 0.427
	Biot's coefficient B	dense: 0.976, loose: 0.983
	Biot's Modulus M	dense: 180 Mpa, loose: 168 Mpa
Macroscopic property in FEM	Fluid bulk modulus K_f	0.1 GPa
	Initial permeability k	$1 \times 10^{-9}\ m^2/(Pa \cdot s)$
	Solid density ρ_s	$2700\ kg/m^3$
	Fluid density ρ_f	$1000\ kg/m^3$

Table 6.2: *Material parameters in globally undrained shear problem*

We also assess the local diffusion effect via color maps of pore pressure developed during the deformation, as shown in Fig. 6.9. The dense sample with local seepage has developed negative pore pressure and the pressure distribution is nearly uniform, since fluid flow could take place inside the specimen to dissipate pressure difference between neighboring pores. Without local seepage of water, the pore pressure is concentrated to four corners of the sample, with the upper left and bottom right corners compressed (positive pressure) and the other two dilated (negative pressure). Furthermore, these corners have maximum pressure gradient $||\nabla p^f||$.

The multiscale nature of our method offers more insight into the local states of granular sample. With the granular material behavior homogenized from responses of RVEs, the grain displacements, the effective stress paths (shear stress $q = \sigma_1 - \sigma_3$ vs. effective mean stress $p' = \frac{\sigma_1+\sigma_2+\sigma_3}{3}$) and the volumetric strain paths (ε_v vs. p') in each DEM unit cell are directly accessible. As an example, the local distribution of q at the end of shearing for globally undrained yet locally diffused dense sample (6.10) shows a concentration of shear stress in upper left and bottom right corners, while the corners correspondent to the other diagonal sustain comparably very little shear stress. The deformed configuration of spheres in three representative RVEs are colored according to the dimensionless displacement magnitude $\frac{||\boldsymbol{u}||_2}{\text{inital size of unit cell}}$ compared to initial RVE configuration. We present stress paths of these three RVEs providing evidence that strain-softening (Fig. 6.11(a)), limited strain-softening (Fig. 6.11(b)) and strain-hardening (Fig. 6.11(c)) could locally occur in a dense sample which globally behaves in a strain-hardening manner. A critical state line $q = \eta p'$ is drawn for three stress paths and the value of slope η is identified as 1.16. η and the Mohr-Coulomb friction angle β' is computed to be 29.1° by the following relation for cohesionless soil [Wood, 1990]:

$$\sin \beta' = \frac{3\eta}{6 + \eta} \tag{6.56}$$

, which is close to the inter-particle friction angle $\beta = 30^\circ$. Paths of ε_v further demonstrate that large local volume change up to 5.5% is possible even globally the sample is only dilated about 0.07%. According to these figures, the small strain and finite strain shear responses are almost identical. The stress path curves exhibit little difference. However, geometrical non-linearity has more significant effect on volumetric strain path. A major remark is that, inside the strain-softening spot as 6.11(d), the small strain solution has large fluctuation when the mean effective stress is very small, because DEM assemblies are highly unstable with nearly zero confining stress. On the contrary, finite strain scheme avoids this unstable regime and yield smooth solutions.

Lastly, we investigate the rate-dependent shearing behavior using the proposed coupling scheme. A faster shearing of saturated granular sample influences its mechanical response mainly by speeding up the solid matrix re-arrangement and also by allowing less fluid diffusion inside the sample between loading steps. The former effect leads to swelling of the sample, while the latter renders the specimen more locally undrained. Fig.6.12 illustrates the combined effect of these two mechanisms on a dense sample with local seepage. The evolution of shear stress and volumetric strain with shearing rates of 0.1% and 0.5% per second are compared. When shearing is completed, shear stress sustained by the sample increases about 4.6% under higher shearing rate. The rate effect on volumetric strain is more prominent, by the fact that the sample experiences more volume expansion of about 13.5% at the end.

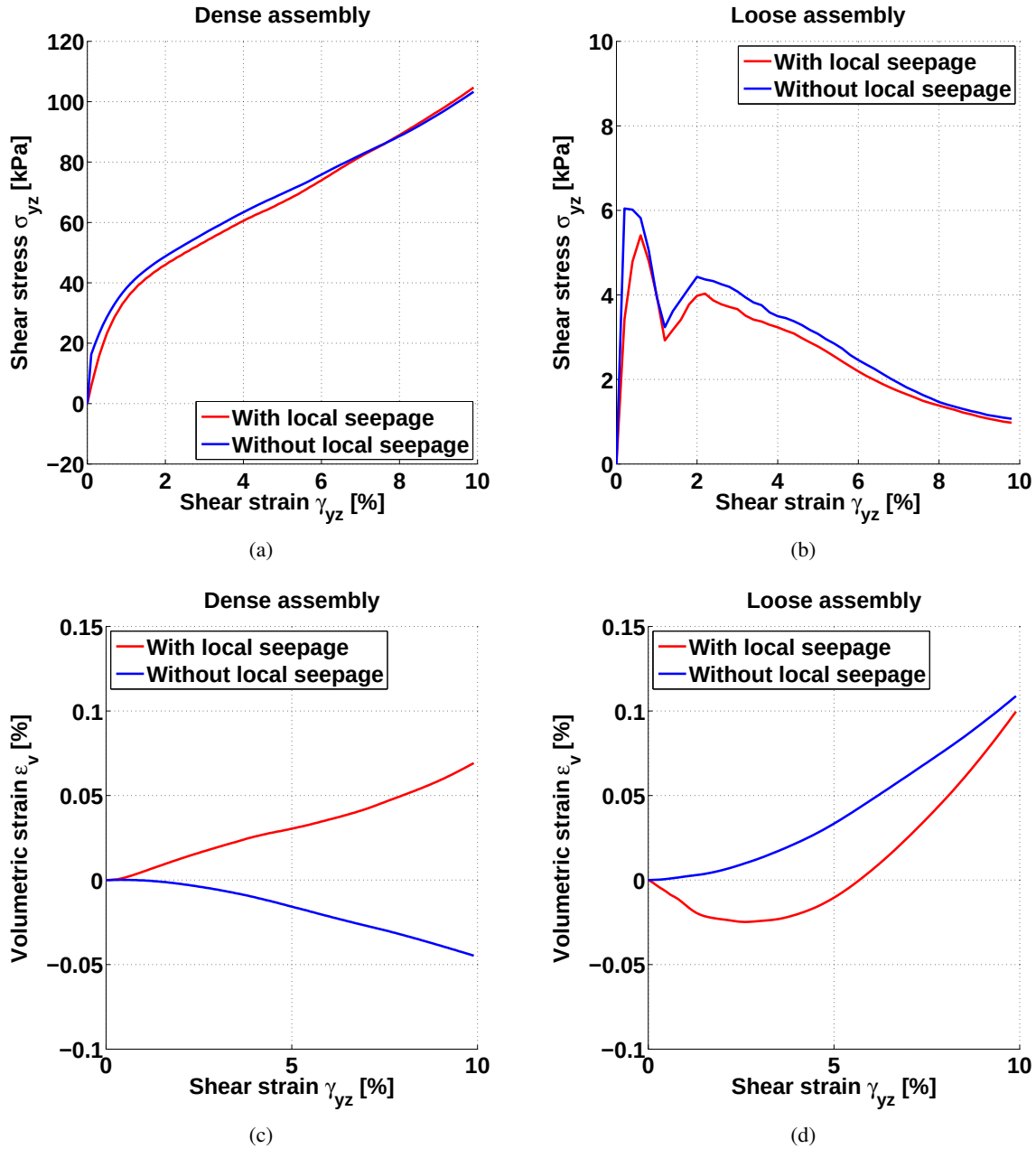

Figure 6.6: *Comparison of global shear stress and volumetric strain behavior between globally undrained dense and loose assemblies with and without local diffusion*

6.5.3 Globally drained triaxial compression test

The third example consists of the globally drained triaxial compression test on an isotropically consolidated cylindrical specimen. This example demonstrates the applicability of the proposed multiscale finite strain scheme on 3D problems. In this numerical example, we analyze (1) the difference between quarter-domain and full-domain simulations for material subjected to axial-symmetrical loading, (2) the consequence of the build-up of excess pore pressure due to a high loading rate and (3) the evolution of the fabric tensor inside and outside the shear band and the implications on the critical state of the materials. As a result, water is allowed to flow through the bottom and the top of the specimen. However, triaxial compression simulation is intentionally not conducted under a fully drained condition at a material point level. Instead, the rate dependence of the constitutive responses introduced via the hydro-mechanical coupling effect is studied to quantify what is the acceptable range of the prescribed loading rate that can prevent significant amount of excess pore pressure.

In addition, microscopic information such as the Biot's coefficient, Biot's modulus and micro-structure fabric are provided to highlight the advantage of the DEM-FEM coupled model. The convergence profile of this simulation is also presented. In an experimental setting, the drained triaxial test is performed on a

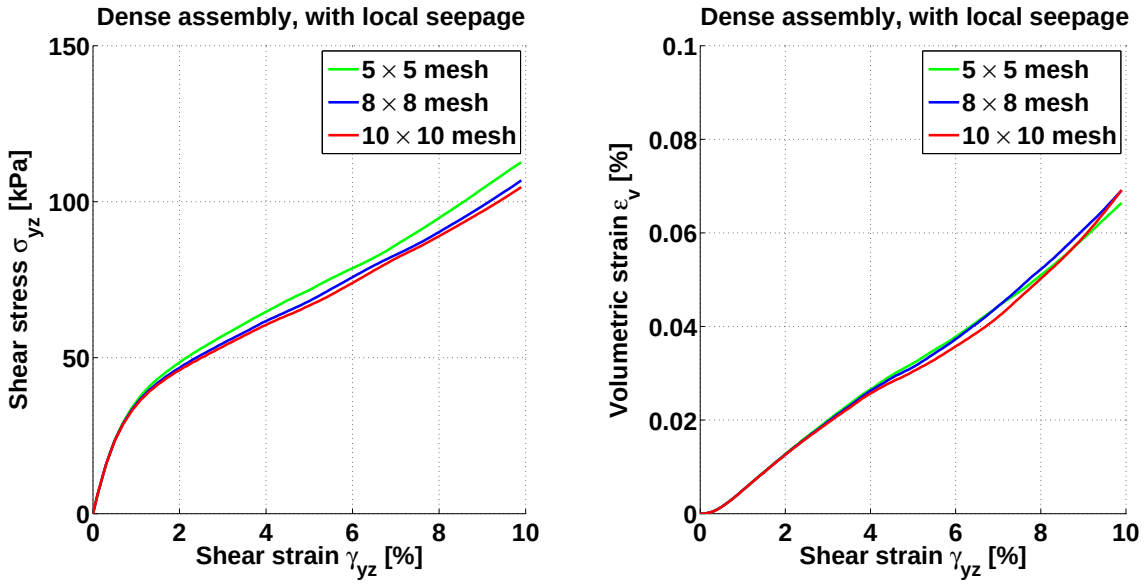

(a) (b)

Figure 6.7: *Comparison of global shear stress and global volumetric strain behavior between coarse mesh (1×5×5), medium mesh (1×8×8), fine mesh (1×10×10), finite strain formulation*

cylindrical water-saturated soil specimen, laterally enveloped by rubber membrane and drained through top and bottom surfaces. One of the idealized 3D numerical model constitutes only a quarter of the cylinder by assuming the rotational symmetry. The constant confining pressure is directly applied on the lateral surface, neglecting the effect of rubber membrane. The quasi-static compression is achieved by gradually increasing the axial strain ε_z at the rate of 0.05% per second. The lateral surface is impermeable and a no-flux boundary condition is imposed, while the pore water pressure on both top and bottom surfaces are constrained to be 0. Another simulation is triaxial compression of the full cylindrical domain. Similar confining pressure and pore pressure boundary conditions are applied. The middle point of the bottom surface is fixed to prohibit rigid body translation. The geometry, mesh and boundary conditions of the quarter-/full-domain simulations are illustrated in Fig. 6.13. The DEM assembly adopted in these simulations is identical to the dense sample in the previous section. The fluid bulk modulus in this example is 2.2 GPa.

Fig. 6.14 compares the global shear stress and volumetric strain behavior from quarter-domain and full domain simulations. The shear stress curve obtained from full-domain simulation exhibits less peak stress and more significant softening than quarter-domain simulation. The volumetric strain curves, however, only show notable difference after the axial strain approaches 7%. This discrepancy may be attributed to the strain localization in full-domain simulation, as shown by the distribution of deviatoric strain and porosity in Fig. 6.15. A dilatant shear band is developed inside the cylindrical specimen, while in the quarter-domain, the deformation is nearly homogeneous. This difference is more profound given the fact that the proposed model also incorporates the geometrical effect at the finite strain range. Results from this set of simulations show that the quarter-domain simulation is insufficient to capture the deformed configuration when bifurcation occurs. While the assumption of axial-symmetry is valid before the onset of strain localization, enforcing axial-symmetry via reduced domain and additional essential boundary condition may eliminate the bifurcation mode(s) that is not axial-symmetric.

An additional full-domain simulation is performed at a strain rate ten times slower: $\dot{\epsilon_z} = 0.005\%$ per second. The global shear stress and volumetric strain behavior are compared for the two loading rates in Fig. 6.16. The specimen under higher strain rate can sustain higher shear stress, but the strain rate has very little influence on volumetric strain behavior. The evolution of pore pressure at the center of the cylindrical specimen in two cases are also shown in Fig. 6.17. At a high strain rate, the pore water does not have time to fully diffuse through local pores and reach steady state. As a result, excess pore pressure builds up to about 5 kPa while the specimen shrinks. The pressure then decreases and becomes negative when the specimen dilates. In the low-strain-rate case, the magnitude of pore pressure is about five times smaller while the trend looks similar of the high-strain-rate counterpart.

One of the advantages of substituting macroscopic phenomenological constitutive model with DEM sim-

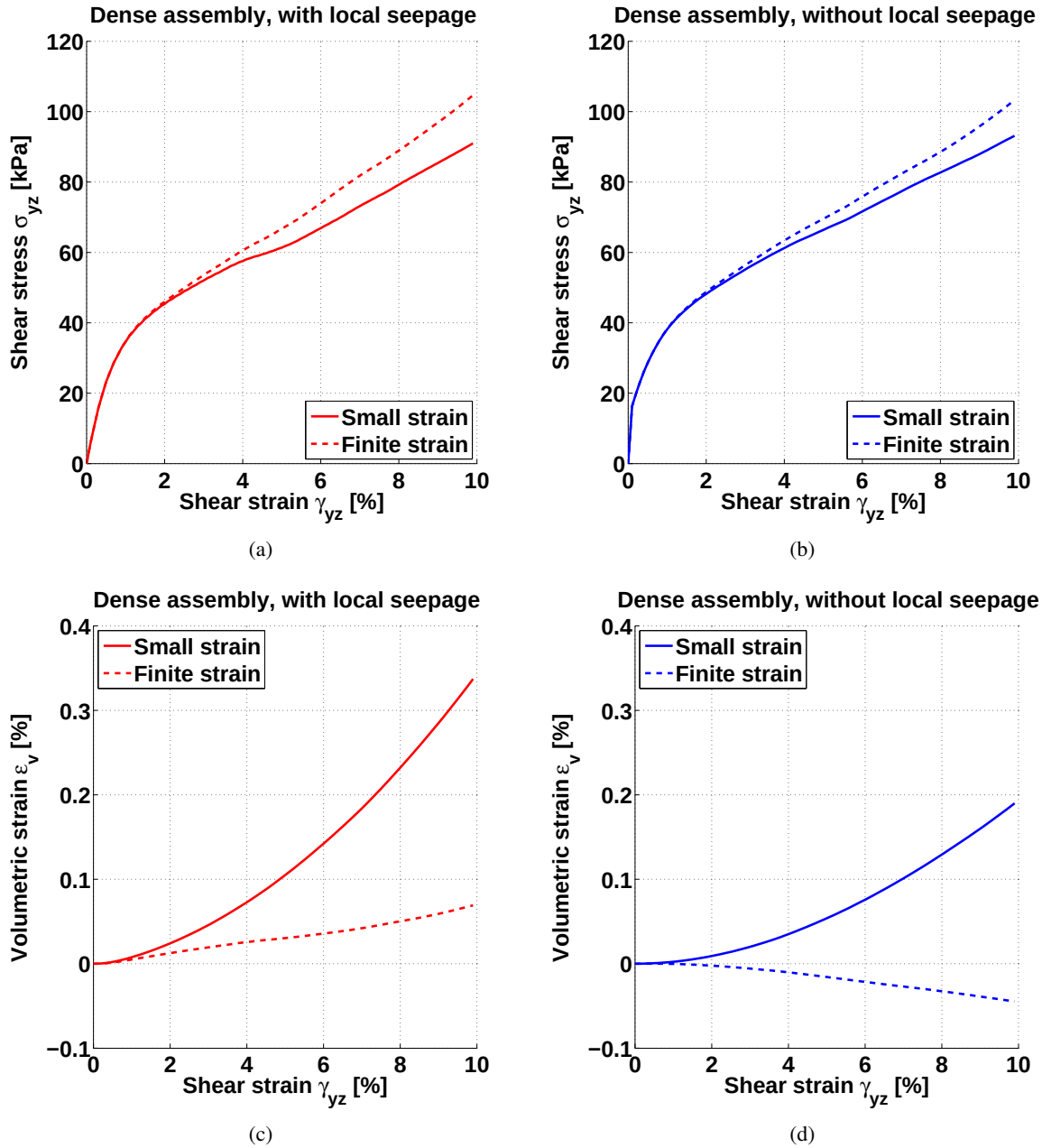

Figure 6.8: *Comparison of global shear stress and global volumetric strain behavior between small strain and finite strain formulation. Left: globally undrained with local diffusion condition, Right: globally undrained but without local diffusion condition*

ulations for the poromechanics problem is that the macroscopic poro-elasticity properties, such as Biot's coefficient B, Biot's modulus M and effective permeability k could be inferred and updated from DEM at each Gauss point. As a result, the spatial variability of these poro-elasticity parameters triggered by material bifurcation or non-homogeneous loading can be properly captured. As an example, we monitor the evolution of these poro-elasticity parameters against axial strain ε_z for a RVE inside the shear band (RVE A, shown in Fig. 6.15(c)) and another RVE outside the shear band (RVE B, shown in Fig. 6.15(c)) in the $\dot{\epsilon_z} = 0.05\%$-per-second, full-domain simulation (Fig. 6.18). The evolution of the Biot's coefficient B shown in Fig. 6.18)(a) suggests that the effective bulk modulus of the solid skeleton (K_T^{DEM}) first increases and then decreases presumably due to the porosity changes in both RVEs A and B. The Biot's modulus M, which is related to the Biot's coefficient B and porosity ϕ, exhibits an initial reduction and largely increases after about $\varepsilon_z = 2\%$ for RVE A. For RVE B, M stays at a constant value. The effective permeability k also evolves with the porosity according to the Kozeny-Carmen relation.

Another advantage of the multiscale scheme is the accessibility to evolution of micro-structures during

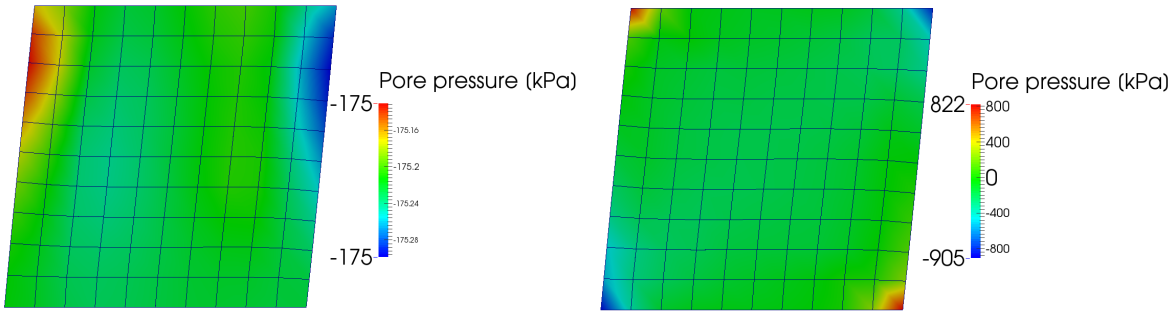

(a) (b)

Figure 6.9: *Comparison of pore pressure at 10% shear strain between (a) dense sample with local seepage and (b) dense sample without local seepage*

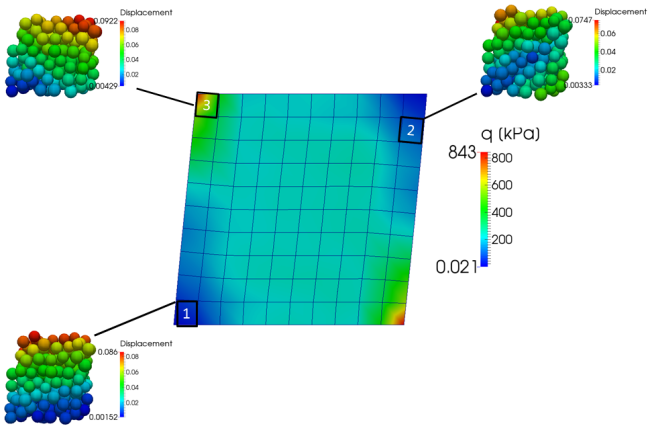

Figure 6.10: *Spatial distribution of shear stress q at 10% shear strain for globally undrained dense sample allowing seepage within the specimen, attached with displacement magnitude of grains in unit cells (normalized by the initial cell size)*

deformations. To demonstrate this, we perform a simple microstructural analysis in which the Anisotropic Critical State Theory (ACST) introduced by Li and Dafalias [2012], Zhao and Guo [2013], Li and Dafalias [2015] is adopted to analyze the fabric of the fluid-saturated granular assemblies at the finite strain range. The fabric anisotropy of two RVEs, one taken inside the shear band (RVE A) and another one in the host matrix (RVE B) are analyzed and compared against each other. The fabric tensor $\boldsymbol{G}_{\text{fabric}}$ is contact-normal-based and is computed from a DEM RVE via Li and Dafalias [2015]

$$G_{\text{fabric } ij} = \frac{1}{N_c} \sum_{c \in N_c} n_i^c n_j^c \tag{6.57}$$

where $\boldsymbol{n}^c$ is the unit vector of contact normal and N_c is the number of contacts inside the RVE. The tensor $\boldsymbol{F}_{\text{fabric}}$ characterizes the fabric anisotropy of the RVE and is written as [Zhao and Guo, 2013]

$$F_{\text{fabric } ij} = \frac{15}{2}(G_{\text{fabric } ij} - \frac{1}{3}\delta_{ij}) \tag{6.58}$$

where δ_{ij} is the Kronecker delta. Its norm F_{fabric} and direction $\boldsymbol{n}_F$ are defined by

$$\boldsymbol{F}_{\text{fabric}} = F_{\text{fabric}} \boldsymbol{n}_F, \quad F_{\text{fabric}} = \sqrt{\boldsymbol{F}_{\text{fabric}} : \boldsymbol{F}_{\text{fabric}}} \tag{6.59}$$

To analyze whether and how fabric evolves differently inside shear band and the host matrix, we compute the normalized fabric anisotropy variable (FAV) $A = \boldsymbol{n}_F : \boldsymbol{n}_s$ (a measure introduced in Li and Dafalias [2012],

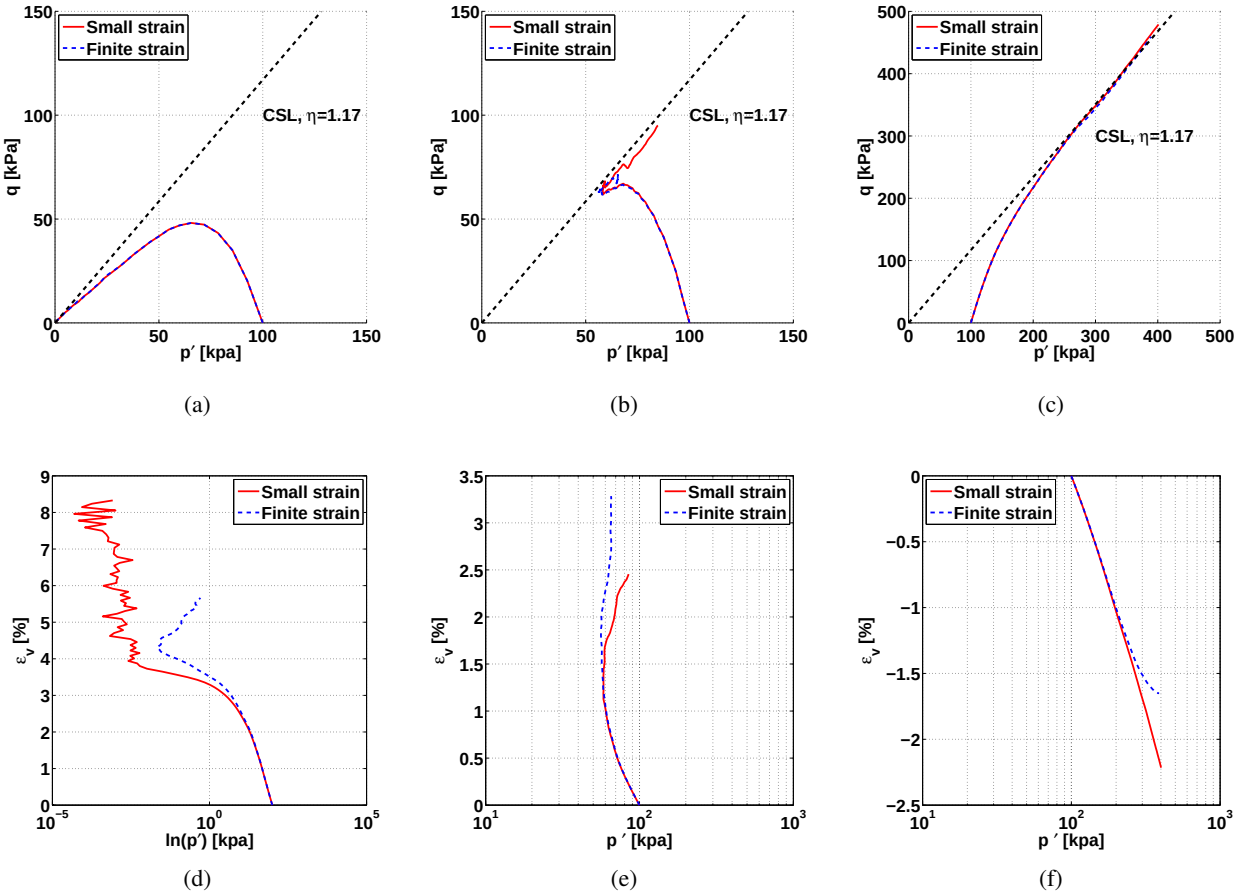

Figure 6.11: *Shear stress vs. effective mean stress at different locations indexed as Fig. 6.10: (b) stress path at point 1 (c) stress path at point 2 (d) stress path at point 3; Volumetric strain vs. effective mean stress at different locations: (e) volume path at point 1 (f) volume path at point 2 (g) volume path at point 3*

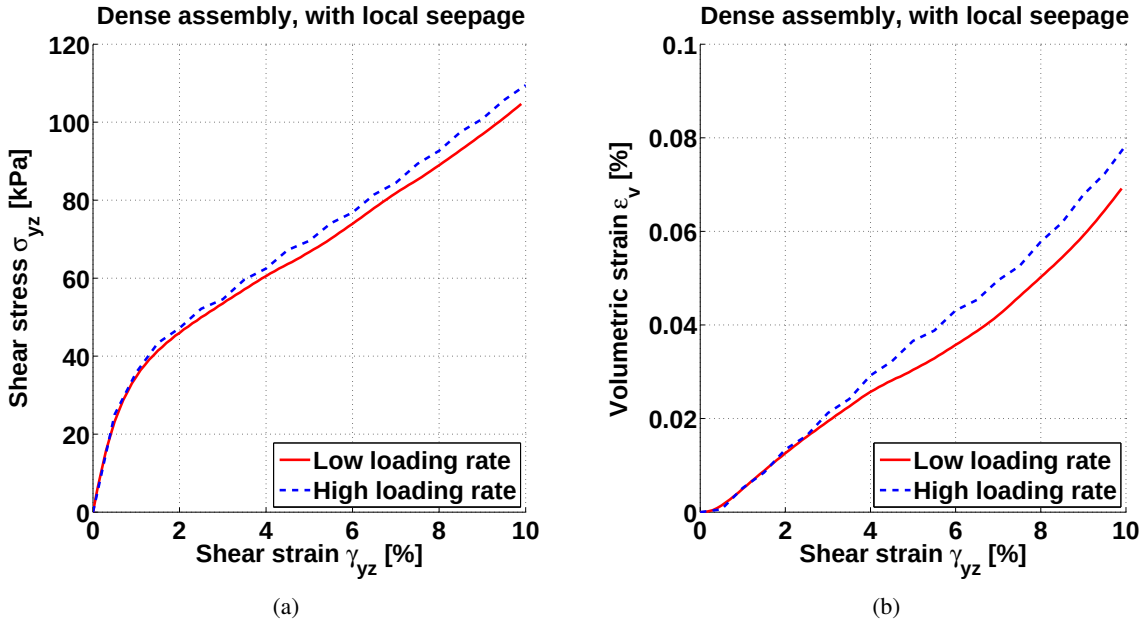

Figure 6.12: *Comparison of global shear stress and global volumetric strain behavior between low loading rate (0.1% shear strain per second) and high loading rate (0.5% shear strain per second), finite strain formulation*

Zhao and Guo [2013] that quantifies the relative orientation of the tensor $\boldsymbol{F}_{\text{fabric}}$ and the deviatoric stress tensor

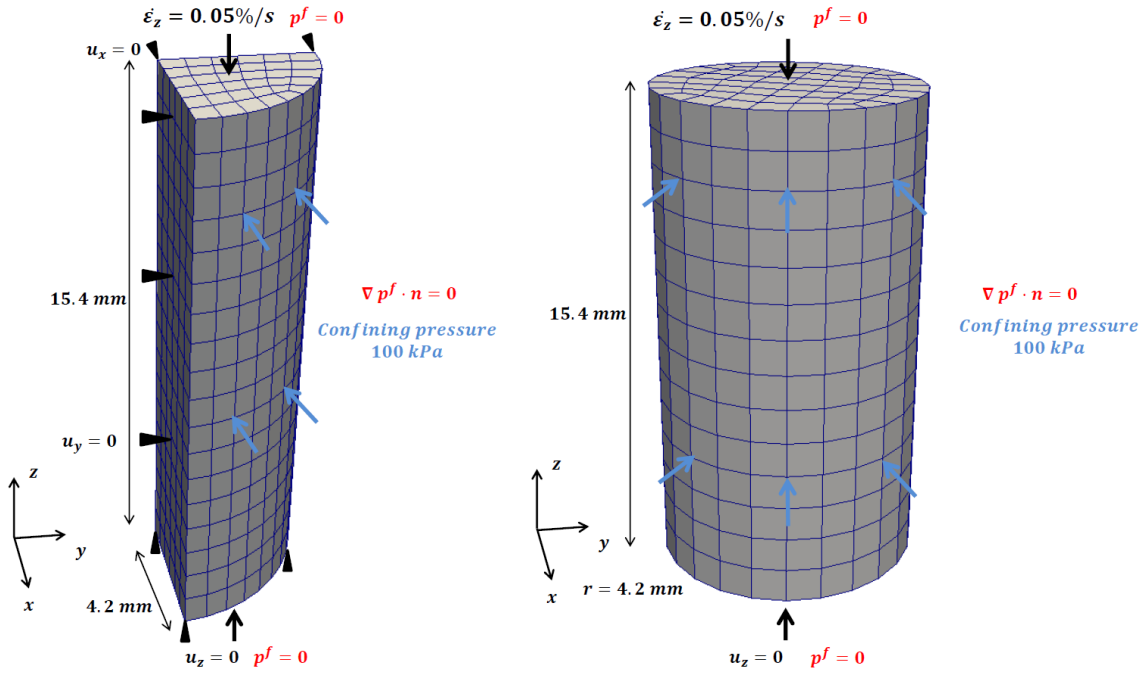

Figure 6.13: *Geometry, mesh and boundary conditions for globally drained triaxial compression test. (a) Quarter-domain simulation. (b) Full-domain simulation*

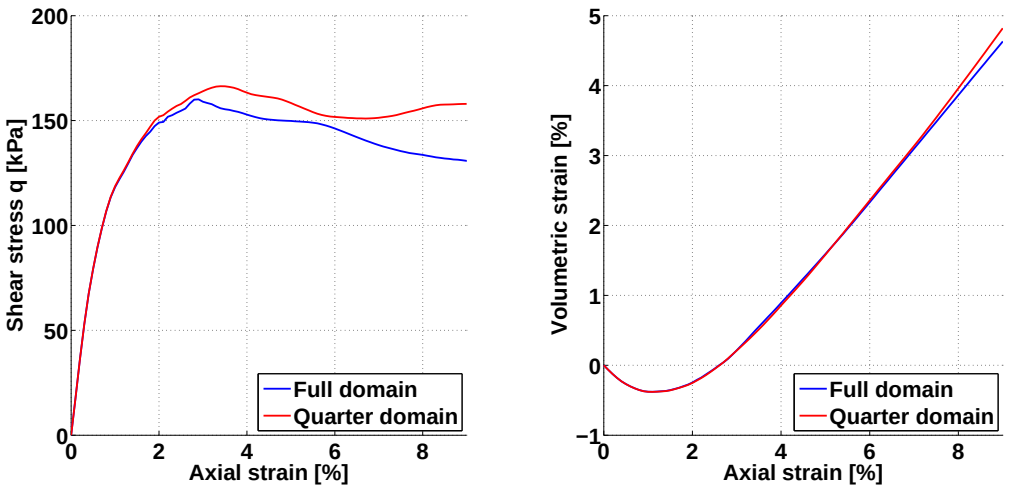

Figure 6.14: *Global shear stress and volumetric strain behavior in globally drained triaxial compression test. Comparison of quarter-domain and full-domain simulations*

$\boldsymbol{s}$) for RVE A (inside shear band) and RVE B (outside shear band). The evolution of deviatoric stress q and porosity against axial strain ε_z are also monitored to measure how close the materials in the two RVEs reach the critical state according to the anisotropic critical state theory, i.e.,

$$\eta = \eta_c,\ e = e_c = \hat{e}_c(p) \text{ and } A = A_c = 1 \tag{6.60}$$

where η is the ratio between the effective mean pressure p' and the deviatoric stress q and e is the void ratio. η_c, $e_c = \hat{e}_c(p)$ and $A_c = 1$ are critical state values of the stress ratio, void ratio and fabric anisotropy variable (cf. Li and Dafalias [2012, 2015]).

The results are summarized in Fig. 6.19. The stress-strain response shown in Fig. 6.19(a) indicates that RVE A becomes unstable after the peak shear stress and experiences significant dilation until the critical state

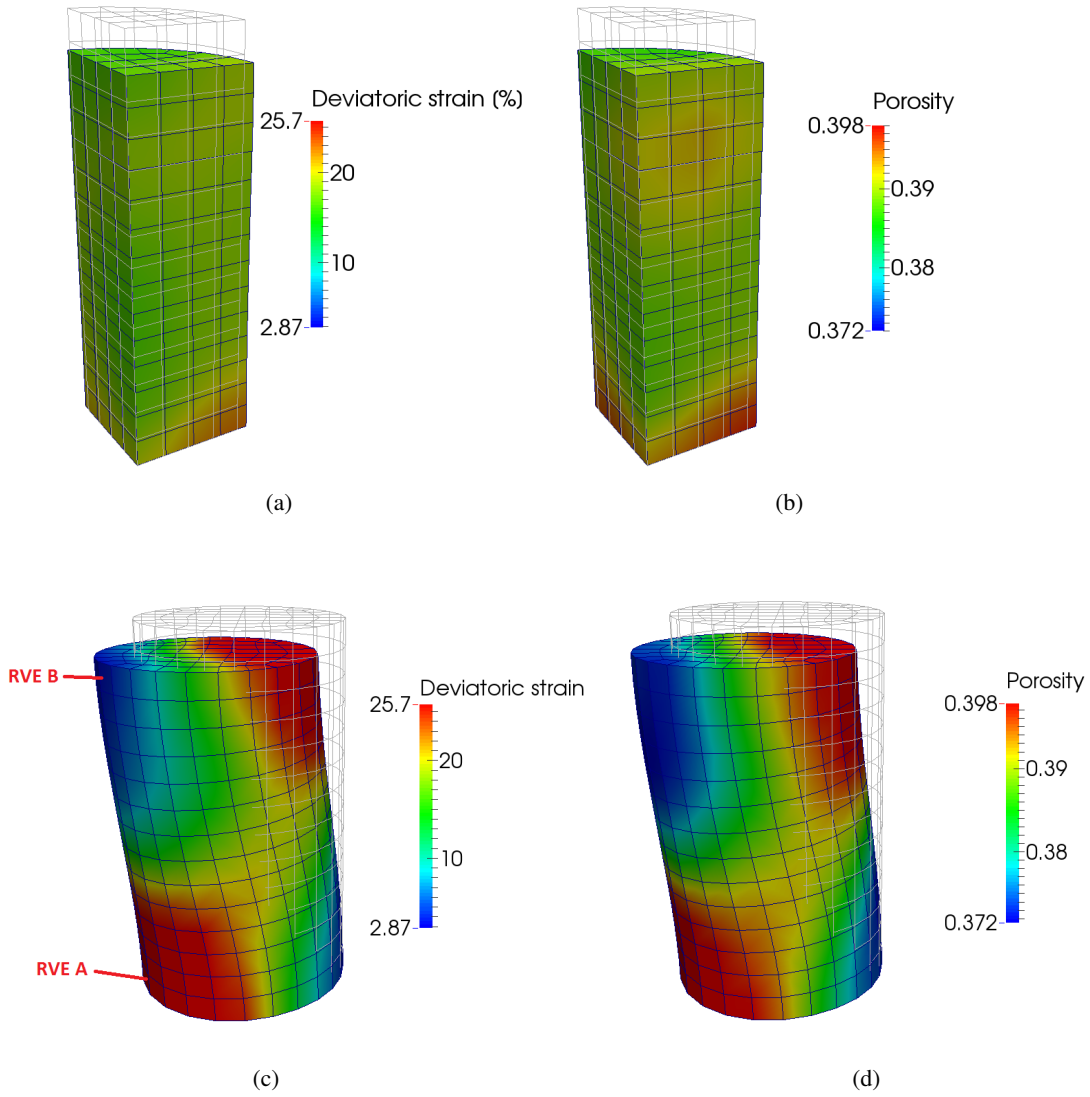

Figure 6.15: *Distribution of deviatoric strain and porosity in globally drained triaxial compression test at 9% axial strain. Comparison of quarter-domain and full-domain simulations.*

indicated by the plateau in the porosity curve. The normalized FAV of RVE A rises to about 0.96 quickly upon subjected to the triaxial loading. Then, normalized FAV stay close to 1, which indicates that the fabric and stress directions in RVE A is nearly coaxial, as the RVE A approaches the critical state.

On the other hand, RVE B, which lies outside the shear band, experiences slightly more softening, but the dilatancy is much less than RVE A. The FAV curve of RVE B deviates from the curve of RVE A after axial strain of 2% and exhibits opposite trend that the fabric and stress directions loss coaxiality. This observation suggests that the critical states are not achieved simultaneously within an specimen that forms deformation band.

To demonstrate the performance of the multiscale semi-implicit scheme, the convergence rate of the quarter-domain simulation is illustrated in Fig. 6.20 as an example. At different strain levels, the convergence curves show linear profiles in the logarithm-scale plot. The first step converges the fastest since the RVEs are linear elastic at $\varepsilon_z = 0.1\%$. The number of iterations required for convergence increases to 11 when the global shear stress reaches the peak (about $\varepsilon_z = 2\%$). In the softening stage, the explicitly treated the elastic-plastic contribution K^{ep} to the material tangential stiffness becomes more significant. Therefore the convergence rate is further reduced and each time step requires about 20 iterations.

6.5.4 Submerged slope stability problem

The last numerical example is the submerged slope stability problem. We select this problem for two reasons. First, we want to showcase how to use the DEM-mixed-FEM model to obtain high fidelity responses at a localized domain of interest, while using conventional mixed FEM in the far-field domain. Second, we

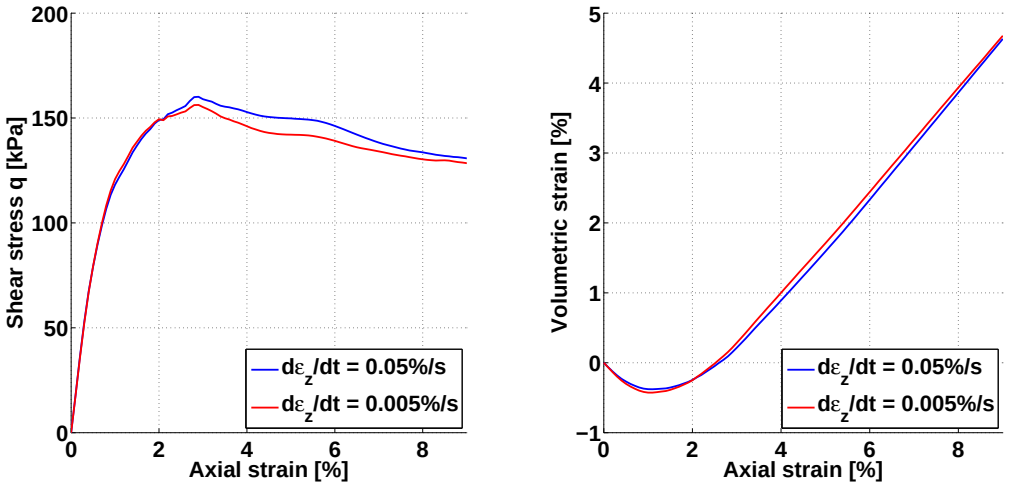

(a) (b)

Figure 6.16: *Global shear stress and volumetric strain behavior in globally drained triaxial compression test. Comparison of two loading rate.*

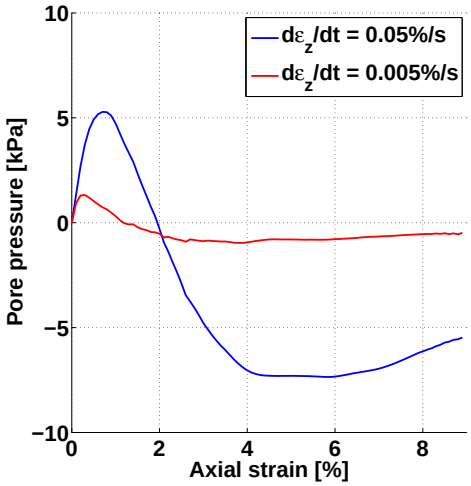

Figure 6.17: *Evolution of pore pressure at the center of the cylindrical specimen during triaxial compression test subjected to two loading rate.*

want to demonstrate the applicability of the proposed DEM-mixed-FEM model with a very common and simple field-scale problem.

The slope problem we consider consists of a 1:1 slope sitting on a bedrock that is assumed to be both impermeable and rigid. The slope is fully submerged underneath 2 meters of water. We conduct a classical slope stability analysis using the commercial software SLOPE/W and compare it with the results obtained from the DEM-mixed-FEM simulation. In particular, we compute the factor of safety using both the classical Bishop's method available in SLOPE/W and the proposed DEM-mixed-FEM model. The factor of safety (FOS) is defined as the ratio between the shear stress at failure τ_f and the current shear stress on the slip surface τ:

$$FOS = \frac{\tau_f}{\tau} \tag{6.61}$$

where τ_f is determined by the material's effective cohesion c', effective friction angle ϕ', total normal stress σ_n, and the pore pressure u as [Bishop, 1955, Borja et al., 2012]:

$$\tau_f = c' + (\sigma_n - u)\tan\phi' \tag{6.62}$$

To make the comparison between the SLOPE/W and the DEM-mixed-FEM model feasible, the DEM unit cell adopted in this simulation is firstly subjected to drained triaxial compression test under different confining

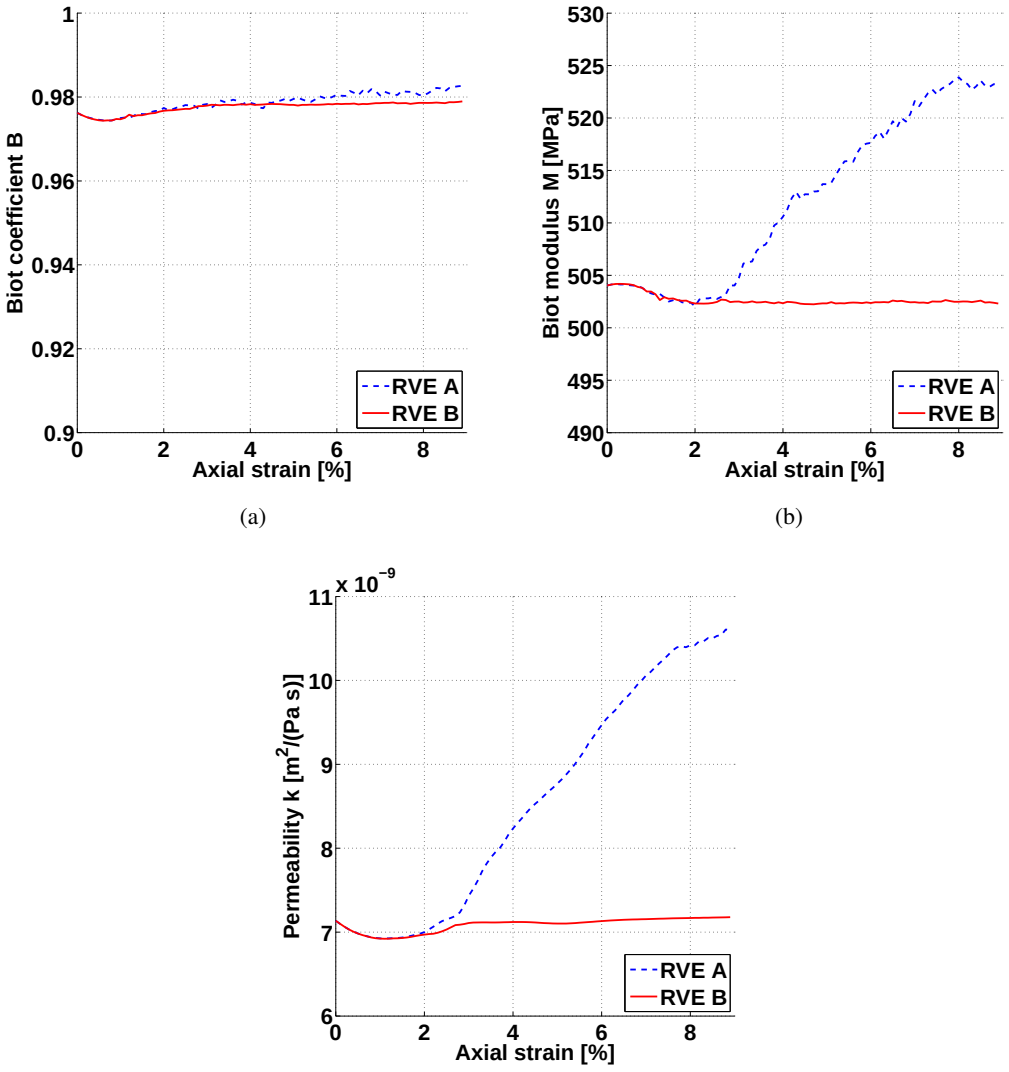

Figure 6.18: *Evolution of (a) Biot's coefficient, (b) Biot's modulus and (c) effective permeability for RVE A (inside shear band, Fig. 6.15(c)) and RVE B (outside shear band, Fig. 6.15(c)).*

pressures to obtain the Mohr-Coulomb failure envelope. The grain contact model we employed in this example is from Bourrier et al. [2013], which includes the modified frictional-normal contact law that includes cohesive normal and shear force in (**??**) and (**??**). As a result, we obtain the frictional angle $\phi' = 30°$ and cohesion $c' = 2.5$ kPa from the simulated DEM responses.

The modified Bishop method implemented in the commercial software SLOPE/W assumes that strain localization may take place upon the slope failure and the localized zone is a circular slip surface. For a fully submerged 1:1 slope composed of materials with $\phi' = 30°$ and $c' = 2.5$ kPa, we calculate the center and radius of slip surface, as well as FOS which is assumed to be constant along the surface. The FOS computed by SLOPE/W is 1.281, as shown in Fig. 6.21.

The FEM-mixed-DEM simulation we conduct here assumes that the model fails with the same slip surface as the geometry calculated above. Thus only the material constitutive relation in elements along the slip surface comes from the DEM solver while as the other elements outside the critical surface are assumed to have a linear elastic behavior, possessing the same elastic properties as the DEM samples. Here we follow the simple approach used in Cappa and Rutqvist [2011] to model both the bulk and the critical surface with 8-node brick elements, but the the thickness of the critical surface elements are set be of the order of the material length scale (i.e. 5cm). In the future, we will explore the usage of finite strain localization element [Yang et al., 2005] or embedded localization zone model [Fish and Belytschko, 1988] to couple DEM with FEM for problems with weak or strong discontinuities. These treatments, nevertheless, are out of the scope of this study.

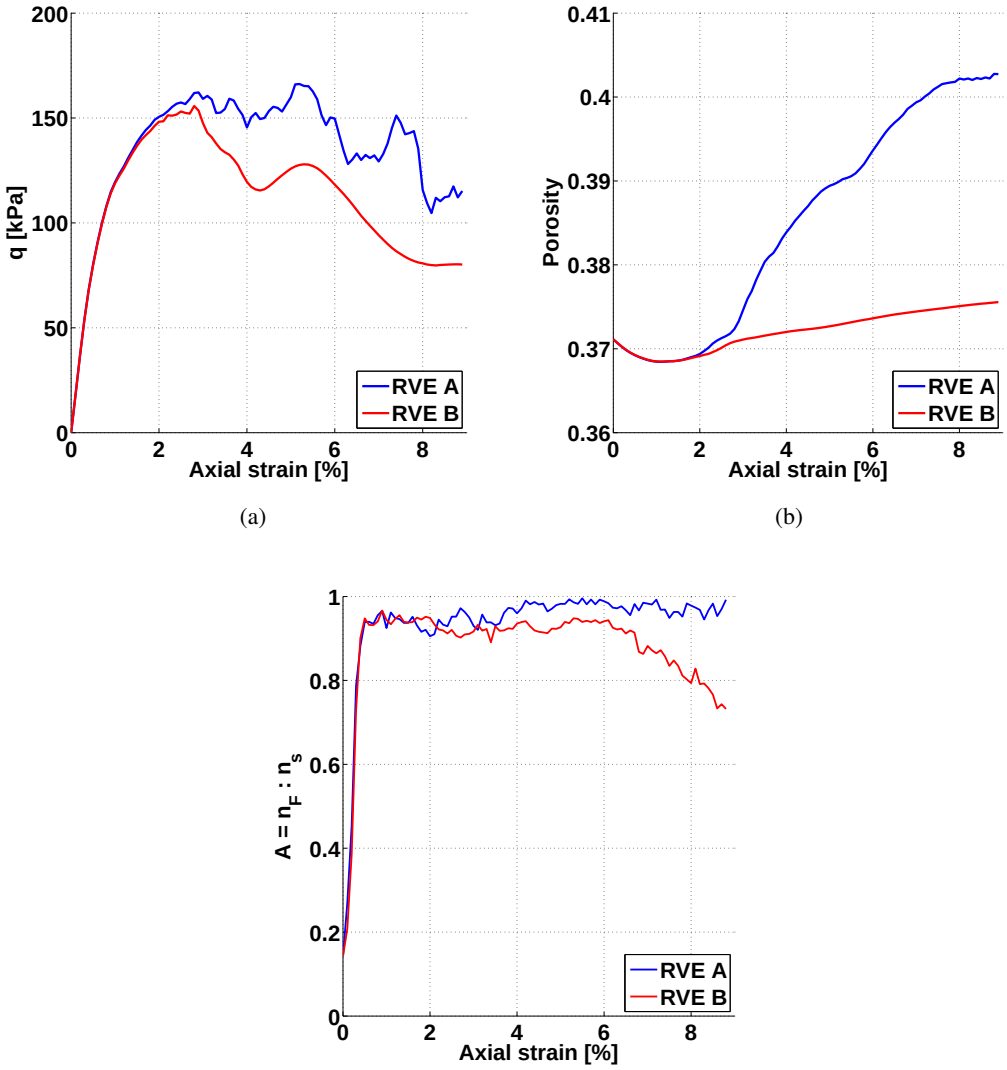

Figure 6.19: *Evolution of (a) deviatoric stress q (b) porosity (c) $A = \boldsymbol{n}_F : \boldsymbol{n}_s$ (relative orientation between anisotropic fabric and deviatoric stress directions) during triaxial compression test ($\dot{\epsilon_z} = 0.05\%/s$) for RVE A (inside shear band, Fig. 6.15(c)) and RVE B (outside shear band, Fig. 6.15(c)).*

In this multiscale study, the factor of safety is estimated by gradually applying the gravity load αg at a very low rate to maintain the drained condition, where α is known as the loading factor [de Borst et al., 2012]. The FOS is equal to α when the slope suddenly collapses along the slip surface, indicated by a sudden increase of displacement of upper crest (settlement). Since a DEM assembly with neither confining pressure nor cohesive force is not stable when sheared, we start the simulation from $0.1g$. Then α is increased gradually until it approaches the critical value that causes the slip surface slides. Here we chose a small increment of α ($0.001g$) in order to capture the slope response near and after the sliding. The u-p poromechanics formulation is advantageous in the sense that one may prescribe directly the pore pressure as boundary condition to represent the hydraulic load changes of groundwater level. As a result, there is no need to estimate the total traction caused by hydraulic force at the upper boundaries as what typically did in single-phase finite element analysis, e.g., Griffiths and Lane [1999].

Fig. 6.22 shows the distribution of accumulated plastic strain $\bar{\varepsilon}^{\boldsymbol{p}}$ inside the slip surface on the verge of collapse, which is defined as:

$$\bar{\varepsilon}^{\boldsymbol{p}} = \int_0^t \sqrt{\frac{2}{3}\dot{\boldsymbol{\varepsilon}}^{\boldsymbol{p}} : \dot{\boldsymbol{\varepsilon}}^{\boldsymbol{p}}}dt = \int_0^t \sqrt{\frac{2}{3}}||\dot{\boldsymbol{\varepsilon}}^{\boldsymbol{p}}||dt = \int_0^t \sqrt{\frac{2}{3}}||\dot{\boldsymbol{\varepsilon}} - \dot{\boldsymbol{\varepsilon}}^{\boldsymbol{e}}||dt = \int_0^t \sqrt{\frac{2}{3}}||\dot{\boldsymbol{\varepsilon}} - \boldsymbol{K}^{\boldsymbol{e}\text{-}1}\dot{\boldsymbol{\sigma}}||dt \tag{6.63}$$

The deformed configurations of three RVEs on the top, in the middle and at the toe along the slip surface

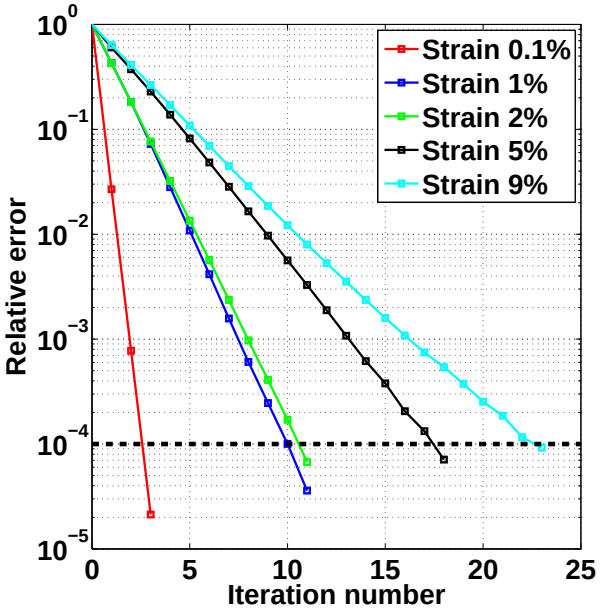

Figure 6.20: *Convergence profiles of the triaxial compression test at different axial strain levels. The relative error is defined as* $\frac{||\Delta \boldsymbol{F}^i||}{||\Delta \boldsymbol{F}^{(i=0)}||}$*, where* $\Delta \boldsymbol{F}^i$ *is the residual force at the iteration step* i*. The convergence is reached when the error falls below* 10^{-4}.

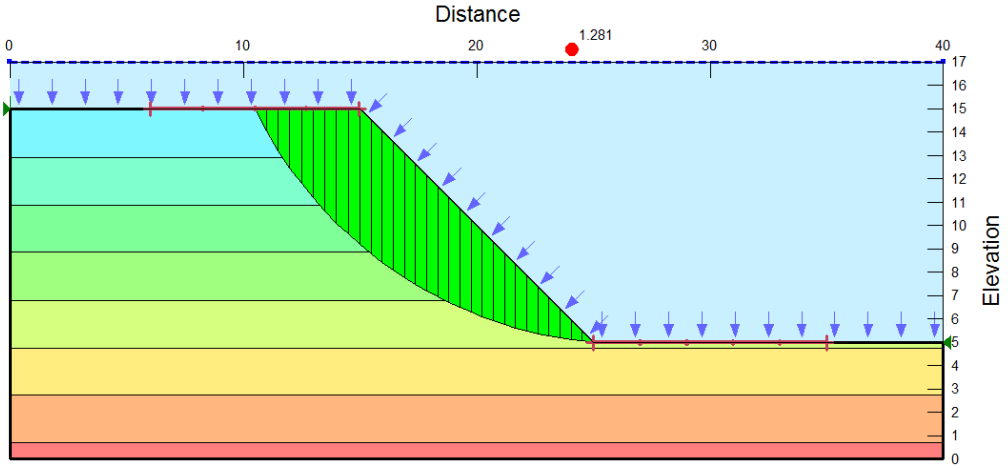

Figure 6.21: *Slip surface and factor of safety of 1.281 estimated by SLOPE/W for a 1:1 submerged slope. The unit of the spatial dimensions is meter.*

are colored according to the displacement with respect to the initial RVE configuration. Their state-paths are plotted in Fig. 6.23, which explain that different locations of the slip surface experience different loading pattern, the multiscale study of safety factor is thus more realistic. The safety factor predicted by the numerical analysis is shown in Fig. 6.24, compared with FOS predicted by the former analytical solution. The result suggests that the multiscale study yields more conservative prediction.

6.6 Conclusions

In this work, we present a finite strain dual-scale hydro-mechanical model that couples grain-scale granular simulations with a macroscopic poro-plasticity model at low Reynolds number. Using effective stress principle, the macroscopic total stress is partitioned into effective stress, which is homogenized from grain-scale simulations and macroscopic pore pressure, which is updated from macroscopic simulation. To improve computational efficiency, we adopt a semi-implicit predictor-multicorrector scheme that splits the internal force into macroscopic and microscopic components. By updating the macroscopic poro-elastic contribution (FEM)

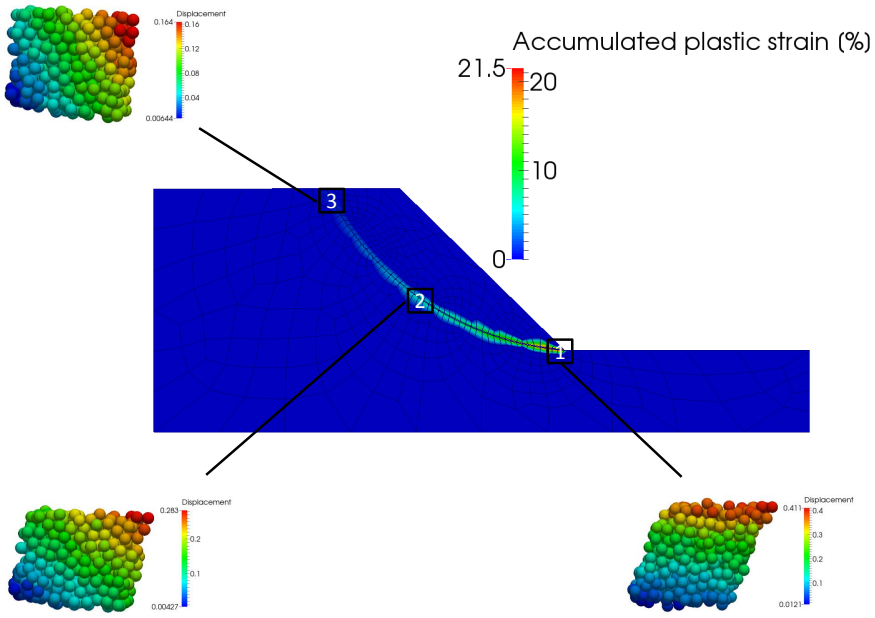

Figure 6.22: *Accumulated plastic strain $\bar{\varepsilon}^p$ inside the slip surface on the verge of collapse (Load factor $\alpha = 1.23$)*

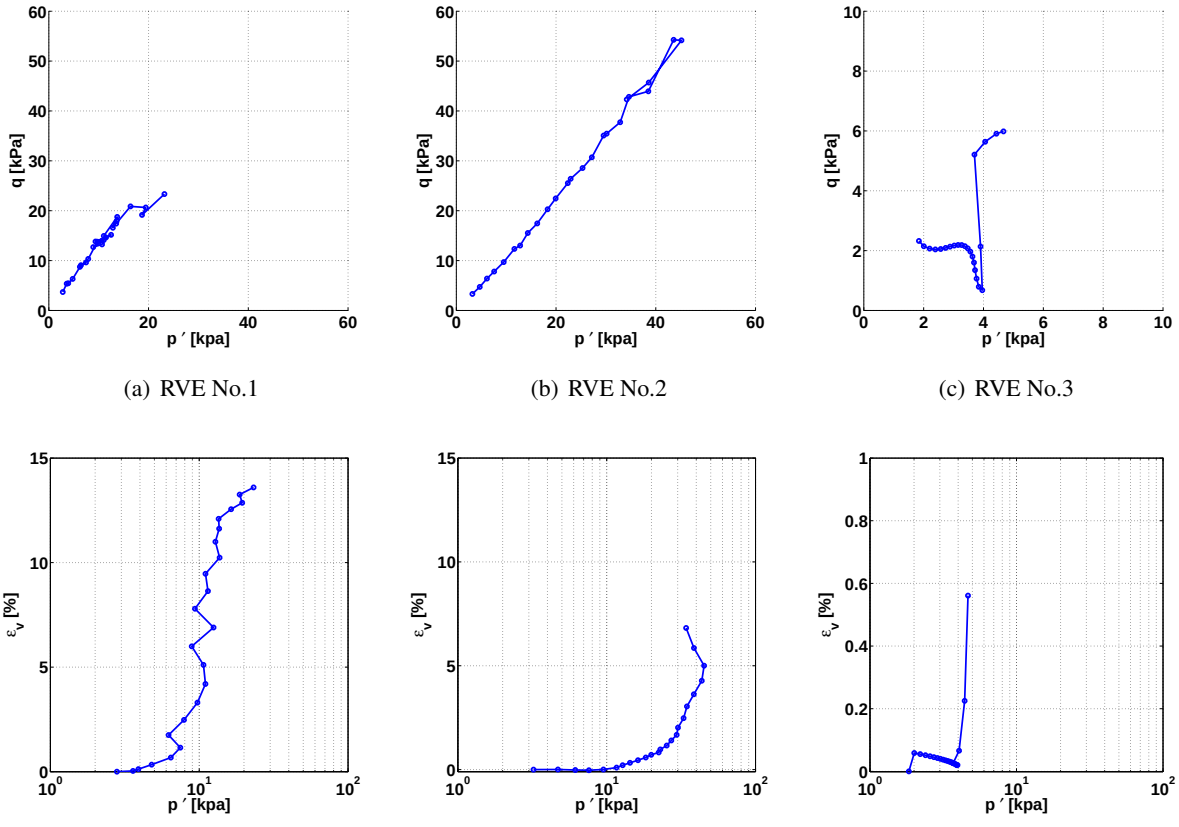

(a) RVE No.1 (b) RVE No.2 (c) RVE No.3

(d) RVE No.1 (e) RVE No.2 (f) RVE No.3

Figure 6.23: *State paths of unit cells as labeled in Fig.6.22 until slope collapses. Left: RVE No. 1; Middle: RVE No. 2; Right: RVE No. 3;*

implicitly and the microscopic counterpart (DEM) explicitly, we establish a multiscale scheme that is unconditionally stable and therefore allows simulations to advance in time steps large enough for practical applications. The dual-scale poromechanics model is first tested against Terzaghi's one-dimensional consolidation problem in

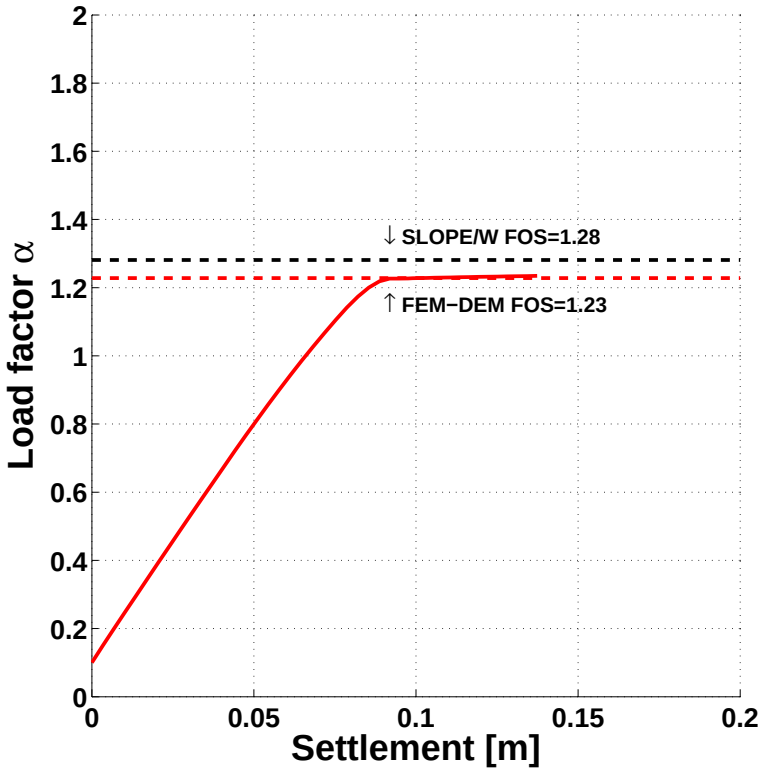

(a)

Figure 6.24: *Slope stability. Load-settlement diagram*

both geometrically linear and nonlinear regimes. Additional multiscale simulations at specimen- and field-scale are also conducted to showcase the potentials of the proposed method to solve a wide spectrum of problems across spatial length scales. To the best of our knowledge, this is the first time a hierarchical multiscale coupling scheme is established to resolve finite strain poro-plasticity problem. Due to the introduction of semi-implicit scheme across length scales, the proposed method is not only suitable for specimen-level simulations, but also shown to be efficient enough to resolve field-scale problem within limited computational resource.

Chapter 7

Key findings on verification and validation of multiscale models with micro-CT images

Granular matters are one of the most commonly encountered materials in our daily lives. Ranging from natural materials, such as sand, slit, gravel, fault gauges to the man-made materials, such as pills, sugar powder and candy, granular matters may be composed of grains with various shapes, sizes and forms. The mechanical behavior of granular assemblies are therefore not only depending on the material properties of the grains that form the assemblies, but also the evolution of the grain contact topology or fabrics [Satake, 1993, Subhash et al., 1991, Walker et al., 2016, Lenoir et al., 2010, Li and Dafalias, 2011, O'Sullivan, 2011, Sun et al., 2013c, Wang and Sun, 2015, Kuhn et al., 2015]. In the past decades, theoretical and numerical studies have achieved great success to describe and predict the granular materials that exhibit solid-like behavior when subjected to sufficient confining pressure. In those cases, granular materials are often treated as first-order Boltzmann continua which possess no internal microstructures or length scale. For instance, constitutive models that employ the critical state soil mechanics concept are now able to replicate the monotonic and cyclic responses of sand of different relative densities, confining pressure and initial states [Schofield and Wroth, 1968, Lade and Duncan, 1975, Been and Jefferies, 1985, Wu et al., 1996, Manzari and Dafalias, 1997, Pestana and Whittle, 1999, Dafalias and Manzari, 2004, Borja and Sun, 2007, Sun, 2013]. In these macroscopic models, microstructural attributes, such as pore size distribution, grain shapes and size distribution, grain-scale heterogeneity are not explicitly taken into account at the grain scale. Instead, they are represented by a set of internal variables that represents the loading history. The evolution of these internal variables are then governed by phenomenological evolution laws that require material parameters calibrated from experiments. Nevertheless, the success on replicating constitutive responses at a material point level often does not automatically lead to realistic simulated responses. For instance, the classical first-order continuum model does not possess physical length scale and this may cause finite element or finite difference models that employ the first-order continuum models to exhibit spurious mesh dependence, unless a regularization limiter is applied [Bazant et al., 1984, Lasry and Belytschko, 1988, Belytschko et al., 1988, Needleman, 1988, Fish et al., 2012, Sun and Mota, 2014, Liu et al., 2015, Na and Sun, 2016]. This regularization limiter can be introduced via various means, ranging from incorporating rate-dependence, inserting embedded strong discontinuity to adapting nonlocal and gradient-based constitutive relations.

For instance, classical bifurcation analysis by Rudnicki and Rice [1975] and Issen and Rudnicki [2000] can be used to predict the onset and orientiation of a deformation band. Beyond the bifurcation point, additional degree of freedoms that represents an embedded strong discontinuity can be introduced via assumed strain (e.g. Borja [2000]), extended finite element (e.g. [Song et al., 2006]) or localization or bifurcated elements (e.g. Ortiz et al. [1987], Belytschko et al. [1988], Yang et al. [2005]). Nevertheless, recent experimental and theoretical studies have both indicated that granular materials may initially form multiple deformation bands at the bifurcation point, but the interaction among deformation band may lead to some of the deformation band vanished. Meanwhile, a dominated persistent shear band may emerge among them in the post-bifurcation regime. [Gajo et al., 2004, Rechenmacher, 2006, Borja et al., 2013]. This discovery indicates that the adaptive insertion of the enhanced mode(s) may lead to mesh bias unless there is a coarsen mechanism in place to prevent the fixture of shear band localization [Lin et al., 2015].

As opposite to the enrichment approach, higher-order continuum theory is another attractive option to circumvent the pathological mesh dependence exhibited in the Boltzmann continua. The history of generalized

continuum theories can be tracked back to the work of Cosserat brothers who published a book titled T̈héorie des corps déformablesïn 1909 [Cosserat and Cosserat, 1909]. As pointed out by Maugin and Metrikine [2010], there exists multiple interpretations and generalizations of Cosserats' work. Nevertheless, the necessary ingredients of the higher-order continuum theory are the incorporation of higher-order kinematics (micro-rotation, micro-stretch, micro-torsion..etc) and additional internal degree of freedom of mechanical that breaks the symmetry of the Cauchy stress [Mindlin, 1964, Eringen, 1999, Maugin and Metrikine, 2010]. The micropolar continuum theory is a sub-class of the generalized continuum theory in which the material point is associated with micro-structures exhibiting not only deformation but changing orientations that are independent of the macroscopic deformation. These changes of orientations can be represented by Euler's angle, quaternions and spinors, among other mathematical tools [Duhem, 1893]. By incorporating the additional rotational degree of freedoms at the microscopic level, micropolar effect of granular materials, especially those associated with the onset of strain localization as observed by Desrues and Viggiani [2004], Hall et al. [2010], can be replicated properly in numerical simulations without exhibiting the spurious mesh dependence.

Nevertheless, incorporating the micropolar effect to improve the accuracy and physical underpinning of the numerical models also comes with a price. For instance, the identification of the the micropolar material parameters in addition to the non-polar counterparts can be difficult for material testing procedures that are originally designed for homogeneous specimen subjected to first-order boundary conditions. The assumption that the strain field developed inside the specimen remains approximately homogeneous in convectional triaxial and shear apparatus is unavoidably violated when high-order kinematics and couple stress are considered. These difficulties are partly responsible for the limited applications of higher-order continuum theory in engineering practices.

Our objective is to overcome this technical barrier by introducing a simple experimental-numerical method designed specific for identifying material parameters for higher-order continua. In particular, we introduce the meso-scale kinematics data from X-ray tomographic images obtained from drained triaxial compression tests to construct a multiscale objective function. The tomographic images at selected axial strain levels are combined with the conventional macroscopic stress-strain curve and the state path to constitute the measured data set. A new objective function is then defined to simultaneously minimize the discrepancy between the simulated and measured macroscopic responses while enforcing the simulated grain-scale responses to be consistent with the kinematics information provided by the tomographic images. Our results show that the incorporation of microstructural information from the grain scale may profoundly change the predicted length scale and failure mode of the numerical specimen. More importantly, the predicted couple stress response is also highly sensitive to the way microstructural information incorporated in the inverse problem.

To the best knowledge of the authors, this work is the first contribution to employ X-ray tomographic images to identify material parameters via multiscale inverse problem for granular materials. In addition, the proposed method provides a new method to quantify the sensitivity of characteristic length predicted by material identification procedure. The findings from the Hostun sand experiment indicate that a multiscale model capable of replicating the macroscopic responses may nevertheless produce incorrect bifurcation modes and completely different micro-scale responses. This result has important implication for material modeling, as it clearly shows that calibrating macroscopic responses alone is insufficient to provide reliable forward prediction for multiscale models. In other words, a seemingly good match between experimental and simulated responses at the macroscopic level may be a consequence of high-quality grain-scale simulations or a product manufactured by excess tuning and manipulations of meso-scale material parameters.

7.1 Experiments and micro-CT images for validations

This section introduces the triaxial test performed for this research at 3SR lab and details the experimental procedures followed. The objective of performing the triaxial tests is to provide a multiscale benchmark database for model calibration and material identification. The bemchmark data consist of the macroscopic stress-strain curve and the grains position at different stress levels during the shearing, characterizing the grains scale behavior of the granular media. These data form the basis for a multiscale objective function to search the optimal material parameters to predict the most consistent mechanical behavior measured by a weighted norm that minimizes the discrepancy between simulations and experimental observations at both grain- and specimen-scales.

7.1.1 X-ray CT

X-ray micro-CT is a non-destructive, 3D high resolution imaging method that allows the internal structure of the scanned objects to be investigated [Lenoir et al., 2010, Hall et al., 2010, Sun et al., 2011c, Andò et al., 2012]. Micro-CT technology yields images that map the variation of x-ray attenuation within the objects, based on the composition of the object. Because sand and water have different x-ray attenuation coefficients, a significant contrast for the two phases is observed in an x-ray transmission image, Fig. 7.4. A quantitative analysis that provides detailed information on the arrangement and distribution of particles can be built from the processed 3D images.

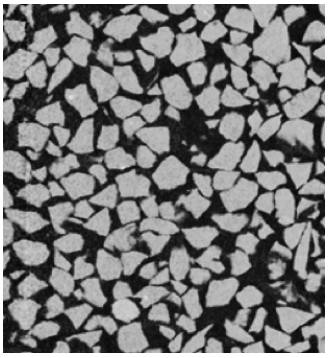

Figure 7.1: *Reconstructed x-Ray image shows the clear contrast between grain and water and air The experiments in this study are performed using x-ray setup of laboratory 3SR at Grenoble University.*

The imaging process can be summarized as follows: the cell first is placed on a turntable stage whose rotation can be accurately controlled. An x-ray source generates a continuous x-ray beam; the beam passes through the object and casts an x-ray shadow onto the detector, see Fig. 7.2. The radiation that hits the detector is converted into an electronic charge, [ref] that is subsequently passed to a computer to create a radiograph (i.e., digital image). A series of images (radiographies) is acquired while rotating the object step by step through 360° at a pre-defined angular increment. These radiographies record projections that contain cumulative information on the position and density of the absorbing features within the specimen. The data obtained can be used to perform the numerical reconstruction of the final 3D image [Hall et al., 2010, Andò et al., 2012].

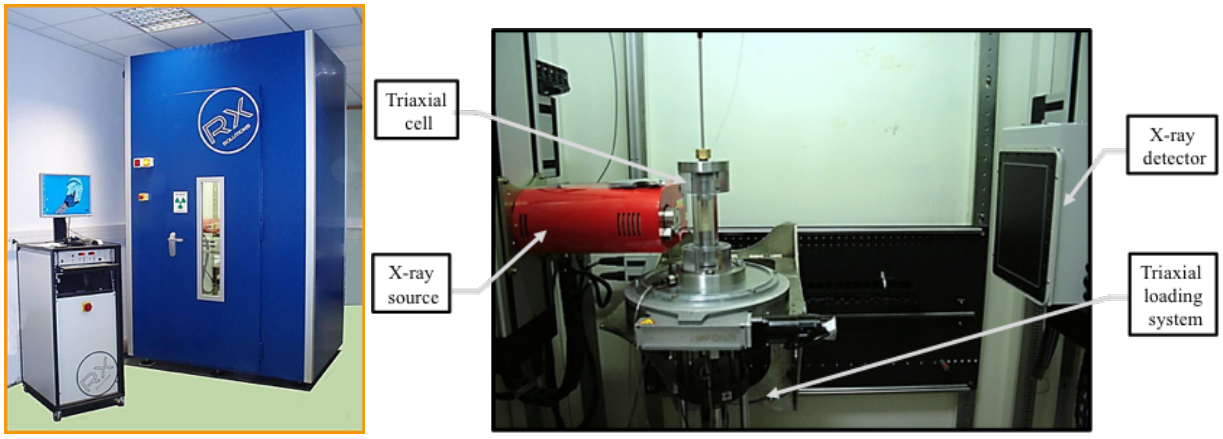

Figure 7.2: *X-Ray CT scanner at Laboratory 3SR (left) and the whole arrangement of triaxial setup inside x-ray cabinet (right).*

7.1.2 Triaxial cell

The triaxial cell used in this work is designed to allow x-ray scanning and to fit to the mechanical loading system available in 3SR Laboratory. The cell is made of PMMA which is transparent to X-rays, and quite resistant to cell pressure (confinement) applied in triaxial tests. Fig 7.3 shows the PMMA cell in front of X-ray source, with the specimen installed at its place inside the cell. The loading system applies and measures the axial force compressing the specimen from below, and the vertical displacement of the lower piston. The maximum axial force that can be measured by the force meter, which is in contact with the bottom of the lower

piston, is 0.5 kN. The measurement of the axial displacement is made by an LVDT which is attached to a tie bar and measures the vertical displacement of the loading head. These measurements allow plotting the relation between the axial stress and axial shortening during the triaxial test. The speed range for the loading head is from 0.1 μ m / min to 100 μ m / min, which corresponds to a strain rate from 0.0005 % to 0.5 % per minute (for a specimen of height 20 mm). The speed range considered in this work for the three triaxial tests is 20 μ m / min (strain rate is 0.1% for a specimen of height 20 mm). The motor is driven remotely from a laptop used for data acquisition. The system of data acquisition registers the force, the confinement pressure and LVDT measurements which were calibrated at the beginning of the test.

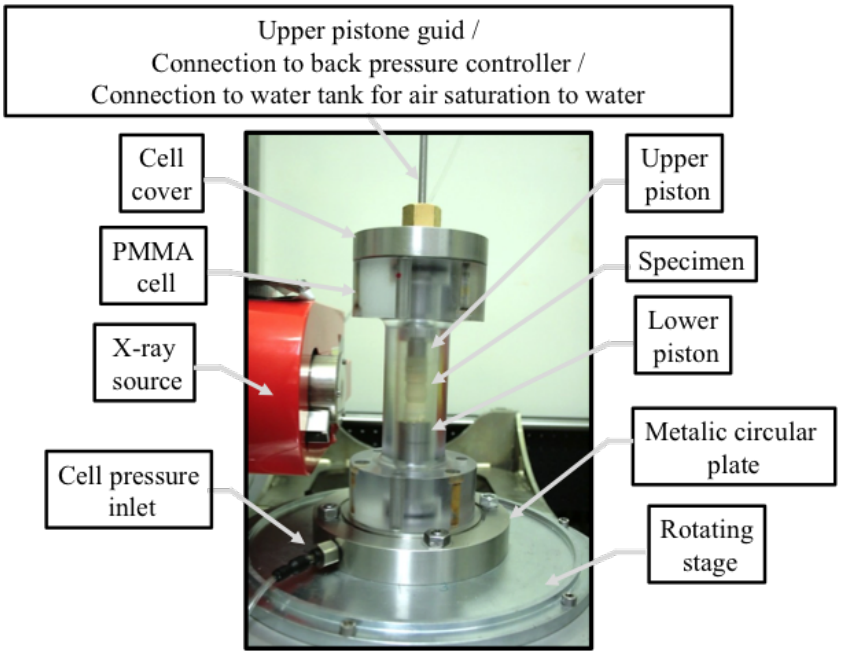

Figure 7.3: *The PMMA cell infront of x-ray source with the specimen installed at its place inside the cell.*

7.1.3 Material used

The experimental program is conducted on Hostun sand (HN31). Hostun sand is used as a reference material in different laboratories (cf. Sadek et al. [2007], Amat [2008], Desrues and Andò [2015]. Its chemical components principally consist of silica ($SiO2 > 98\%$). The grain shape is angular as shown in the Scanning Electron Microscope image (SEM) of a few grains of Hostun sand, taken from Flavigny et al. [1990], in Fig. 7.4(a). A particle size distribution analysis for Hostun sand is shown in Fig. 7.4(b).

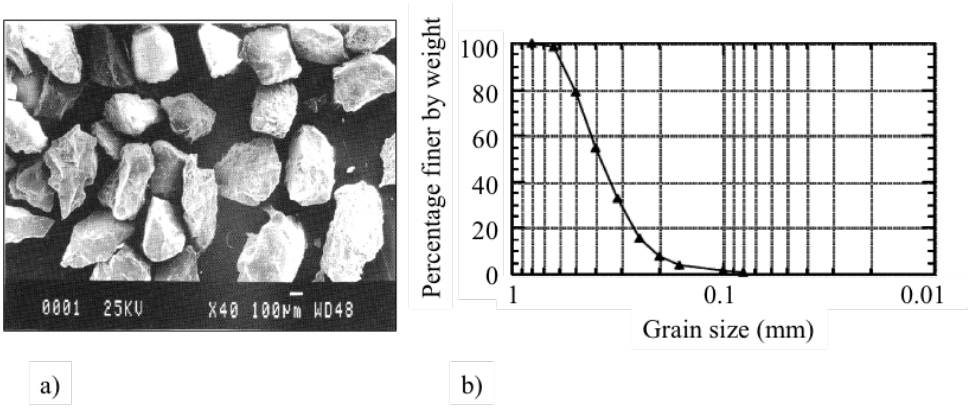

Figure 7.4: *SEM image of Hostun sand from Flavigny et al. [1990] b) Grain size distribution of Hostun sand from Amat [2008]*

.

7.1.4 Specimen preparation

The specimen prepared for the triaxial tests is a cylindrical specimen of 1 cm diameter and 2 cm height (slenderness ratio 2).The technique used for specimen preparation in the three triaxial tests is water pluviation, and thus all the pores in the specimen are completely filled with demineralized water in the initial state. This procedure ensures that the specimen is fully saturated at the beginning of the mechanical tests.

7.1.5 Macroscopic response

The axial stress is calculated by the axial force measured over the cross-section of the specimen at the initial state. The axial force comes from the raw measurement of force. The membrane correction has not been applied to these data. The axial strain (in $\%$) is obtained from the shortening applied by axial compression of the specimen, with respect to its initial height. The specimen behaves as expected for a dense granular material: there is a peak in the specimenâĂŹs axial stress response, followed by strain softening until a plateau of residual stress is reached. The peak is reached at axial strain $\epsilon_a = 5.5\%$, and at axial stress $\sigma = 620$ kPa. The residual stress is $\sigma = 440$ kPa.Figure 7.5 shows the cross section of the deformed specimen at different axial strain level. While the initial deformation remains relatively homogeneous at low axial strain, the specimen subsequently deforms into a barrel shape while large strain ($epsilon_a = 22\%$) develops toward the end of the test.

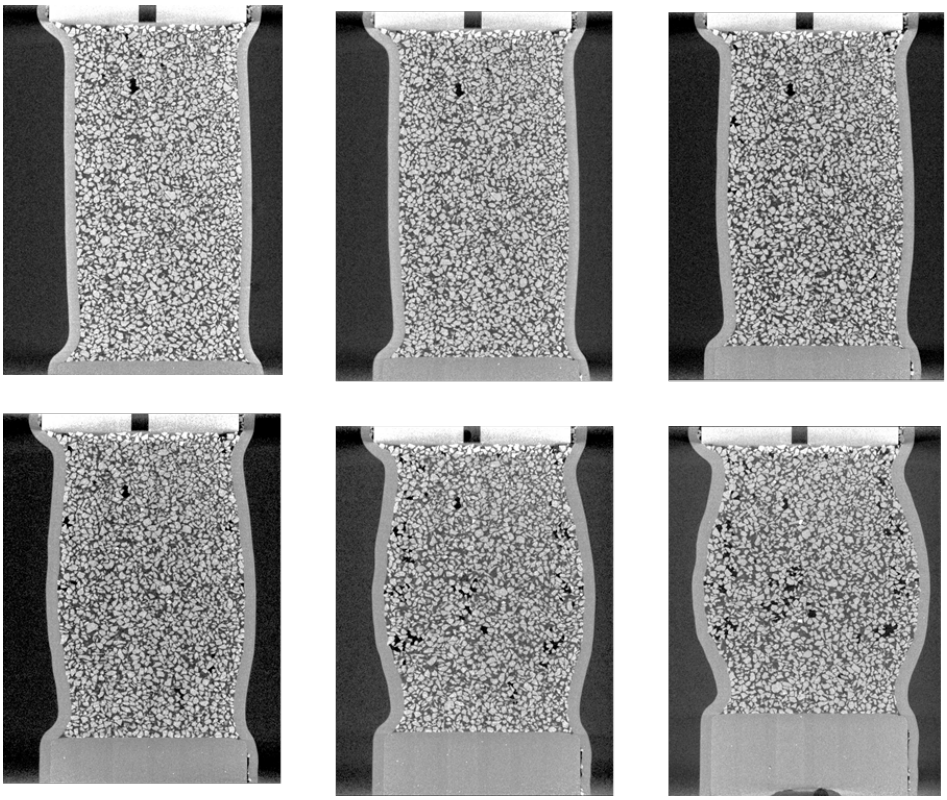

Figure 7.5: *Micro-CT images of the cross section of the specimen at different axial strain level.*

7.1.6 Segmentation

Measurements of the spatial distribution of grains require a separation of the two phases. The volume has been âĂIJbinarisedâĂİ using a thresholds , one between air and water peaks and the second one between water and grain peaks. This last one is chosen in such a way that volume of voxels identified as grain phase correspond to volume of grains that has been estimated from the weight of the sample (in a dry state). The threshold between air and water is chosen to correspond to the local minimum in the grey level distribution. Figure 7.6 shows the cross section of the processed images of which the spatial distribution of the solid and water phases are idenified based on the threshold values.

7.1.7 Grains position

Water phase is separated from the whole 3D volume using Visilog by setting the threshold to a gray value equal to 128. In order to remove the noise inside the images, represented by water volumes of one voxel, a morphological process of erode and dilate by one voxel is applied. Later, water clusters are labeled. Labeling

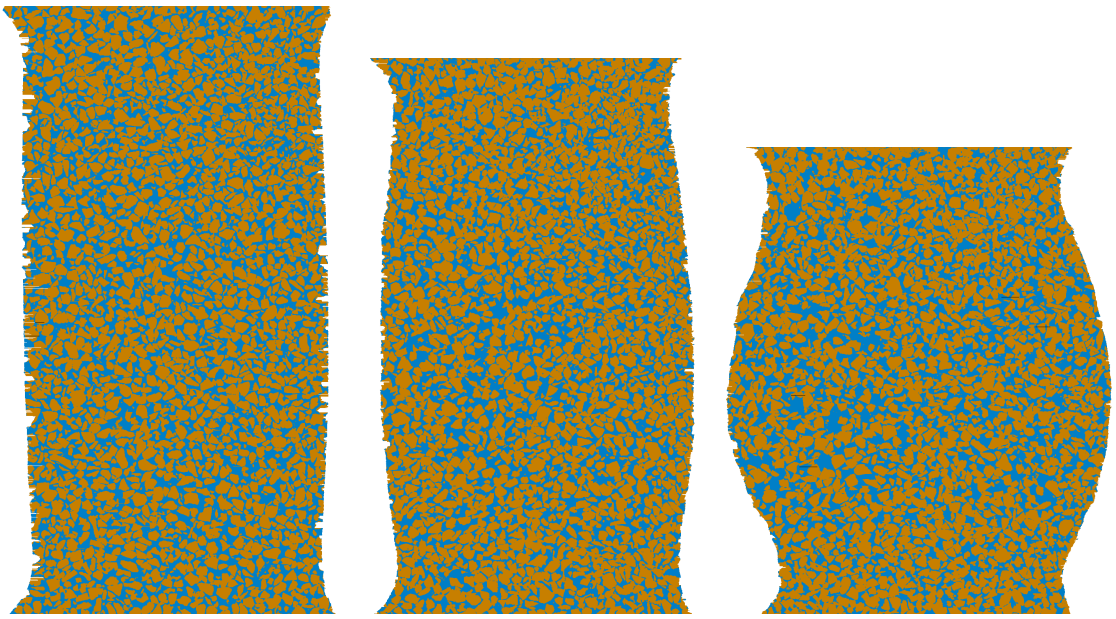

Figure 7.6: *Cross sections of the "Binarized" two-phase images at axial strain = 0, 8 and 21 %.*

process can be summarized as giving each individual water cluster an Identification (Id). This Id is represented in the images by colors (i.e., each color represent a specific water cluster). The process of labeling is very useful to be able to refer to any water cluster directly by its Id number. These images where each water cluster has a specific Id and color can be considered as a mask applied to the reconstructed image (i.e., the gray scale information are always kept). At this point, more information about water clusters is needed as the number of clusters, the center of mass, 3D volume, 3D area, âĂę etc. Theses information is obtained using another tool of Visilog âĂIJanalysis individualâĂİ. The measurements of clusters properties are saved in a DAT file type associated primarily with data which can be read by a text editor.

7.2 Inverse problems for micropolar plasticity model

This section presents the calibration procedure for the micropolar hypoplasticity model via the micro-CT images. The macroscopic constitutive model and the parameter identification procedure conducted via the open source toolkit Dakota are briefly described. We will first treat the entire specimen as a single unit cell and we will use the gradient based approach to obtain the material parameters. The open-source optimization code Dakota is employed [Adams et al., 2009]. Then we make use of the micro-CT images to construct the geometry of the Hostun sand sample at the beginning of the triaxial compression loading. The initial distribution of void ratio is also inferred from micro-CT information. They serve as the starting point of the model simulations. We calibrate the material parameters by two sets of benchmark data. One set consists of the macroscopic stress ratio and volumetric strain vs. the axial strain curves. The other set contains the geometry and void ratio distribution when the axial stress reaches the peak and at the residual stage.

7.2.1 Micro-polar finite element model

The inverse problem introduced in this paper is applicable to a wide spectrum of constitutive laws that considers high-order kinematics. In this study, we extend the previous two-dimensional implementation of the micropolar hypoplasticity model in Lin and Wu [2015], Lin et al. [2015] to a 3D formulation and use the 3D model to calibrate with experimental data. This model can be considered as an extension of the non-polar hypoplasticity model in Wu et al. [1996] and is suitable to characterize the Houston sand specimen obtained for this study. For completeness, we include a brief outline of the 3D finite element formulation of the micropolar hypoplasticity model. Readers interested at the details of the micropolar hypoplasticity constitutive model may refer to Wu et al. [1996], Lin and Wu [2015], Lin et al. [2015].

The non-symmetric Cauchy stress $\boldsymbol{s}$ and the couple stress $\boldsymbol{\mu}$ are given in nonlinear path-dependent rate-form in terms of the current state of the stresses, the strain rate $\dot{\boldsymbol{e}}$, the curvature rate $\dot{\boldsymbol{\kappa}}$ and the void ratio e. The

micropolar constitutive equations writes,

$$\begin{aligned}\overset{\circ}{\boldsymbol{s}} &= C_1 tr(\boldsymbol{s})\dot{\boldsymbol{e}} + C_2 tr(\dot{\boldsymbol{e}})\boldsymbol{s} + C_3\psi\boldsymbol{s} + C_4 f_d\sqrt{||\dot{\boldsymbol{e}}||^2 + l^2||\dot{\boldsymbol{\kappa}}||^2}(\boldsymbol{s}+\boldsymbol{s'}) \,,\\ \overset{\circ}{\boldsymbol{\mu}} &= C_1 l^2 tr(\boldsymbol{s})\dot{\boldsymbol{\kappa}} + C_2 tr(\dot{\boldsymbol{e}})\boldsymbol{\mu} + C_3\psi\boldsymbol{\mu} + 2C_4 f_d\sqrt{||\dot{\boldsymbol{e}}||^2 + l^2||\dot{\boldsymbol{\kappa}}||^2}\boldsymbol{\mu} \,,\end{aligned} \tag{7.1}$$

where $\overset{\circ}{\boldsymbol{s}}$ and $\overset{\circ}{\boldsymbol{\mu}}$ are the Jaumann rates of $\boldsymbol{s}$ and $\boldsymbol{\mu}$, $\boldsymbol{s'}$ is the deviatoric part of $\boldsymbol{s}$, and

$$\psi = \frac{tr(\boldsymbol{s}\cdot\dot{\boldsymbol{e}}) - tr(\boldsymbol{\mu}\cdot\dot{\boldsymbol{\kappa}})}{tr(\boldsymbol{s})} \,, \tag{7.2}$$

whereas

$$f_d = (1-a)\frac{e - e_{\min}}{e_c - e_{\min}} + a \tag{7.3}$$

is a linear scalar function that accounts for the effect of critical state on the constitutive behavior. The material parameters to be determined are C_1, C_2, C_3, C_4, a, the critical void ratio e_c, the minimum void ratio $e_{\min}$ and the characteristic length l, which is the only additional parameter in micropolar framework compared to classical continuum hypoplasticity model. Note that this micropolar hypoplasticity model is valid under the assumption that $\dot{\boldsymbol{\kappa}}$, $\boldsymbol{\mu}$ and $\overset{\circ}{\boldsymbol{\mu}}$ are all skew-symmetric. An explicit numerical integration scheme (Forward-Euler) is adopted to integrate the highly nonlinear constitutive equations Eq. (7.1), i.e.,

$$\begin{aligned}\boldsymbol{s}_{t_1} &\approx \boldsymbol{s}_{t_0} + \dot{\boldsymbol{s}}_{t_0}(\boldsymbol{s}_{t_0}, \boldsymbol{\mu}_{t_0}, \dot{\boldsymbol{e}}, \dot{\boldsymbol{\kappa}}, \boldsymbol{e}_{t_0})\Delta t \,,\\ \boldsymbol{\mu}_{t_1} &\approx \boldsymbol{\mu}_{t_0} + \dot{\boldsymbol{\mu}}_{t_0}(\boldsymbol{s}_{t_0}, \boldsymbol{\mu}_{t_0}, \dot{\boldsymbol{e}}, \dot{\boldsymbol{\kappa}}, \boldsymbol{e}_{t_0})\Delta t \,.\end{aligned} \tag{7.4}$$

The finite element implementation for 2D small strain problems was previously described in great details [Lin et al., 2015]. However, the 3D finite element counterpart has not yet been established. Since the tomographic images are three-dimensional and the bifurcation modes can be either symmetric or non-symmetric, an extension to three-dimensional space is necessary for comparing experimental data and simulated responses at the meso-scale level. As a result, the micropolar hypoplasticity model is implemented with a 3D micropolar finite element model. Consequently, the degrees of freedom for each node consist of three translational DOFs and three rotational DOFs, i.e., $\boldsymbol{u} = [u_1 \;\; u_2 \;\; u_3 \;\; \phi_1 \;\; \phi_2 \;\; \phi_3]^{\mathrm{T}}$. Adopting the Voigt notation, the vectors that store the components of the generalized strain and stress tensors read,

$$\begin{aligned}\{\boldsymbol{s}\} &= [s_{11} \;\; s_{22} \;\; s_{33} \;\; s_{12} \;\; s_{21} \;\; s_{23} \;\; s_{32} \;\; s_{13} \;\; s_{31} \;\; \mu_{21} \;\; \mu_{32} \;\; \mu_{31}]^{\mathrm{T}} \,,\\ \{\boldsymbol{e}\} &= [e_{11} \;\; e_{22} \;\; e_{33} \;\; e_{12} \;\; e_{21} \;\; e_{23} \;\; e_{32} \;\; e_{13} \;\; e_{31} \;\; \kappa_{21} \;\; \kappa_{32} \;\; \kappa_{31}]^{\mathrm{T}} \,.\end{aligned} \tag{7.5}$$

The element strain-displacement matrix $\boldsymbol{B}^e$ is modified accordingly and takes the form:

$$\boldsymbol{B}^e = [\boldsymbol{B}_1, \;\; \boldsymbol{B}_2, \;\; \ldots \;\; \boldsymbol{B}_{n_{en}}] \,, \;\; \boldsymbol{B}_a = \begin{bmatrix} N_{a,1} & 0 & 0 & 0 & 0 & 0 \\ 0 & N_{a,2} & 0 & 0 & 0 & 0 \\ 0 & 0 & N_{a,3} & 0 & 0 & 0 \\ N_{a,2} & 0 & 0 & 0 & 0 & N_a \\ 0 & N_{a,1} & 0 & 0 & 0 & -N_a \\ 0 & N_{a,3} & 0 & N_a & 0 & 0 \\ 0 & 0 & N_{a,2} & -N_a & 0 & 0 \\ N_{a,3} & 0 & 0 & 0 & N_a & 0 \\ 0 & 0 & N_{a,1} & 0 & -N_a & 0 \\ 0 & 0 & 0 & 0 & N_{a,1} & 0 \\ 0 & 0 & 0 & 0 & 0 & N_{a,2} \\ 0 & 0 & 0 & 0 & 0 & N_{a,1} \end{bmatrix} , \tag{7.6}$$

where n_{en} is the number of element nodes, N_a is the shape function of element node a, $N_{a,1}$, $N_{a,2}$, $N_{a,3}$ are the derivatives of the shape function N_a with respect to $\boldsymbol{x}_1$, $\boldsymbol{x}_2$, $\boldsymbol{x}_3$ directions in a Cartesian coordinate system.

Consider a body $\mathcal{B}$ subjected to traction $\boldsymbol{t}$ and body force $\boldsymbol{b}$ partitioned into element $\mathcal{B}^e$. The matrix form of the balance of linear and angular momentum therefore reads,

$$\boldsymbol{F}_{\text{INT}} = \boldsymbol{F}_{\text{EXT}}, \tag{7.7}$$

where

$$\boldsymbol{F}_{\text{INT}} = \mathrm{A}_{e=1}^{nel} \int_{\mathcal{B}^e} \boldsymbol{B}^{e\mathrm{T}} \cdot \boldsymbol{s}\, \mathrm{dV} \;\; ; \;\; \boldsymbol{F}_{\text{EXT}} = \mathrm{A}_{e=1}^{nel} \Big(\int_{\mathcal{B}^e} \boldsymbol{N}^{e\mathrm{T}} \cdot \boldsymbol{b}\, \mathrm{dV} + \int_{\partial\mathcal{B}^e} \boldsymbol{N}^{e\mathrm{T}} \cdot \boldsymbol{t} \Big)\, \mathrm{dV}. \tag{7.8}$$

where A is the assembly operator (cf. Hughes [2012]) and $\boldsymbol{N}^e = [\boldsymbol{N}_1, \boldsymbol{N}_2, \boldsymbol{N}_3, ...\boldsymbol{N}_{n_{en}}]$.

7.2.2 Optimization algorithms for material parameter identification

Material parameter identification of soil samples can be done via solving inverse problems. Previous works, such as Herle and Gudehus [1999], use multiple simple experiments, such as angle of repose, minimum and maximum index density, shear test, and oedometric compression test to identify material parameters in an almost one-by-one fashion for a non-polar hypolasticity model parameter for granular materials. Meanwhile, Ehlers and Scholz [2007] introduce a two-step staggered procedure for micropolar constitutive model for granular materials in which the identification algorithm first seeks the standard non-polar elasto-plastic material parameters from a series of cyclic triaxial tests that keeps the specimen in homogeneous states, then search for the optimal values for the micropolar counterpart with another set of biaxial compression tests. In both approaches, the material identification procedure requires multiple mechanical tests on multiple specimens for the same materials. Nevertheless, due to the particulate nature of the granular materials, it is almost impossible to reconstruct specimens that have identical microstructural attributes.

In this work, we propose a different approach that only requires one mechanical test to identify all material parameters. Instead of using multiple tests to constitute sufficient constraints to identify all material parameters, the new approach uses tomographic imaging techniques to track the spatial variability of the void ratio and deformation and use these kinematics information as the additional constraints for the objective function. One key assumption we made here is that the spatial relative density or porosity variation is the dominating factor for the post-bifurcation responses, but the material parameter variation is negligible. This approximated approach has been found to be successful in yielding consistent macroscopic constitutive responses and bifurcation modes for sand specimen that evolves with complex bifurcation modes. In particular, Borja et al. [2013] found that by taking account only the relative density variation, one may correctly predict the onset of multiple shear bands at the bifurcation points, the sequential interaction mechanisms of these shear bands, and the persistent shear band that lasts till the end of the loading program.

The calibration of the micropolar hypoplasticity model is completed by finding the optimal values of the material parameters that minimize the discrepancy between the simulated results and the experimental data via iterations. How “optimal" the values of the material parameters are determined by the specific objective function used for the inverse problem. If a global minimum of the objective function exists, then an optimization algorithm may start from differential initial guess but find the same set of optimal material parameters. In this work, we use a gradient-based method to find the optimal values of the material parameters. As a result, multiple boundary value problems are run and the results and their corresponding gradient with respect to the parametric space are computed. The objective function we used takes the following form,

$$f(\boldsymbol{x}) = \sum_{i=1}^{N} w_i\, r_i[s_i(\boldsymbol{x}), d_i]^2\,, \tag{7.9}$$

where $\boldsymbol{x}$ is the vector of all material parameters, N is the number of available experimental data for calibration, d_i is the i-th data point, w_i is its weight, and $s_i(\boldsymbol{x})$ is the corresponding result obtained from model simulation using the parameter set $\boldsymbol{x}$. r_i is the residual between the simulation data $s_i(\boldsymbol{x})$ and the experimental data d_i. In this work, we normalize the residuals by defining them as the relative errors, i.e.,

$$r_i[s_i(\boldsymbol{x}), d_i] = \frac{s_i(\boldsymbol{x}) - d_i}{d_i}\,, \tag{7.10}$$

since the laboratory data we employed for parameter calibration include the stress ratio, volumetric strain and void ratio, which are not in the same order.

In this work, we employ the Dakota analysis toolkit which provides flexible interface between simulation codes and robust optimization algorithms [Adams et al., 2009]. Among the available methods we choose the gradient-based least-squares algorithm (NL2SOL) which minimizes $f(x)$ using its gradient:

$$\nabla f(\boldsymbol{x}) = \boldsymbol{J}(\boldsymbol{x})\boldsymbol{r}(\boldsymbol{x}), \quad J_{ij} = \frac{\partial r_i}{\partial x_j} \tag{7.11}$$

and approximates the Hessian matrix with Gauss-Newton method:

$$\nabla^2 f(\boldsymbol{x}) = \boldsymbol{J}(\boldsymbol{x})^2 \,. \tag{7.12}$$

The parameter calibration procedure requires an input file specifying the chosen optimization algorithm, the parameters to be determined, their initial values, upper and lower limits, and the experimental data set to be compared. At the beginning of each iteration, Dakota passes the current guess of the material parameters to the finite element simulation code developed for this study. It should be noted that the focus of this research is not the development of staqte-of-the-art optimization algorithm to identify material parameters. Interested readers may refer to, for instance, Mahnken and Stein [1996], Cooreman et al. [2007], Adams et al. [2009], Hu and Fish [2015] for details.

The finite element code then runs the simulations using the material parameters provided by Dakota and returns the simulation results back to Dakota to compute the discrepancy measured by the objective function, and the corresponding gradient. Based on these input, Dakota then determines the next iteration of material parameters and repeat the gradient estimation procedure and the discrepancy is again measured after another run of the simulation code [Adams et al., 2009]. This procedure repeats until the discrepancy is below a pre-defined tolerance or when the number of iterations reach its maximum.

7.3 Unit cell calibration

The Dakota calibration scheme is first applied to calibrate a unit cell represented by a tri-linear 8-node quadrilateral element representing the entire granular sample. This test is conducted under the additional assumptions that (1) the specimen is composed of an effective medium of homogeneous properties inferred from the real heterogeneous specimen and (2) the deformation remains homogeneous. With these additional assumptions, the inverse problem is simplified such that only macroscopic responses from the experiment is utilized in the objective function, (as demonstrated previously in Liu et al. [2016]). The target data for curve-fitting are the stress ratio s $(\frac{\sigma_1}{\sigma_3})^{\text{lab}}$ and volumetric strain e_v^{lab} along the triaxial compression test. As a result, the objective function reads,

$$f(\boldsymbol{x}) = \sum_{i=1}^{N_{\sigma_1/\sigma_3}} w_i r_i [(\frac{\sigma_1}{\sigma_3})_i^{\text{model}}(\boldsymbol{x}), (\frac{\sigma_1}{\sigma_3})_i^{\text{lab}}]^2 + \sum_{j=1}^{N_{e_v}} w_j r_j [e_{v_j}^{\text{model}}(\boldsymbol{x}), e_{v_j}^{\text{lab}}]^2 \,, \tag{7.13}$$

where N_{σ_1/σ_3} and N_{e_v} are the number of stress ratio data and volumetric strain data, respectively. Both data have 30 data points and the weights are equal to 1. The subscript i denotes the i-th data point. The unit cell and the boundary conditions are presented in Fig. 7.7. The initial void ratio and the minimum void ratio are set to be 0.6, which is the average value of the sample. Note that there is no micropolar effect in this single element example, thus the material length l does not effect the macroscopic response. It is set to be equal to the element size 10 mm. The parameters to be identified via Dakota are C_1, C_2, C_3, C_4, e_c and a.

The Dakota calibration procedure takes in total 92 evaluations, of which 72 evaluations are performed for determination of the gradient of the 6 material parameters, while the rest 20 evaluations are making guesses based on the gradients. To demonstrate the convergence of the material parameters, the trial material parameters and the corresponding values of the objective function are presented in Table 7.1. The macroscopic responses obtained by the trial material parameters compared with the experimental data are shown in Fig. 7.8. Despite the large discrepancy between the initial guess and the laboratory results, $f(\boldsymbol{x})$ decreases rapidly: it is reduced by about 95.7 % after 50 evaluations. This example demonstrates the robustness of the NL2SOL scheme in Dakota for nonlinear models and least-squares problems for which the residuals do not tend to vanish.

7.4 Micropolar hypoplastic model calibration with micro-CT images from triaxial compression test

To analyze how the spatial variability of porosity (or relative density) affects the macroscopic responses, we reconstruct a detailed 3D numerical specimen with the exact geometry and porosity distribution of the

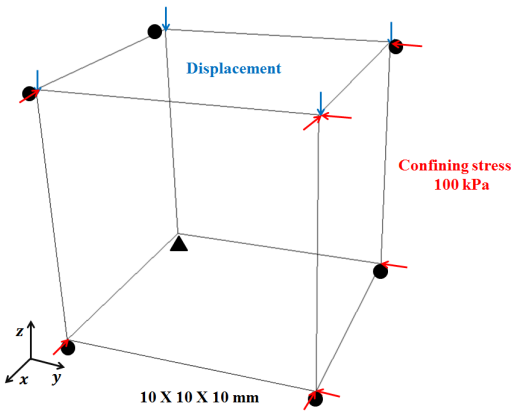

Figure 7.7: *Domain and boundary condition for single unit cell calibration.*

	C_1	C_2	C_3	C_4	e_c	a	$f(\boldsymbol{x})$
Initial guess	-33.33	-104.61	-336.44	-105.90	0.800	0.900	143.77
Evaluation 20	-31.63	-62.44	-484.71	-107.15	0.650	0.905	97.60
Evaluation 50	-40.60	-1054.35	-1565.66	-138.86	0.651	0.923	6.18
Calibration result	-63.14	-1831.49	-2563.92	-237.52	0.732	0.848	2.85

Table 7.1: *Evolution of the material parameters during the Dakota calibration procedure*

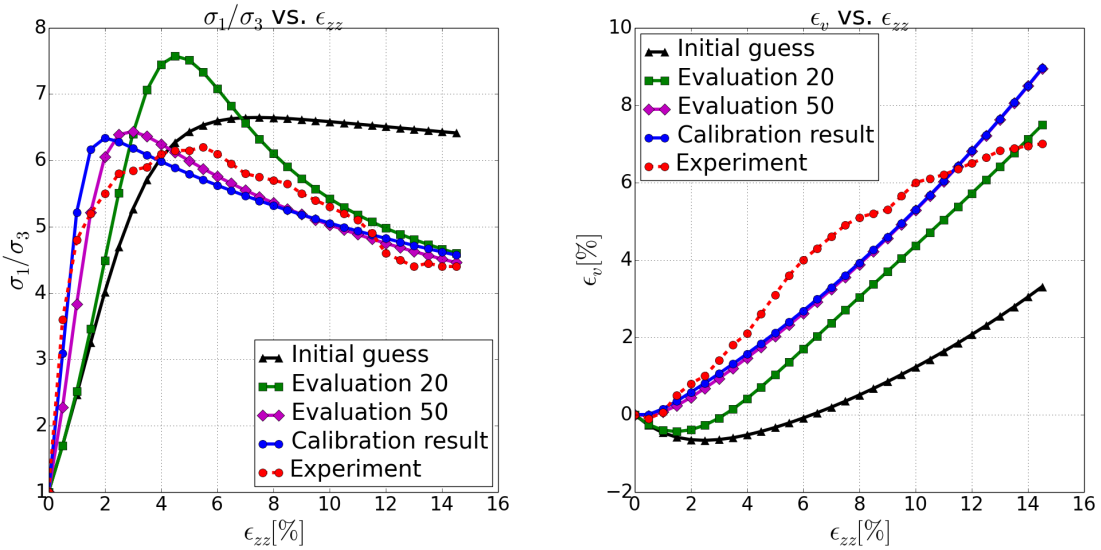

Figure 7.8: *Macroscopic stress ratio (left) and volumetric strain (right) responses from selected value sets of material parameters in unit cell calibration*

laboratory specimen using the data extracted from micro-CT image analysis. The process of converting the micro-CT experimental data into numerical specimen is illustrated in Fig. 7.9. After obtaining the images from the X-ray CT scan, the position and effective diameter of each grain are recorded. Three micro-CT images taken at initial (0 % axial strain), peak (6 % axial strain) and residual (15 % axial strain) stages are used. The boundary particles are identified and thus the outer boundary of the 3D specimen can be extrapolated from the position of these particles. Following this step, the domain of the specimen is discertized by finite element and the void ratio of each finite element is calculated by established the total solid volume using the positions and effective diameters of the particles, as shown in Fig. 7.9.

All micro-CT based finite element simulations are performed on the numerical specimen with identified initial geometry and initial void ratio distribution. Here we adopt the hypothesis that the dominating factor that governs the transition from compressive to dilatant behavior of granular materials is the relative density or porosity, the same simplification used in Borja et al. [2013]. As a result, the material parameters C_1, C_2, C_3,

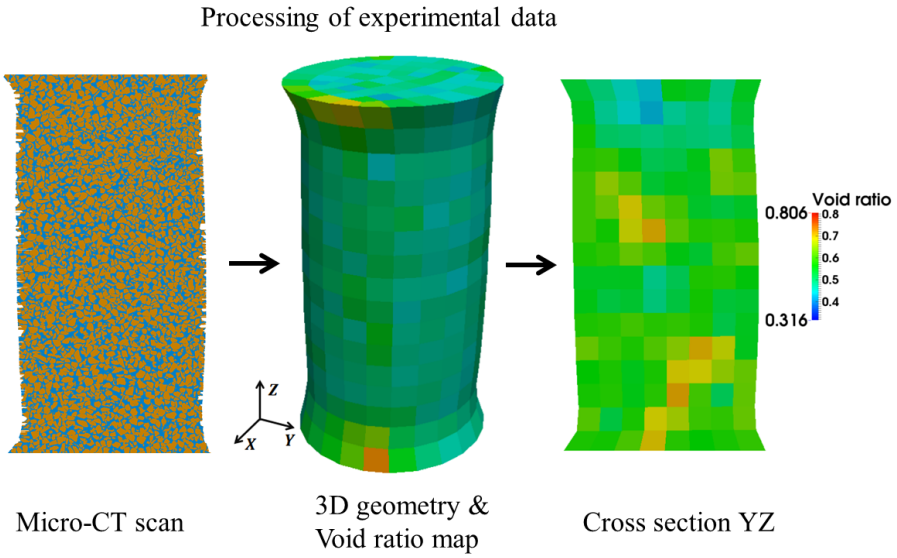

Figure 7.9: *Construction of the numerical sample and void ratio distribution from micro-CT experimental data at the initial stage (0 % axial strain) of the triaxial compression test*

C_4, e_c, a and l are assumed to be homogeneous within the specimen, while the spatial variation of the void ratio inferred from micro-CT image of the initial configuration is incorporated to study the effect of the spatial variation of void ratio. Note that the results of the inverse problem depend on how the boundary conditions are applied in model simulations. In this study, these conditions are defined based on the experimental setup with assumptions and simplifications. For example, because of the complexity of the interaction between the Hostun sand sample and the loading pistons of the triaxial cell, the top and bottom surfaces of the specimen are not fully constrained, neither in terms of the transnational nor rotational degrees of freedom (as shown in Figure 7.4). In particular, we observed that the loading plates placed on the top of the specimen has slided. In this study, the authors assume that the nodal displacements on the top surface of the specimen are totally constrained, while the bottom surface is compressed under a constant strain rate in the Z direction and all nodes at the bottom boundary have the same vertical displacement in the XY plane in order that the surface area does not change. This constraint is applied via the Lagrange multipliers. Meanwhile, the rotations on both surfaces are prohibited. The lateral surface of the FEM model is under constant confining pressure of 100 kPa and is free to rotate, neglecting the effect of the rubber membrane in the testing apparatus.

The Dakota calibration procedure of the material parameters is carried out for two inverse problems. In the first problem (Case A), only the macroscopic responses serve as the constraints for material parameters. The second problem (Case B) takes into account, apart from the macroscopic curves, the local void ratio developed at the peak and residual stages, thus adopting information from micro-CT images as additional target. The weight of the void ratio data in Case B is much higher than the macroscopic data. These two extreme cases are studied to separate the influence of either macroscopic behavior or meso-scale behavior on the parameter calibration. As the second step of each case, the objective function is modified to balance the weights of macro- and meso-data, and the calibration procedures continue with the results of Case A and Case B.

7.4.1 Case A: results from macroscopic objective function

The objective function for Case A is the same as Eq. 7.13, which only consists of macroscopic stress ratio and volumetric strain data. Both data types contain 30 data points, thus their weights are identical. Unlike elasto-plastic models for granular materials, the micropolar hypoplastic constitive model does not separate elastic and plastic parameters. Thus the material parameters are calibrated simultaneously, not in a stepwise manner [Ehlers and Scholz, 2007]. The initial guess of the material parameters and the calibrated results in Case A is presented in the Table 7.2. The macroscopic responses obtained by the parameter sets from initial guess, the 20th evaluation, the 50th evaluation and the final calibration result are compared in Fig. 7.10. The evolution of the curves shows that the iterations converge to the final solution that minimizes the objective function. However, the local void ratio distribution does not converge to the actual experiment data. This is shown in Fig. 7.11 where the experimental data of void ratio map in cross-section YZ and the relative error map (defined in Eq. 7.10) computed from simulations are presented. Since the sample geometry and void ratio distribution are not included in the objective function of Case A, the calibration procedure dose not correct the

	Number of iterations	C_1	C_2	C_3	C_4	e_c	a	l
Initial guess	-	-68.00	-767.60	-2742.70	-257.50	0.650	0.980	0.200 mm
Case A	74	-70.57	-832.40	-2524.10	-261.70	0.637	0.960	0.468 mm
Case A1	30	-69.67	-1372.67	-2075.62	-251.90	0.641	0.976	0.364 mm
Case B	117	-67.21	-920.08	-2312.79	-259.45	0.636	0.971	0.977 mm
Case B1	30	-67.91	-1229.29	-2244.82	-262.41	0.6358	0.970	0.979 mm

Table 7.2: *Calibration of material parameters of entire sample using Case A: only macroscopic responses; Case A1: equal weights of stress ratio, volumetric strain and local void ratio data, starts from results of Case A; Case B: macroscopic responses and local void ratio distributions; Case B1: equal weights of stress ratio, volumetric strain and local void ratio data, starts from results of Case B.*

void ratio discrepancy with the initial guess and leads to a numerical solution that a dominant shear band is formed inside the sample, while the actual specimen developed a 'barrel' shape that exhibit diffusive bands [Ikeda et al., 2003].

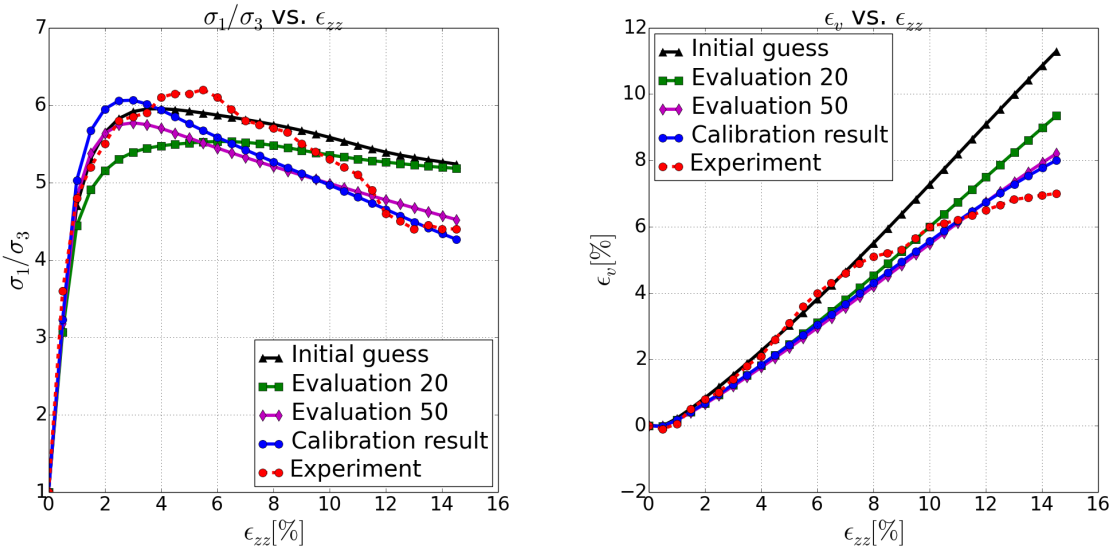

Figure 7.10: *Stress ratio and volumetric strain responses of full sample simulation during the calibration procedure using only macroscopic responses (Case A).*

As the correction step (Case A1), the former calibrated results are used as the initial guess for a modified objective function that incorporates additionally the void ratio data:

$$
\begin{aligned}
f_2(\boldsymbol{x}) = & \frac{1}{N_{\sigma_1/\sigma_3}} \sum_{i=1}^{N_{\sigma_1/\sigma_3}} w_i r_i[(\frac{\sigma_1}{\sigma_3})_i(\boldsymbol{x}), (\frac{\sigma_1}{\sigma_3})_i^{\text{lab}}]^2 + \frac{1}{N_{e_v}} \sum_{j=1}^{N_{e_v}} w_j r_j[e_{v_j}(\boldsymbol{x}), e_{v_j}^{\text{lab}}]^2 \\
& + \frac{1}{N_{\text{element}}} \sum_{k=1}^{N_{\text{element}}} w_k r_k[e_k^{\text{peak}}(\boldsymbol{x}), e_k^{\text{peak}^{\text{lab}}}]^2 + \frac{1}{N_{\text{element}}} \sum_{m=1}^{N_{\text{element}}} w_m r_m[e_m^{\text{residual}}(\boldsymbol{x}), e_m^{\text{residual}^{\text{lab}}}]^2 ,
\end{aligned}
\tag{7.14}
$$

where e_i are void ratio in element i, N_{element} is the number of elements in the FEM model. The contributions of stress ratio, volumetric strain, local void ratio data are balanced by the number of data points of each type. The weights of each data type equal to 1.

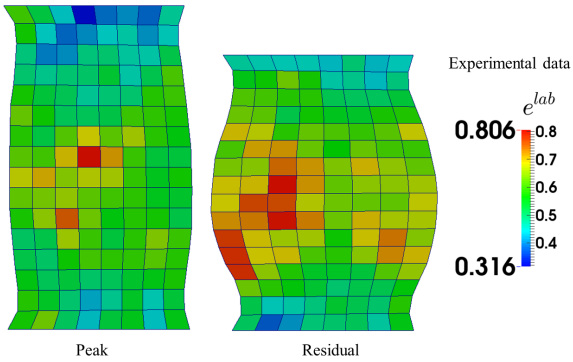

(a) Void ratio distribution from Micro-CT images

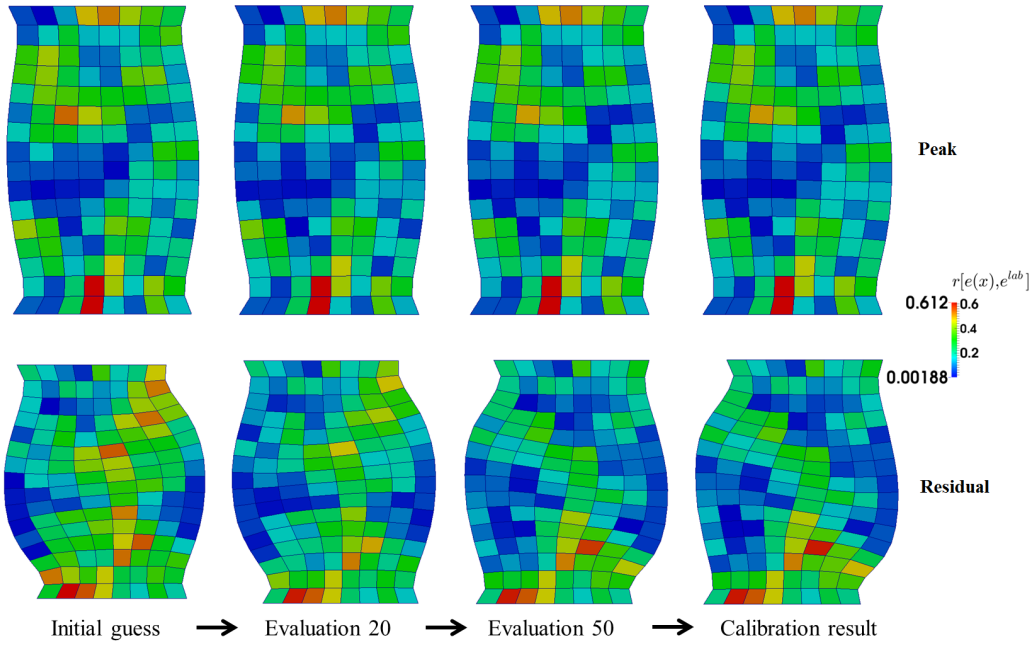

(b) Distribution of residuals (defined in Eq. 7.10) at selected steps of the Dakota calibration in Case A

Figure 7.11: *Relative error of local void ratio distribution between full sample simulation and micro-CT data (shown in cross-section in plane YZ) during Dakota calibration procedure using Case A: only macroscopic responses*

7.4.2 Case B: results from multiscale objective function

The objective function for Case B takes the form:

$$
\begin{aligned}
f_2(\boldsymbol{x}) = & \sum_{i=1}^{N_{\sigma_1/\sigma_3}} r_i[(\frac{\sigma_1}{\sigma_3})_i(\boldsymbol{x}), (\frac{\sigma_1}{\sigma_3})_i^{\text{lab}}]^2 + \sum_{i=1}^{N_{ev}} r_i[e_{v_i}(\boldsymbol{x}), e_{v_i}^{\text{lab}}]^2 \\
& + \sum_{i=1}^{N_{\text{element}}} r_i[e_i^{\text{peak}}(\boldsymbol{x}), e_i^{\text{peak}^{\text{lab}}}]^2 + \sum_{i=1}^{N_{\text{element}}} r_i[e_i^{\text{residual}}(\boldsymbol{x}), e_i^{\text{residual}^{\text{lab}}}]^2.
\end{aligned}
\tag{7.15}
$$

In this function the residuals of experimental data are simply summed. The number of elements is much larger than the number of stress ratio and volumetric strain data. Hence, the objective function Eq.7.15 has much larger weight on micro-CT data than the macroscopic responses. The calibration in Case B starts from the same initial guess of the material parameters as the Case A and the calibrated results are also shown in the Table 7.2 to show comparison. Compared to other hypoplastic material parameters, the material length parameter l, which accounts for the micropolar effect in the model, varies more significantly when experimental data of local void ratio are included in the least square problem. The macroscopic responses obtained by the parameters sets from initial guess, the 20th evaluation, the 50th evaluation and the final calibration result are compared in Fig. 7.12. Although the volumetric strain response approaches the experiment data along the iterations, the macroscopic stress ratio response deviates from the experimental response in the sense that the peak stress and residual stress

are not coincide and the softening phenomenon is not apparent. As for the meso-scale data, as shown in Fig. 7.13, the calibrated parameters result in a much closer predication of actual specimen geometry and void ratio compared to Case A. This observation emphasizes the necessity of including micro-structural information in material parameter identification procedures. Note that the relative errors of void ratio near the top and bottom surfaces, unlike the central areas, are not significantly reduced during the Dakota calibrations. This is because the boundary conditions in model simulation does not perfectly represent the experimental setup.

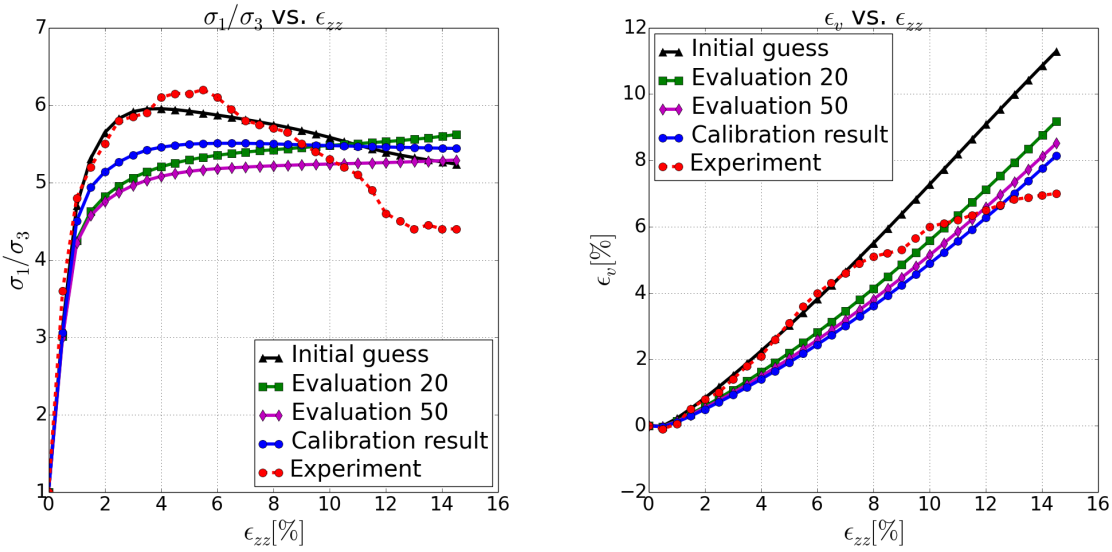

(a) (b)

Figure 7.12: *Stress ratio and volumetric strain responses of full sample simulation during the calibration procedure using macroscopic responses and local void ratio distribution (Case B).*

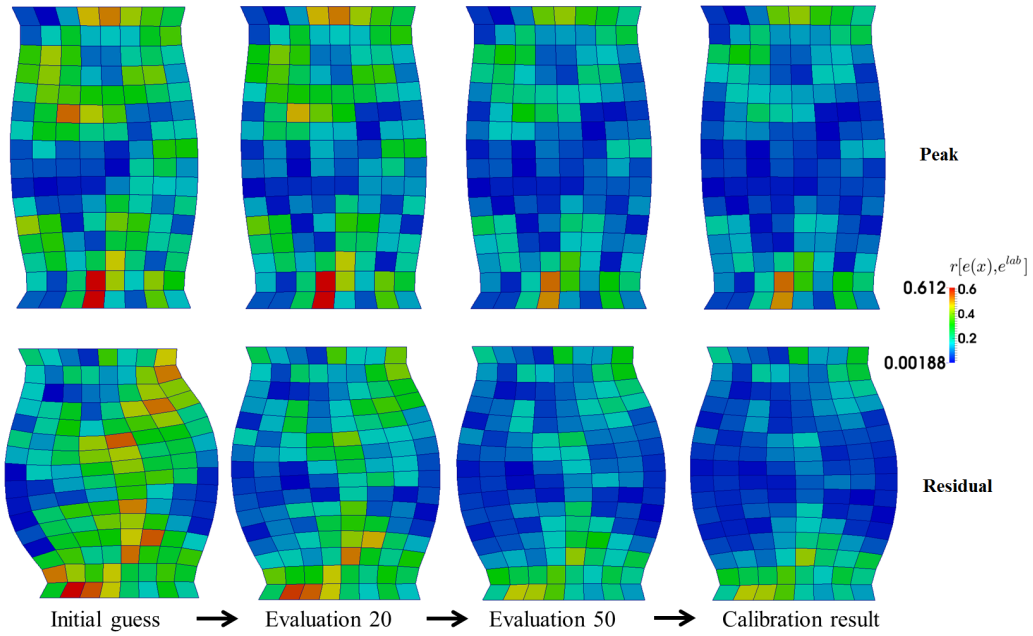

(a) Distribution of residuals at selected steps of the Dakota calibration in Case B

Figure 7.13: *Relative error of local void ratio distribution between full sample simulation and micro-CT data (shown in cross-section in plane YZ) during Dakota calibration procedure using Case B: macroscopic responses and local void ratio distribution*

The objective function Eq. (7.14) is again adopted to perform a further calibration step from the calibrated results (Case B1). The correction is made by using the equilibrium weights of different types of experimental

data. The results are recapitulated in Table 7.2 and the macroscopic responses in different cases are compared in Fig 7.14. After the correction step Case A1, the prediction of peak stress is improved, while the discrepancy between the model response and experimental data in Case B1 is further enlarged.

7.4.3 Discussion

Two calibration strategies are employed in this study. The resultant material parameters and calibrated simulations are analyzed. In the first strategy, we find material parameter that allows the finite element simulations replicate the macroscopic responses as close as possible, but neglect all meso-scale information provided by the micro-CT images. This optimized material parameter set (optimized in terms of macroscopic responses only), are then used as the initial guess of the next inverse problem. Following this predictor step, another inverse problem is defined by a new multiscale objective function that takes account of both the macroscopic data and local void ratio properties are used for calibration. This approach mimics the idea in Ehlers and Scholz [2007] for determining material parameters for micropolar constitutive laws. The major departure here is the usage of micro-CT image and the elimination of the needs to use multiple experimental tests to generate constraints for the objective function. To analyze the importance of the initial guess and whether a global optimal values for the material parameter set exists, we employ another alternative strategy in which the meso-scale information is used right at the predictor step. Then, the same multiscale objective function used in the corrector step (i.e. Equation (7.14)) is used balance the weights of global and local data.

Comparisons of results

At the first look, the approach that starts with calibrating macroscopic parameter seems to be better in terms of replicating compatible shear stress history as shown in Fig. 7.14(a), even though both calibrated finite element simulations yield similar volumetric responses. In particular, the second approach is unable to capture the macroscopic peak and residual shear stresses at the predictor step, and again fails to make any significant improvement in capturing the peak and residual shear strength after switching to the multiscale objective function, as shown in Fig. 7.14. As a result, evidence provided in the macroscopic responses seems to favor the staggered approach similar to the one proposed in [Ehlers and Scholz, 2007] in which the calibration process begins with an inverse problem that first curve-fit macroscopic behaviors, followed by a correction step that uses multiscale objective function to enforce consistency of kinematics.

However, closer look at the deformed configuration and the meso-scale responses may lead to an opposite conclusion. In particular, we find that the weight modification approach that begins with calibrating meso-sclae information from micro-CT images actually yield the experimentally-observed bifurcation mode, while the macro-then-microscopic approach does not. In Case A where $l = 0.468\ mm$, which is close to the mean particle diameter $d_{50} = 0.338\ mm$, a persistent shear band has developed in the specimen. This persistent shear band is non-symmetric and has not been observed in the micro-CT images captured during the drained triaxial compression test. In Case B, however, $l = 0.977\ mm$, which is 2.5 times larger than the mean particle diameter and the barrel-shaped deformed specimen develops a barrel deformed configuration followed by the development of a X-shaped shear localization zone. This kinematic features are consistent with what observed in the physical experiment, even though the Case B simulation does not replicate the shear stress responses as close as the Case A simulation does.

In other words, the set of material parameters that leads to the best replica of macroscopic responses observed in laboratory does not necessarily yield the correct bifurcation mode. As a result, the one other reasonable strategy is to design an objective function that acts as a compromise between the desire of matching macroscopic responses and maintaining consistent kinematics at meso-scale level. Furthermore, the notable difference in the macroscopic and microscopic responses predicted by the staggered approach and weight modification approach indicates that the calibration exercise is highly path-dependent and multiple local minimum is likely to exist, and thus making it difficult to find the global minimum point for the multiscale objective function in the parametric space.

Source of Error

The discrepancy between the experimental data and simulation results may also attributed to the idealized boundary condition applied on numerical specimen. In particular, the specimen-loading-plate interaction between the sample and the loading pistons as well as the elastic membrane are not accurately and explicitly modeled [Albert and Rudnicki, 2001]. Moreover, the assumption that material parameters are homogeneous

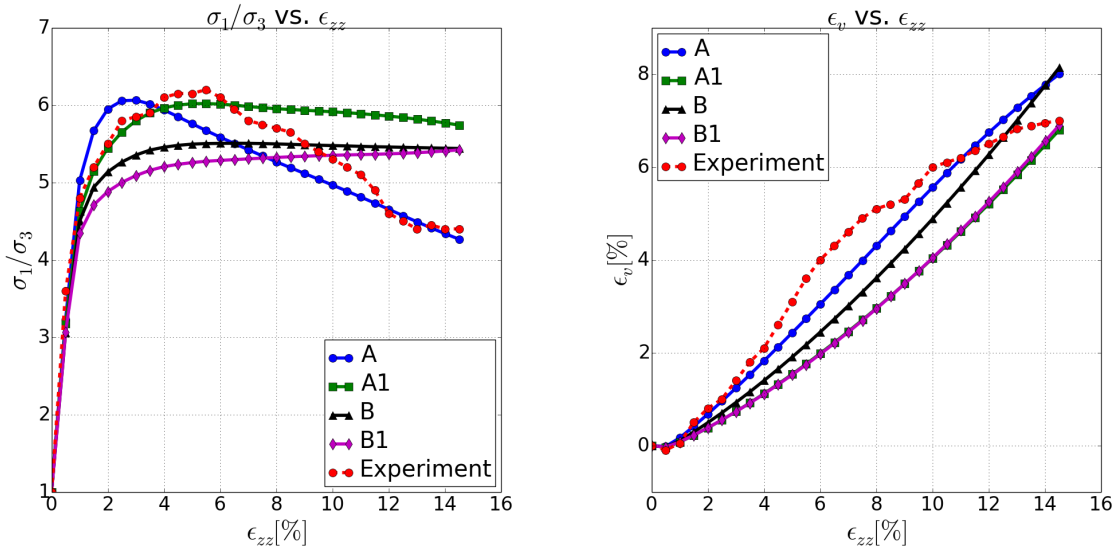

(a) (b)

Figure 7.14: *Stress ratio and volumetric strain responses of full sample simulation during the calibration procedure using Case A: only macroscopic responses; Case A1: equal weights of stress ratio, volumetric strain and local void ratio data, starts from results of Case A; Case B: macroscopic responses and local void ratio distribution; Case B1: equal weights of stress ratio, volumetric strain and local void ratio data, starts from results of Case B.*

throughout the specimen may also over-simplified the spatial variability of the physical specimens. Finally, the micropolar finite element model is formulated using the Jaumann rate of the Cauchy stress. The Jaumann rate is an objective rate which is suitable for materials in the geometrical nonlinear regime with small strain and large rotation. However, some previous works, such as Molenkamp [1986], has pointed out that the Jaumann rate should be avoided for problems with large deviatoric strain. These limitations will be considered in future studies.

Length scale, higher-order kinematics and bifurcation modes

The higher-order quantities, namely the curvature $\boldsymbol{\kappa}$ and the couple stress $\boldsymbol{\mu}$, can be computed from the micropolar model simulation, while these information are not available from micro-CT images. In this study, two types of shear bands are encountered with different material parameters in the finite element simulations even though both simulations began with the same initial geometry and void ratio distribution. In Case A and B, the calibrated material length l varies significantly, compared to other material parameters.

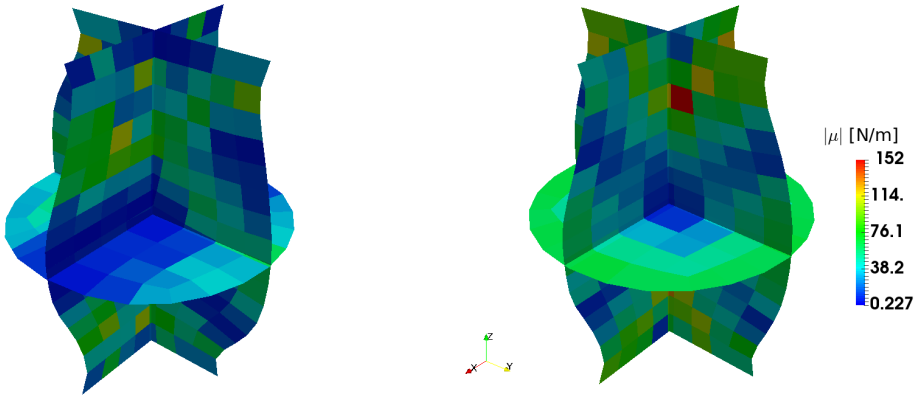

(a) Case A (b) Case B

Figure 7.15: *Norm of the couple stress tensor* $|\boldsymbol{\mu}| = \sqrt{\mu_{21}^2 + \mu_{32}^2 + \mu_{31}^2}$ *for results of inverse problems A and B at the residual stage.*

In both cases, the distribution of the norm of the couple stress tensor $|\boldsymbol{\mu}| = \sqrt{\mu_{21}^2 + \mu_{32}^2 + \mu_{31}^2}$ and the norm of the curvature tensor $|\boldsymbol{\kappa}| = \sqrt{\kappa_{21}^2 + \kappa_{32}^2 + \kappa_{31}^2}$ are shown in Fig. 7.15 and Fig. 7.16, respectively. The couple stress and curvature localize in the transition zone from the shear localization region to homogeneously deformed region, suggesting that the micropolar effect becomes very important when high-gradient deformation occurs in granular materials. This observation is in consistent with numerical experiments conducted with discrete element method [Oda and Iwashita, 2000, Ehlers et al., 2003, Wang and Sun, 2016a,b].

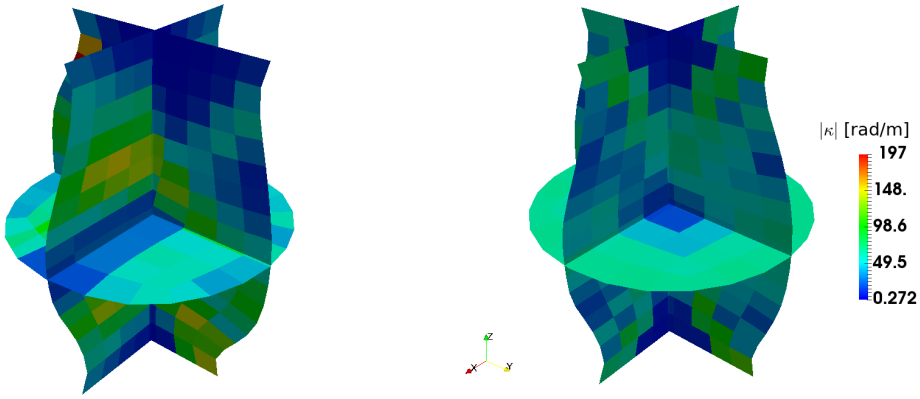

(a) Case A (b) Case B

Figure 7.16: *Norm of the curvature tensor* $|\kappa| = \sqrt{\kappa_{21}^2 + \kappa_{32}^2 + \kappa_{31}^2}$ *for results of inverse problems A and B at residual stage*

The evolution of shear bands simulated in Case A and Case B are illustrated in Fig. 7.17 using color map of $|\boldsymbol{\mu}|$, as well as in Fig. 7.18 using color map of $|\boldsymbol{\kappa}|$. At the beginning of the triaxial loading, two-axes symmetric localization patterns emerge for both simulations [Ikeda et al., 2003]. After the peak stress of Case A (at 3% axial strain), the pattern bifurcates to an asymmetry pattern: one shear band becomes stronger than the other. Upon further loading, the dominant shear band becomes persistent and the other weak band gradually die out. As for Case B, the two bands compete with each other along the deformation but neither predominates. The initial pattern bifurcates to bilateral symmetry that the symmetry with respect to the horizontal axis is broken. The diffuse mode is preserved to the end of the loading. This analysis shows that, even though the spatial variability of the material parameters is neglected, the numerical values of the material parameters, particularly the material length l, still impose strong effects on the failure mode of numerical specimen.

Critical state

The anisotropy density function f_d of Eq. 7.3 is an indicator of the critical state, a condition at which particulate materials keep deforming in shear at constant void ratio and stress [Casagrande, 1936, Roscoe et al., 1958]. In the micropolar hypoplasticity adopted in this study, the local void ratio approaches the critical void ratio e_c, f_d approaches 1. The distribution of f_d of the two numerical specimens captured at residual stage of Cases A and B are presented in Fig. 7.19. Since the different calibrated material parameters used in Case A and B, the failure modes as well as the locations where the Hostun sand first reaches the critical state are also different. In Case A, the elements residing in the persistent shear band are close to the critical state, while the elements outside the zone are not close to it. In Case B, the pattern of f_d also coincides with the diffuse failure mode presented in Fig. 7.17, showing that the unit cells inside the shear band are also closer to critical state than the host matrix, but the difference between the numerical value of f_d within the host matrix and inside the shear band are less significant than Case A. Both findings are consistent with Tejchman and Niemunis [2006], Wang and Sun [2016b] where the strain localization triggered by the material bifurcation in dense assemblies tends to have the void ratio approaching its critical value locally, but the specimen itself does not necessarily reach critical state globally. Comparing this observations with the couple stress norm shown in Fig. 7.17, we observed that the shear band is not only much closer to the critical state, but also has significantly lower coupled stress magnitude. This result is consistency with the norm of the curvature tensor shown in Figure 7.18 where the specimen has significant amount of micro-rotation at the boundary of the shear band and the host matrix but the micro-polar kinematics is not significant inside the shear band and in the host matrix.

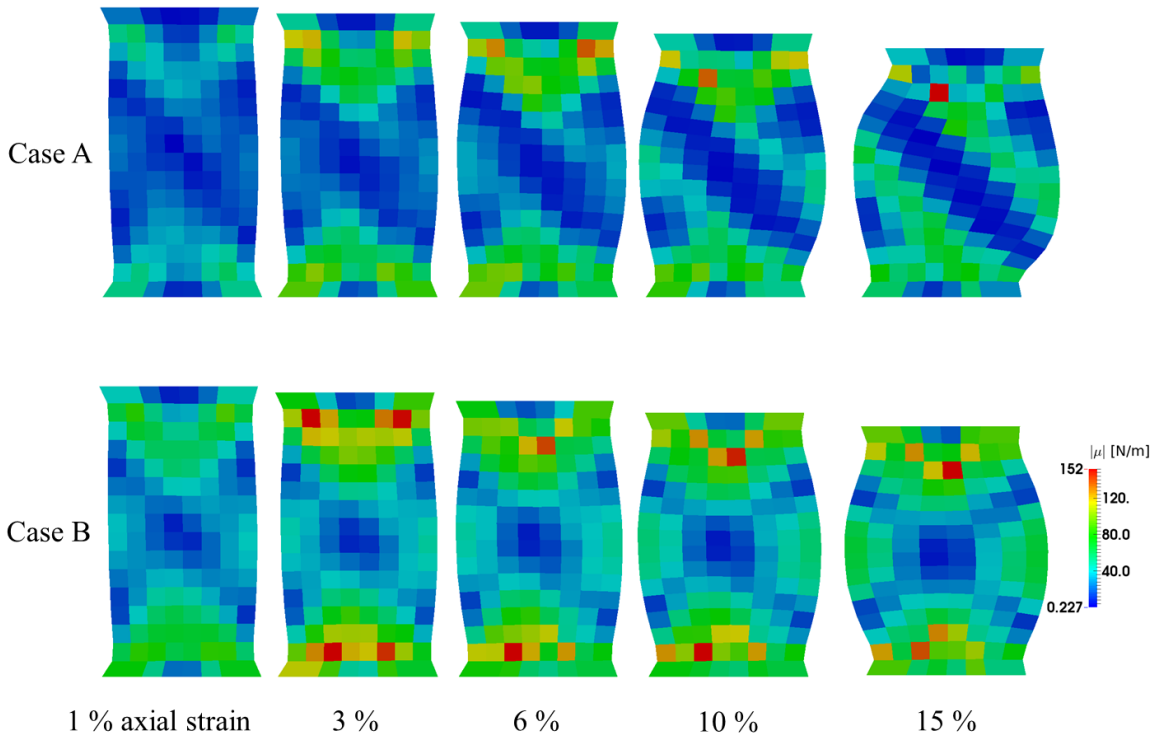

Figure 7.17: *Evolution of shear localization in cross section YZ of calibraion results of Case A and Case B, illustrated in the norm of couple stress.*

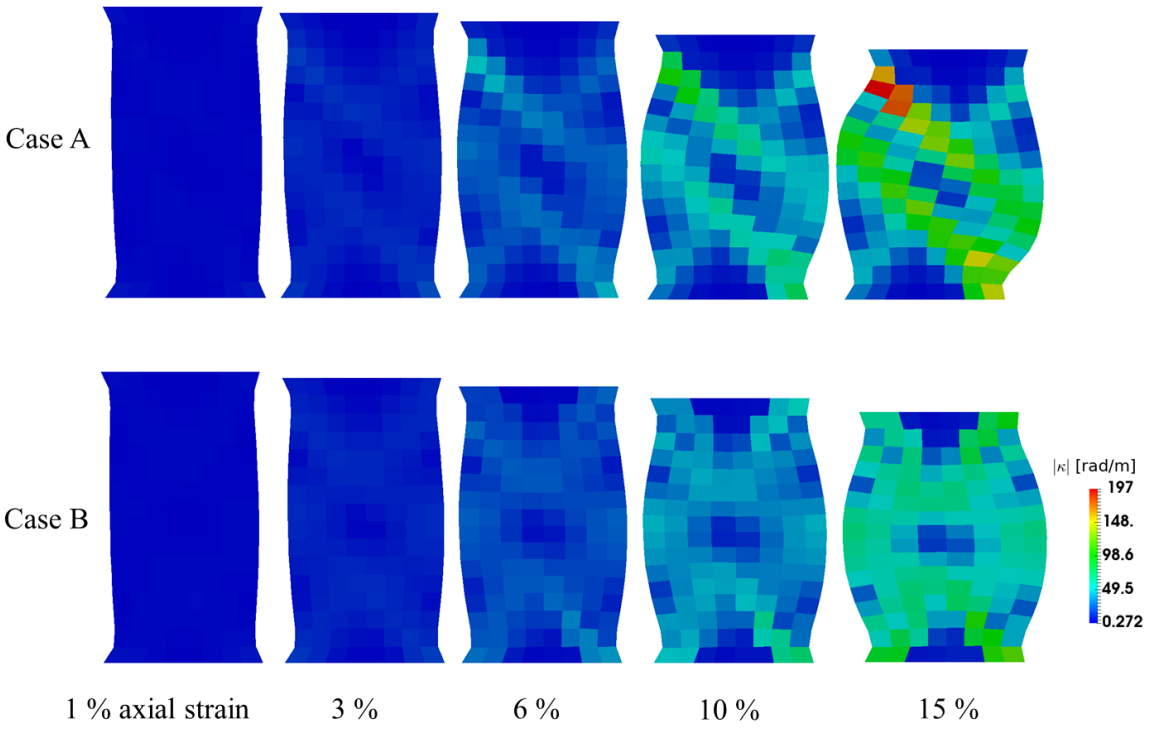

Figure 7.18: *Evolution of shear localization in cross section YZ of calibraion results of Case A and Case B, illustrated in the norm of curvature tensor.*

7.5 Conclusions

In this work, we incorporate information obtained from both macroscopic measurement and meso-scale kinematics to analyze the sensitivity of the predicted characteristic length and mechanical responses of a 3D micropolar hypoplasticity finite element model. To the best knowledge of the authors, this is the first contribution

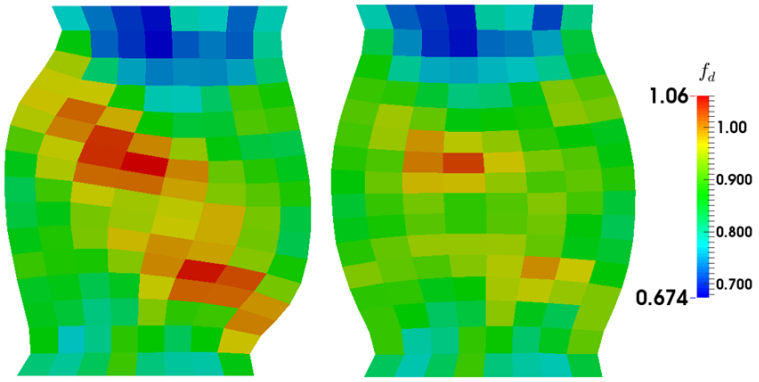

Figure 7.19: *Distribution of f_d for results of inverse problems A and B at the residual stage. $f_d = 1$ indicates that the material is in critical state.*

that incorporates micro-CT images and multiscale objective function into the material parameter identification procedure for micropolar plasticity for granular materials.

The results show that the incorporation of meso-scale information may significantly change the predicted length scale obtained from the inverse problems and leads to different bifurcation modes in the finite element simulations. Even though similar macroscopic responses are observed from simulations conducted with single-scale and multiscale objective functions, the macroscopic responses in the former case may yield meso-scale responses that are not consistent with those of the real specimen. As a result, the apparently good curve-fitting of macroscopic response is not a good indicator of forward prediction capacity. This result has important implications for the validations of grain-scale simulation tools (such as discrete element, lattice-beam and lattice spring models) in which macroscopic stress-strain responses are often the only experimental data available for benchmark and validations. The numerical results, particularly the difference of the failure modes obtained from different objective functions, indicate that using macroscopic stress-strain curve alone to evaluate or validate grain-scale simulations is neither productive nor reliable.

Although the higher-order quantities, the curvature $\boldsymbol{\kappa}$ and the couple stress $\boldsymbol{\mu}$, are not available from micro-CT images, they are computed from the micropolar simulations with the material parameters optimized for different objective functions. Depending on which set of material parameters is employed, the numerical specimen may either develop a persistent shear band, which is not observed in the experiment, or a diffuse failure mode, which is observed from micro-CT images. Comparisons between the simulation results with micro-CT images, suggest that a staggered predictor-corrector procedure that first employs the macroscopic objective function to curve-fit the macroscopic responses, then use the multiscale objective function to enforce kinematic constraints seem to yield a more compatible macroscopic constitutive responses with the experimental counterpart, but the material parameters that lead to the best curve-fitting macroscopic responses also leads to an incorrect bifurcation mode. This finding is alerting, as the material parameters that leads to the wrong bifurcation mode in the backward calibration exercise is also likely to generate even more unrealistic forward prediction. The apparently good match in the macroscopic curve can be misleading and generate a false sense of confidence for the numerical model. This is a noteworthy concern, as there is an alerting trend in which the forward-predictive capacity of grain-scale models are often incorrectly measured by how well they curve-fit the macroscopic stress-strain curve, rather than how well they are able to generate compatible and consistent mechanical behaviors across length scales. The issue associated with this calibration approach is not apparent when calibration is conducted at the unit cell level in which only homogeneous deformation is considered. However, when macroscopic stress-strain curve is used to calibrate meso-scale or grain-scale models, the dimensions of the parametric space can be larger than the number of constraints provided by the macroscopic responses. The insufficiency of constraints then makes it possible to generate simulations that apparently match the macroscopic calibration with a completely inconsistent microstructure. By incorporating microscopic information from microCT images to calibrate material parameters, this research provides important evidence to suggest that constraining micro-mechanical model to match macroscopic responses is not sufficient. Nor is it a meaningful way to measure the quality of numerical predictions. These lessons are important for the calibration and validation of high-order and multiscale finite element models.

Chapter 8

Key findings on themro-hydro-mechanical coupling effect at finite deformation ranges

Thermo-hydro-mechanics (THM) is a branch of mechanics aimed to predict how deformable porous media behave, while heat transfer and fluid transport simultaneously occur in the pores filled by fluid and in the bulk of solid skeleton. Understanding these multiphysical responses is important for a wide spectrum of modern engineering applications, such as tissue scaffolding, geothermal heating, mineral exploration and mining, hydraulic fracture, and nuclear waste storage and management [McTigue, 1986, Coussy, 2004a]. Many of these engineering applications involve porous media undergoing substantial deformation with rapid changes on temperature and pore pressure.

In the last three decades, a considerable progress has been made for deriving mathematical theories and implementing computer models to replicate the fully coupled thermo-hydro-mechanical processes. For instance, a monolithic small strain finite element code, FRACON, has been developed by Nguyen and Selvadurai [1995]. In this code, the balance of linear momentum and mass are fully coupled, while thermal transport may affect the solid deformation and pore-fluid diffusion but not vice versa. A generalized trapezoidal rule is used to discretize temporal space. Li et al. [2005] introduces a co-rotational FEM formulation and incorporate plasticity into THM model to model the non-isothermal elastoplastic responses of porous media at large strain. In this formulation, stabilized one-point quadrature element is used to cut computational cost and avoid locking. In addition, logarithmic finite strain formulation has been derived and implemented in Karrech et al. [2012] to overcome the aberrant oscillations encountered in large simple shear. Recent work by Preisig and Prévost employed a fully coupled implicit THM simulator to compare the numerical solutions against the field data in a case study for carbon dioxide injection at In Salah, Algeria [Preisig and Prévost, 2011]. Kolditz et al. [2012] introduces an open-source project OpenGeoSys, which takes advantage of an object-orient framework and provide software engineering tools such as platform-independent compiling and automated benchmarking for developers.

In addition to the monolithic finite element scheme, attempts have been made to sequentially couple multiphase flow and geomechanical simulators by establishing proper feedback and information exchange mechanisms. This strategy is often referred as operator-splitting method for which several aliases, such as fractional step, projection and pressure correction method, exist, as pointed out by Markert et al. [2010]. One such example is TOUGH-FLAC, which links flow simulator TOUGH2 with a small strain finite difference code FLAC [Rutqvist, 2011]. This sequential coupling approach is an attractive alternative to the monolithic approach, as it is easier to implement and maintain flow and solid simulators separately. This sequential coupling approach is based on the operator-splitting technique, for which several aliases, such as fractional step, projection and pressure correction method, exist [Markert et al., 2010]. As noted by Markert et al. [2010], the idea behind the operator-splitting approach is to decouple the unfavorable volume constraint from the balance of linear momentum via an immediate step. The separation of pore pressure update from the solid mechanics solver therefore provides numerical stability. However, proper communication must be established to ensure the correctness and numerical stability of numerical solutions [Schrefler, 1995, Schrefler et al., 1997, Jha and Juanes, 2007, Preisig and Prévost, 2011, Sun et al., 2013d]. The sequential coupling scheme used to link the fluid and solid simulators may have profound impact on the efficiency, stability and accuracy of the numerical solutions. If the fluid and solid simulators use different grids or meshes, then a proper data projection scheme is required to transfer information from Gauss points and nodes of the solid mesh to the fluid mesh and vice versa [Goumiri

and Prevost, 2011]. For large scale parallel simulations, the sequential couplings must be carefully designed to avoid causing bottleneck due to the difference in solver speed. This can be a significant problem if either the solid or fluid solver runs only in serial. Recent work by Kim et al. [2015] systematically compared fully implicit, fully explicit, semi-implicit monolithic and staggered schemes for unsaturated porous media under the isothermal condition. Numerical examples presented in Kim et al. [2015] show that the fully implicit monolithic scheme with either inf-sup stable or stabilized equal-order finite element is advantageous on resolving sharp pore pressure gradient, but is also less efficient than the semi-implicit counterparts.

As noted in Zienkiewicz et al. [1999b], Wan [2002], Mira et al. [2003], Truty and Zimmermann [2006a], Simoni et al. [2008], White and Borja [2008a], Preisig and Prévost [2011], Sun et al. [2013d], Borja [2013], numerical stability is often a major challenge for monolithic implicit schemes that solve poromechanics models. Due to the lack of inf-sup condition [Babuška, 1973, Brezzi et al., 1985, Bathe, 2001, Bochev et al., 2006], pore pressure and temperature fields may exhibit spurious oscillation patterns and/or checkerboard modes if the displacement, pore pressure and temperature are spanned by the same set of basis function. While these spurious oscillations are less severe at the drained/isothermal limit, they may intensify when a small time step is used or when materials are near undrained/adiabatic limit. From a mathematical viewpoint, these non-physical results are due to the kernel (null space) of the discrete gradient operator being non-trivial. This non-trivial kernel makes it possible to have certain spatially oscillating pore pressure and temperature fields that have no impact on the solid deformation in a numerical simulation. To cure the numerical instability due to the lack of inf-sup condition, previous researches have established a number of techniques that employ different basis functions to interpolate displacement and pore pressure and obtain stable solutions. For instance, Zienkiewicz and coworkers [Zienkiewicz et al., 1999b], and Borja [Borja et al., 1998a] used Taylor-Hood finite element (quadratic basis functions for displacement and linear basis function for pore pressure) to satisfy inf-sup condition and maintain numerical stability for isothermal implicit hydromechanics problems. On the other hand, Jha and Juanes [Jha and Juanes, 2007] have shown that linear displacement combined with pore fluid velocity in the lowest-order Raviart-Thomas space, and piecewise constant pore pressure may also lead to stable solutions for isothermal poromechanics problems. Nevertheless, inf-sup stable mixed finite element models require multiple meshes for displacement, pore pressure and/or fluid velocity. As a result, they require additional programming effort to pre- and post-processing data and maintain the more complex data structure.

To avoid the complications of using multiple meshes for each solution field, an alternative is to use one single equal-order finite element mesh with stabilization procedures. Many stabilization procedures have been proven to be able to eliminate the spurious oscillation modes in implicit scheme without introducing extra diffusion for small strain isothermal poromechanics problems. For instance, White and Borja [2008a] employed a polynomial projection scheme originated from [Dohrmann and Bochev, 2004] to simulate slip weakening of a fault segment. This work is extended to the large deformation regime in Sun et al. [2013d], where the stabilization term is adaptively adjusted to avoid over-diffusion. Nevertheless, to the best of the authors' knowledge, stabilization procedure for finite strain non-isothermal poromechanics has never been proposed.

The objective of this research is to fill this knowledge gap by establishing large deformation thermo-hydro-mechanics theory, and develop the corresponding stabilized finite element model suitable for equal-order discretized displacement, pore pressure and temperature. The resultant system of equation is solved fully implicitly and monolithically to preserve the Mandel-Cryer effect when the multiphysical coupling is strong. The necessary condition for numerical stability for thermo-hydro-mechanics problem and the corresponding combined inf-sup condition are derived. A new stabilization procedure is established based on the combined inf-sup condition.

The rest of the paper is organized as follows. We first establish the field theory for the thermo-hydro-mechanics problem in the geometrical nonlinear regime (Section 2). We then formulate the weak and Galerkin forms (Section 3.1-2), derive stabilization techniques (Section 3.3). Based on the mass lumping technique, we suggest stabilization parameters that are large enough to eliminate spurious oscillations without over-diffusing the solution (Section 3.4). Selected benchmark and engineering application problems are simulated via the stabilized formulations (Section 4). Finally, concluding remarks are given in Section 5.

As for notations and symbols, bold-faced letters denote tensors; the symbol '$\cdot$' denotes a single contraction of adjacent indices of two tensors (e.g. $\boldsymbol{a} \cdot \boldsymbol{b} = a_i b_i$ or $\boldsymbol{c} \cdot \boldsymbol{d} = c_{ij} d_{jk}$); the symbol ':' denotes a double contraction of adjacent indices of tensor of rank two or higher (e.g. $\boldsymbol{C} : \boldsymbol{\epsilon}^e = C_{ijkl} \epsilon^e_{kl}$); the symbol '$\otimes$' denotes a juxtaposition of two vectors (e.g. $\boldsymbol{a} \otimes \boldsymbol{b} = a_i b_j$) or two symmetric second order tensors (e.g. $(\boldsymbol{\alpha} \otimes \boldsymbol{\beta}) = \alpha_{ij} \beta_{kl}$). As for sign conventions, we consider the direction of the tensile stress and dilative pressure as positive. Throughout this paper, we employ the standard notation $H^l(\Omega), ||\cdot||_l, (\cdot,\cdot)_l, l \geq 0$, for the Sobolev

spaces of all functions having square integrable derivative up to order l on a simply connected bounded domain Ω in $\mathbb{R}^3$, the corresponding Sobolev norm and inner product respectively.

8.1 Governing equations at Finite Strain

In this section, we present the balance principles of mass, momentum and energy that define the strong form of the thermo-hydro-mechanics problem. Following the saturated porous media theory for isothermal solid-water mixture at finite strain [Borja and Alarcón, 1995a, Armero, 1999, Sun et al., 2013d], we describe the kinematics of the solid skeleton with the Lagrangian coordinates, while describing the motion of the pore fluid with the Eulerian coordinates with respect to the current configuration of the solid skeleton. In addition, the following assumptions are made.

1. Mass exchanges between solid and fluid constituents do not occur.
2. No phase transition occurs.
3. Pores inside the solid skeleton are fully saturated by one fluid constituent.
4. The pore-fluid advection is negligible.
5. The pore-fluid flow is in laminar range.
6. No chemical reactions take place among the fluid's species.
7. Inertial effects are negligible.
8. The effective stress principle is valid.
9. The temperature of solid and fluid constituents that occupy the same material point $\boldsymbol{X} \in \mathbb{B}$ are identical.

We consider both the fluid and solid constituents compressible and that both the pore fluid and the solid skeleton may exhibit mechanical and thermal deformation.

8.1.1 Kinematics and Volume Fraction

Consider a body of fully saturated porous medium $\mathcal{B}$ composed of both solid constituent and the pore fluid in the pore space, as shown in Figure 8.1. For a sufficiently large volume, the solid constituent and the pore fluid can be modeled as a homogenized continuum mixture. Here we apply the continuum approach in which the solid skeleton of the body $\mathcal{B}$ is described by a set of continuously distributed points $X \in \mathcal{B}$ which occupied by a region within the Euclidean space $\mathbb{R}^3$. Notice that, except in the undrained limit, material points of pore fluid and solid skeleton do not share the same trajectory in the space-time continuum. As a result, materials at a point $\boldsymbol{x}$ of the current configuration may come from the reference configuration of the solid skeleton $\boldsymbol{X}^{\mathrm{s}}$ and/or the pore fluid counterpart $\boldsymbol{X}^{\mathrm{f}}$, i.e.,

$$\boldsymbol{x} = \varphi^{\alpha}(\boldsymbol{X}^{\alpha}, t) \;\; \alpha = \mathrm{s}, \mathrm{f}. \tag{8.1}$$

Apparently, one may choose to formulate governing equations via both mappings, φ^{s} and φ^{f}. However, since most of the constitutive laws of the solid skeleton are formulated with respect to the configurations described by φ^{s}, we formulate the finite strain thermo-hydro-mechanics model with respect to the trajectory of the solid skeleton to simplify the derivations. The motion of the pore fluid is therefore taken into account by considering the relative motion between the pore fluid and the solid skeleton. For brevity, we drop the designation of the solid phase such that,

$$\boldsymbol{x} = \varphi^{\mathrm{s}}(\boldsymbol{X}^{\mathrm{s}}, t) = \varphi(\boldsymbol{X}, t). \tag{8.2}$$

Therefore, the motion of the solid skeleton is described by an one-to-one mapping $\varphi : \mathcal{B} \times [0, T] \to \mathbb{R}^3$ which places a particle at the reference point $\boldsymbol{X} \in \mathcal{B}$ to a position in $\mathbb{R}^3$ in a typical time internal T. Since the solid-fluid mixture is homogenized as continuum, the density of a fully saturated porous medium can be written as,

$$\rho = \rho^{\mathrm{s}} + \rho^{\mathrm{f}} = \phi^{\mathrm{s}}\rho_{\mathrm{s}} + \phi^{\mathrm{f}}\rho_{\mathrm{f}}, \tag{8.3}$$

where $\rho_{\alpha}, \alpha = s, f$ is mass of the α constituent divided by the current volume of the α constituent, while ρ^{α} is the partial density of the α constituent, defined as the mass of the α constituent divided by the volume of the mixture in the current configuration. ϕ^{s} is the volume fraction of the solid constituent in the current

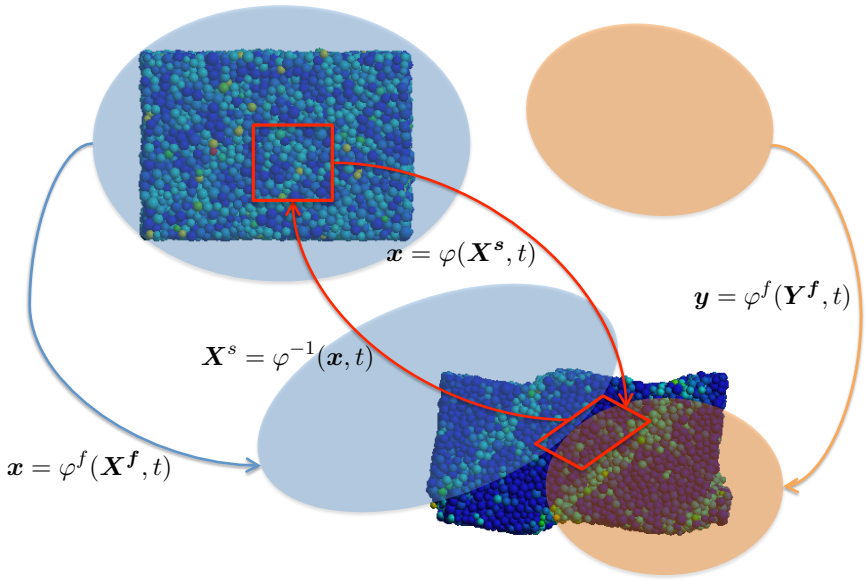

Figure 8.1: *Trajectories of the solid and fluid constituents $\varphi^s = \varphi$ and φ^f. The motion φ conserves all the mass of the solid constituent, while the fluid may enter or leave the body of the solid constituent. Figure reproduced from Sun et al. [2013d].*

configuration. ϕ^{f} is the porosity of the porous medium in the current configuration, which is referred as Eulerian porosity in [Coussy, 2004a]. For fully saturated porous media, $\phi^{\mathrm{s}} + \phi^{\mathrm{f}} = 1$. Thus, the total current density also reads,

$$\rho = (1 - \phi^{\mathrm{f}})\rho_{\mathrm{s}} + \phi^{\mathrm{f}}\rho_{\mathrm{f}}, \tag{8.4}$$

where the densities of the solid and fluid constituents both depend on the pore pressure and the temperature.

8.1.2 Balance of Linear Momentum

Under the non-isothermal condition, solid skeleton may deform due to external mechanical loading, thermal expansion (or contraction) and interactions with pore-fluid. Assuming that the mixture theory is valid for porous media, we have,

$$\boldsymbol{\sigma} = \boldsymbol{\sigma}^{\mathrm{s}} + \boldsymbol{\sigma}^{\mathrm{f}} = \phi^{\mathrm{s}}\boldsymbol{\sigma}_{\mathrm{s}} + \phi^{\mathrm{f}}\boldsymbol{\sigma}_{\mathrm{f}}. \tag{8.5}$$

where $\boldsymbol{\sigma}_{\mathrm{s}}$ and $\boldsymbol{\sigma}_{\mathrm{f}}$ are the intrinsic partial Cauchy stress defined in the volume of the solid grains V^{s} and pore space V^{f} respectively. The total Cauchy stress is the volume averaged stress defined in the current volume $V = V^{\mathrm{s}} + V^{\mathrm{f}}$. Neglecting the shear resistance of the pore fluid, intrinsic partial stress of fluid consistent $\boldsymbol{\sigma}_{\mathrm{f}}$ is therefore isotropic and holds the following relation with the macroscopic pore pressure p^{f}, i.e.,

$$\boldsymbol{\sigma}^{\mathrm{f}} = \phi^{\mathrm{f}}\boldsymbol{\sigma}_{\mathrm{f}} = -\phi^{\mathrm{f}}p_{\mathrm{f}}\boldsymbol{I} = -p^{\mathrm{f}}\boldsymbol{I}. \tag{8.6}$$

The partial stress of the solid constituent $\boldsymbol{\sigma}_{\mathrm{s}}$ depends on the effective stress $\boldsymbol{\sigma'}$ and the stress exerted on the solid grains by the pore fluid $Kp^{\mathrm{f}}/K_{\mathrm{s}}\boldsymbol{I}$, i.e.,

$$\boldsymbol{\sigma}^{\mathrm{s}} = \boldsymbol{\sigma'} + \frac{K}{K_{\mathrm{s}}}p^{\mathrm{f}}\boldsymbol{I}. \tag{8.7}$$

This definition is from [Nur and Byerlee, 1971a], which assumes that the non-uniform localization of stress at the grain scale, grain crushing, and damage are all insignificant to the skeleton (cf. [Zienkiewicz et al., 1999b] p.8-11). By substituting (8.6) and (8.7) into (8.5), the total Cauchy stress now reads,

$$\boldsymbol{\sigma} = \boldsymbol{\sigma'} - Bp^{\mathrm{f}}\boldsymbol{I}, \tag{8.8}$$

where B is the Biot's coefficient defined as [Nur and Byerlee, 1971a],

$$B = 1 - \frac{K}{K_{\mathrm{s}}}. \tag{8.9}$$

Typically, Biot's coefficient B is close to unity for sand, but can be ranged from 0.5 to 0.8 for rocks or concrete. Notice that B in (8.8) have been defined in a number of different ways in the literature. For instance, Terzaghi and Rendulic defined B as a function of the effective area of solid grains [Terzaghi and Rendulic, 1934, Skempton, 1984]. For bio-materials and composites, Cowin and Doty [2009] generalize the effective stress concept in [Biot, 1941a] and introduce the effective stress coefficient tensor $\boldsymbol{B}$, i.e.

$$\boldsymbol{\sigma} = \boldsymbol{\sigma'} - p^{\mathrm{f}}\boldsymbol{B}. \tag{8.10}$$

This definition of effective stress is not adopted in this work, but will be considered in future study. The balance of linear momentum therefore reads,

$$\nabla^{\boldsymbol{x}}\cdot\boldsymbol{\sigma} + \rho\boldsymbol{G} + \boldsymbol{h}^{\mathrm{s}} + \boldsymbol{h}^{\mathrm{f}} = \boldsymbol{0}, \tag{8.11}$$

where $\boldsymbol{G}$ is the acceleration due to gravity. $\boldsymbol{h}^{\mathrm{s}}$ and $\boldsymbol{h}^{\mathrm{f}}$ are the interactive body forces per unit reference volume exerted on their corresponding phases due to drag, lift, virtual mass effect, history effects and the relative spinning (Magnus effect) which balance out internally, i.e., $\boldsymbol{h}^{\mathrm{s}} + \boldsymbol{h}^{\mathrm{f}} = \boldsymbol{0}$ [Rajagopal and Tao, 1995]. In the total Lagrangian formulation, balance of linear momentum in Equation (8.11) is rewritten in reference configuration via the Piola transformation [Holzapfel, 2000], i.e.,

$$\nabla^{\boldsymbol{X}}\cdot\boldsymbol{P} + J\rho\boldsymbol{G} = \boldsymbol{0}, \tag{8.12}$$

where $\boldsymbol{P}$ denotes the total first Piola-Kirchhoff stress and $J = \det(\boldsymbol{F})$ is the determinant of the deformation gradient of the solid skeleton $\boldsymbol{F}$. Similar to the total Cauchy stress, the total first Piola-Kirchhoff stress can be partitioned into two parts, the effective first Piola-Kirchhoff stress $\boldsymbol{P'}$ and the pull-back of the pore fluid contribution $JBp^{\mathrm{f}}\boldsymbol{F}^{-T}$. The effective first Piola-Kirchhoff stress $\boldsymbol{P'}$ is the amount of stress carried by the solid skeleton. For solid skeleton exhibiting elasto-plastic responses, the effective first Piola-Kirchhoff stress can be determined from the deformation gradient and the internal variable(s) $\boldsymbol{z}$ of the solid skeleton.

$$\boldsymbol{P}(\boldsymbol{F}, \boldsymbol{z}, p^f, \theta) = \boldsymbol{P'}(\boldsymbol{F}, \boldsymbol{z}, \theta) - JBp^f\boldsymbol{F}^{-T}. \tag{8.13}$$

Under the non-isothermal condition, the multiplicative decomposition of the deformation gradient can be written as [Holzapfel, 2000],

$$\boldsymbol{F} = \frac{\partial\boldsymbol{\varphi}(\boldsymbol{X},t)}{\partial\boldsymbol{X}} = \boldsymbol{F}_M\cdot\boldsymbol{F}_\theta \;\;;\;\; \boldsymbol{F}_\theta = \frac{\partial\boldsymbol{\varphi}_\theta(\boldsymbol{X},t)}{\partial\boldsymbol{X}} \;;\boldsymbol{F}_M = \frac{\partial\boldsymbol{\varphi}_M(\boldsymbol{X}_\theta,t)}{\partial\boldsymbol{X}_\theta}\;, \tag{8.14}$$

where $\boldsymbol{F}_\theta$ and $\boldsymbol{F}_M$ are the pure thermal and mechanical splits of the deformation gradient.

As shown in Figure 8.2, the mechanical split $\boldsymbol{F}_M$ of the deformation gradient can be further decomposed into the elastic and plastic parts such that,

$$\boldsymbol{F}_M = \boldsymbol{F}\cdot\boldsymbol{F}_\theta^{-1} = \boldsymbol{F}^e\cdot\boldsymbol{F}^p \;\;;\;\; \boldsymbol{F}^p = \frac{\partial\boldsymbol{\varphi}^p(\boldsymbol{X}_\theta,t)}{\partial\boldsymbol{X}_\theta} \;\;;\;\; \boldsymbol{F}^e = \frac{\partial\boldsymbol{\varphi}^e(\boldsymbol{X}_{\boldsymbol{\sigma'}=\boldsymbol{0}},t)}{\partial\boldsymbol{X}_{\boldsymbol{\sigma'}=\boldsymbol{0}}}\;, \tag{8.15}$$

where $\boldsymbol{\varphi}_\theta(\mathcal{B})$ is the intermediate thermal effective-stress-free configuration caused by thermal expansion or contraction. Similarly, $\boldsymbol{\varphi}^p(\boldsymbol{\varphi}_\theta(\mathcal{B}))$ is the intermediate effective-stress-free configuration, which can be obtained by deforming the current configuration via $\boldsymbol{\varphi}^{e-1}$. Notice that we do not consider the possibility of having the pore pressure split for the deformation gradient of the solid skeleton. In addition, we assume that the thermal expansion is isotropic. To replicate the thermal effect accurately, anisotropy of thermal effect must be considered for composite or reinforced materials. Nevertheless, anisotropy of thermal conductivity is often neglected in the literature, partly due to the lack of data to characterize detailed tensorial thermal conductivity in field and experimental settings. As a result, $\boldsymbol{F}_\theta$ can be characterized by the thermal expansion coefficient $\alpha_{\mathrm{sk}}(\theta)$, i.e.,

$$\boldsymbol{F}_\theta = \exp[\int_{\hat{\theta}}^{\theta}\alpha_{\mathrm{sk}}(\hat{\theta})d\hat{\theta}]\boldsymbol{I}\;. \tag{8.16}$$

If the thermal expansion coefficient is constant, then we have,

$$\boldsymbol{F}_\theta = \exp[\alpha_{\mathrm{sk}}(\theta-\theta_o)]\boldsymbol{I} \;\;;\;\; J_\theta = \exp[3\alpha_{\mathrm{sk}}(\theta-\theta_o)], \tag{8.17}$$

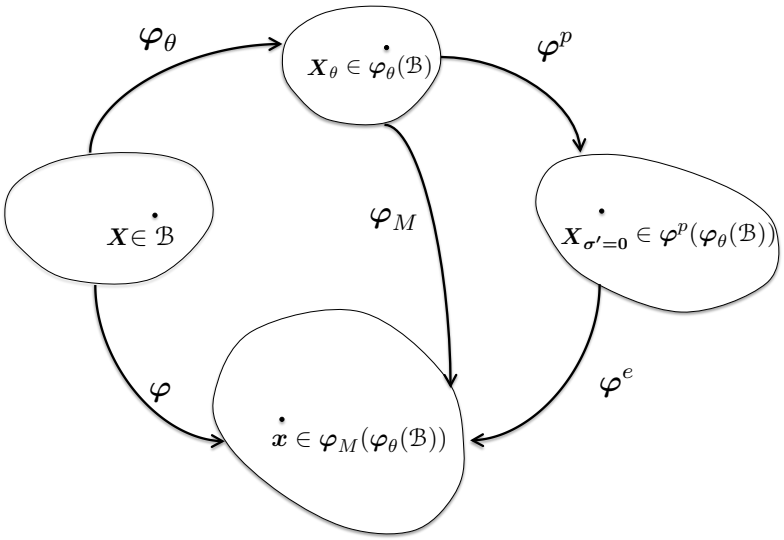

Figure 8.2: *Multiplicative decomposition of the thermohydromechanics deformation.*

where θ_o is the reference temperature at which there is no thermal-induced deformation. Notice that linearizing the thermal expansion defined in (8.17) leads to the classical thermal strain $\epsilon_v = \log J_\theta = 3\alpha_{\text{sk}}(\theta - \theta_o)$. Recall that the configuration $\boldsymbol{\varphi}_\theta(\mathcal{B})$ is stress free, and the thermal-induced deformation gradient is isotropic, thus, $\boldsymbol{F} = \boldsymbol{F}_\theta \boldsymbol{F}_M = \boldsymbol{F}_M \boldsymbol{F}_\theta$. As a result, Equation (8.13) can be rewritten as,

$$\boldsymbol{P}(\boldsymbol{F}_M, \boldsymbol{z}, p^f) = \boldsymbol{P'}(\boldsymbol{F}_M, \boldsymbol{z}) - JBp^f \boldsymbol{F}^{-T}, \tag{8.18}$$

in which the thermal expansion alone does not induce any change in the effective stress of the solid skeleton.

8.1.3 Balance of Fluid Content

The three-dimensional balance of fluid content equation for fully saturated porous media was first derived by Biot [1941a]. Rice and Cleary [1976b] extended this study by taking account of the compressiblity of fluid and solid constituents and provided analytical solution for pressuized cylindrical and spherical cavity under the isothermal condition. This version of balance of fluid content was then further generalized by McTigue [1986] which takes account of the thermal coupling effect of fluid-saturated porous media in the geometrical linear regime. In this study, our new contribution is to provide the derivations for the balance of fluid mass in the geometrical nonlinear regime. In particular, we adopt the notations of Eulerian and Lagrangian porosities introduced by Coussy [2004a]. Using this as a starting point, we derive the balance of fluid content equation of the non-isothermal porous media in reference configuration.

Let us first define the Lagrangian fluid content $M^{\text{f}} : \mathcal{B} \times [0, T] \to \mathbb{R}^+$ as the fluid mass per unit reference volume. The fluid content is therefore a function of the porosity and the fluid density, i.e.,

$$M^{\text{f}} = J\rho^{\text{f}} = J\phi^{\text{f}}\rho_{\text{f}} = \Phi^{\text{f}}\rho_{\text{f}}, \tag{8.19}$$

where $\Phi^{\text{f}}(\boldsymbol{X}, t) = J(\boldsymbol{X}, t)\phi^{\text{f}}(\boldsymbol{\varphi}(\boldsymbol{X}, t), t)$ is the Lagrangian porosity, the ratio between current void volume to the initial total volume (cf. [Coussy, 2004a], p.5). In the current configuration, the balance of fluid mass content reads, i.e.,

$$\frac{D}{Dt}\int_{\boldsymbol{\varphi}(\mathcal{B})} \phi^{\text{f}}\rho_{\text{f}} dv = -\int_{\partial\boldsymbol{\varphi}(\mathcal{B})} \boldsymbol{w}\cdot\boldsymbol{n}\, da. \tag{8.20}$$

Applying Reynold's transport theorem and Gauss theorem, we obtain the corresponding local fluid content continuity equation in the current configuration,

$$\frac{DJ\phi^{\text{f}}\rho_{\text{f}}}{Dt} + J\,\nabla^{\boldsymbol{x}}\cdot\boldsymbol{w} = 0\,, \tag{8.21}$$

where $D\phi^{\text{f}}\rho_f/Dt$ is the material time derivative of the current fluid density that reads,

$$\frac{DJ\phi^{\text{f}}\rho_f}{Dt} = \frac{\partial J\phi^{\text{f}}\rho_{\text{f}}}{\partial t} + \phi^{\text{f}}\rho_{\text{f}}\dot{J}\,, \tag{8.22}$$

where $\dot{(\cdot)} = D(\cdot)/Dt$. In (8.20) and (8.21), $\boldsymbol{w}$ is the relative pore-fluid mass flux in the deforming solid skeleton body. Assuming that the pore-fluid flow is Darcian, then the relative pore-fluid mass flux is related to both the gradient of the pore pressure and the temperature under non-isothermal condition, i.e.,

$$\boldsymbol{w} = \rho_{\mathrm{f}} \boldsymbol{k} \cdot \left[-\nabla^{\boldsymbol{x}} p^{\mathrm{f}} + \rho_{\mathrm{f}} \boldsymbol{G} \right] - \rho_{\mathrm{f}} s_T \nabla^{\boldsymbol{x}} \theta, \tag{8.23}$$

where $\boldsymbol{k}$ is the permeability tensor divided by the viscosity; S_T is the Soret coefficient. In particular, the latter term $s_T \nabla^{\boldsymbol{x}} \theta$ represents a phenomenon analogous to the Ludwig-Soret effect (the flux induced by the gradient of temperature) [Bear, 1972, McTigue, 1986, Postelnicu, 2004].

The balance of mass content in the Lagrangian configuration can be obtained from (8.21) via Piola transformation, i.e.,

$$\frac{DM^{\mathrm{f}}}{Dt} = -\nabla^{\boldsymbol{X}} \cdot \boldsymbol{W}. \tag{8.24}$$

The Lagrangian relative mass flux $\boldsymbol{W}$ can be obtained via the Piola identity, i.e.

$$\boldsymbol{W} = J \boldsymbol{F}^{-1} \cdot \boldsymbol{w}. \tag{8.25}$$

Furthermore, let us assume that the inertial force is negligible, $\boldsymbol{a}^f = \boldsymbol{0}$. After a pull-back operation, the Lagrangian mass flux reads,

$$\boldsymbol{W} = \rho_{\mathrm{f}} \boldsymbol{Q}_{\mathrm{f}} = \rho_{\mathrm{f}} \boldsymbol{K} \cdot (-\nabla^{\boldsymbol{X}} p^{\mathrm{f}} + \rho_{\mathrm{f}} \boldsymbol{F}^{\mathrm{T}} \cdot \boldsymbol{G}) - \rho_{\mathrm{f}} \boldsymbol{S}_T \nabla^{\boldsymbol{X}} \theta \ , \tag{8.26}$$

where both the permeability tensor and Soret coefficient tensor are both positive semi-definite, i.e.,

$$\boldsymbol{K} = J \boldsymbol{F}^{-1} \cdot \boldsymbol{k} \cdot \boldsymbol{F}^{\text{-T}} \ ; \ \boldsymbol{S}_T = J s_T \boldsymbol{C}^{-1} \ , \tag{8.27}$$

where $\boldsymbol{C} = \boldsymbol{F}^{\mathrm{T}} \cdot \boldsymbol{F}$ is the right Cauchy-Green tensor. Next, we consider the local rate of change of the fluid content M^{f} in the left hand side of (8.24). The material time derivative of the fluid mass content can be partitioned by applying the chain rule on (8.19),

$$\dot{M}^{\mathrm{f}} = \Phi^{\mathrm{f}} \dot{\rho}_{\mathrm{f}} + \rho_{\mathrm{f}} \dot{\Phi}^{\mathrm{f}}. \tag{8.28}$$

To complete the formulation, we need to re-express (8.28) in terms of the two fields $\boldsymbol{\varphi}$ and p^{f}. As a result, we assume that the pore fluid density only depends on temperature θ and pore pressure p^{f}. Hence, we have

$$\dot{\rho}_{\mathrm{f}}(\theta, p^{\mathrm{f}}) = \left.\frac{\partial \rho_{\mathrm{f}}}{\partial p^{\mathrm{f}}}\right|_{\theta} \dot{p^{\mathrm{f}}} + \left.\frac{\partial \rho_{\mathrm{f}}}{\partial \theta}\right|_{p^{\mathrm{f}}} \dot{\theta}. \tag{8.29}$$

In the above expression, $\partial \rho^{\mathrm{f}} / \partial p^{\mathrm{f}}|_{\theta}$ represents the change of the density due to pore pressure rise/drop at a fixed temperature, while $\partial \rho^{\mathrm{f}} / \partial \theta|_{p^{\mathrm{f}}}$ represents the change of density due to a temperature rise/drop at a fixed pore pressure. Assuming that the bulk modulus K_{f} and thermal expansion coefficient α_{f} of the pore fluid remains constant, we have,

$$\rho_{\mathrm{f}}(\theta, p^{\mathrm{f}}) = \rho_{\mathrm{fo}} \exp\left(\frac{p^{\mathrm{f}} - p^{\mathrm{f}}_o}{K_{\mathrm{f}}} - 3\alpha_{\mathrm{f}}(\theta - \theta_o) \right). \tag{8.30}$$

Hence, $\partial \rho^{\mathrm{f}} / \partial p^{\mathrm{f}}|_{\theta}$ and $\partial \rho^{\mathrm{f}} / \partial \theta|^{\mathrm{f}}_{p}$ can be written as,

$$\left.\frac{\partial \rho_{\mathrm{f}}}{\partial p^{\mathrm{f}}}\right|_{\theta} = \frac{\rho_{\mathrm{f}}}{K_{\mathrm{f}}} \ ; \ \left.\frac{\partial \rho_{\mathrm{f}}}{\partial \theta}\right|_{p^{\mathrm{f}}} = -3\rho_{\mathrm{f}}\alpha_{\mathrm{f}}. \tag{8.31}$$

Meanwhile, the constitutive relation of the Lagrangian porosity Φ^{f} is a function of $\boldsymbol{\varphi}$, p^{f} and θ. For example, one may generalize Athy's exponential porosity-pressure relation [Athy, 1930] and express the Lagrangian porosity as shown in (8.32).

$$\Phi^{\mathrm{f}} = \Phi^{\mathrm{f}}_o \exp\left(B \log J + \frac{B - \Phi^{\mathrm{f}}}{K_{\mathrm{s}}} (p^{\mathrm{f}} - p^{\mathrm{f}}_o) - 3(J - \Phi^{\mathrm{f}})\alpha_{\mathrm{s}}(\theta - \theta_o) \right), \tag{8.32}$$

where $\log J = \log(\det \boldsymbol{F}) = \operatorname{tr} \boldsymbol{\epsilon}$ and $\boldsymbol{\epsilon}$ is the Eulerian logarithm strain tensor and α_{s} is the thermal expansion coefficient of the solid constituent. This version of porosity constitutive law features a multiplicative decomposition which reads,

$$\Phi^{\mathrm{f}} = J^{\boldsymbol{\varphi}} J^{p^{\mathrm{f}}} J^{\theta} \Phi^{\mathrm{f}}_o \,, \tag{8.33}$$

where,

$$J^{\boldsymbol{\varphi}} = \exp(B \log J) \;\; ; \;\; J^{p^{\mathrm{f}}} = \exp(\frac{B - \Phi^{\mathrm{f}}}{K_{\mathrm{s}}}(p^{\mathrm{f}} - p^{\mathrm{f}}_o)) \;\; ; \;\; J^{\theta} = \exp(-3(J - \Phi^{\mathrm{f}})\alpha_{\mathrm{s}}(\theta - \theta_o)). \tag{8.34}$$

The advantage of a constitutive law like (8.32) is that it will not predict an unphysical negative porosity even under extreme loading conditions. However, as argued by Armero in [Armero, 1999] and subsequently in [Callari and Armero, 2004, Karrech et al., 2012], it is more consistent with the nature of the fluid content, a scalar field, to be modeled by additive decompositions in both infinitesimal [Coussy, 2004a] and finite deformation regimes [Armero, 1999, Callari and Armero, 2004]. Since for porous media with incompressible fluid constituents, $\dot{M}^{\mathrm{f}} = \rho_{\mathrm{f}} \dot{\Phi}^{f}$, an additive decomposition of fluid content implies that the Lagrangian porosity should also be defined in an additive decomposition. As a result, we employ a linear approximation of (8.32), i.e.,

$$\Phi^{\mathrm{f}} - \Phi^{\mathrm{f}}_o \approx \log J^{\boldsymbol{\varphi}} + \log J^{p^{\mathrm{f}}} + \log J^{\theta} = B \log J + \frac{B - \Phi^{\mathrm{f}}}{K_{\mathrm{s}}}(p^{\mathrm{f}} - p^{\mathrm{f}}_o) - 3(J - \Phi^{\mathrm{f}})\alpha_s(\theta - \theta_o). \tag{8.35}$$

Equation (8.35) is identical to the Lagrangian porosity defined in [Coussy, 2004a, 2007] if the thermal coefficient term in [Coussy, 2004a, 2007] $\alpha_\phi = \Phi^s \alpha_{\mathrm{s}} = (J - \Phi^f)\alpha_{\mathrm{s}}$. Taking the material time derivative of (8.35), the material time derivative of Lagrangian porosity now reads,

$$\dot{\Phi}^{\mathrm{f}} = \frac{\partial \Phi^{\mathrm{f}}}{\partial J}\Big|_{(p^{\mathrm{f}},\theta)} \dot{J} + \frac{\partial \Phi^{\mathrm{f}}}{\partial p^{\mathrm{f}}}\Big|_{(\boldsymbol{\varphi},\theta)} \dot{p^{\mathrm{f}}} + \frac{\partial \Phi^{\mathrm{f}}}{\partial \theta}\Big|_{(\boldsymbol{\varphi},p^{\mathrm{f}})} \dot{\theta}. \tag{8.36}$$

Assuming that B and K_{s} remain constant and taking the material time derivative of (8.35) leads to,

$$\left(1 + \frac{p^{\mathrm{f}} - p^{\mathrm{f}}_o}{K_{\mathrm{s}}} - 3\alpha_s(\theta - \theta_o)\right) \dot{\Phi}^{\mathrm{f}} = \frac{B}{J}\dot{J} - 3\alpha_{\mathrm{s}}(\theta - \theta_o)\dot{J} + \frac{B - \Phi^{\mathrm{f}}}{K_{\mathrm{s}}}\dot{p^{\mathrm{f}}} - 3(J - \Phi^{\mathrm{f}})\alpha_{\mathrm{s}}\dot{\theta}. \tag{8.37}$$

For simplicity, let $|p^{\mathrm{f}}| << K_s$ and $|\alpha_{\mathrm{s}}(\theta - \theta_o)| << 1$. Substituting (8.29), (8.31) and (8.37) into (8.28) and working through algebra, we obtain the expression of the material time derivative of the fluid content $\dot{M}^{\mathrm{f}}$ which reads,

$$\dot{M}^{\mathrm{f}} = \rho_{\mathrm{f}} \left((\frac{B}{J} - 3\alpha_{\mathrm{s}}(\theta - \theta_o))\dot{J} + \frac{1}{M}\dot{p^{\mathrm{f}}} - 3\alpha^{\mathrm{m}}\dot{\theta} \right), \tag{8.38}$$

where M is the Biot's modulus as defined in [Nur and Byerlee, 1971a, Coussy, 2004a]. α^{m} is the thermal expansion coefficient of the mixture. In infinitesimal range where $\Phi^{\mathrm{f}} \approx \phi^{\mathrm{f}}$, this definition is identical to the thermal expansion coefficient in [Preisig and Prévost, 2011], i.e.,

$$M = \frac{K_{\mathrm{s}} K_{\mathrm{f}}}{K_f(B - \Phi^{\mathrm{f}}) + K_{\mathrm{s}}\Phi^{\mathrm{f}}} \;\; ; \;\; \alpha^{\mathrm{m}} = \Phi^{\mathrm{s}}\alpha_{\mathrm{s}} + \Phi^{\mathrm{f}}\alpha_{\mathrm{f}} = (J - \Phi^{\mathrm{f}})\alpha_{\mathrm{s}} + \Phi^{\mathrm{f}}\alpha_{\mathrm{f}}. \tag{8.39}$$

Combining (8.26) and (8.38), we obtain the strong form of the balance of fluid content equation,

$$\Big(\frac{B}{J} - 3\alpha_{\mathrm{s}}(\theta - \theta_o)\Big)\dot{J} + \frac{1}{M}\dot{p^{\mathrm{f}}} - 3\alpha^{\mathrm{m}}\dot{\theta} + \frac{1}{\rho_{\mathrm{f}}}\nabla^{\boldsymbol{X}} \cdot \boldsymbol{W} = 0. \tag{8.40}$$

Notice that if both constituents are incompressible, then $B = 1$, $1/M = 0$ and $\nabla^{\boldsymbol{x}} \rho_{\mathrm{f}} = 0$. Applying the Piola transform and assuming isothermal condition, (8.40) reduces to the form identical to that seen in [Borja and Alarcón, 1995a],

$$\nabla^{\boldsymbol{x}} \cdot \boldsymbol{v} + \nabla^{\boldsymbol{x}} \cdot \boldsymbol{q} = 0, \tag{8.41}$$

where $\boldsymbol{q} = (1/\rho_f)\boldsymbol{w}$. In summary, the balance law expressed in (8.40) captures the influence of the skeleton deformation and heat transfer on fluid transport in the following ways:

1. compression or expansion of fluid induced by solid skeleton deformation.
2. shrinkage or expansion of the pore space that leads to the change of the change of specific storage.
3. expansion or shrinkage of solid and fluid constituents due to temperature changes.
4. the Soret effect, i.e., the thermo-induced diffusion of pore fluid.
5. the geometrical nonlinear effect due to the deformation of solid skeleton.

One important observation of the derivation shown in (8.32)-(8.40) is that both the balance of energy and the balance of fluid content equations depend strongly on the porosity evolution law in the geometrically nonlinear regime.

8.1.4 Balance of Energy

In the vast body of literature on thermo-hydro-mechanics, the balance of energy for thermohydromechanics problems differs significantly due to the variety of underlying assumptions. For the sake of simplification, some THM models assume that both the skeleton deformation and pore-flow diffusion processes impose negligible influences on the heat transfer process and thus lead to a decoupled heat transfer equation in the infinitesimal regime [McTigue, 1986, Nguyen and Selvadurai, 1995, Selvadurai and Nguyen, 1997, Selvadurai and Suvorov, 2012], i.e.,

$$\nabla^{\boldsymbol{x}}\cdot k_\theta\,\nabla^{\boldsymbol{x}}\,\theta = \rho C_p\dot{\theta}, \tag{8.42}$$

where k_θ and C_p are the volume averaged thermal conductivity and heat capacity of the fluid-solid mixture. Similar assumptions are made in several other small strain thermohydromechanics codes reported in international co-operative research project DECOVALEX [Jing et al., 1995] and in the open source simulation code OpenGeoSys [Kolditz et al., 2012].

Our objective here is to provide a more complete energy balance law to bring new sights on the thermo-hydro-mechanical responses of porous media. In particular, we consider the contribution of the mechanical work done by the solid skeleton and pore-fluid, the density variation and size changes of pore space due to thermal-hydro-mechanical coupling and the geometrical nonlinear effect in finite strain regime. To simplify the derivation, we consider that all phases of the saturated porous media are locally in thermal equilibrium and hence the temperature of both solid and fluid constituents are identical locally (in a homogenized sense of each elementary representative volume), i.e. $\theta_s = \theta_f = \theta$. Except the additional advection term, the local balance of energy is in analogous to that of the single-phase thermo-plasticity materials [Simo and Miehe, 1992],

$$c_{\boldsymbol{F}}\dot{\theta} = [D_{\text{mech}} - H_\theta] + [-J\,\nabla^{\boldsymbol{x}}\cdot q_\theta + \frac{\phi^{\text{f}} c_{\boldsymbol{F}\text{f}}}{\rho_{\text{f}}} J\boldsymbol{w}\cdot\nabla^{\boldsymbol{x}}\,\theta + R_\theta], \tag{8.43}$$

where $c_{\boldsymbol{F}}$ is the specific heat capacity per unit volume of the porous media **at constant deformation** [Holzapfel, 2000]. For the fully saturated, two-phase porous media, the specific heat capacity of the solid-fluid mixture can be obtained by volume averaging the specific heat capacities of the solid and fluid constituents, i.e.,

$$c_{\boldsymbol{F}} = (J-\Phi^{\text{s}})c_{\boldsymbol{F}\text{s}} + \Phi^{\text{f}} c_{\boldsymbol{F}\text{f}} = (J-\Phi^{\text{s}})\rho_{\text{f}o} c_{\text{s}} + \Phi^{\text{f}}\rho_{so} c_{\text{f}}\ , \tag{8.44}$$

where ρ_{fp} and ρ_{so} are the initial densities, and c_{f} and c_{s} are the specific heat capacities (per unit mass) of the fluid and solid constituents. D_{mech} denotes the contribution to the dissipation due to pure mechanical load. On the other hand, H_θ is the non-dissipative (latent) structural heating or cooling [Holzapfel, 2000]. At the adiabatic limit without heat source, the last three terms in (8.43) can be neglected. By contrary, for many petroleum and geotechnical engineering applications, the life-cycle of the thermo-hydro-mechanical system is in the order of years. For those applications, it is common to neglect the contribution from the structural heating and dissipation as shown in [McTigue, 1986, Lewis et al., 1986, Nguyen and Selvadurai, 1995, Selvadurai and Suvorov, 2012, Li et al., 2005, Simoni et al., 2008, Rutqvist, 2011, Kolditz et al., 2012].

Here we assume that the structural heating is thermoelastic. This leads to the classical Gough-Joule coupling effect in which local temperature changes may occur when a porous medium undergoes adiabatic deformation. R_θ is the heat source term. $-J\,\nabla^{\boldsymbol{x}}\cdot(q_\theta/J)$ is the heat conduction term. Pulling back (8.43) into the reference configuration via the Piola transformation yields,

$$c_{\boldsymbol{F}}\dot{\theta} = [D_{\text{mech}} - H_\theta] + [-\nabla^{\boldsymbol{X}}\cdot\boldsymbol{Q}_\theta + \frac{\Phi^{\text{f}} c_{\boldsymbol{F}\text{f}}}{\rho_{\text{f}}}\boldsymbol{W}\cdot\boldsymbol{F}^{-T}\nabla^{\boldsymbol{X}}\,\theta + R_\theta], \tag{8.45}$$

where Q_θ is the Piola-Kirchhoff heat flux. Assuming that both the solid and fluid constituents obey Fourier's law, the Cauchy heat flux is often written as the dot product of the volume averaged heat conductivity tensor and the gradient of temperature [Prevost, 1982], i.e.,

$$q_\theta = \phi^{\mathrm{f}} \boldsymbol{k}_\theta^{\mathrm{f}} \nabla^{\boldsymbol{x}} \theta + (1-\phi^{\mathrm{f}}) \boldsymbol{k}_\theta^{\mathrm{s}} \nabla^{\boldsymbol{x}} \theta = \boldsymbol{k}_\theta \nabla^{\boldsymbol{x}} \theta, \tag{8.46}$$

where $\boldsymbol{k}_\theta = \phi^{\mathrm{f}} \boldsymbol{k}_\theta^{\mathrm{f}} + (1-\phi^{\mathrm{f}}) \boldsymbol{k}_\theta^{\mathrm{s}}$ is the volume averaged heat conductivity tensor. However, this volume averaged approach is only valid if the solid and fluid constituents are connected in parallel. Presumably, calculating the correct homogenized effective heat conductivity requires knowledge of the pore geometry and connectivity, which can be obtained from three dimensional tomographic images [Sun et al., 2011b,d] or directly from experiments. However, since micro-structural attributes of pore space is not always available, we adopt an alternative homogenization approach where equivalent inclusion method is used to determine effective heat conductivity tensor of the two-phase materials [Hiroshi and Minoru, 1986]. Assuming that the pore fluid as the bulk material and the solid grains as spherical inclusions, the effective thermal conductivity may be estimated via Eshelby equivalent inclusion method reads,

$$\boldsymbol{k}_\theta = \left(k_\theta^f + \frac{(1-\phi^{\mathrm{f}})(k_\theta^{\mathrm{s}} - k_\theta^{\mathrm{f}}) k_\theta^{\mathrm{f}}}{(k_\theta^{\mathrm{s}} - k_\theta^{\mathrm{f}})\phi^{\mathrm{f}} + k_\theta^{\mathrm{f}}} \right) \boldsymbol{I} = \left(k_\theta^f + \frac{(J-\Phi^{\mathrm{f}})(k_\theta^{\mathrm{s}} - k_\theta^{\mathrm{f}}) k_\theta^{\mathrm{f}}}{(k_\theta^{\mathrm{s}} - k_\theta^{\mathrm{f}})\Phi^{\mathrm{f}} + J k_\theta^{\mathrm{f}}} \right) \boldsymbol{I}, \tag{8.47}$$

where k_θ^{s} and k_θ^{f} are the isotropic thermal conductivity coefficient of the solid and the fluid consitituents. Applying the Piola transformation and using the relations $\Phi^{\mathrm{s}} + \Phi^{\mathrm{f}} = J$ and $\phi^{\mathrm{s}} + \phi^{\mathrm{f}} = 1$, (8.46) can be rewritten in reference configuration, i.e.,

$$J^{-1} \boldsymbol{F} Q_\theta = -\boldsymbol{k}_\theta \boldsymbol{F}^{-T} \nabla^{\boldsymbol{X}} \theta \, . \tag{8.48}$$

Hence, the Piola-Kirchhoff heat flux Q_θ corresponding to (8.46) reads,

$$Q_\theta = -K_\theta \nabla^{\boldsymbol{X}} \theta \, , \tag{8.49}$$

where K_θ is the pull-back thermal conductivity tensor, i.e.,

$$\boldsymbol{K}_\theta = J \boldsymbol{F}^{-1} \cdot \boldsymbol{k}_{\boldsymbol{\theta}} \cdot \boldsymbol{F}^{-T} \, . \tag{8.50}$$

Simplified Heat Transfer Equation in Geometrically Nonlinear Regime

If both the mechanical dissipation and the Gough-Joule coupling effect are neglected, then we recover the finite deformation version of the heat transfer equation in [Lewis et al., 1986, Kolditz et al., 2012, Nguyen and Selvadurai, 1995, Selvadurai and Nguyen, 1997, Selvadurai and Suvorov, 2012], which reads,

$$c_{\boldsymbol{F}} \dot{\theta} - \nabla^{\boldsymbol{X}} \cdot \boldsymbol{K}_\theta \nabla^{\boldsymbol{X}} \theta + \frac{\Phi^{\mathrm{f}} c_{\boldsymbol{F}^{\mathrm{f}}}}{\rho_{\mathrm{f}}} \boldsymbol{W} \cdot \boldsymbol{F}^{-T} \cdot \nabla^{\boldsymbol{X}} \theta - R_\theta = 0; \, . \tag{8.51}$$

Notice that the thermal diffusion process is fully coupled with the skeleton deformation in the geometrical non-linear regime, even if the mechanical dissipation and Gough-Joule coupling effect are both neglected. This coupling effect is captured by the porosity changes and volumetric deformation that lead to changes in the effective specific heat $C_{\boldsymbol{F}}$, the pull-back conductivity tensor and the convection term. If the both structural heat and dissipation mechanisms exhibit little influence on the thermal diffusion process of the porous medium, the (8.51) is sufficient. However, for more general cases, particularly biological tissues or other rubber-like materials, both the structural heat and dissipation mechanism must be taken into account properly.

Structural Heating and the Gough-Joule Coupling Effect

Giving the fact that the actual expressions of both structural heating and dissipation vary significantly for different material models, we consider Equation (8.45) a general statement for the energy conservation law. However, we may introduce additional assumptions to express the balance of energy in a more explicit form. For instance, we may assume that the structural heating contains no latent plastic terms and this is identical with the thermoelastic heating Simo and Miehe [1992]. To further particularize the problem, assume that the non-dissipative (latent) structural heating or cooling H_θ are the sum of the power contributed by the solid skeleton and the pore fluid, i.e.,

$$H_\theta = H_\theta^{\mathrm{s}} + H_\theta^{\mathrm{f}}, \tag{8.52}$$

where power contributed by the volumetric deformation of the solid skeleton reads [Simo and Miehe, 1992],

$$H_\theta^{\mathrm{s}} = -\theta \frac{\partial}{\partial \theta} \boldsymbol{P'} : \dot{\boldsymbol{F}} = -\theta \frac{\partial^2}{\partial J \partial \theta} 3\alpha_{\mathrm{sk}} K \log J (\theta - \theta_o) \dot{J} = -3K\alpha_{sk}\theta \frac{\dot{J}}{J}. \tag{8.53}$$

Following the derivation in Coussy [2004a], the pore-fluid contribution reads,

$$H_\theta^{\mathrm{f}} = -\theta \frac{\partial}{\partial \theta} 3\alpha^{\mathrm{m}} (\theta - \theta_o) \dot{p^{\mathrm{f}}} = -3\alpha^{\mathrm{m}} \theta \dot{p^{\mathrm{f}}}. \tag{8.54}$$

Substituting (8.53) and (8.54) into (8.45) and neglect the mechanical dissipation, we obtain the energy balance equation that takes account of the Gough-Joule coupling effect,

$$c_{\boldsymbol{F}} \dot{\theta} - 3K\alpha_{sk}\theta \frac{\dot{J}}{J} - 3\alpha^{\mathrm{m}} \theta \dot{p^{\mathrm{f}}} - \nabla^{\boldsymbol{X}} \cdot \boldsymbol{K}_\theta \nabla^{\boldsymbol{X}} \theta + \frac{\Phi^{\mathrm{f}} c_{\boldsymbol{F}^{\mathrm{f}}}}{\rho_{\mathrm{f}}} \boldsymbol{W} \cdot \boldsymbol{F}^{-T} \cdot \nabla^{\boldsymbol{X}} \theta - R_\theta = 0. \tag{8.55}$$

8.2 Stabilized Variational Formulation

In this section, we consider the stabilized variational form for the equal-order displacement-pressure-temperature finite element model, with assumed deformation gradient that prevents volumetric locking. We first define the standard weak form of the poromechanics problem based on the balance law derived in Section 2. By applying a multiplicative split, we introduce the assumed deformation gradient for the thermo-hydro-mechanics problem. To prevent spurious modes due to the usage of equal-order interpolations, we introduce a stabilization mechanism into the weighted-residual statement of the mass and energy balance equations. A simple scheme for choosing the stabilization parameters is also presented.

8.2.1 Galerkin Form

Our objective is to derive a weighted-residual statement suitable for a total Lagrangian scheme. We first specify the appropriate boundary and initial conditions. Following the standard line, we consider a domain $\mathcal{B}$ whose boundary $\partial\mathcal{B}$ is the direct sum of the Dirichlet and von Neumann boundaries, i.e.,

$$\partial\mathcal{B} = \overline{\partial\mathcal{B}_{\boldsymbol{u}} \cup \partial\mathcal{B}_{\boldsymbol{t}}} = \overline{\partial\mathcal{B}_{p^{\mathrm{f}}} \cup \partial\mathcal{B}_{\boldsymbol{Q}_{\mathrm{f}}}} = \overline{\partial\mathcal{B}_\theta \cup \partial\mathcal{B}_{\boldsymbol{Q}_\theta}}, \tag{8.56}$$

$$\emptyset = \partial\mathcal{B}_{\boldsymbol{u}} \cap \partial\mathcal{B}_{\boldsymbol{t}} = \partial\mathcal{B}_{p^{\mathrm{f}}} \cap \partial\mathcal{B}_{\boldsymbol{Q}_{\mathrm{f}}} = \partial\mathcal{B}_\theta \cap \partial\mathcal{B}_{\boldsymbol{Q}_\theta}, \tag{8.57}$$

where $\partial\mathcal{B}_{\boldsymbol{u}}$ is the solid displacement boundary; $\partial\mathcal{B}_{\boldsymbol{t}}$ is the solid traction boundary; $\partial\mathcal{B}_p$ is the pore pressure boundary; $\partial\mathcal{B}_{\boldsymbol{Q}_{\mathrm{f}}}$ is the pore-fluid flux; $\partial\mathcal{B}_\theta$ is the temperature boundary; $\partial\mathcal{B}_{\boldsymbol{Q}_{\mathrm{f}}}$ is the heat flux; boundary, as illustrated in Figure 8.3.

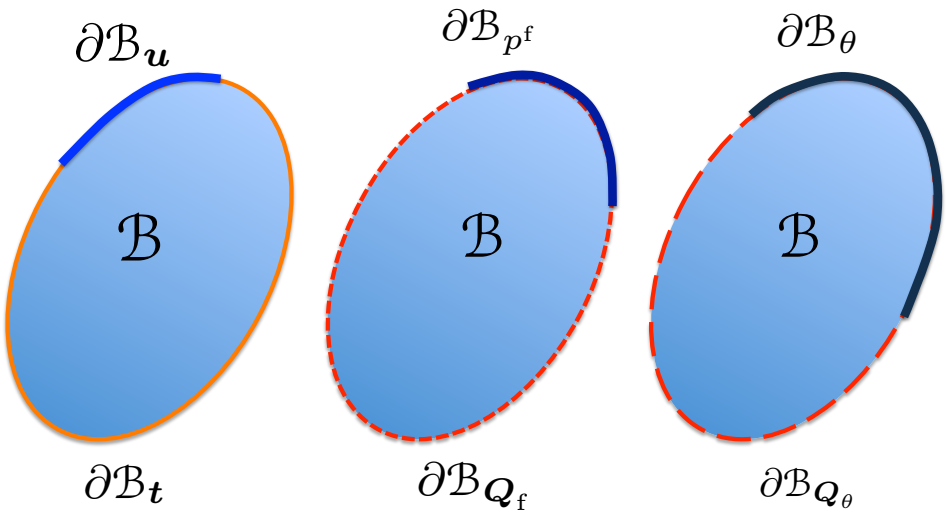

Figure 8.3: *Domain and the corresponding boundaries of the thermo-hydro-mechanics problem. Figure reproduced from [Liu et al., 2009].*

In summary, Dirichlet boundary conditions for the thermo-hydro-mechanics problem read,

$$\begin{aligned} \boldsymbol{u} &= \overline{\boldsymbol{u}} \text{ on } \partial\mathcal{B}_{\boldsymbol{u}}, \\ p^{\mathrm{f}} &= \overline{p} \text{ on } \partial\mathcal{B}_{p}, \\ \theta &= \overline{\theta} \text{ on } \partial\mathcal{B}_{\theta}. \end{aligned} \tag{8.58}$$

Meanwhile, the von Neumann boundary conditions that describe the traction and fluxes read,

$$\begin{aligned} \boldsymbol{N}\cdot\boldsymbol{P} &= \bar{\boldsymbol{t}} \text{ on } \partial\mathcal{B}_{\boldsymbol{t}}, \\ -\boldsymbol{N}\cdot\boldsymbol{Q}_{\mathrm{f}} &= \overline{Q}_{\mathrm{f}} \text{ on } \partial\mathcal{B}_{\boldsymbol{Q}_{\mathrm{f}}}, \\ -\boldsymbol{N}\cdot\boldsymbol{Q}_{\theta} &= \overline{Q}_{\theta} \text{ on } \partial\mathcal{B}_{\boldsymbol{Q}_{\theta}}. \end{aligned} \tag{8.59}$$

In addition, the spaces for the trial displacement, pore pressure and temperature read,

$$\begin{aligned} \boldsymbol{V}_{\boldsymbol{u}} &= \{\boldsymbol{u} : \mathcal{B} \to \mathbb{R}^3 | \boldsymbol{u} \in [H^1(\mathcal{B})]^3, \boldsymbol{u}|_{\partial B_{\boldsymbol{u}}} = \overline{\boldsymbol{u}}\}, \\ V_p &= \{p^{\mathrm{f}} : \mathcal{B} \to \mathbb{R} | p^{\mathrm{f}} \in L^2(\mathcal{B}), p^{\mathrm{f}}|_{\partial B_{p^{\mathrm{f}}}} = \overline{p^{\mathrm{f}}}\}, \\ V_{\theta} &= \{\theta : \mathcal{B} \to \mathbb{R} | \theta \in L^2(\mathcal{B}), \theta|_{\partial B_{\theta}} = \overline{\theta}\}, \end{aligned} \tag{8.60}$$

where H^1 denotes the Sobolev space of degree one. The admissible variations of displacement $\boldsymbol{\eta}$, pore pressure ψ and temperature θ therefore read,

$$\begin{aligned} \boldsymbol{V}_{\boldsymbol{\eta}} &= \{\boldsymbol{\eta} : \mathcal{B} \to \mathbb{R}^3 | \boldsymbol{\eta} \in [H^1(\mathcal{B})]^3, \boldsymbol{\eta}|_{\partial B_{\boldsymbol{\eta}}} = \boldsymbol{0}\}, \\ V_{\psi} &= \{\psi : \mathcal{B} \to \mathbb{R} | \psi \in L^2(\mathcal{B}), \psi|_{\partial B_{p^{\mathrm{f}}}} = 0\}, \\ V_{\omega} &= \{\omega : \mathcal{B} \to \mathbb{R} | \psi \in L^2(\mathcal{B}), \omega|_{\partial B_{\theta}} = 0\}. \end{aligned} \tag{8.61}$$

For brevity, the spatial argument $\boldsymbol{X} \in \mathcal{B}$ is not explicitly written. The weighted-residual statement of the balance of linear momentum, fluid content and energy is as follows.

Find $\boldsymbol{u} \in \boldsymbol{V}_{\boldsymbol{u}}$, $p^{\mathrm{f}} \in V_{p^{\mathrm{f}}}$ and $\theta \in V_{\theta}$ such that for all $\boldsymbol{\eta} \in V_{\boldsymbol{\eta}}$ and $\psi \in V_{\psi}$ such that

$$G(\boldsymbol{u}, p^{\mathrm{f}}, \theta, \boldsymbol{\eta}) = H(\boldsymbol{u}, p^{\mathrm{f}}, \theta, \psi) = L(\boldsymbol{u}, p^{\mathrm{f}}, \theta, \omega) = 0, \tag{8.62}$$

where $G : \boldsymbol{V}_{\boldsymbol{u}} \times V_{p^{\mathrm{f}}} \times V_{\theta} \times V_{\eta} \to \mathbb{R}$ is the weak statement of the balance of linear momentum i.e.,

$$\begin{aligned} G(\boldsymbol{u}, p^{\mathrm{f}}, \theta, \boldsymbol{\eta}) &= \int_{\mathcal{B}} \nabla^{\boldsymbol{X}} \cdot \boldsymbol{\eta} : \boldsymbol{P} - J(\rho^{\mathrm{f}} + \rho^{s})\boldsymbol{\eta}\cdot\boldsymbol{g} \,\mathrm{dV} \\ &\quad - \int_{\partial\mathcal{B}_t} \boldsymbol{\eta}\cdot\bar{\boldsymbol{t}} \,\mathrm{d\Gamma}, \end{aligned} \tag{8.63}$$

$H : \boldsymbol{V}_{\boldsymbol{u}} \times V_{p^{\mathrm{f}}} \times V_{\theta} \times V_{\psi} \to \mathbb{R}$ is the weak statement of the balance of fluid content, i.e.,

$$\begin{aligned} H(\boldsymbol{u}, p^{\mathrm{f}}, \theta, \psi) &= \int_{\mathcal{B}} \psi\Big(\frac{B}{J} - 3\alpha_s(\theta - \theta_o)\Big)\dot{J} \,\mathrm{dV} \\ &\quad + \int_{\mathcal{B}} \psi\frac{1}{M}\dot{p^f} - 3\psi\alpha^{\mathrm{m}}\dot{\theta} \,\mathrm{dV} \\ &\quad - \int_{\mathcal{B}} \nabla^{\boldsymbol{X}}\,\psi\cdot\frac{1}{\rho_{\mathrm{f}}}\boldsymbol{W} \,\mathrm{dV} \\ &\quad - \int_{\partial B_Q} \psi\overline{Q}_{\mathrm{f}} \,\mathrm{d\Gamma}, \end{aligned} \tag{8.64}$$

and $L : \boldsymbol{V}_{\boldsymbol{u}} \times V_{p^{\mathrm{f}}} \times V_{\theta} \times V_{\omega} \to \mathbb{R}$ is the weak statement of the balance of energy, i.e.,

$$\begin{aligned} L(\boldsymbol{u}, p^{\mathrm{f}}, \theta, \omega) &= \int_{\mathcal{B}} \omega\big(c_{\boldsymbol{F}}\dot{\theta} - 3\alpha_{\mathrm{sk}}K\theta\frac{\dot{J}}{J} - 3\alpha^{\mathrm{m}}\theta\dot{p^{\mathrm{f}}}\big) \,\mathrm{dV} \\ &\quad + \int_{\mathcal{B}} \nabla^{\boldsymbol{X}}\,\omega\boldsymbol{K}_{\theta}\,\nabla^{\boldsymbol{X}}\,\dot{\theta} + \omega\frac{\Phi^f c_{\mathrm{f}}}{\rho_{\mathrm{f}}}\boldsymbol{W}\cdot\boldsymbol{F}^{-T}\cdot\nabla^{\boldsymbol{X}}\,\theta - \omega R_{\theta} \,\mathrm{dV} \\ &\quad - \int_{\partial B_Q} \omega\overline{Q}_{\theta} \,\mathrm{d\Gamma}. \end{aligned} \tag{8.65}$$

8.2.2 Temporal discretization

Due to the transient nature of the thermo-hydro-mechanics problem, the weak statement must be discretized in time. Typically, this temporal discretization is often conducted after the spatial discretization [Radovitzky and Ortiz, 1999]. Here we use a different approach in which temporal discretization will be considered before applying spatial discretization. This treatment is due to the usage of the template-based generic programming based package called Phalanx [Pawlowski et al., 2012a], which enables a component-based implementation and thus significantly simplify the programming efforts. This implementation method will be discussed in Section 8.3). As a result, we first derive an equivalent static problem [Radovitzky and Ortiz, 1999] by discretizing the temporal domain before introducing basis functions for the spatial discretization. Here we use finite difference approach in temporal domain such that the pore pressure and temperature at time step $n+1$ can be written as

$$p^{\mathrm{f}}_{n+1} \approx p^{\mathrm{f}}_{n} + (1-\hat{\beta})\Delta t\, \dot{p^{\mathrm{f}}}_{n} + \hat{\beta}\dot{p^{\mathrm{f}}}_{n+1}, \tag{8.66}$$

$$\theta_{n+1} \approx \theta_{n} + (1-\hat{\beta})\Delta t\, \dot{\theta}_{n} + \hat{\beta}\dot{\theta}_{n+1}. \tag{8.67}$$

To simplify the formulation, we use the unconditionally stable fully backward Euler scheme by setting $\hat{\beta}=1$. However, directly applying Euler scheme to discretize the Jacobian J in time will lead to erroneous results that make negative Jacobian possible. As a result, we take advantage of the following identity obtained via the chain rule,

$$\frac{D(\log J)}{Dt} = \frac{D\log J}{DJ}\frac{DJ}{Dt} = \frac{\dot{J}}{J}\,, \tag{8.68}$$

where $J \in \mathbb{R}^{+}$, $\log J \in \mathbb{R}$. Hence, we may obtain the material derivative of the Jacobian J by discretizing $\log J$ in time, i.e.,

$$J^{-1}_{n+1}\dot{J}_{n+1} = \frac{D}{Dt}(\log J_{n+1}) \approx \frac{\log J_{n+1} - \log J_{n}}{\Delta t}. \tag{8.69}$$

Substituting (8.66), (8.67) and (8.69) into weighted-residual form (8.62), the time discretized weighted residual form reads,

$$\hat{G}(\boldsymbol{u}_{n+1}, p^{\mathrm{f}}_{n+1}, \theta_{n+1}, \boldsymbol{\eta}) = \hat{H}(\boldsymbol{u}_{n+1}, p^{\mathrm{f}}_{n+1}, \theta_{n+1}, \psi) = \hat{L}(\boldsymbol{u}_{n+1}, p^{\mathrm{f}}_{n+1}, \theta_{n+1}, \omega) = 0, \tag{8.70}$$

where the discrete weak form of the balance of linear momentum now reads,

$$\begin{aligned}
\hat{G}(\boldsymbol{u}_{n+1}, p^{\mathrm{f}}_{n+1}, \theta_{n+1}, \boldsymbol{\eta}) \;=\; & \int_{\mathcal{B}} \nabla^{\boldsymbol{X}}\cdot\boldsymbol{\eta} : \boldsymbol{P_{n+1}}\, \mathrm{dV} \\
& - \int_{\mathcal{B}} J_{n+1}(\rho^{\mathrm{f}}_{n+1} + \rho^{\mathrm{s}}_{n+1})\boldsymbol{\eta}\cdot\boldsymbol{g}\, \mathrm{dV} \\
& - \int_{\partial\mathcal{B}_t} \boldsymbol{\eta}\cdot\bar{\boldsymbol{t}}_{\boldsymbol{n+1}}\, \mathrm{d\Gamma}.
\end{aligned} \tag{8.71}$$

Similarly, the discrete weak form of the balance of fluid content and balance of energy can be written as,

$$\begin{aligned}
\hat{H}(\boldsymbol{u}_{n+1}, p^{\mathrm{f}}_{n+1}, \theta_{n+1}, \psi) \;=\; & \int_{\mathcal{B}} \psi\Big(B - 3\alpha_s(\theta_{n+1}-\theta_o)J_{n+1}\Big)\frac{\log J_{n+1} - \log J_n}{\Delta t}\, \mathrm{dV} \\
& + \int_{\mathcal{B}} \psi\Big(\frac{1}{M_{n+1}}\frac{p^{\mathrm{f}}_{n+1} - p^{\mathrm{f}}_{n}}{\Delta t} - 3\alpha^{\mathrm{m}}_{n+1}\frac{\theta_{n+1}-\theta_n}{\Delta t}\Big)\, \mathrm{dV} \\
& - \int_{\mathcal{B}} \nabla^{\boldsymbol{X}}\psi\cdot\frac{1}{\rho_{\mathrm{f}n+1}}\boldsymbol{W_{n+1}}\, \mathrm{dV} - \int_{\partial B_{Q_{\mathrm{f}}}} \psi\overline{\boldsymbol{Q}}_{\mathrm{f}\boldsymbol{n+1}}\, \mathrm{d\Gamma}.
\end{aligned} \tag{8.72}$$

$$\begin{aligned}
\hat{L}(\boldsymbol{u}_{n+1}, p^{\mathrm{f}}_{n+1}, \theta_{n+1}, \omega) \;=\; & \int_{\mathcal{B}} \omega\Big(c_{\boldsymbol{F}n+1}\frac{\theta_{n+1}-\theta_n}{\Delta t} - 3K\alpha_{sk}\theta_{n+1}\frac{\log J_{n+1} - \log J_n}{\Delta t}\Big)\, \mathrm{dV} \\
& - \int_{\mathcal{B}} \omega\Big(3\alpha^{\mathrm{m}}\theta_{n+1}\frac{p^{\mathrm{f}}_{n+1} - p^{\mathrm{f}}_{n}}{\Delta t} + \frac{\Phi^{\mathrm{f}}_{n+1}c_{\mathrm{f}}}{\rho_{\mathrm{f}n+1}}\boldsymbol{W}_{n+1}\cdot\boldsymbol{F}^{-T}_{n+1}\cdot\nabla^{\boldsymbol{X}}\theta_{n+1}\Big)\, \mathrm{dV} \\
& - \int_{\mathcal{B}} \nabla^{\boldsymbol{X}}\omega\cdot\boldsymbol{Q}_{\theta n+1}\, \mathrm{dV} - \int_{\partial B_{Q_\theta}} \psi\overline{\boldsymbol{Q}}_{\boldsymbol{\theta n+1}}\, \mathrm{d\Gamma}.
\end{aligned} \tag{8.73}$$

Consider the case where the testing functions and the interpolated displacement, pore pressure and temperature are spanned by the same basis functions. In that case, the following approximation holds,

$$\begin{aligned}\boldsymbol{u} \approx \boldsymbol{u}^h = \sum_{a=1}^{n} \boldsymbol{N}_a \boldsymbol{u}_a \;\; ; \;\; p^{\mathrm{f}} \approx p^{\mathrm{f}h} = \sum_{a=1}^{n} N_a p_a^{\mathrm{f}} \;\; ; \;\; \theta \approx \theta^h = \sum_{a=1}^{n} N_a \theta_a \;, \\ \boldsymbol{\eta} \approx \boldsymbol{\eta}^h = \sum_{a=1}^{n} \boldsymbol{N}_a \boldsymbol{\eta}_a \;\; ; \;\; \psi \approx \psi^h = \sum_{a=1}^{n} N_a \psi_a \;\; ; \;\; \omega \approx \omega^h = \sum_{a=1}^{n} N_a \omega_a \;,\end{aligned} \tag{8.74}$$

where $\boldsymbol{u}_a$, p_a^{f} and θ_a are the nodal values of displacement, pore pressure and temperature. $\boldsymbol{\eta}_a$, ψ_a and ω_a are nodal values of the corresponding test functions. The resultant finite dimensional spaces for the interpolated displacement, pore pressure and temperature are denoted as $\boldsymbol{V}_{\boldsymbol{u}}^h$, V_p^h and V_θ^h respectively. Similarly, we denote the finite dimensional space of the corresponding testing functions as $\boldsymbol{V}_{\boldsymbol{\eta}}^h$, V_ψ^h and V_ω^h. The integer n is the number of node per element. By substituting (8.74) into (8.70), we obtain the equal-order Galerkin form of the thermo-hydro-mechanical problem.

8.2.3 Assumed Deformation Gradient for Volumetric Locking

In this section, we derive an assumed deformation gradient for the thermo-hydro-mechanics problem to circumvent the volumetric locking numerical deficiency. Recall that the kinematic split of the deformation gradient $\boldsymbol{F}$ is formulated as,

$$\boldsymbol{F} = \boldsymbol{F}_{\mathrm{vol}} \cdot \boldsymbol{F}_{\mathrm{iso}}, \tag{8.75}$$

where,

$$\boldsymbol{F}_{\mathrm{vol}} = J^{1/3}\boldsymbol{I} \;\; ; \;\; \boldsymbol{F}_{\mathrm{iso}} = J^{-1/3}\boldsymbol{F}. \tag{8.76}$$

Previously, the assumed deformation gradient method is often used to avoid the over-constraint associated with equal-order interpolations of the volumetric and isochoric parts of the deformation gradient [Simo et al., 1985, Moran et al., 1990, Wriggers and Reese, 1996, de Souza Neto et al., 2008, Sun et al., 2013d]. The key to avoid overconstraint is to replace the interpolated volumetric deformation field $J = \det \boldsymbol{F}$ with a reduced order volumetric field $\overline{J}$ such that fewer volumetric constraints occur when incompressibility limit is approached. The resultant assumed deformation gradient is therefore composed of the modified volumetric deformation field and the original interpolated isochoric deformation gradient. In other words, the interpolated volumetric split $\boldsymbol{F}_{\mathrm{vol}} = J^{1/3}\boldsymbol{I}$ is replaced by an modified definition $\overline{\boldsymbol{F}}_{\mathrm{vol}} = \bar{J}^{1/3}\boldsymbol{I}$ such that,

$$\overline{\boldsymbol{F}} = \bar{J}^{1/3}\boldsymbol{F}_{\mathrm{iso}} = \bar{J}^{1/3}J^{-1/3}\boldsymbol{F}. \tag{8.77}$$

While the relaxation provided by the modification of deformation gradient definition is able to cure the locking issue, the usage of non-standard deformation gradient may lead to numerical instability as exhibited in Broccardo et al. [2009], Castellazzi and Krysl [2012]. Moran et al. [1990] suggested replacing the assumed deformation gradient $\overline{\boldsymbol{F}}$ with a linear interpolation between the original and the assumed deformation gradient, i.e., $\widetilde{\boldsymbol{F}} = \alpha\boldsymbol{F} + (1-\alpha)\overline{\boldsymbol{F}}$. where α is a stabilization parameter in which $\alpha = 0$ leads to the pure F-bar formulation and $\alpha = 1$ leads to the standard formulation. The idea is to introduce stiffness to spurious zero-energy mode by increasing the magnitude of α whenever the numerical instability is encountered.

However, as deformation gradient belongs to multiplicative group, linear interpolation may lead to significant error. For instance, linearly interpolating rigid body rotations may lead to tensor not belonging to $\mathrm{SO}(3)$ group. To cure locking without comprising stability, we introduce a simple combined/standard F-bar element by recourse to exponential/logarithmic mapping for the thermo-hydro-mechanics problem in which the modified deformation gradient reads ,

$$\widetilde{\boldsymbol{F}} = \widetilde{J}^{1/3}\boldsymbol{F}_{\mathrm{iso}} = \widetilde{J}^{1/3}J^{-1/3}\boldsymbol{F} \;, \tag{8.78}$$

where $\widetilde{J}$ is the modified volumetric split of the deformation gradient, i.e.,

$$\widetilde{J} = \exp\Big(\frac{1-\beta}{\mathrm{V}_{\mathcal{B}^e}}\int_{\mathcal{B}^e} \log J \; \mathrm{dV} + \beta \log J\Big), \tag{8.79}$$

where $\beta \in [0,1]$ is a weighing parameter that partitions the standard and assumed deformation gradient. Augmented with the (8.17) and assumed that the thermal expansion coefficient α_{sk} is constant, the logarithmic volumetric strain $\log J$ reads,

$$\log J = \log J^e + \log J^p + 3\alpha_{sk}(\theta - \theta_o). \tag{8.80}$$

The mechanical contribution of the assumed deformation gradient therefore reads,

$$\widetilde{\boldsymbol{F}}_M = \widetilde{J}_M^{1/3} \boldsymbol{F}_{\text{iso}} \ , \tag{8.81}$$

where,

$$\widetilde{J}_M = \exp\Big(\log \widetilde{J} - 3\big(\frac{1-\beta}{\mathrm{V}_{\mathcal{B}^e}} \int_{\mathcal{B}^e} \alpha_{sk}\big(\theta - \theta_o\big) \, \mathrm{dV} + \beta \alpha_{sk}(\theta - \theta_o \,)\Big) \ . \tag{8.82}$$

The combined formulation may reduce to the standard or F-bar formulation by adjusting α. Furthermore, it can be easily shown that (8.78) is identical to the mid-point assumed deformation gradient formulation in [de Souza Neto et al., 2008] if $\alpha = 0$ and the volume averaging of $\log J(X)$ is computed via one-point quadrature at the centroid of the element. In all the simulations presented in this paper, we found that setting $\alpha = 0.05$ appeared to eliminate the zero energy modes.

At present, the optimal value of β is not known. While the assumed deformation gradient may lead to spurious modes for certain single-phase solid mechanics problems, non-zero β is not required in the solutions presented in the example section.

8.2.4 Inf-sup Conditions and Stabilization Procedures

It is well known that isothermal hydro-mechanical responses near drained limit may maintain stability, even though displacement and pore pressure are interpolated by the same set of basis functions White and Borja [2008a]. This seemingly stable responses nevertheless does not imply that the pore pressure and temperature will be free of spurious oscillations under different thermal and hydraulic conditions. In fact, when a very fine temporal discretization is used or when a simulation is conducted near the undrained limit, spurious pore pressure may occur due to the lack of inf-sup condition [Zienkiewicz et al., 1999b, White and Borja, 2008a, Sun et al., 2013d]. Similar spurious behaviors have also been observed in the thermo-hydro-mechanics problem. For instance, Liu et al. [2009] study the onset of spurious temperature and pore pressure in small strain non-isothermal hydro-mechanical finite element model and subsequently propose the usage of an interior penalty method to eliminate the oscillations in the pore pressure and temperature fields. The goal of this section is to develop a stabilized $\boldsymbol{u} - p^{\mathrm{f}} - \theta$ equal-order finite element THM problem, which eliminate spurious oscillation defined in (8.70).

We limit focus our attention on a simplified model problem in which (1) the heat transfer and pore-fluid diffusion are both negligible, (2) the skeleton deformation is only infinitesimal such that derivatives in material and current configurations are approximately the same.

Assumption (1) allows us to analyze the numerical stability of a porous medium at both the undrained and isentropic limits. Both undrained and isentropic conditions often constitute the worst-case scenario that is prone to spurious oscillations of pore pressure and temperature. Assumption (2) allows us to analyze the inf-sup condition raised in the linearized governing equation. This means that we will study the linear thermo-hydro-mechanics problem in the hope that this may give some indications on the more general nonlinear thermo-hydro-mechanical problem. A similar strategy has been adopted in Pantuso and Bathe [1997], Auricchio et al. [2005] and Auricchio et al. [2013] to analyze the stability range of mixed finite element formulations for the large strain incompressible elasticity problem. As pointed out previously by Pantuso and Bathe [1997] and Auricchio et al. [2013], schemes that are inf-sup stable in the linearized problem may still exhibit unphysical instabilities. Nevertheless, the inf-sup condition of the linear problem is still a valuable tool because it may serve as a necessary (but not sufficient) condition for maintaining numerical stability [Pantuso and Bathe, 1997].

Here we use the results from Howell and Walkington [2011], which proves that finite element model with a saddle point structure form: $(\boldsymbol{u}^h, p^{\mathrm{f}h}, \theta^h) \in \boldsymbol{V_u}^h \times V_p^h \times V_\theta^h$, is well-posed if the finite dimensional spaces $\boldsymbol{V_u}^h$, V_p^h V_θ^h chosen for the displacement, pore pressure and temperature interpolation satisfy the two-fold int-sup condition, i.e., there exists a constant $C_o > 0$ such that,

$$\sup_{\boldsymbol{w}^h \in V_{\boldsymbol{u}}{}^h} \frac{\int_{\mathcal{B}} \Big(p^{\mathrm{f}h} B + 3\theta K \alpha_{\mathrm{sk}} \Big) \nabla^{\boldsymbol{x}} \cdot \boldsymbol{w}^h \, d\mathrm{V}}{||\boldsymbol{w}^h||_{\boldsymbol{V_u^h}}} \geq C_o \Big(||p^{\mathrm{f}h}||_{V_p^h} + ||\theta^h||_{V_\theta^h} \Big) \ , \ (p^{\mathrm{f}h}, \theta^h) \in V_p^h \times V_\theta^h, \tag{8.83}$$

where $||\cdot||_{\boldsymbol{V_u^h}}$, $||\cdot||_{V_p^h}$ and $||\cdot||_{V_\theta^h}$ are the norms corresponding to the finite dimensional space $\boldsymbol{V}_u^h$, V_p^h and V_θ^h. Here we equip the spaces of the solutions and their corresponding testing functions with the same associated

norms, i.e.,

$$
\begin{aligned}
||\boldsymbol{u}||_{\boldsymbol{V}_{\boldsymbol{u}}^h} &= ||\boldsymbol{u}||_1 = \sqrt{\int_{\mathcal{B}} \nabla^{\boldsymbol{x}}\, \boldsymbol{u} \cdot \nabla^{\boldsymbol{x}}\, \boldsymbol{u}\; dV}\;, \\
||p||_{V_{p^{\mathrm{f}}}^h} &= \sqrt{\int_{\mathcal{B}} Bp^2\; dV}\;, \\
||\theta||_{V_\theta^h} &= \sqrt{\int_{\mathcal{B}} 3\Big(\alpha_{\mathrm{sk}} K\Big)\theta^2\; dV}\;.
\end{aligned}
\tag{8.84}
$$

Note that $||\cdot||_{V_{p^{\mathrm{f}}}^h}$, $||\cdot||_{V_\theta^h}$ and $||\cdot||_0$ are equivalent norms. Unfortunately, if displacement, pore pressure and temperatures are all spanned by the same basis function, then the condition listed in (8.83) does not hold [Brezzi and Fortin, 1991].

Our new contribution here is twofold. First, we prove that a weaker inf-sup bound also exists for the compound matrix $\mathbb{B}$. Then, for the first time, we propose a proper stabilization term that may eliminate the spurious oscillations of pore pressure and temperature for the thermo-hydro-mechanics problem.

Weak Inf-Sup Conditions of Coupling Terms

To derive stabilized finite element formulation, we may first quantify the inf-sup "deficiency" of the unstable, equal-order discretization, then propose additional terms to eliminate the spurious modes due to the inf-sup "deficiency". Previously, this strategy is used in Bochev et al. [2006] where a weaker inf-sup bound is first identified for the Stokes equations, then a stabilization term is derived to restore stability for two interpolated velocity-pressure pairs.

To determine the weak inf-sup bound of individual coupling terms, let us first recall that the divergence is an isomorphism of the orthogonal complement of divergence-free functions in $\boldsymbol{H}_0^1(\mathcal{B})$ onto $L_0^2(\mathcal{B})$ space. Given that the pressure $p^{\mathrm{f}h} \in V_p^h \subset L_0^2(\mathcal{B})$, then the isomorphism of the divergence operator guarantees the existence of a $\boldsymbol{w} \in \boldsymbol{H}_0^1(\mathcal{B})$ such that,

$$
\nabla^{\boldsymbol{x}} \cdot \boldsymbol{w} = p^{\mathrm{f}h} \;\text{ and }\; ||\boldsymbol{w}||_1 \leq ||p^{\mathrm{f}h}||_{V_{p^{\mathrm{f}}}^h}\,. \tag{8.85}
$$

With (8.85) in mind, we then have,

$$
\sup_{\boldsymbol{v}\in\boldsymbol{H}_o^1(\mathcal{B})} \frac{|\int_{\mathcal{B}} p^{\mathrm{f}h} B\, \nabla^{\boldsymbol{X}} \cdot \boldsymbol{v}\; d\mathrm{V}\,|}{||\boldsymbol{v}||_1} \geq \frac{\int_{\mathcal{B}} |\, p^{\mathrm{f}h} B\, \nabla^{\boldsymbol{X}} \cdot \boldsymbol{w}\; d\mathrm{V}\,|}{||\boldsymbol{w}||_1} \geq \frac{\int_{\mathcal{B}} |\, p^{\mathrm{f}h} B p^{\mathrm{f}h}\; d\mathrm{V}\,|}{||p^{\mathrm{f}h}||_{V_{p^{\mathrm{f}}}^h}} \geq \tilde{C}_p ||p^{\mathrm{f}h}||_{V_{p^{\mathrm{f}}}^h}\,, \tag{8.86}
$$

where $\tilde{C}_p$ os a constant such that,

$$
|\int_{\mathcal{B}} p^{\mathrm{f}h} B\, \nabla^{\boldsymbol{x}} \cdot \boldsymbol{w}\; d\mathrm{V}\,| \geq \tilde{C}_p ||p^{\mathrm{f}h}||_{V_{p^{\mathrm{f}}}^h} ||\boldsymbol{w}||_1. \tag{8.87}
$$

By letting $\boldsymbol{w}^h$be the interpolant of $\boldsymbol{v}$ ot of $\boldsymbol{V}^{\boldsymbol{u}}$, and using the well-known approximation result in page 217 of Girault and Raviart [1986] , i.e., $||\boldsymbol{w} - \boldsymbol{w}^h||_{V_{p^{\mathrm{f}}}^h} \leq Ch||\boldsymbol{w}||_1$; $||\boldsymbol{w}^h||_1 \leq C||\boldsymbol{w}||_1$ and the fact that $||\cdot||_0$ and $||\cdot||_{V_{p^{\mathrm{f}}}^h}$ are equivalent norms , we obtain,

$$
\begin{aligned}
\sup_{\boldsymbol{v}^h\in\boldsymbol{V}_{\boldsymbol{u}}^{\boldsymbol{h}},\boldsymbol{v}\neq\boldsymbol{0}} \frac{\int_{\mathcal{B}} p^{\mathrm{f}h} B\, \nabla^{\boldsymbol{x}} \cdot \boldsymbol{v}^h\; d\mathrm{V}}{||\boldsymbol{v}^h||_1} &\geq \frac{|\int_{\mathcal{B}} p^{\mathrm{f}h} B\, \nabla^{\boldsymbol{x}} \cdot \boldsymbol{w}^h\; d\mathrm{V}\,|}{||\boldsymbol{w}||_1} \\
&\geq \frac{\int_{|\mathcal{B}} p^{\mathrm{f}h} B\, \nabla^{\boldsymbol{x}} \cdot \boldsymbol{w}\; d\mathrm{V}\,|}{||\boldsymbol{w}||_1} - \frac{|\int_{\mathcal{B}} p^{\mathrm{f}h} B\, \nabla^{\boldsymbol{x}} \cdot (\boldsymbol{w} - \boldsymbol{w}^h)\; d\mathrm{V}\,|}{||\boldsymbol{w}||_1} \\
&\geq \frac{\tilde{C}_p}{C} ||p^{\mathrm{f}h}||_{V_{p^{\mathrm{f}}}^h} - \frac{||\nabla^{\boldsymbol{x}}\, p^{\mathrm{f}h}||_{V_{p^{\mathrm{f}}}^h} ||\boldsymbol{w}^h - \boldsymbol{w}||_{V_{p^{\mathrm{f}}}^h}}{C||\boldsymbol{w}||_{V_{p^{\mathrm{f}}}^h}}.
\end{aligned}
\tag{8.88}
$$

Therefore,

$$\sup_{\boldsymbol{v}^h \in \boldsymbol{V}_{\boldsymbol{u}}^{\boldsymbol{h}}, \boldsymbol{v} \neq \boldsymbol{0}} \frac{\int_{\mathcal{B}} p^{\mathrm{f}h} B \, \nabla^{\boldsymbol{x}} \cdot \boldsymbol{v}^h \, d\mathrm{V}}{||\boldsymbol{v}^h||_1} \geq \alpha_1 ||p^{\mathrm{f}h}||_{V_{p^{\mathrm{f}}}^h} - \alpha_2 h || \nabla^{\boldsymbol{x}} p^{\mathrm{f}h}||_{V_{p^{\mathrm{f}}}^h}, p^{\mathrm{f}h} \in V_p^h \,, \tag{8.89}$$

where h is the mesh size and C, α_1 and α_2 are constants. Following the same logic, it is trivial to show that the same procedure can be applied to the thermo-elastic coupling term, i.e.,

$$\sup_{\boldsymbol{w}^h \in \boldsymbol{V}_{\boldsymbol{u}}^{\boldsymbol{h}}, \boldsymbol{v} \neq \boldsymbol{0}} \frac{\int_{\mathcal{B}} 3K\alpha_{\mathrm{sk}} \theta^h \, \nabla^{\boldsymbol{x}} \cdot \boldsymbol{w}^h \, d\mathrm{V}}{||\boldsymbol{w}^h||_1} \geq \beta_1 ||\theta^h||_{V_{\theta^h}} - \beta_2 h || \nabla^{\boldsymbol{x}} \theta^h||_{V_{\theta^h}} \,, \theta^h \in V_\theta^h \,, \tag{8.90}$$

where β_1 and β_2 are positive constant.

Combined Weak Inf-sup Condition

Our goal here is to use the weak inf-sup bounds of individual coupling terms expressed in (8.89) and (8.90) to define a weak inf-sup bound for the thermo-hydro-mechanics problem.

First, note that (8.89) can be written as,

$$\begin{aligned} \sup_{\boldsymbol{v}^h \in \boldsymbol{V}_{\boldsymbol{u}}^{\boldsymbol{h}}, \boldsymbol{v} \neq \boldsymbol{0}} \frac{\int_{\mathcal{B}} p^{\mathrm{f}h} B \, \nabla^{\boldsymbol{x}} \cdot \boldsymbol{v}^h \, d\mathrm{V}}{||\boldsymbol{v}^h||_1} &= \sup_{\boldsymbol{v}^h \in \boldsymbol{V}_{\boldsymbol{u}}^{\boldsymbol{h}}, \boldsymbol{v} \neq \boldsymbol{0}} \int_{\mathcal{B}} p^{\mathrm{f}h} B \, \nabla^{\boldsymbol{x}} \cdot \left(\frac{\boldsymbol{v}^h}{||\boldsymbol{v}^h||_1} \right) d\mathrm{V} \\ &= \sup_{\boldsymbol{v}^h \in \boldsymbol{V}_{\boldsymbol{u}}^{\boldsymbol{h}}, ||\boldsymbol{v}^h||_1 = 1} \int_{\mathcal{B}} p^{\mathrm{f}h} B \, \nabla^{\boldsymbol{x}} \cdot \boldsymbol{v}^h \, d\mathrm{V}. \end{aligned} \tag{8.91}$$

As a result, (8.89) can be rewritten as,

$$\sup_{\boldsymbol{v}^h \in \boldsymbol{V}_{\boldsymbol{u}}^{\boldsymbol{h}}, ||\boldsymbol{v}^h||_1 = 1} \int_{\mathcal{B}} p^{\mathrm{f}h} B \, \nabla^{\boldsymbol{x}} \cdot \boldsymbol{v}^h \, d\mathrm{V} \geq \alpha_1 ||p^{\mathrm{f}h}||_{V_{p^{\mathrm{f}}}^h} - \alpha_2 h || \nabla^{\boldsymbol{x}} p^{\mathrm{f}h}||_{V_{p^{\mathrm{f}}}^h} \,. \tag{8.92}$$

Applying the same argument on (8.90), we have,

$$\sup_{\boldsymbol{w}^h \in \boldsymbol{V}_{\boldsymbol{u}}^{\boldsymbol{h}}, ||\boldsymbol{v}^h||_1 = 1} \int_{\mathcal{B}} 3K\alpha_{\mathrm{sk}} \theta^h \, \nabla^{\boldsymbol{x}} \cdot \boldsymbol{w}^h \, d\mathrm{V} \geq \beta_1 ||\theta^h||_{V_{\theta^h}} - \beta_2 h || \nabla^{\boldsymbol{x}} \theta^h||_{V_{\theta^h}} \,. \tag{8.93}$$

Note that (8.92) implies the existence of $\boldsymbol{v}^h \in \boldsymbol{V}_{\boldsymbol{u}^h}$ with $||\boldsymbol{v}^h||_1 = 1$ such that

$$\int_{\mathcal{B}} p^{\mathrm{f}h} B \, \nabla^{\boldsymbol{x}} \cdot \boldsymbol{v}^h \, d\mathrm{V} \geq C_1 ||p^{\mathrm{f}h}||_{V_{p^{\mathrm{f}}}^h} - C_2 h || \nabla^{\boldsymbol{x}} p^{\mathrm{f}h}||_{V_{p^{\mathrm{f}}}^h}, p^{\mathrm{f}h} \in V_p^h \,. \tag{8.94}$$

On the other hand, (8.93) implies the existence of $\boldsymbol{w}^h \in \boldsymbol{V}_{\boldsymbol{w}^h}$ with $||\boldsymbol{w}^h||_1 = 1$ such that

$$\int_{\mathcal{B}} 3K\alpha_{\mathrm{sk}} \theta^h \, \nabla^{\boldsymbol{x}} \cdot \boldsymbol{w}^h \, d\mathrm{V} \geq \beta_1 ||\theta^h||_{V_\theta^h} - \beta_2 h || \nabla^{\boldsymbol{x}} \theta^h||_{V_\theta^h} \,, \theta^h \in V_\theta^h \,. \tag{8.95}$$

Now let $\boldsymbol{u} = \boldsymbol{v}^h + \boldsymbol{w}^h$, then,

$$\begin{aligned} \int_{\mathcal{B}} p^{\mathrm{f}h} B \, \nabla^{\boldsymbol{x}} \cdot \boldsymbol{u} \, d\mathrm{V} &= \int_{\mathcal{B}} p^{\mathrm{f}h} B \, \nabla^{\boldsymbol{x}} \cdot \boldsymbol{v}^h \, d\mathrm{V} + \int_{\mathcal{B}} p^{\mathrm{f}h} B \, \nabla^{\boldsymbol{x}} \cdot \boldsymbol{w}^h \, d\mathrm{V} \\ &= \int_{\mathcal{B}} p^{\mathrm{f}h} B \, \nabla^{\boldsymbol{x}} \cdot \boldsymbol{v}^h \, d\mathrm{V} + \int_{\mathcal{B}} \frac{B p^{\mathrm{f}h}}{3K\alpha_{\mathrm{sk}}} (3K\alpha_{\mathrm{sk}}) \, \nabla^{\boldsymbol{x}} \cdot \boldsymbol{w}^h \, d\mathrm{V} \,, \\ \int_{\mathcal{B}} 3K\alpha_{\mathrm{sk}} \theta^h \, \nabla^{\boldsymbol{x}} \cdot \boldsymbol{u} \, d\mathrm{V} &= \int_{\mathcal{B}} 3K\alpha_{\mathrm{sk}} \theta^h \, \nabla^{\boldsymbol{x}} \cdot \boldsymbol{v}^h \, d\mathrm{V} + \int_{\mathcal{B}} 3K\alpha_{\mathrm{sk}} \theta^h \, \nabla^{\boldsymbol{x}} \cdot \boldsymbol{v}^w \, d\mathrm{V} \\ &= \int_{\mathcal{B}} \frac{3K\alpha_{\mathrm{sk}} \theta^h}{B} B \, \nabla^{\boldsymbol{x}} \cdot \boldsymbol{v}^h \, d\mathrm{V} \int_{\mathcal{B}} 3K\alpha_{\mathrm{sk}} \theta^h \, \nabla^{\boldsymbol{x}} \cdot \boldsymbol{w}^h \, d\mathrm{V} \,. \end{aligned} \tag{8.96}$$

Recall that $V_{p^{\mathrm{f}}}^h$ and V_θ^h are spanned by the same set of basis functions. Thus, $\widetilde{p}^h = (3K\alpha_{\mathrm{sk}}/B)\theta^h$ and $\widetilde{\theta}^h = \big(B/(3K\alpha_{\mathrm{sk}})\big)p^{\mathrm{f}h}$, we have,

$$\begin{aligned}\int_{\mathcal{B}} \big(p^{\mathrm{f}h}B + 3K\alpha_{\mathrm{sk}}\theta^h\big)\,\nabla^{\boldsymbol{x}}\cdot\boldsymbol{u}\;d\mathrm{V} &= \int_{\mathcal{B}}(p^{\mathrm{f}h}+\widetilde{p}^h)B\,\nabla^{\boldsymbol{x}}\cdot\boldsymbol{v}^h\;d\mathrm{V} + \int_{\mathcal{B}} 3K\alpha_{\mathrm{sk}}(\theta^h+\widetilde{\theta}^h)\,\nabla^{\boldsymbol{x}}\cdot\boldsymbol{w}^h\;d\mathrm{V}\\ &\geq \gamma_1\big(||p^{\mathrm{f}h}||_{V_{p^{\mathrm{f}}}^h} + ||\theta^h||_{V_\theta^h}\big) - \gamma_2 h\big(||\,\nabla^{\boldsymbol{x}}\,p^{\mathrm{f}h}||_{V_{p^{\mathrm{f}}}^h} + ||\,\nabla^{\boldsymbol{x}}\,\theta^h||_{V_\theta^h}\big),\end{aligned} \tag{8.97}$$

where $\gamma_1 = \min(\alpha_1,\beta_1)$ and $\gamma_2 = \max(\alpha_2,\beta_2)$. Thus, according to the definition of supremum, we may express the combined weaker inf-sup bound as,

$$\sup_{\boldsymbol{v}^h\in\boldsymbol{V}_{\boldsymbol{u}}^{\boldsymbol{h}},\boldsymbol{v}\neq\boldsymbol{0}} \frac{\int_{\mathcal{B}}\big(p^{\mathrm{f}h}B + 3K\alpha_{\mathrm{sk}}\theta^h\big)\,\nabla^{\boldsymbol{x}}\cdot\boldsymbol{v}^h\;d\mathrm{V}}{||\boldsymbol{v}^h||_1} \geq C_1\big(||p^{\mathrm{f}h}||_{V_{p^{\mathrm{f}}}^h} + ||\theta^h||_{V_\theta^h}\big) - C_2 h\big(||\,\nabla^{\boldsymbol{x}}\,p^{\mathrm{f}h}||_{V_{p^{\mathrm{f}}}^h} + ||\,\nabla^{\boldsymbol{x}}\,\theta^h||_{V_\theta^h}\big), \tag{8.98}$$

where C_1 and C_2 are positive constant.

Projection-based Stabilization

By comparing (8.83) and (8.98), we notice that the difference between the inf-sup bound and the weak inf-sup bound is the gradient term in (8.98), i.e.,

$$-C_2 h\big(||\,\nabla^{\boldsymbol{x}}\,p^{\mathrm{f}h}||_{V_{p^{\mathrm{f}}}^h} + ||\,\nabla^{\boldsymbol{x}}\,\theta^h||_{V_\theta^h}\big). \tag{8.99}$$

This term can be used as a template for the design of stabilization terms. For instance, a simple remedy to restore numerical stability by directly adding perturbation gradient terms in (8.98) such that the inf-sup deficiency is counterbalanced. Here we consider an alternative characterization of the inf-sup deficiency formulated in terms of projection operators. The upshot of a projection-based stabilization method is that it does not depend on the mesh size h or the type of element shapes, hence easier to be implemented. As discussed in Sun et al. [2013d], the rationale of the projection-based stabilization is based on the inverse inequality, which guarantees the existence of a positive constant C_I such that,

$$C_I h\big(||\,\nabla^{\boldsymbol{x}}\,p^{\mathrm{f}h}||_{V_{p^{\mathrm{f}}}^h} + ||\,\nabla^{\boldsymbol{x}}\,\theta^h||_{V_\theta^h}\big) \leq ||p^{\mathrm{f}h} - \Pi p^{\mathrm{f}h}||_{V_{p^{\mathrm{f}}}^h} + ||\theta^h - \Pi\theta^h||_{V_\theta^h}\,, \tag{8.100}$$

where $\Pi(\cdot)$ is a projection operator leads to a piecewise constant field. Here we define $\Pi(\cdot)$ as simply the element average operator that reads,

$$\Pi(\cdot) = \frac{1}{V^e}\int_K (\cdot)\;d\mathrm{V}\;\;;K\in\mathcal{B}. \tag{8.101}$$

Furthermore, since it is not clear whether the two-way couplings between pore-fluid diffusion and heat transfer may destabilize the system if either the pore-fluid or the thermal conductivity is too low, we introduce a third term as a safety measure. The resultant perturbation functional reads,

$$W^{per}(\theta^h,p^{\mathrm{f}h}) = C\Big(\frac{1}{2}||p^{\mathrm{f}h} - \Pi p^{\mathrm{f}h}||^2_{V_{p^{\mathrm{f}}}^h} + \frac{1}{2}||\theta^h - \Pi\theta^h||^2_{V_\theta^h} + \sum_{K\in\Omega}\,|\int_K 3\alpha^m(p^{\mathrm{f}h} - \Pi p^{\mathrm{f}h})(\theta^h - \Pi\theta^h)d\mathrm{V}\,|\Big)\,, \tag{8.102}$$

where C is a positive constant. The stabilization term added to the discrete balance of mass equation (8.72) is simply the first variation of (8.102) with respect to pore pressure, i.e.,

$$\begin{aligned}\hat{H}^{\mathrm{stab}}(\psi,p^{\mathrm{f}h}_{n+1},\theta^h_{n+1}) = &\sum_{K\in\mathcal{B}}\int_K C_{p1}(\psi-\Pi\psi)\big(p^{\mathrm{f}h}_{n+1} - p^{\mathrm{f}h}_n - \Pi(p^{\mathrm{f}h}_{n+1} - p^{\mathrm{f}h}_n)\big)d\mathrm{V}\\ &+ \sum_{K\in\mathcal{B}}\int_K C_{p2}(\psi-\Pi\psi)\big(\theta^h_{n+1} - \theta^h_n - \Pi(\theta^h_{n+1} - \theta^h_n)\big)d\mathrm{V}\,.\end{aligned} \tag{8.103}$$

On the other hand, the stabilization term added to the balance of energy (8.72) is obtained by taking the first variation of (8.102) with respect to temperature and multiply the result by the temperature, i.e.,

$$\begin{aligned}\hat{L}^{\text{stab}}(\omega, p^{\text{fh}}_{n+1}, \theta^h_{n+1}) = &\sum_{K\in\mathcal{B}}\int_K C_{\theta 1}(\omega - \Pi\omega)\theta^h_{n+1}\big(p^{\text{fh}}_{n+1} - p^{\text{fh}}_n - \Pi(p^{\text{fh}}_{n+1} - p^{\text{fh}}_n)\big)d\text{V} \\ &+ \sum_{K\in\mathcal{B}}\int_K C_{\theta 2}(\omega - \Pi\omega)\big(\theta^h_{n+1} - \theta^h_n - \Pi(\theta^h_{n+1} - \theta^h_n)\big)d\text{V}\ ,\end{aligned} \tag{8.104}$$

where C_{p1}, C_{p2}, $C_{\theta 1}$ and $C_{\theta 2}$ are the stabilization parameters. Finally, applying the stabilized formulation in the discrete variational equation (8.70) yields,

$$\begin{aligned}\hat{G}(\boldsymbol{u}^h_{n+1}, p^{\text{fh}}_{n+1}, \theta^h_{n+1}, \boldsymbol{\eta}) &= 0\ , \\ \hat{H}(\boldsymbol{u}^h_{n+1}, p^{\text{fh}}_{n+1}, \theta^h_{n+1}, \psi) - \hat{H}^{\text{stab}}(\boldsymbol{u}^h_{n+1}, p^{\text{fh}}_{n+1}, \theta^h_{n+1}, \psi) &= 0\ , \\ \hat{L}(\boldsymbol{u}^h_{n+1}, p^{\text{fh}}_{n+1}, \theta^h_{n+1}, \omega) - \hat{L}^{\text{stab}}(\boldsymbol{u}^h_{n+1}, p^{\text{fh}}_{n+1}, \theta^h_{n+1}, \omega) &= 0\ .\end{aligned} \tag{8.105}$$

While stabilization procedure provides a convenient and simple way to eliminate spatial oscillations from equal-order mixed finite element, the selection of stabilization parameter(s) remains a challenging problem [Tezduyar and Osawa, 2000]. This problem is further complicated by the fact that the heat transfer and pore fluid diffusion may occur at different spatial and time scales, and therefore making it difficult to select a stabilization parameter that ensures both spatial stability but avoid over-diffusion for both processes.

Our objective here is to provide an rough estimation of the optimal value of stabilization parameters. These estimated parameters can be served as useful guidelines for tuning the stabilization parameters but they should not be viewed as the definitive choices for a given THM problem. The influence of the stabilization parameter will be further tested via numerical experiments presented in the Section 8.4. Here we recommend the following stabilization parameters for Equations (8.105),

$$\begin{aligned}C_{p1} &= \alpha\Big[\frac{2G(1-\nu)}{1-2\nu}\Big(\frac{B^2(1+\nu_u)^2(1-2\nu)}{9(1-\nu_u)(\nu_u-\nu)}\Big)\Big]^{-1}\ , \\ C_{p2} &= \alpha\frac{2(\nu_u-\nu)}{B(1+\nu_u)(1-\nu)}\Big[\alpha_{\text{sk}} + \frac{B(1-\nu)(1+\nu_u)}{2(\nu_u-\nu)}\alpha_m\Big]\ , \\ C_{\theta 1} &= \alpha\Big[c_{\boldsymbol{F}} + \frac{9\theta\alpha^2_{\text{sk}}K^2}{K+4G/3}\Big]\ , \\ C_{\theta 2} &= \alpha\Big[\frac{3\alpha_{sk}K}{K+4/3G} - 3\alpha_m\Big]\theta\ ,\end{aligned} \tag{8.106}$$

where α is the safety factor. ν_u is the undrained void ratio, which reads,

$$\nu_u = \frac{3\nu + B(1-2\nu)(1-K/K_s)}{3 - B(1-2\nu)(1-K/K_s)}\ . \tag{8.107}$$

The stabilization parameters are inferred from the simplified linear thermo-hydro-mechanical problem in Coussy [2004a] (see p.136). In particular, we use the previous results from Preisig and Prévost [2011] and Sun et al. [2013d], which show that by setting parameter $\alpha = 1$, one may recover the stable lumped mass formulation for one dimensional problems.

8.3 Highlights of the Implementation Method

The thermo-hydro-mechanics model described in the previous sections is implemented in an open source, component-based finite element code called Albany [Pawlowski et al., 2012b,c, Salinger et al., 2013]. Broadly speaking, the Albany code acts as a "glue code" that integrate a multiple re-usable libraries. Many of these libraries are available in the Trilinos project [Heroux et al., 2005]. The key feature of Albany is the template-based programming approach, which allows developers to implement the finite element residuals by decomposing them into expression objects. These expression objects can be physical quantities (e.g. permeability, thermal conductivity, deformation), or mathematical entities, such as sets, points, lines, graphs, functions and boundary conditions.

The Albany code also features a graph-based software design, which has been employed previously in Notz et al. [2012] to model thermo-fluid problem and in Sun et al. [2013d] to model isothermal hydro-mechanical responses of porous media. This section is intended to provide a brief account about the implementation of the thermo-hydro-mechanics problem via this new technique developed by Salinger et al. [2013]. Readers interested at the software design and details of the Albany code, please refer to Pawlowski et al. [2012b], Notz et al. [2012] and Salinger et al. [2013] for further details.

Our starting point is the stabilized Galerkin form listed in (8.105) where the standard Gaussian integration is used to compute the integrands. To assembly the balance laws listed in (8.105), we decompose the discretized PDE systems into a directed graph, a mathematical object formed by a collection of vertices and directed edges. In our case, the vertices are the expressions that form the discretized PDE system and the directed edges indicate the data hierarchical dependence. The decomposition of residuals are done while following the rules listed below.

- The residual equations are always at the top of the hierarchy, i.e., the source vertices in the directed graph.
- The nodal solutions are always at the bottom of the hierarchy, i.e., the sink vertices of the directed graph.
- The directed graph formed by the decomposed expression objects must be acyclic, which means that there must be no cycle in the directed graph.
- All expressions in the directed graph must be connected, i.e., no isolated vertex in the directed graph.

Figure 8.4 shows a directed graph used to assemble the residuals of the thermo-hydro-mechanical model. One salient feature of this implementation approach is the transparency of data dependence. Even for multi-physical processes with very complicated coupling mechanisms, such as the THM problem, one may still explore, examine, and modify the topology of mathematical models in a visual way.

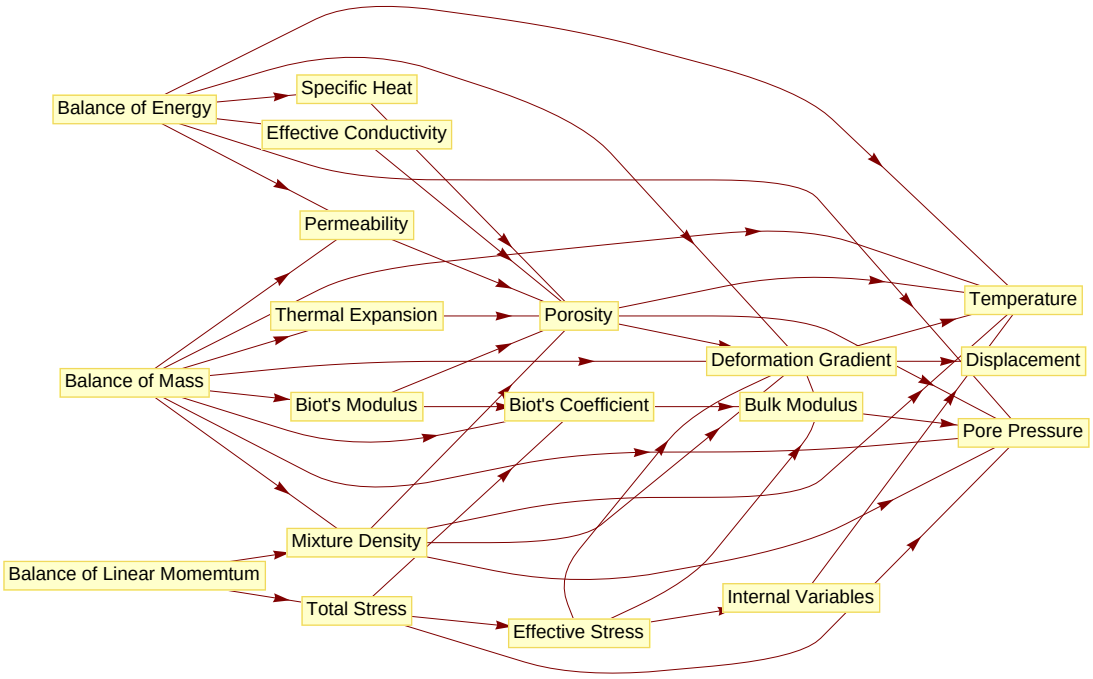

Figure 8.4: *Directed graph that represents the hierarchy of mathematical expressions for thermo-hydro-mechanical problems.*

In the thermo-hydro-mechanical model, each expression in the vertex is implemented as an evaulator [Pawlowski et al., 2012b,c]. An evaluator stores numerical values of the expression (e.g. permeability, thermal

conductivity and equivalent plastic strain at the quadrature points of each finite element), record the location of the expression in the directed graph and contains the actual code that compute the numerical values of the expressions (e.g. Equations (8.9), (8.39), (8.79) and 8.26). Residual vectors and the consistent tangent stiffness matrix are then computed via automatic differentiation performed on the directed graph via the Phalanx package [Pawlowski et al., 2012b,c]. As a result, there is no need to derive the linearized forms of the variational equations.

8.4 Numerical Examples

We present a selection of numerical examples to validate the implementation of the finite element model and demonstrate the three-way coupling effects of thermo-sensitive porous media at geometrically nonlinea regime. In particular, we will use the first example to address the numerical stability issue associated with material near undrained and adiabatic limits. The mechanical response of the solid skeleton is assumed to be elastic and replicated by a rate-independent neo-Hookean model. Due to the three-way coupling effects, the pore pressure evolves in a non-monotonic manner. This non-monotonic change is due to the Mandel-Cryer effect. Previously, the Mandel-Cryer effect has been observed in small strain numerical simulations of drained sphere [Selvadurai and Suvorov, 2012]. Here our new contribution is to demonstrate the Mandel-Cryer effect of the undrained sphere at finite strain.

In the second example, we will examine the formation of shear band in a globally undrained specimen. The specimen is not in an isothermal condition. Thus, solid response is affected by the thermal expansion of both the solid and fluid constituents. The heat transfer is governed by a coupled diffusion-convection equation in which temperature changes at a material point can be caused by the structural heating, plastic dissipation as well as the heat and pore-fluid fluxes. In both examples, we assume that there is no phase transition occurred.

8.4.1 Heated Globally Undrained Porous Sphere

In this numerical example, we simulate an undrained porous sphere heated by a raised temperature prescribed at the outer boundary. The purpose of this example is to demonstrate the performance of the stabilization scheme when thermal and pore-fluid diffusion occur at different time scales. The outer boundary of the sphere is subjected to a zero-Darcy-velocity boundary condition and thus the sphere is globally undrained. The temperature of the surface of the sphere is prescribed, while the rest of the sphere is initially at zero degree. Due to the rotational symmetry, only $1/8$ of the spherical domain is meshed. The radius of the sphere is one meter. The material parameters used to conduct these simulations are listed in Table 8.1. To illustrate how the stabilization term may alter the numerical solution, we conduct three numerical simulations with different stabilization parameters ($\alpha = 0, 1, 8$). It should be noted that the globally undrained porous sphere problem presented here might not be the worst case scenario for spatial stability. For instance, other benchmark problems, such as the generalized Terzaghi's one-dimensional consolidation problem coupled with heat transfer and the heated porous spherical problem with a fully permeable boundary, are also known to generate sharp pressure gradients and spurious oscillations at early time. For brevity, these problems are not included in this paper but will be explored in future study. In this example, a combination of low permeability and small time step is used to trigger the spurious oscillation in this numerical examples. This method has been used in Preisig and Prévost [2011], Sun et al. [2013a] to trigger spurious oscillation for isothermal poromechanics problem. The theoretical basis for the onset of spurious oscillation can be founded in the one-dimensional analyses by Harari [2004], Preisig and Prévost [2011], Sun et al. [2013a].

Verification of A Limiting Case

Figure 8.5 shows the simulated and analytical transient thermal responses of center when the prescribed temperature $\theta_o = 5, 50$ and $500°$C. The analytical solution is obtained by neglecting the poroelasticity coupling effect. Using Laplace transform [Selvadurai and Suvorov, 2012], the temperature at the center is,

$$\theta(t) = \theta_o - 2\theta_o[\sum_{n=1}^{\infty}(-1)^{n+1}\exp(-n^2\pi^2\tau)] \;;\; \tau = \frac{K_\theta t}{R_o^2((1-\phi^{\mathrm{f}})\rho_\theta^s c_s + \phi^{\mathrm{f}}\rho_\theta^f c_f)}, \tag{8.108}$$

where $R_0 = 1m$ is the radius of the sphere and θ_o is the temperature prescribed at the surface. Previously, Selvadurai and Suvorov [2012] observed that, for certain limited case where (1) fluid and solid constituents are incompressible, and (2) thermal convection and structural heating are not important, thermal diffusion of a spherical object can be solved via Laplace transform in a decoupled manner. In this example, we purposely

Parameter	Description	Value	Unit
E	Young's modulus	2000	MPa
ν	Poisson's ratio	0.1	dimensionless
T_{o}	Reference Temperature	0	$^{\circ}$C
α_{s}	Skeleton Thermal Expansion	8.3×10^{-5}	1/$^{\circ}$C
α_{f}	Pore-fluid Thermal Expansion	6.9×10^{-5}	1/$^{\circ}$C
ρ_{s}	Solid Constituent Density	2700	kg/m^3
ρ_{f}	Fluid Constituent Density	1000	kg/m^3
c_{s}	Solid Specific Heat	1700	J/kg/$^{\circ}$C
c_{f}	Fluid Specific Heat	4200	J/kg/$^{\circ}$C
k_{θ}^{s}	Solid Thermal Conductivity	2.5	W/m/$^{\circ}$C
k_{θ}^{f}	Fluid Thermal Conductivity	2.5	W/m/$^{\circ}$C
K_{s}	Solid Grain Bulk Modulus	50	GPa
K_{f}	Fluid Bulk Modulus	20	GPa
k_o	Kozeny-Carman Coefficient	1×10^{-19}	m/s
μ	Viscosity	1.0×10^{-3}	Pa $\cdot$ s
ϕ^{f}	Initial Porosity	0.25	dimensionless

Table 8.1: *Material properties of the undrained sphere in non-isothermal condition.*

use nearly incompressible constituents, and make the solid skeleton nearly impermeable to compare analytical and finite element solutions. According to Figure 8.5, the temperature obtained from the finite strain THM simulation is very similar to the analytical solution obtained via (8.108) when $\theta_o = 5^{\circ}$C. This is attributed to the fact the permeability is relatively low and the material is stiff. The temperature changes due to structural heating and convection due to fluid transport are therefore very limited, when the prescribed temperature is close to the initial body temperature. Nevertheless, as we increase the prescribed temperature while holding the initial body temperature constant, the discrepancy between the coupled and decoupled simulations does become more significant, as shown in Figure 8.5, where $\theta_o = 50^{\circ}$C and $\theta_o = 500^{\circ}$C.

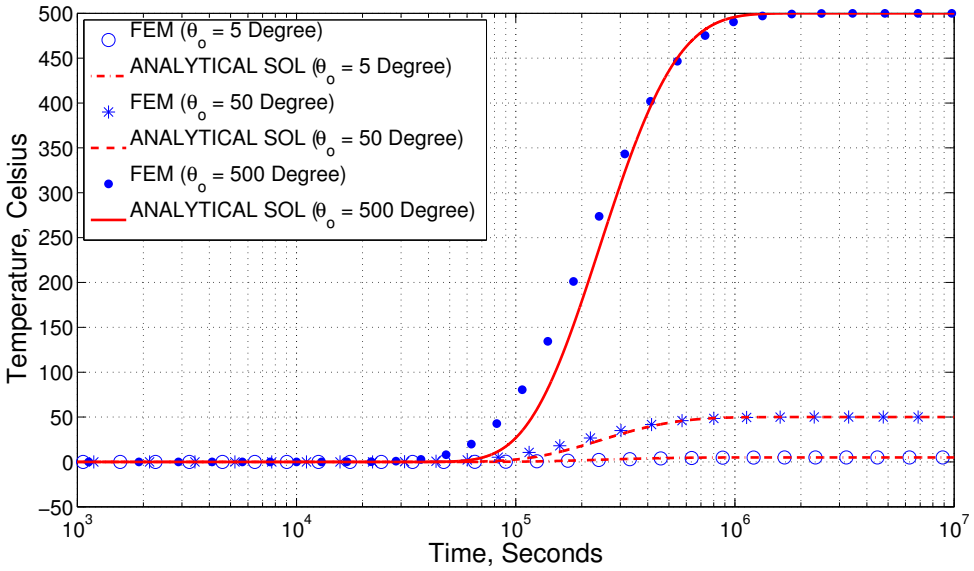

Figure 8.5: *Comparison of the finite element solution and the analytical solution for three cases where* $\theta_o = 5, 50$ *and* $500^{\circ}C$.

The code has also been verified via a number of analytical solutions under the isothermal condition in Sun et al. [2013d]. For brevity, the verification problems for the isothermal case are not included in this article. Interested readers please refer to Sun et al. [2013d] for details.

Assessments of the Stabilization Procedure

Figure 8.6 shows the pore pressure of the undrained sphere 1 second after it was put into the 5 degree heat bath. Figure 8.6(a) is obtained from the stabilized FEM simulation, while Figure 8.6(b) is obtained without any stabilization procedure. Due to the low permeability, spatial oscillations of pore pressure occur in the standard equal-order THM element, while the stabilized equal-order THM element is able to deliver smooth pore pressure. On the other hand, Figure 8.7 compares the temperature at time = 1 second from the stabilized

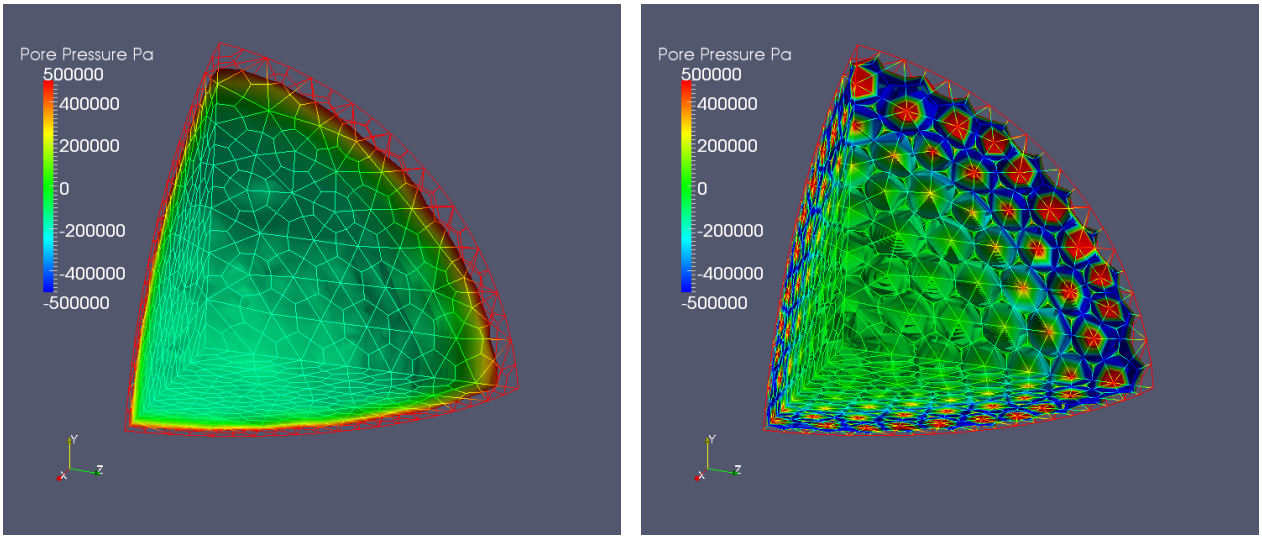

(a) Stabilized FEM response

(b) Standard FEM response

Figure 8.6: *Pore Pressure Profile of undrained porous sphere in heat bath.*

and standard FEM simulations. Since the thermal conductivity is relatively high, one may expect that the temperature would not exhibit any spatial oscillation even with standard FEM simulations. Yet, the simulation results show that the coupling between pore-fluid diffusion and heat transfer alone is significant enough to trigger spatial oscillation in the temperature field. This example demonstrates that the spurious oscillation of the temperature field can be triggered by an unstable pore pressure field, even when the thermal diffusivity is high. On the other hand, results demonstrated in Figures 8.6 and 8.7 indicate that the stabilization procedure is able to eliminate the spurious oscillations in both pore pressure and temperature. As reported in Tezduyar and Osawa [2000], White and Borja [2008a], Sun et al. [2013d], stabilization procedures may eliminate spurious oscillations, but it may also over-diffuse the numerical solutions and lead to incorrect conclusion. To determine whether the stabilization procedure proposed in Section 8.2.4 is able to eliminate spurious modes without over-diffusing the solutions, we conduct two numerical simulations on the undrained sphere, one with stabilization (i.e., $\alpha = 1$), and a control test without stabilization (i.e., $\alpha = 0$).

Figure 8.8 compares the temperature and pore pressure at the center of the globally undrained sphere. The thermal responses shown in Figure 8.8(a) indicate that the stabilization procedure does not lead to significant changes in thermal responses. The hydraulic responses exhibited in Figure 8.8 indicate that a large stabilization parameter may alter the simulated hydraulic responses at the undrained limit and steady steady responses are not significantly affected by the stabilization procedure. Figure 8.9 shows the surface displacement obtained with different stabilization parameters. Again, we note that the discrepancies among standard and stabilized responses are insignificant in the transient and steady state regimes. The results presented in this example indicate that the stabilization procedure is able to eliminate spurious oscillations even when permeability is very low. Nevertheless, over-diffusion may occur if the stabilization parameter assigned in the simulations is larger than the optimal value. The rough estimation of the optimal value described in Section 8.2.4 seems to be working for this particular problem. However, the optimal value of stabilization parameters is usually problem-dependent, and its determination should be done with cautious.

To study how the selection of stabilization parameters affects the convergence rate, we conduct additional simulations with stabilization parameter $\alpha = 0, 1, 10$ and 100. Table 8.2 shows the residual norms of the Newton-Raphson algorithm taken at the first time step when the undrained sphere has just been put into the

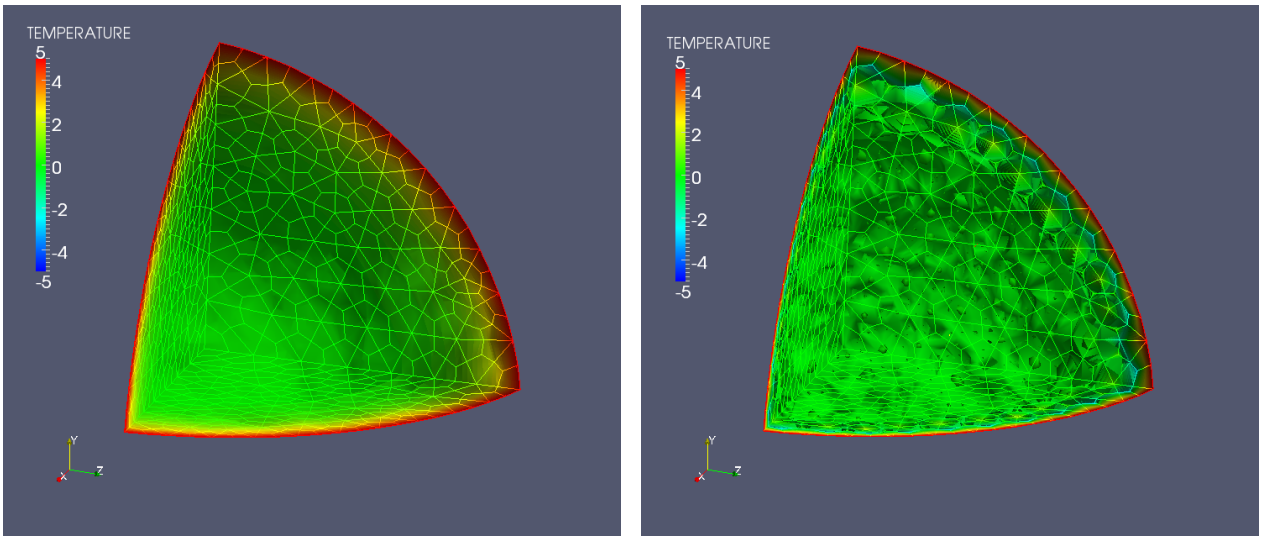

(a) Stabilized FEM response

(b) Standard FEM response

Figure 8.7: *Temperature Profile of undrained porous sphere in heat bath.*

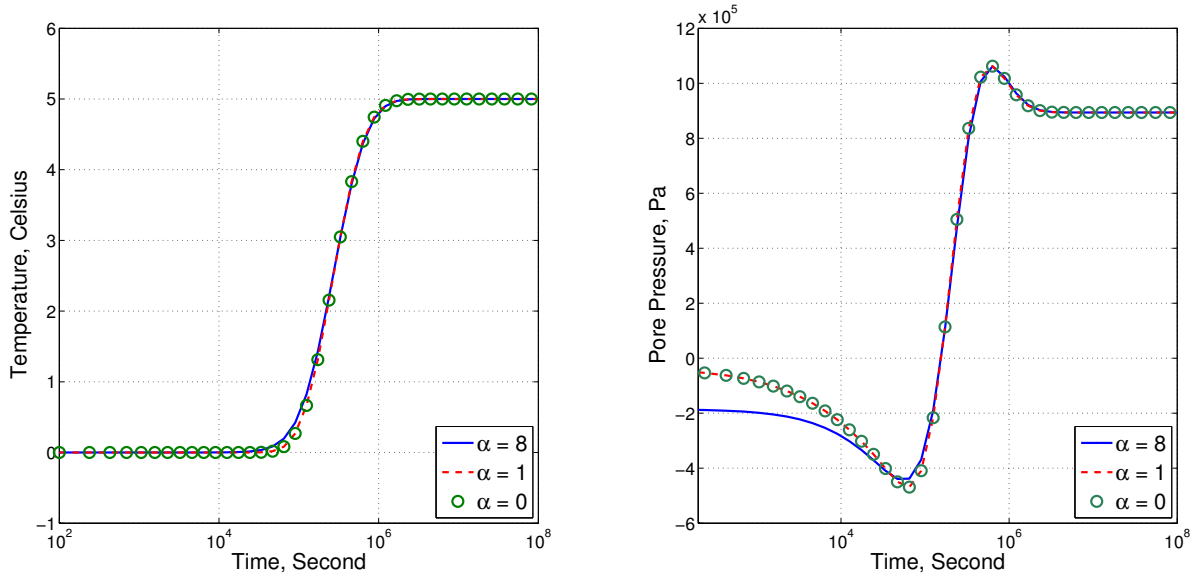

(a) Temperature at Center

(b) Pore Pressure at Center

Figure 8.8: *Time-history of the (a) temperature and (b) pore pressure at the center of the undrained sphere. The stabilization parameter equals to 0 (green dot), 1 (red dash line), and 8 (blue line).*

heat bath. The residual norms of the trial step and the first 4 iteration steps are recorded. The numerical experiment indicates that while increasing the value of stabilization parameter α does lead to noticeable higher residual at the first two iterations, the convergence rate is not severely affected by the choice of the stabilization parameter.

8.4.2 Bi-axial Undrained Compression Test With Insulated Boundaries

The second example deals with the simulation of a bi-axial undrained compression test. Our goal here is to demonstrate that the nonlinear coupling effect, as depicted in Figure 8.4, has been fully implemented in the finite element model and to assess how the coupling mechanism evolves before and after the shear band is formed.

A rectangular sample of homogeneous thermo-sensitive elasto-plastic material of $4\text{cm} \times 1\text{cm} \times 14\text{cm}$ is

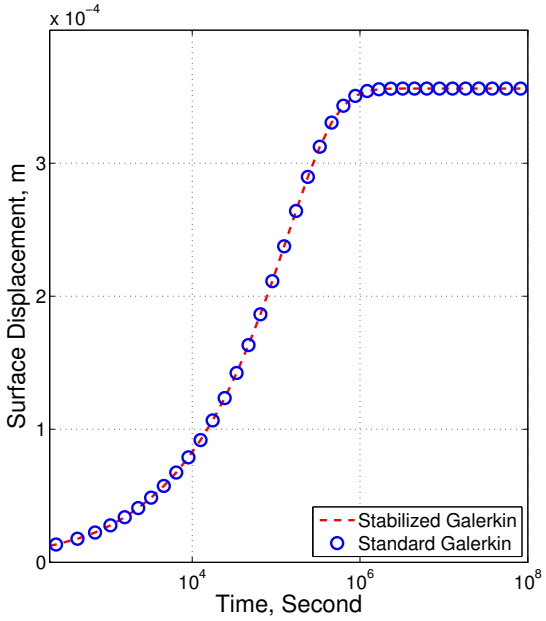

Figure 8.9: *Radial displacement of the boundary of the undrained sphere. The stabilization parameter equals to 0 (green dot), 1 (red dash line), and 8 (blue line).*

	$\alpha = 0$	$\alpha = 1$	$\alpha = 10$	$\alpha = 100$
Trial Step	5.911e-01	5.911e-01	5.911e-01	5.911e-01
Iteration 1	2.168e+01	4.446e+01	1.049e+02	1.538e+02
Iteration 2	4.058e-03	1.559e-02	6.413e-02	1.099e-01
Iteration 3	2.075e-10	2.349e-10	1.495e-09	3.720e-09
Iteration 4	1.327e-10	1.316e-10	1.323e-10	1.426e-10

Table 8.2: *Residence norm (square root of the inner product of residual column vector) of the heated undrained sphere simulations at the first 4 iteration steps.*

.

subjected to a prescribed vertical displacement on the top surface of the specimen, while the bottom of the specimen is fixed. The loading rate is -1.4cm/hour and the vertical displacement remains constant after reaching -1.4cm. The specimen is globally undrained and thus no-fluid-flux boundary conditions are prescribed at all six surfaces. To simplify the problem, gravity is neglected for this small specimen and we also assumed that no phase transition occurred in both the fluid and solid constituents. The temperature is initially uniform at ambient value (zero degree). All six surfaces are thermally insulated and thus no-thermal-flux condition applied to these surfaces. In other words, both the pore pressure and temperature fields have no corresponding Dirichlet boundary condition. To control where the shear band initiates, the right hand side of the specimen is tapered at $z = 7$cm, as shown in Figure 8.10. The material parameters used to conduct these simulations are listed in Table 8.3.

One key departure of this numerical example from previous work on thermo-hydro-mechanics is that it takes account of the plastic dissipation in the balance of energy equation. For the Von Mises J2 plasticity with no mechanical hardening, the thermomechanical dissipation D_{mech} reads [Simo and Miehe, 1992],

$$D_{\text{mech}} = \sqrt{\frac{2}{3}}\dot{\epsilon^p}\Big[\sigma_Y(\theta) - \theta\frac{\partial\sigma_Y(\theta)}{\partial\theta}\Big]\,, \tag{8.109}$$

where ϵ^p is the equivalent plastic strain, $\partial\sigma_Y\theta/\partial\theta$ is the thermal softening coefficient and σ_Y is the flow stress, which corresponds to the Mises yield criterion,

$$||\,\text{dev}[\boldsymbol{\tau}']|| - \sqrt{\frac{2}{3}}\sigma_Y \leq 0 \;\;;\;\; \boldsymbol{\tau}' = \boldsymbol{P}' \cdot \boldsymbol{F}^T\,. \tag{8.110}$$

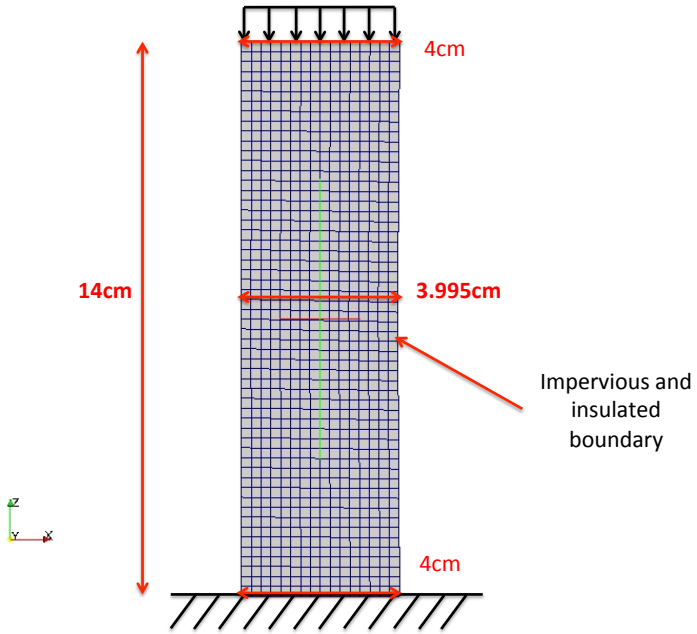

Figure 8.10: *Description of the geometry, boundary and loading conditions of the bi-axial compression problem.*

Parameter	Description	Value	Unit
E	Young's modulus	2000	MPa
ν	Poisson's ratio	0.3	dimensionless
σ_Y	Initial Yield Strength	100	MPa
$\partial\sigma_Y/\partial\theta$	Thermal Hardening Parameter	-1.6	MPa/°C
H	Mechanical Hardening Modulus	0	MPa
T_o	Reference Temperature	0	°C
α_s	Skeleton Thermal Expansion	8.3×10^{-6}	1/°C
α_f	Pore-fluid Thermal Expansion	6.9×10^{-6}	1/°C
ρ_s	Solid Constituent Density	2700	kg/m^3
ρ_f	Fluid Constituent Density	1000	kg/m^3
c_s	Solid Specific Heat	1700	J/kg/°C
c_f	Fluid Specific Heat	4200	J/kg/°C
k_θ^s	Solid Thermal Conductivity	1.0	W/m/°C
k_θ^f	Fluid Thermal Conductivity	100.0	W/m/°C
K_s	Solid Grain Bulk Modulus	50	GPa
K_f	Fluid Bulk Modulus	20	GPa
k_o	Kozeny-Carmen Coefficient	1×10^{-17}	m/s
μ	Viscosity	1.0×10^{-3}	Pa · s
ϕ^f	Initial Porosity	0.25	dimensionless

Table 8.3: *Material properties of the specimen in non-isothermal condition.*

Solid Responses

The mechanical response is influenced by the pore-fluid trapped inside the specimen and the thermal diffusion. Nevertheless, since there is no heat source in the boundary, the thermal effect on the mechanical response is insignificant. Figure 8.11 shows the spatial distribution of equivalent plastic strain at various time during the bi-axial loading test. We found that plastic strain first initiates at the left lower corner of the specimen at around 900 seconds. The region with plastic strain enlarges between 900 seconds and 3600 seconds, while a shear

band is formed at the defect point. After 3600 seconds of simulation, the vertical displacement is hold between 3600 seconds and 7200 seconds and the plastic strain distribution remains almost identical.

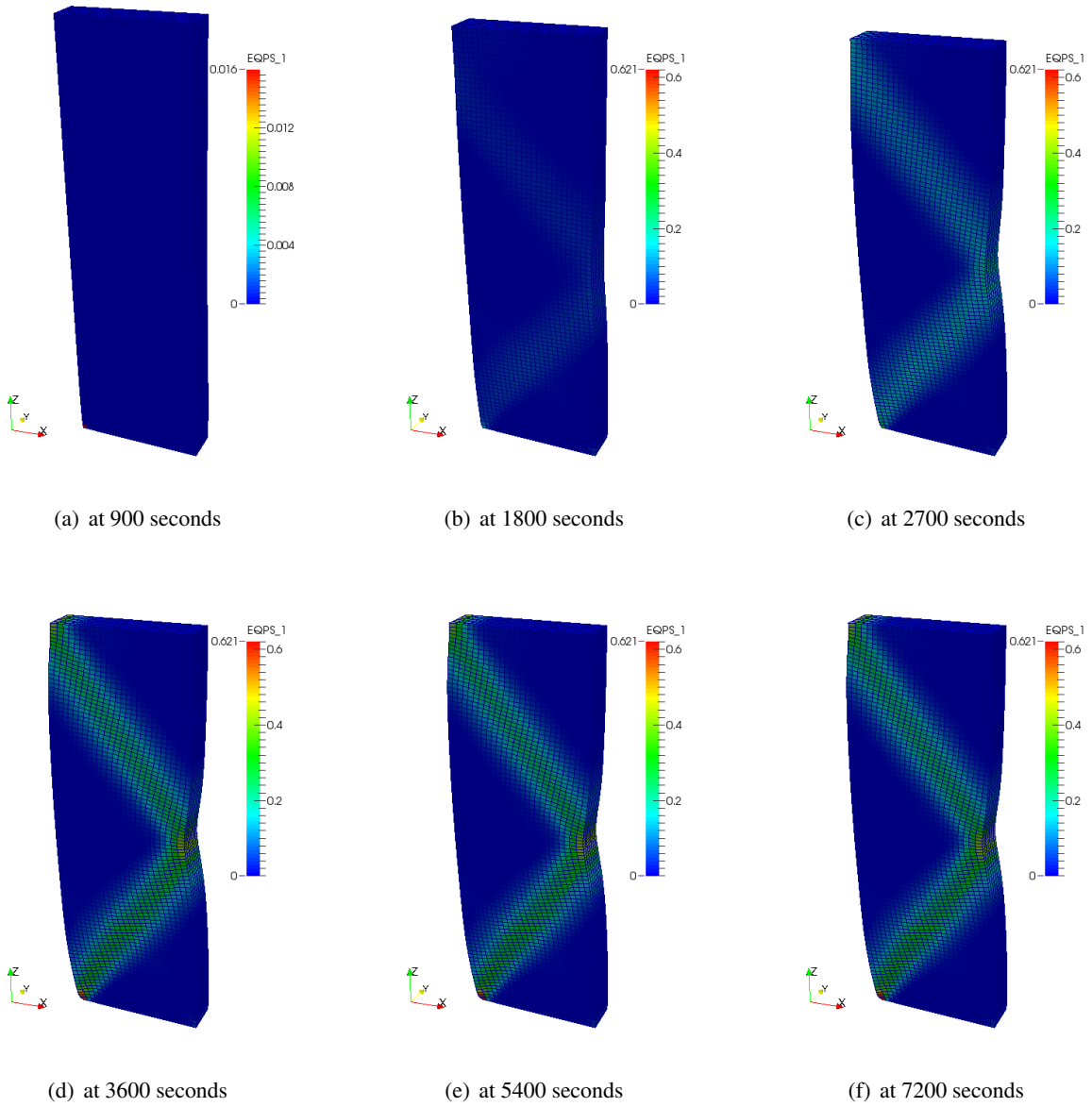

(a) at 900 seconds (b) at 1800 seconds (c) at 2700 seconds

(d) at 3600 seconds (e) at 5400 seconds (f) at 7200 seconds

Figure 8.11: *Equivalent plastic strain at various time during the biaxial loading test.*

Since the bulk moduli of the solid and fluid constituents are both one order higher than the bulk modulus of the solid skeleton, the global undrained response of the material is expected to be nearly isochoric if the specimen is under the isothermal condition. Nevertheless, as the thermo-hydro-mechanical simulation is run under the non-isothermal condition, the solid skeleton may expand or shrink due to temperature change. This temperature change is due to the mechanical plastic work that converts into heat. The heat in return causes expansion of the solid skeleton. Figures 8.12 and 8.13 show the Jacobian of the deformation gradient, $\det \boldsymbol{F}$ and the (Eulerian) porosity ϕ^{f} of the solid skeleton at different time during the bi-axial loading. Due to the globally undrained status, both the Jacobian and porosity do not change much before the onset of plastic yielding and shear band as shown in Figures 8.12(a) and 8.13(a). This nearly incompressible response also indicates that structural heating has negligible influence on temperature for this particular simulation. On the other hand, the solid skeleton exhibits a noticeable volmetric expansion/contraction pattern inside the shear band at 3600 seconds after the vertical loading is prescribed. We record the maximum and minimum of the Jacobian changing from 1 to 1.05 and 0.76 respectively, while the maximum and minimum of the porosities also change 0.25 to 0.26 and 0.19 respectively after the shear band is formed, as shown in Figures 8.12(c) and 8.13(c). This

pattern is located at the region where plastic deformation is concentrated (as shown in Figure 8.11). Due to the coupling of the thermo-hydro-mechanical processes, this plastic work inside the shear band may trigger multiple deformation mechanism. For instance, the plastic work that converted into heat may cause volumetric expansion of both the solid and fluid constituents, but also lead to the shrinkage of the yield surface in stress space and more plastic strain to be accumulated. Meanwhile, as porosity changes due to the thermal effect, both the thermal and hydraulic diffusivities also changes accordingly.

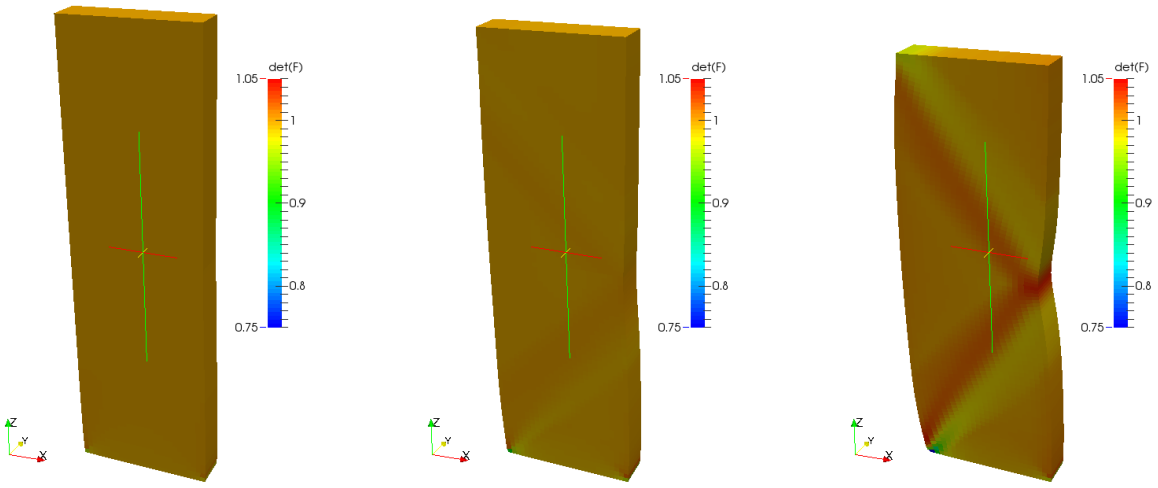

(a) at 900 seconds (b) at 1800 seconds (c) at 3600 seconds

Figure 8.12: *Determinant of the deformation gradient at various time during the biaxial loading test.*

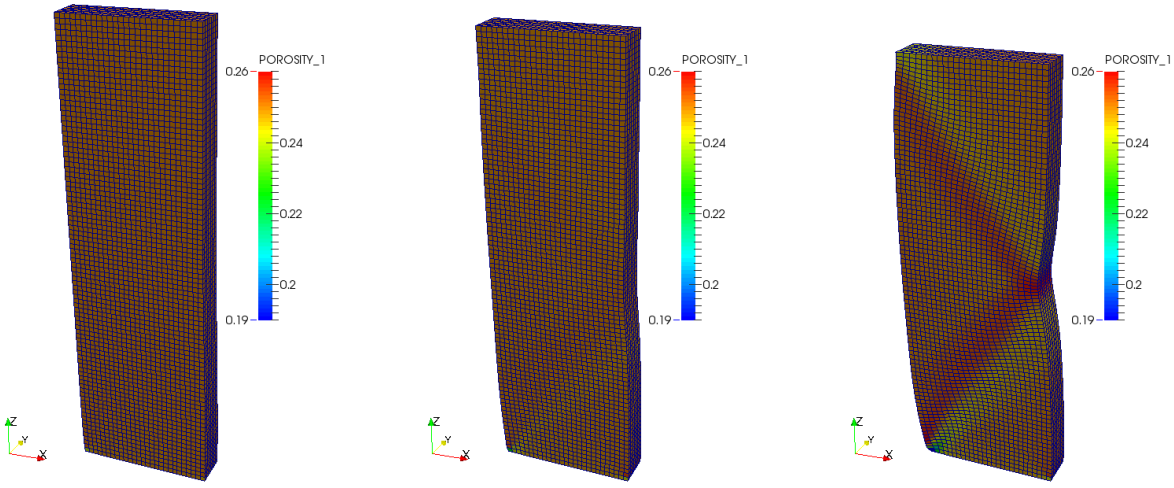

(a) at 900 seconds (b) at 1800 seconds (c) at 3600 seconds

Figure 8.13: *Porosity at various time during the biaxial loading test.*

Heat Transfer

Since the surface of the specimen is thermally insulated, the temperature increase in the specimen is due to the structural heating and plastic dissipation. Figure 8.14 shows how temperature distributes in the specimen during the ramp-and-hold loading. We observe that temperature first raised in the plastic zone, as the vertical

displacement is accumulating between t = 0 and t = 3600 seconds. The heat generated by the plastic work then transfers in the solid specimen through two mechanisms, the convection due to pore fluid transport, and the thermal diffusion. In this particular simulation, the effective permeability is very low (10×10^{-19} m/s), and thus the heat transfer process is dominated by the thermal diffusion. As a result, temperature first raised in the region where plastic strain initiated, while the thermal boundary layer gradually propagates. As shown in Figure 8.14, the thermal diffusion continues when no more displacement is prescribed between t=3600 seconds and t= 7200 seconds. Since the equivalent plastic strain becomes stable at this phase, the heat source vanishes and the spatial gradient of temperature reduces. In particular, the maximum and minimum temperature changes from 2.28 and 1.12 Celsius at t= 3600 seconds to 1.79 and 1.71 at t= 7200 seconds.

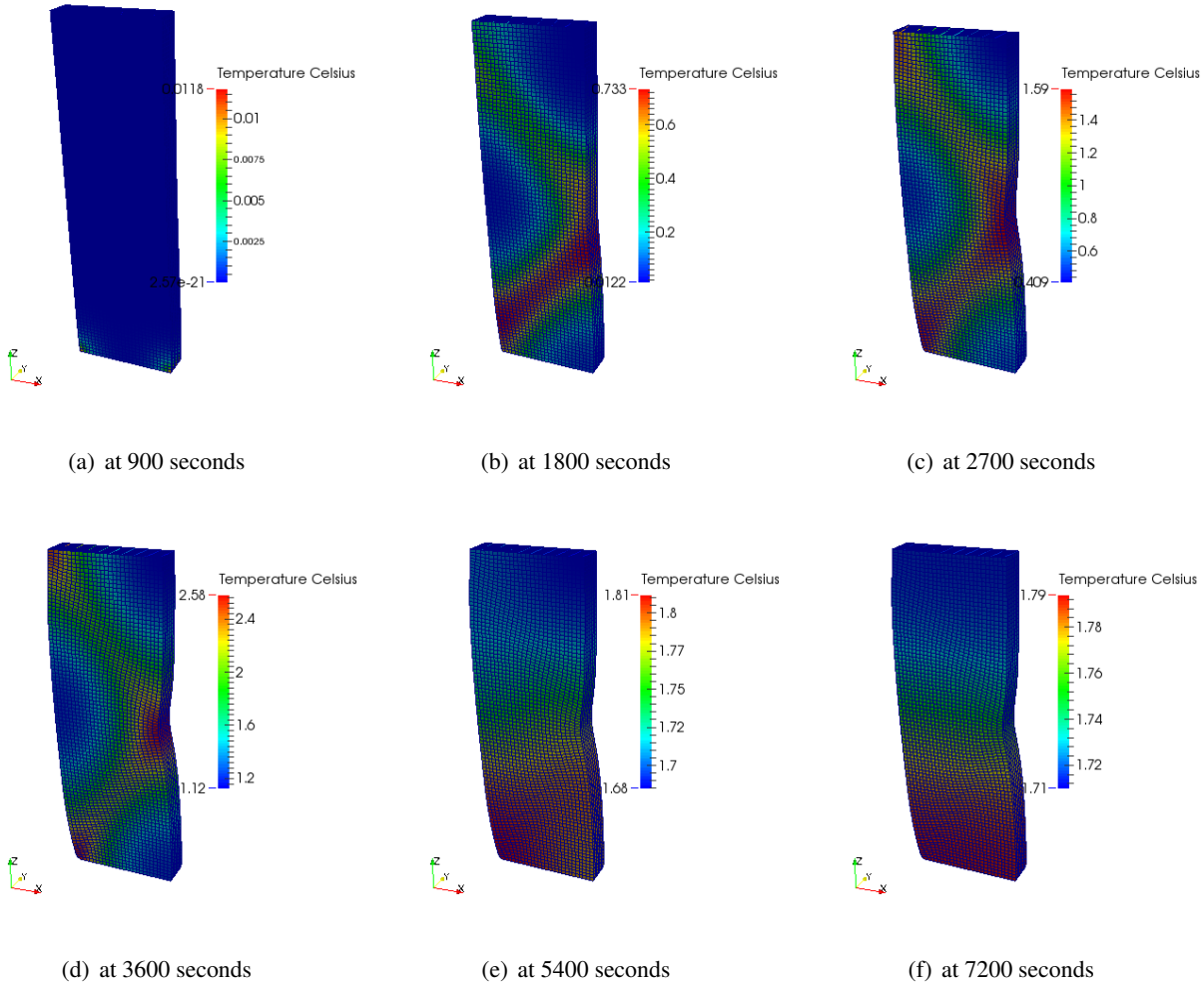

(a) at 900 seconds (b) at 1800 seconds (c) at 2700 seconds

(d) at 3600 seconds (e) at 5400 seconds (f) at 7200 seconds

Figure 8.14: *Temperature at various time during the biaxial loading test.*

Pore-fluid Flow

The pore-fluid inside the specimen is trapped inside the specimen due to the no-flux boundary condition. Figure 8.15 shows how pore pressure distributes during the ramp-and-hold loading. Due to the low permeability of the specimen, the excess pore pressure easily builds up in the specimen between t = 0 and t = 3600 seconds due to the solid skeleton deformation. While this excess pore pressure may dissipate, the low permeability of the specimen and the globally undrained boundary condition may both cause the pore pressure taking longer time to reach steady state. As a result, the pore pressure at the end of the simulations remains less evenly distributed than the temperature. Furthermore, due to the thermal effect on the solid and fluid constituents, temperature may affect the amount of excess pore pressure accumulated in the pores. By comparing Figure 8.15 with Figure 8.14, we notice that the hotter region generally has higher pore pressure, although the distributions of pore pressure and temperature do not resemble the same pattern.

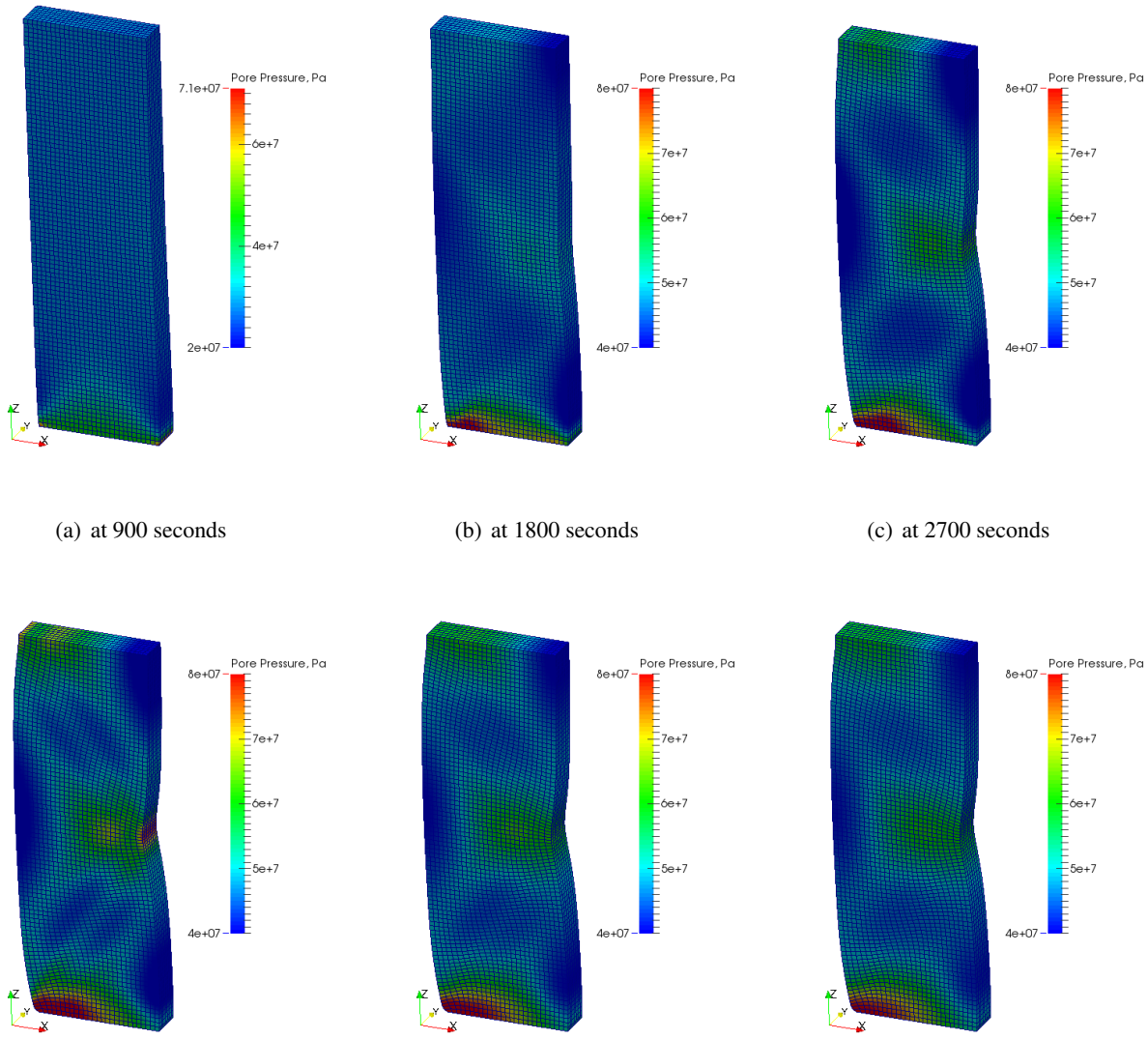

(a) at 900 seconds (b) at 1800 seconds (c) at 2700 seconds

(d) at 3600 seconds (e) at 5400 seconds (f) at 7200 seconds

Figure 8.15: *Pore Pressure at various time during the biaxial loading test.*

Refinement Study

To assess the mesh sensitivity of the thermo-hydro-mechanical responses, a mesh refinement study is conducted. Figure 8.16 shows the three meshes obtained from subdivision refinement. The total number of the finite elements are 448, 3584 and 28672 accordingly. Figure 8.17 shows the equivalent plastic strain accumulated in the three finite element meshes at the end of the simulation. While the plastic zone remains very similar to all three meshes, it is clear that the finer mesh tends to accumulate higher plastic strain in the shear band. This mesh dependence is difference than the dynamics simulation of isothermal porous media in [Zhang et al., 1999b] where equivalent plastic strain is relatively insensitive to the mesh refinement even though shear band width is found to be narrower in fine meshes. The porosity, which depends on the the volumetric deformation, temperature and pore pressure, also exhibits mesh dependence as shown in Figure 8.18.

Presumably, both thermo-mechanical and hydro-mechanical coupling effects may both introduce rate-dependence on the mechanical responses. Nevertheless, the results demonstrated in Figure 8.17 indicate that this induced rate-dependence is not sufficient to regularize the problem in the transient case. Mesh dependence is also observed in the temperature and pore pressure distribution, as shown in Figures 8.19 and 8.20 respectively. The temperature of the shear band in the fine mesh is found to be higher. This is mainly attributed to the fact that temperature increases inside the plastic strain is caused by plastic dissipation. On the other hand, the

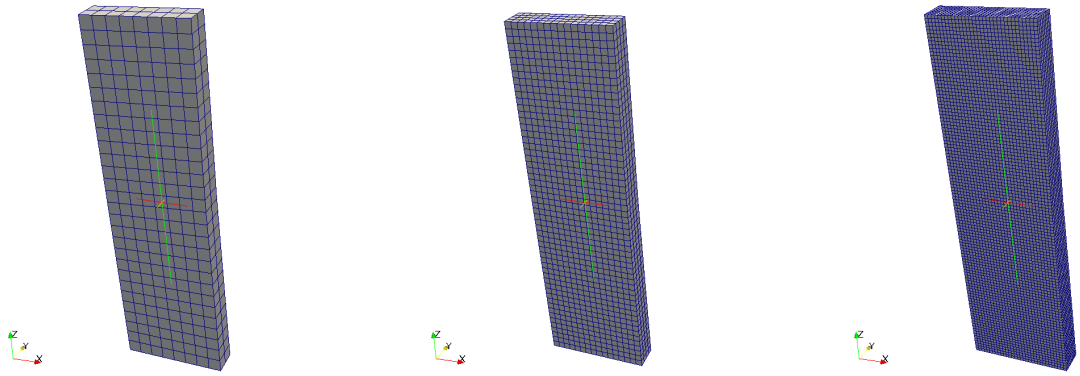

(a) Coarse Mesh (b) Medium Mesh (c) Fine Mesh

Figure 8.16: *Meshes used in refinement study.*

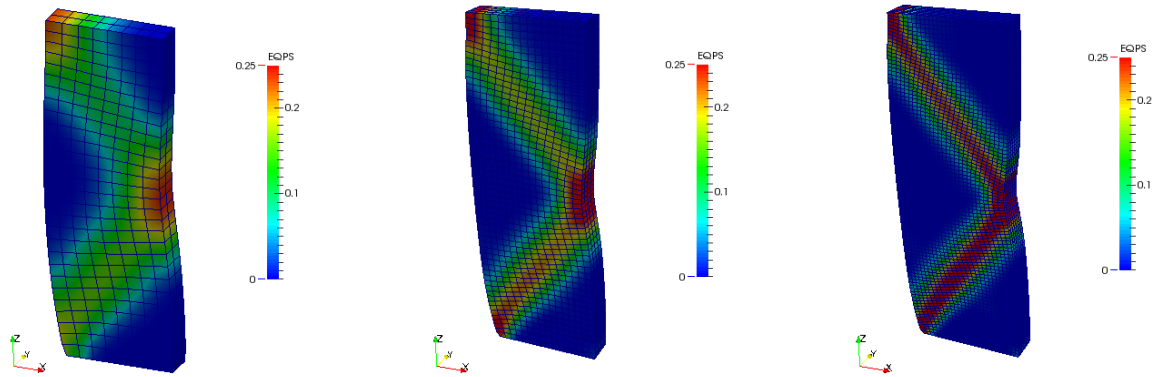

(a) Coarse Mesh (b) Medium Mesh (c) Fine Mesh

Figure 8.17: *Equivalent plastic strain at t= 7200 seconds in three meshes.*

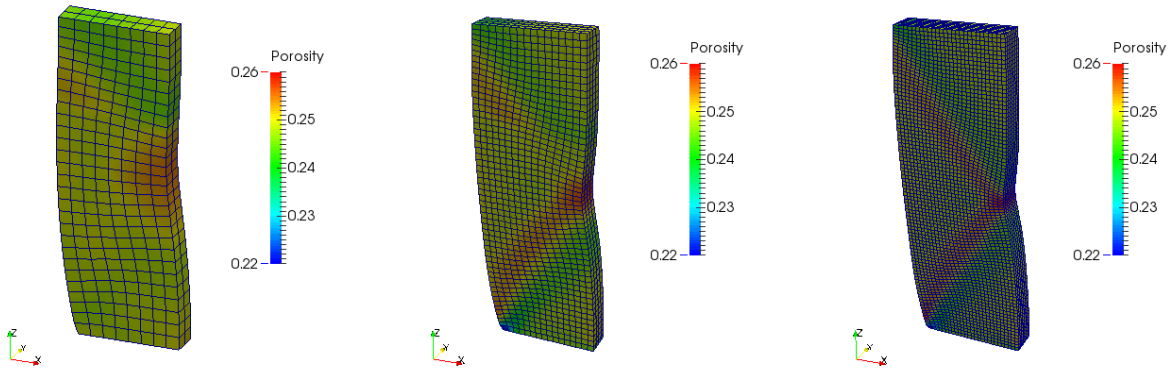

(a) Coarse Mesh (b) Medium Mesh (c) Fine Mesh

Figure 8.18: *Porosity at t= 7200 seconds in three meshes.*

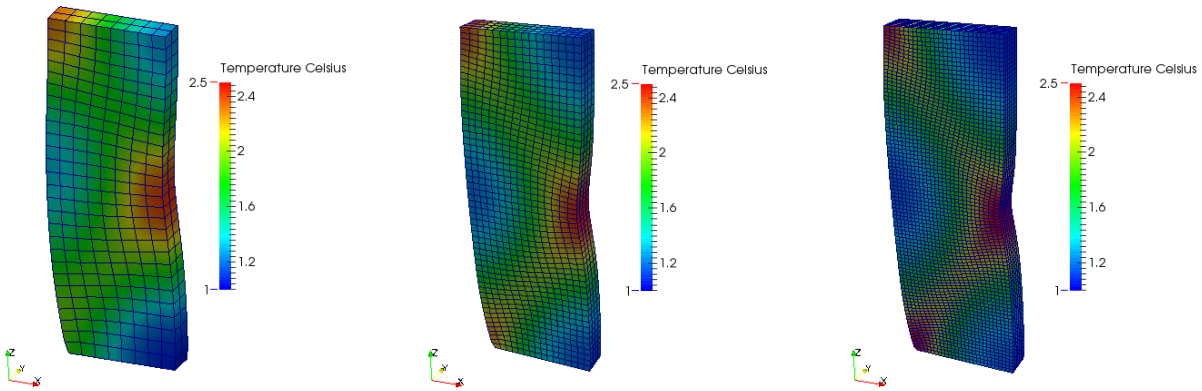

(a) Coarse Mesh (b) Medium Mesh (c) Fine Mesh

Figure 8.19: *Temperature at t= 7200 seconds in three meshes.*

pore pressure is not concentrated in the shear band as shown in Figure 8.20. The pore pressure distributions of all three meshes look similar, except at the corners where pore pressure tends to be lower at coarser mesh.

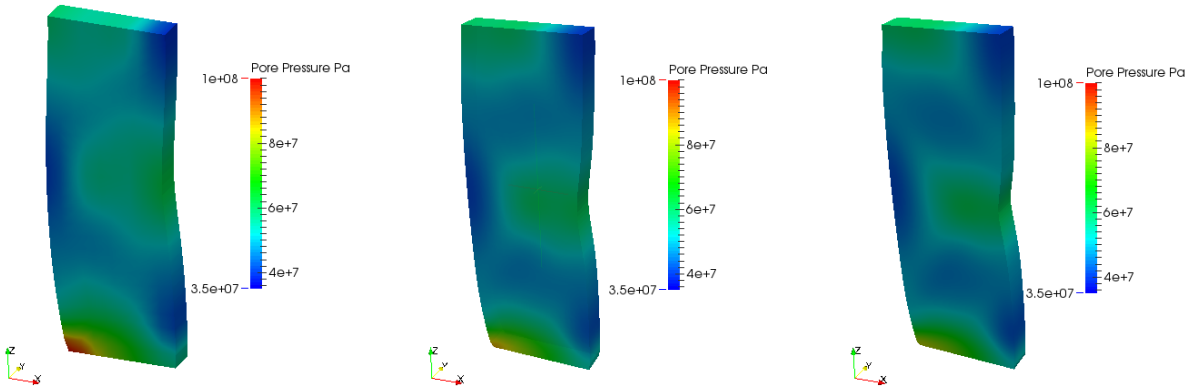

(a) Coarse Mesh (b) Medium Mesh (c) Fine Mesh

Figure 8.20: *Pore Pressure at t= 7200 seconds in three meshes.*

Figure 8.21 shows the time-history of the temperature and pore pressure at the lower left corner of the specimen. Interestingly, plastic deformation seems to play a significant role on the evolution of both pore pressure and temperature. In particular, temperature at the lower left corner is almost unchanged before the yielding. After the yielding, temperature keeps raising until the prescribed vertical displacement increment stops at 3600 seconds. While pore pressure begins to increase right after the simulation begins, the onset of plastic yielding leads to a sudden drop of pore pressure followed by another monotonic increase in pore pressure. Both temperature and pore pressure gradually decrease when vertical displacement holds still from time = 3600 to 7200 seconds.

Note that refining the mesh seems to have opposite effects on temperature and pore pressure at the corner node. While refining the mesh leads to a lower pore pressure accumulated at the corner, the refinement also cause a higher temperature. The increase of the temperature in finer mesh can be explained by the fact that the power that converts plastic dissipation into heat is higher in finer mesh as evidenced by the higher equivalent plastic strain in the fine mesh shown in Figure 8.17 when vertical displacement is increasing. Nevertheless, as heat is transferred via both diffusion and convection, the initially sharp temperature gradient triggered during the formation of shear band fades over time. At 7200 seconds after the simulation, the temperature is close to steady

state as indicated by the vanishing of sharp temperature gradient shown in Figure 8.14. This indicates that the mesh dependence of the temperature field is more severe when plastic deformation provides a significant heat source. However, this mesh dependence seems to be more significant when the material is close to adiabatic limit.

On the other hand, we find that pore pressure at the left lower corner is lower in the finer mesh. This observation is different than the isothermal shear band observed in Sun et al. [2013f] where the magnitude and distribution of pore pressure were insensitive to mesh size, even though equivalent plastic strain was also found to be higher in fine mesh. Furthermore, since the porosity and permeability at the lower left corner are both actually lower in the fine mesh, pore fluid is more likely to be trapped and build up excess pore pressure locally. The fact that the pore pressure drops but not increase upon refinement therefore indicates that the thermal diffusion process may limit the pore pressure build up.

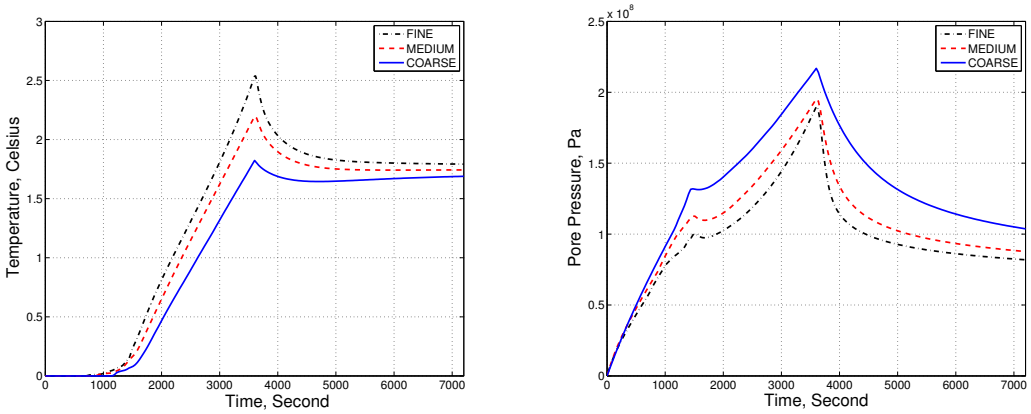

(a) Temperature (b) Pore Pressure

Figure 8.21: *Time histories of temperature and pore pressure at the lower left corner of the three meshes.*

Figure 8.22 shows the vertical force applied on the top of the specimen. The force due to the displacement prescribed at the top of the specimen is found to be around -50kN for the coarse mesh and around -48kN for the medium and fine meshes. In all three cases, the vertical force is at its peak at 3600 seconds where the displacement increment stops. In between 3600 seconds and 7200 seconds, the vertical force drops slightly. By

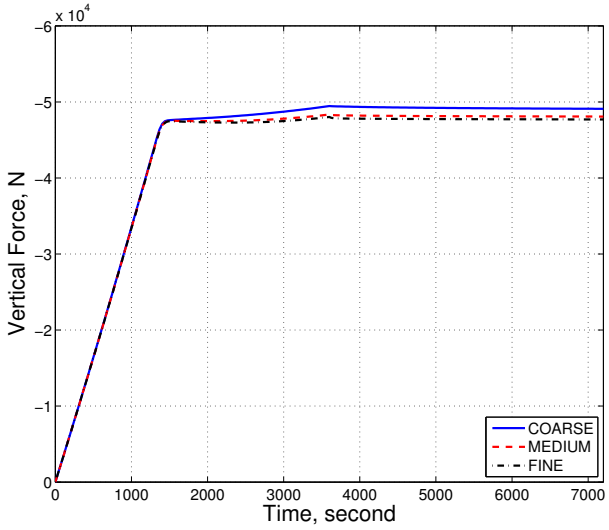

Figure 8.22: *Time-history of vertical force on the top layer of the specimen.*

comparing results from different meshes shown in Figures 8.21 and 8.22, we conclude that the thermo-hydro-

mechanical responses are sensitive to the level of refinement. While the discrepancy of the results seems to be decreased upon each refinement, it is not clear whether the solution will be converged if further refinement takes place.

Thermo-hydro-mechanical Coupling Effects Under Undrained Condition

As reported in [Zhang et al., 1999b], shear band width is influenced by the diffusivity of the pore fluid under isothermal condition. In non-isothermal condition, both pore-fluid and thermal flux may influence mechanical responses of the solid skeleton and vice versa. To determine how thermal and hydraulic diffusivities influence the thermo-hydromechanical responses, we conduct a parametric study by varying the permeability and thermal conductivity.

In the first set of tests, we conduct two numerical simulations with material parameters listed in Table 8.3, but the thermal conductivities of both constituents are both multiplied by 100 in the first simulation and divided by 100 in the second simulation. Figure 8.23 demonstrates the temperature at 7200 seconds after the loading. As expected, the material with lower thermal conductivity reaches higher temperature. The temperature also takes longer time to dissipate. Hence, temperature is higher inside the shear band zone.

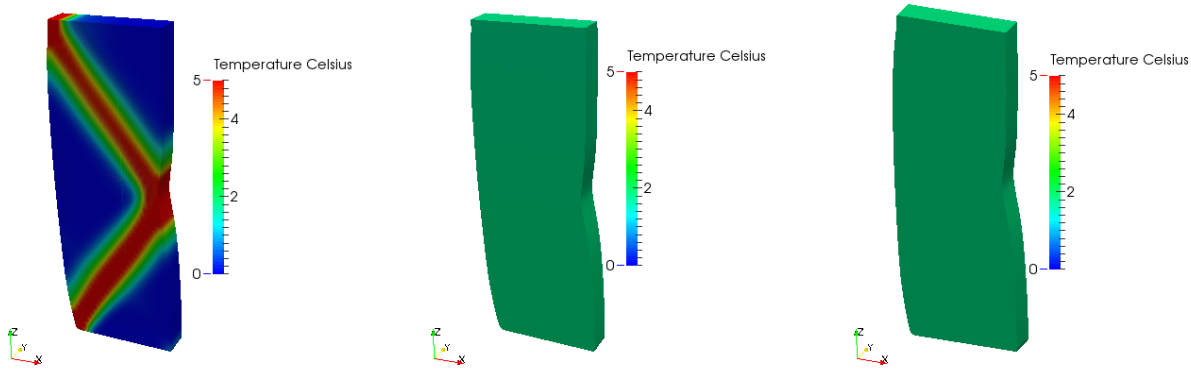

(a) Low Thermal Conductivity (b) Medium Thermal Conductivity (c) High Thermal Conductivity

Figure 8.23: *Temperature profile at time = 7200 seconds, with initial effective thermal conductivity equals to (a)* $0.013 W/m/^{\circ}C$*, (b)* $1.33 W/m/^{\circ}C$ *and (c)* $133 W/m/^{\circ}C$*.*

Interestingly, this higher temperature inside the shear band also influences the hydraulic properties. Figure 8.24 shows the pore pressure distribution and flow streamlines at 7200 seconds after the loading. By comparing Figure 8.23 and 8.24, one may notice that the pore pressure is higher and more concentrated in the shear band in the low thermal conductivity case, even though the initial effect permeability of material are the same in both simulations. Notice that all these features are lost if the heat produced by plastic dissipation is not captured in the balance of energy equation. Varying thermal conductivity nevertheless does not lead to significant changes in the plastic response, as shown in Figures 8.25 and 8.26.

In the second set of tests, we conduct two additional numerical simulations with material parameters listed in Table 8.3, but the Kozeny-Carmen coefficient is changed to $10^{-14} m/s$ and $10^{-20} m/s$ respectively. Figure 8.27 compares the temperature distribution at the end of the numerical simulations. Even though the material is globally undrained, varying permeability does introduce noticeable changes in temperature. This results indicate the importance of coupling effects. Figure 8.28 shows the flow streamline obtained form simulations with permeability coefficient equals to (a) 10^{-16} m/s, (b) 10^{-19} m/s and (c) 10^{-22} m/s. The permeability material clearly has a significant impact on both the magnitude of the pore pressure and the flow patterns in the undrained specimen. Interesting, we found that the plastic responses are not sensitive to changes of permeability and thermal conductivity under the globally undrained and insulated conditions, as shown in Figures 8.29 and 8.30.

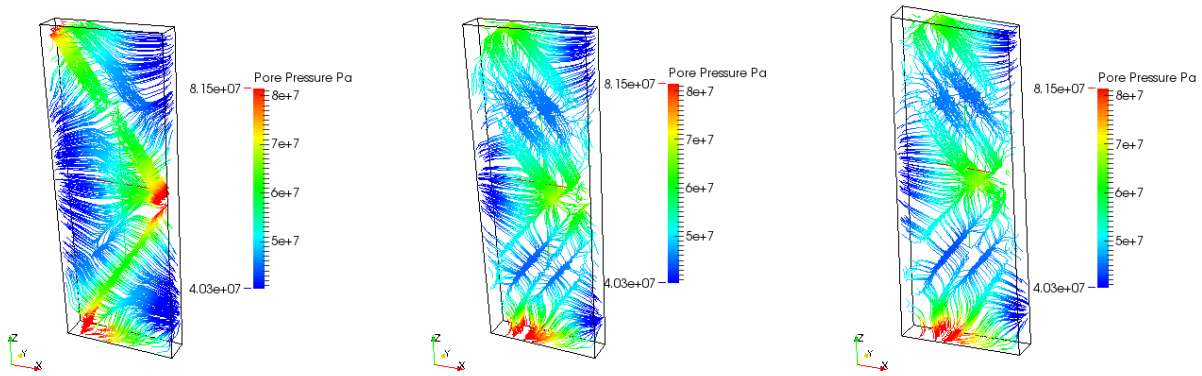

(a) Low Thermal Conductivity (b) Medium Thermal Conductivity (c) High Thermal Conductivity

Figure 8.24: *Flow streamlines at time = 7200 seconds, with initial effective thermal conductivity equals to (a)* $0.013 W/m/^{\circ}C$*, (b)* $1.33 W/m/^{\circ}C$ *and (c)* $133 W/m/^{\circ}C$*.*

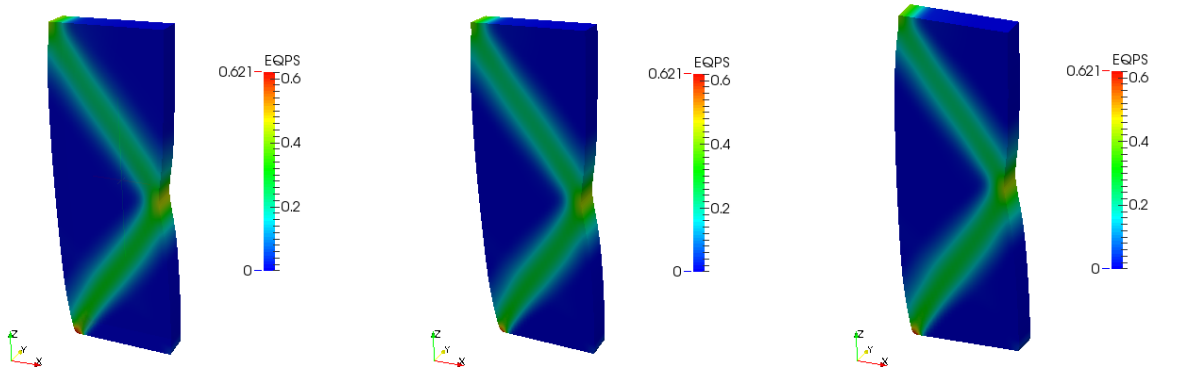

(a) Low Thermal Conductivity (b) Medium Thermal Conductivity (c) High Thermal Conductivity

Figure 8.25: *Equivalent plastic strain at time = 7200 seconds, with initial effective thermal conductivity equals to (a)* $0.013 W/m/^{\circ}C$*, (b)* $1.33 W/m/^{\circ}C$ *and (c)* $133 W/m/^{\circ}C$*.*

Convergence Rate and Stabilization Parameters

Finally, additional biaxial compression simulations with $\alpha = 0, 1, 10$ and 100 were conducted to determine whether the value of the stabilization parameter has a noticeable impact on the convergence rate. Table 8.4 shows the residual norms of the Newton-Raphson algorithm taken at the second time step when a small displacement increment is applied on the top of the domain. The residual norms of the trial step and the first 4 iteration steps are again recorded. The finding is consistent with the results obtained from the heated undrained sphere problem. The numerical experiment again indicates that increasing the value of stabilization parameter α does lead to a slightly higher residuals, but the difference in convergence rate is within an order even when the stabilization parameter α is increased by 10000%. Whether one may expect similar trends for all THM boundary value problems remains unknown, but the two numerical experiments seem to suggest that the convergence rate is not very sensitive to the magnitude of the stabilization parameter.

8.5 Conclusion

The new contribution of this work is twofold. First, we establish a large deformation thermo-hydro-mechanics theory that fully incorporates the influences of the geometrical nonlinearity on the full coupled solid deformation, pore-fluid diffusion and heat transfer processes. Using the automatic-differentiation technique to

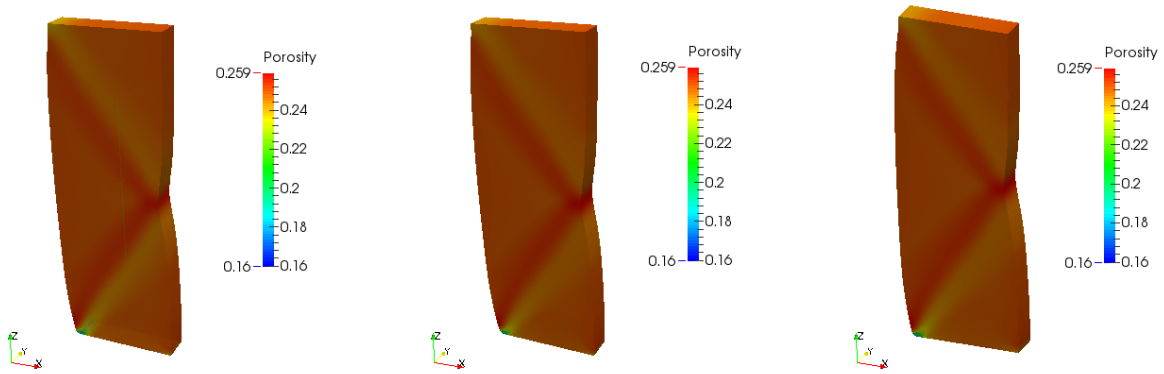

(a) Low Thermal Conductivity (b) Medium Thermal Conductivity (c) High Thermal Conductivity

Figure 8.26: *Porosity at time = 7200 seconds, with initial effective thermal conductivity equals to (a)* $0.013 W/m/^{\circ}C$*, (b)* $1.33 W/m/^{\circ}C$ *and (c)* $133 W/m/^{\circ}C$*.*

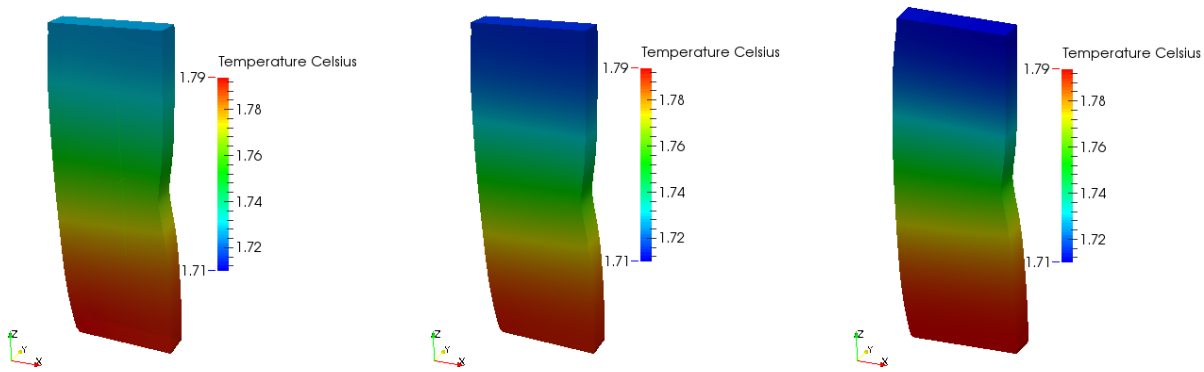

(a) Low Permeability (b) Medium Permeability (c) High Permeability

Figure 8.27: *Temperature profile at time = 7200 seconds, with permeability coefficient equals to (a)* 10^{-16} *m/s, (b)* 10^{-19} *m/s and (c)* 10^{-22} *m/s.*

	$\alpha = 0$	$\alpha = 1$	$\alpha = 10$	$\alpha = 100$
Trial Step	7.275e-04	7.275e-04	7.275e-04	7.275e-04
Iteration 1	2.702e-01	2.667e-01	2.634e-01	2.611e-01
Iteration 2	2.735e-07	2.939e-07	3.297e-07	3.649e-07
Iteration 3	8.147e-11	8.139e-11	8.255e-11	1.426e-10
Iteration 4	6.205e-11	6.343e-11	6.525e-11	8.694e-11

Table 8.4: *Residence norm (square root of the inner product of residual column vector) of biaxial compression simulation at the first 4 iteration steps.*

.

simplify the implementation process, the nonlinear relations between porosity, permeability and thermal conductivity is fully captured. Secondly, we introduce a stabilized equal-order mixed finite element model that provides stable numerical solutions without over-diffusion. The spatial stability is maintained even when pore-fluid and thermal diffusivities are significantly different. To the best of the author's knowledge, this is the first time the large deformation thermo-hydro-mechanical behavior of porous media is captured with an equal-order finite element in the geometrical nonlinear regime. Our numerical results indicate that such a stabilization procedure is able to eliminate the spurious oscillations even near the undrained and adiabatic regimes. Never-

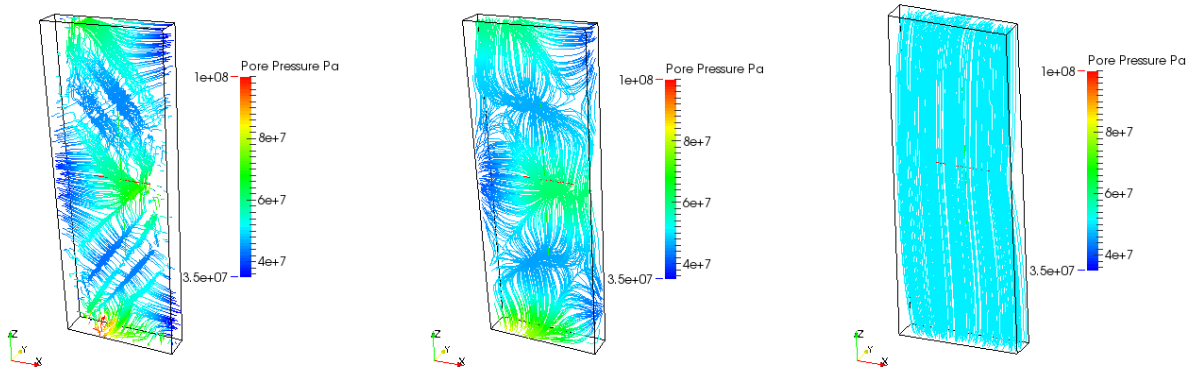

(a) Low Permeability (b) Medium Permeability (c) High Permeability

Figure 8.28: *Flow streamlines at time = 7200 seconds, with permeability coefficient equals to (a)* 10^{-16} *m/s, (b)* 10^{-19} *m/s and (c)* 10^{-22} *m/s.*

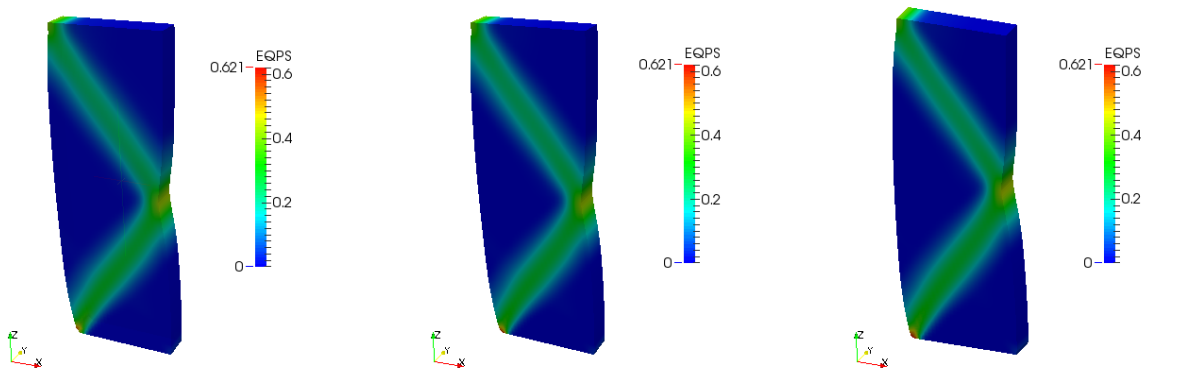

(a) Low Permeability (b) Medium Permeability (c) High Permeability

Figure 8.29: *Temperature profile at time = 7200 seconds, with permeability coefficient equals to (a)* 10^{-16} *m/s, (b)* 10^{-19} *m/s and (c)* 10^{-22} *m/s.*

theless, it is acknowledged that the stabilization parameter introduced in this paper may require tuning through trial-and-error. The numerical simulations also exhibit mesh dependence, which indicate that a regularization procedure (e.g. nonlocal scaling [Bazant and Jirásek, 2002, Sun and Mota, 2014], gradient plasticity Fleck et al. [1994]) is necessary to circumvent the mesh dependence. These shortcomings will be addressed in future studies.

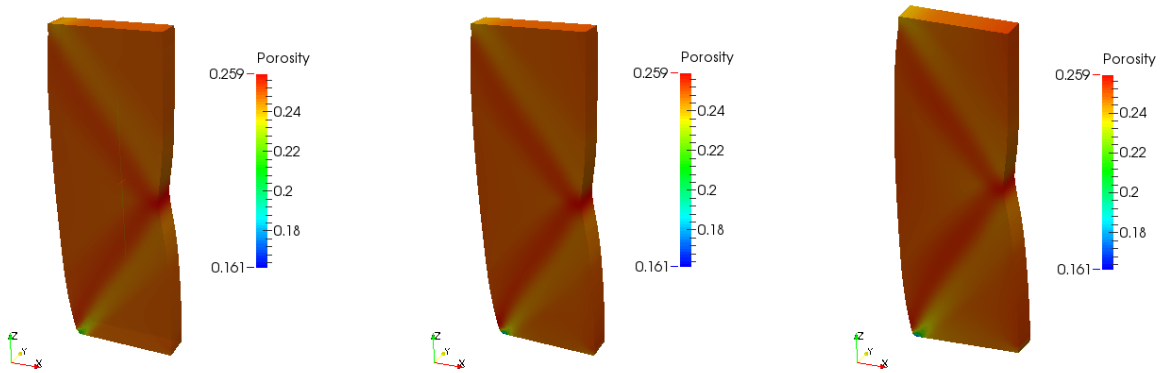

(a) Low Permeability (b) Medium Permeability (c) High Permeability

Figure 8.30: *Temperature profile at time = 7200 seconds, with permeability coefficient equals to (a)* 10^{-16} *m/s, (b)* 10^{-19} *m/s and (c)* 10^{-22} *m/s.*

Bibliography

Brian M Adams, WJ Bohnhoff, KR Dalbey, JP Eddy, MS Eldred, DM Gay, K Haskell, Patricia D Hough, and LP Swiler. Dakota, a multilevel parallel object-oriented framework for design optimization, parameter estimation, uncertainty quantification, and sensitivity analysis: Version 5.0 userâĂŹs manual. *Sandia National Laboratories, Tech. Rep. SAND2010-2183*, 2009.

Richard A Albert and John W Rudnicki. Finite element simulations of tennessee marble under plane strain laboratory testing: Effects of sample–platen friction on shear band onset. *Mechanics of materials*, 33(1): 47–60, 2001.

Eduardo E Alonso, J-M Pereira, Jean Vaunat, and Sebastia Olivella. A microstructurally based effective stress for unsaturated soils. *Géotechnique*, 60(12):913–925, 2010.

Albert Sunyer Amat. *Elastic stiffness moduli of Hostun sand*. PhD thesis, Universitat Politècnica de Catalunya. Escola Tècnica Superior d'Enginyers de Camins, Canals i Ports de Barcelona. Departament d'Enginyeria del Terreny, Cartogràfica i Geofísica, 2008 (Enginyeria Geològica), 2008.

Edward Andò, Stephen A Hall, Gioacchino Viggiani, Jacques Desrues, and Pierre Bésuelle. Grain-scale experimental investigation of localised deformation in sand: a discrete particle tracking approach. *Acta Geotechnica*, 7(1):1–13, 2012.

Francisco Armero. Formulation and finite element implementation of a multiplicative model of coupled poro-plasticity at finite strains under fully saturated conditions. *Computer methods in applied mechanics and engineering*, 171(3):205–241, 1999.

Lawrence Ferdinand Athy. Density, porosity, and compaction of sedimentary rocks. *AAPG Bulletin*, 14(1): 1–24, 1930.

Ferdinando Auricchio, L Beirão da Veiga, Carlo Lovadina, and Alessandro Reali. A stability study of some mixed finite elements for large deformation elasticity problems. *Computer methods in applied mechanics and engineering*, 194(9):1075–1092, 2005.

Ferdinando Auricchio, Lourenço Beirão da Veiga, Carlo Lovadina, Alessandro Reali, Robert L Taylor, and Peter Wriggers. Approximation of incompressible large deformation elastic problems: some unresolved issues. *Computational Mechanics*, pages 1–15, 2013.

Ivo Babuška. The finite element method with lagrangian multipliers. *Numerische Mathematik*, 20(3):179–192, 1973.

Katalin Bagi. Stress and strain in granular assemblies. *Mechanics of materials*, 22(3):165–177, 1996.

K-J. Bathe. The inf-sup condition and its evaluation for mixed finite element methods. *Computers and Structures*, 79(2):243 – 252, 2001. ISSN 0045-7949. doi: 10.1016/S0045-7949(00)00123-1.

Zdenek P Bazant and Milan Jirásek. Nonlocal integral formulations of plasticity and damage: survey of progress. *Journal of Engineering Mechanics*, 128(11):1119–1149, 2002.

Zdenek P Bazant, Ted B Belytschko, and Ta-Peng Chang. Continuum theory for strain-softening. *Journal of Engineering Mechanics*, 110(12):1666–1692, 1984.

J. Bear. *Dynamics of fluids in porous media*. Elsevier Publishing Company, New York, NY, 1972.

Ken Been and Michael G Jefferies. A state parameter for sands. *Géotechnique*, 35(2):99–112, 1985.

Ted Belytschko, Jacob Fish, and Bruce E Engelmann. A finite element with embedded localization zones. *Computer methods in applied mechanics and engineering*, 70(1):59–89, 1988.

R Berger, C Kloss, A Kohlmeyer, and S Pirker. Hybrid parallelization of the liggghts open-source dem code. *Powder Technology*, 278:234–247, 2015.

M.A. Biot. General theory of three dimensional consolidation. *Journal of Applied Physics*, 12(2):155 –164, feb 1941a.

Maurice A Biot. General theory of three-dimensional consolidation. *Journal of applied physics*, 12(2):155–164, 1941b.

Alan W Bishop. The use of the slip circle in the stability analysis of slopes. *Geotechnique*, (5):7–17, 1955.

Alan Wilfred Bishop. *The principles of effective stress*. Norges Geotekniske Institutt, 1960.

AW Bishop and GE Blight. Some aspects of effective stress in saturated and partly saturated soils. *Geotechnique*, 13(3):177–197, 1963.

P.l B. Bochev, C.R. Dohrmann, and M.D. Gunzburger. Stabilization of low-order mixed finite elements for the stokes equations. *SIAM J. Numer. Anal.*, 44(1):82–101, January 2006. ISSN 0036-1429.

Ronaldo I Borja. A finite element model for strain localization analysis of strongly discontinuous fields based on standard galerkin approximation. *Computer Methods in Applied Mechanics and Engineering*, 190(11): 1529–1549, 2000.

Ronaldo I Borja. *Plasticity Modeling and Computation*. Springer, Berlin, 2013.

Ronaldo I Borja and Enrique Alarcón. A mathematical framework for finite strain elastoplastic consolidation part 1: Balance laws, variational formulation, and linearization. *Computer Methods in Applied Mechanics and Engineering*, 122(1):145–171, 1995a.

Ronaldo I Borja and Enrique Alarcón. A mathematical framework for finite strain elastoplastic consolidation part 1: Balance laws, variational formulation, and linearization. *Computer Methods in Applied Mechanics and Engineering*, 122(1):145–171, 1995b.

Ronaldo I Borja and Azad Koliji. On the effective stress in unsaturated porous continua with double porosity. *Journal of the Mechanics and Physics of Solids*, 57(8):1182–1193, 2009.

Ronaldo I Borja and Wai Ching Sun. Estimating inelastic sediment deformation from local site response simulations. *Acta Geotechnica*, 2(3):183–195, 2007.

Ronaldo I Borja, Claudio Tamagnini, and Enrique Alarcón. Elastoplastic consolidation at finite strain part 2: Finite element implementation and numerical examples. *Computer Methods in Applied Mechanics and Engineering*, 159(1):103–122, 1998a.

Ronaldo I Borja, Claudio Tamagnini, and Enrique Alarcón. Elastoplastic consolidation at finite strain part 2: finite element implementation and numerical examples. *Computer Methods in Applied Mechanics and Engineering*, 159(1):103–122, 1998b.

Ronaldo I Borja, Joshua A White, Xiaoyu Liu, and Wei Wu. Factor of safety in a partially saturated slope inferred from hydro-mechanical continuum modeling. *International Journal for Numerical and Analytical Methods in Geomechanics*, 36(2):236–248, 2012.

Ronaldo I Borja, Xiaoyu Song, Amy L Rechenmacher, Sara Abedi, and Wei Wu. Shear band in sand with spatially varying density. *Journal of the Mechanics and Physics of Solids*, 61(1):219–234, 2013.

Franck Bourrier, François Kneib, Bruno Chareyre, and Thierry Fourcaud. Discrete modeling of granular soils reinforcement by plant roots. *Ecological Engineering*, 61:646–657, 2013.

Ray M Bowen. Incompressible porous media models by use of the theory of mixtures. *International Journal of Engineering Science*, 18(9):1129–1148, 1980.

Ray M Bowen. Compressible porous media models by use of the theory of mixtures. *International Journal of Engineering Science*, 20(6):697–735, 1982.

Susanne C Brenner and Ridgway Scott. *The mathematical theory of finite element methods*, volume 15. Springer Science & Business Media, 2008.

F. Brezzi, J. Douglas, and L. D. Marini. Two families of mixed finite elements for second order elliptic problems. *Numerische Mathematik*, 47:217–235, 1985. ISSN 0029-599X.

Franco Brezzi and Michel Fortin. *Mixed and hybrid finite element methods*. Springer-Verlag New York, Inc., 1991.

M Broccardo, M Micheloni, and P Krysl. Assumed-deformation gradient finite elements with nodal integration for nearly incompressible large deformation analysis. *International journal for numerical methods in engineering*, 78(9):1113–1134, 2009.

Michael D Brothers, John T Foster, and Harry R Millwater. A comparison of different methods for calculating tangent-stiffness matrices in a massively parallel computational peridynamics code. *Computer Methods in Applied Mechanics and Engineering*, 279:247–267, 2014.

C Callari and F Armero. Analysis and numerical simulation of strong discontinuities in finite strain poroplasticity. *Computer Methods in Applied Mechanics and Engineering*, 193(27):2941–2986, 2004.

Bernard Cambou, Michel Jean, Farhang Radjaï, et al. *Micromechanics of granular materials*. Wiley Online Library, 2009.

Frédéric Cappa and Jonny Rutqvist. Modeling of coupled deformation and permeability evolution during fault reactivation induced by deep underground injection of co 2. *International Journal of Greenhouse Gas Control*, 5(2):336–346, 2011.

Arthur Casagrande. Characteristics of cohesionless soils affecting the stability of slopes and earth fills. *Contributions to soils mechanics, 1925-1940*, 23(1):13–32, 1936.

G Castellazzi and P Krysl. Patch-averaged assumed strain finite elements for stress analysis. *International Journal for Numerical Methods in Engineering*, 90(13):1618–1635, 2012.

Xavier Chateau and Luc Dormieux. Micromechanics of saturated and unsaturated porous media. *International Journal for Numerical and Analytical Methods in Geomechanics*, 26(8):831–844, 2002.

J Christoffersen, MM Mehrabadi, and S Nemat-Nasser. A micromechanical description of granular material behavior. *Journal of Applied Mechanics*, 48(2):339–344, 1981.

Steven Cooreman, D Lecompte, H Sol, J Vantomme, and Dimitri Debruyne. Elasto-plastic material parameter identification by inverse methods: Calculation of the sensitivity matrix. *International journal of solids and structures*, 44(13):4329–4341, 2007.

Eugène Cosserat and François Cosserat. Théorie des corps déformables. *Paris*, 1909.

O. Coussy. *Poromehcanics*. 2004a.

Olivier Coussy. *Poromechanics*. John Wiley & Sons, 2004b.

Olivier Coussy. Revisiting the constitutive equations of unsaturated porous solids using a lagrangian saturation concept. *International Journal for Numerical and Analytical Methods in Geomechanics*, 31(15):1675–1694, 2007.

Stephen Corteen Cowin and Stephen B Doty. *Tissue mechanics*. Springer, 2009.

Xilin Cui, Jun Li, Andrew Chan, and David Chapman. Coupled dem–lbm simulation of internal fluidisation induced by a leaking pipe. *Powder Technology*, 254:299–306, 2014.

Peter A Cundall and Otto DL Strack. A discrete numerical model for granular assemblies. *Geotechnique*, 29 (1):47–65, 1979.

Jennifer Sinclair Curtis and Berend Van Wachem. Modeling particle-laden flows: A research outlook. *AIChE journal*, 50(11):2638–2645, 2004.

Yannis F Dafalias and Majid T Manzari. Simple plasticity sand model accounting for fabric change effects. *Journal of Engineering mechanics*, 130(6):622–634, 2004.

Reint De Boer. Highlights in the historical development of the porous media theory: toward a consistent macroscopic theory. *Applied Mechanics Reviews*, 49(4):201–262, 1996.

René de Borst, Mike A Crisfield, Joris JC Remmers, and Clemens V Verhoosel. *Nonlinear finite element analysis of solids and structures*. John Wiley & Sons, 2012.

P De Buhan and L Dormieux. On the validity of the effective stress concept for assessing the strength of saturated porous materials: a homogenization approach. *Journal of the Mechanics and Physics of Solids*, 44 (10):1649–1667, 1996.

E. A. de Souza Neto, D. Perić, and D. R. J. Owen. *Computational Methods for Plasticity*. John Wiley & Sons, Ltd, 2008. ISBN 9780470694626.

Jacques Desrues and Edward Andò. Strain localisation in granular media. *Comptes Rendus Physique*, 16(1): 26–36, 2015.

Jacques Desrues and Gioacchino Viggiani. Strain localization in sand: an overview of the experimental results obtained in grenoble using stereophotogrammetry. *International Journal for Numerical and Analytical Methods in Geomechanics*, 28(4):279–321, 2004.

Alberto Di Renzo and Francesco Paolo Di Maio. Comparison of contact-force models for the simulation of collisions in dem-based granular flow codes. *Chemical Engineering Science*, 59(3):525–541, 2004.

Clark R Dohrmann and Pavel B Bochev. A stabilized finite element method for the stokes problem based on polynomial pressure projections. *International Journal for Numerical Methods in Fluids*, 46(2):183–201, 2004.

P Duhem. Le potentiel thermodynamique et la pression hydrostatique. In *Annales scientifiques de l'École Normale Supérieure*, volume 10, pages 183–230, 1893.

W Ehlers, E Ramm, S Diebels, and GA dâĂŹAddetta. From particle ensembles to cosserat continua: homogenization of contact forces towards stresses and couple stresses. *International Journal of Solids and Structures*, 40(24):6681–6702, 2003.

Wolfgang Ehlers and Bernd Scholz. An inverse algorithm for the identification and the sensitivity analysis of the parameters governing micropolar elasto-plastic granular material. *Archive of Applied Mechanics*, 77(12): 911–931, 2007.

Usama El Shamy and Mourad Zeghal. Coupled continuum-discrete model for saturated granular soils. *Journal of engineering mechanics*, 131(4):413–426, 2005.

A Cemal Eringen. Theory of micropolar elasticity. In *Microcontinuum field theories*, pages 101–248. Springer, 1999.

A Fall, B Weber, M Pakpour, N Lenoir, N Shahidzadeh, J Fiscina, C Wagner, and D Bonn. Sliding friction on wet and dry sand. *Physical review letters*, 112(17):175502, 2014.

J Fish and T Belytschko. Elements with embedded localization zones for large deformation problems. *Computers & Structures*, 30(1):247–256, 1988.

Jacob Fish. *Practical multiscaling*. John Wiley & Sons, 2013.

Jacob Fish, Tao Jiang, and Zheng Yuan. A staggered nonlocal multiscale model for a heterogeneous medium. *International Journal for Numerical Methods in Engineering*, 91(2):142–157, 2012.

E Flavigny, J Desrues, and B Palayer. Note technique-le sable d'hostun" rf". *Revue française de géotechnique*, (53), 1990.

NA Fleck, GM Muller, MF Ashby, and JW Hutchinson. Strain gradient plasticity: theory and experiment. *Acta Metallurgica et Materialia*, 42(2):475–487, 1994.

A Gajo, D Bigoni, and D Muir Wood. Multiple shear band development and related instabilities in granular materials. *Journal of the Mechanics and Physics of Solids*, 52(12):2683–2724, 2004.

SA Galindo-Torres, A Scheuermann, HB Mühlhaus, and DJ Williams. A micro-mechanical approach for the study of contact erosion. *Acta Geotechnica*, 10(3):357–368, 2013.

Vivette Girault and Pierre-Arnaud Raviart. *Finite element methods for Navier-Stokes equations, Theory and algorithms, volume 5 of Springer Series in Computational Mathematics*. Springer, Berlin, 1986.

IM Gitman, H Askes, and LJ Sluys. Representative volume: existence and size determination. *Engineering fracture mechanics*, 74(16):2518–2534, 2007.

Christoph Goniva, Christoph Kloss, Alice Hager, and Stefan Pirker. An open source cfd-dem perspective. In *Proceedings of OpenFOAM workshop Gothenburg, Sweden*, 2010.

Imene R. Goumiri and Jean H. Prevost. Cell to node projections: An assessment of error. *International Journal for Numerical and Analytical Methods in Geomechanics*, 35(7):837–845, 2011. ISSN 1096-9853. doi: 10.1002/nag.927. URL http://dx.doi.org/10.1002/nag.927.

William G Gray, Bernhard A Schrefler, and Francesco Pesavento. The solid phase stress tensor in porous media mechanics and the hill–mandel condition. *Journal of the Mechanics and Physics of Solids*, 57(3):539–554, 2009.

William G Gray, Cass T Miller, and Bernhard A Schrefler. Averaging theory for description of environmental problems: What have we learned? *Advances in water resources*, 51:123–138, 2013.

DV Griffiths and PA Lane. Slope stability analysis by finite elements. *Geotechnique*, 49(3):387–403, 1999.

N. Guo, J. Zhao, and W. C. Sun. Multiscale analysis of shear failure of thick-walled hollow cylinder in dry sand. *GÃl'otechnique Letters*, 6(1):null, 2016.

Ning Guo and Jidong Zhao. A coupled fem/dem approach for hierarchical multiscale modelling of granular media. *International Journal for Numerical Methods in Engineering*, 2014.

SA Hall, Michel Bornert, Jacques Desrues, Yannick Pannier, Nicolas Lenoir, Gioacchino Viggiani, and Pierre Bésuelle. Discrete and continuum analysis of localised deformation in sand using x-ray μct and volumetric digital image correlation. *Geotechnique*, 60(5):315–322, 2010.

K Han, YT Feng, and DRJ Owen. Numerical simulations of irregular particle transport in turbulent flows using coupled lbm-dem. *Computer Modeling in Engineering and Sciences*, 18(2):87, 2007.

Yanhui Han and Peter A Cundall. Lattice boltzmann modeling of pore-scale fluid flow through idealized porous media. *International Journal for Numerical Methods in Fluids*, 67(11):1720–1734, 2011.

Yanhui Han and Peter A Cundall. Lbm–dem modeling of fluid–solid interaction in porous media. *International Journal for Numerical and Analytical Methods in Geomechanics*, 37(10):1391–1407, 2013.

Isaac Harari. Stability of semidiscrete formulations for parabolic problems at small time steps. *Computer Methods in Applied Mechanics and Engineering*, 193(15):1491–1516, 2004.

Mir Amid Hashemi, Ghonwa Khaddour, Bertrand François, Thierry J Massart, and Simon Salager. A tomographic imagery segmentation methodology for three-phase geomaterials based on simultaneous region growing. *Acta Geotechnica*, pages 1–16, 2013.

I Herle and G Gudehus. Determination of parameters of a hypoplastic constitutive model from properties of grain assemblies. *Mechanics of Cohesive-frictional Materials*, 4(5):461–486, 1999.

Michael A Heroux, Roscoe A Bartlett, Vicki E Howle, Robert J Hoekstra, Jonathan J Hu, Tamara G Kolda, Richard B Lehoucq, Kevin R Long, Roger P Pawlowski, Eric T Phipps, et al. An overview of the trilinos project. *ACM Transactions on Mathematical Software (TOMS)*, 31(3):397–423, 2005.

P-Y Hicher and CS Chang. A microstructural elastoplastic model for unsaturated granular materials. *International journal of solids and structures*, 44(7):2304–2323, 2007.

Yosuke Higo, Fusao Oka, Tomohiro Sato, Yoshiki Matsushima, and Sayuri Kimoto. Investigation of localized deformation in partially saturated sand under triaxial compression using microfocus x-ray ct with digital image correlation. *Soils and Foundations*, 53(2):181–198, 2013.

Hatta Hiroshi and Taya Minoru. Equivalent inclusion method for steady state heat conduction in composites. *International Journal of Engineering Science*, 24(7):1159–1172, 1986.

Gerhard A Holzapfel. Nonlinear solid mechanics: a continuum approach for engineering. 2000.

Kazuyuki Hotta, Kazuo Takeda, and Koichi Iinoya. The capillary binding force of a liquid bridge. *Powder Technology*, 10(4):231–242, 1974.

Jason S Howell and Noel J Walkington. Inf–sup conditions for twofold saddle point problems. *Numerische Mathematik*, 118(4):663–693, 2011.

Nan Hu and Jacob Fish. Enhanced ant colony optimization for multiscale problems. *Computational Mechanics*, pages 1–17, 2015.

Thomas JR Hughes. *The finite element method: linear static and dynamic finite element analysis*. Courier Corporation, 2012.

Thomas JR Hughes, Karl S Pister, and Robert L Taylor. Implicit-explicit finite elements in nonlinear transient analysis. *Computer Methods in Applied Mechanics and Engineering*, 17:159–182, 1979.

TJR Hughes. The finite element method: linear static and dynamic finite element analysis. 1987.

Kiyohiro Ikeda, Yuki Yamakawa, and Seiichiro Tsutsumi. Simulation and interpretation of diffuse mode bifurcation of elastoplastic solids. *Journal of the Mechanics and Physics of Solids*, 51(9):1649–1673, 2003.

KA Issen and JW Rudnicki. Conditions for compaction bands in porous rock. *Journal of Geophysical Research: Solid Earth (1978–2012)*, 105(B9):21529–21536, 2000.

Kazuyoshi Iwashita and Masanobu Oda. Micro-deformation mechanism of shear banding process based on modified distinct element method. *Powder Technology*, 109(1):192–205, 2000.

JEB Jennings and JB Burland. Limitations to the use of effective stresses in partly saturated soils. *Géotechnique*, 12(2):125–144, 1962.

Boris Jeremić, Zhao Cheng, Mahdi Taiebat, and Yannis Dafalias. Numerical simulation of fully saturated porous materials. *International Journal for Numerical and Analytical Methods in Geomechanics*, 32(13): 1635–1660, 2008.

Birendra Jha and Ruben Juanes. A locally conservative finite element framework for the simulation of coupled flow and reservoir geomechanics. *Acta Geotechnica*, 2:139–153, 2007. ISSN 1861-1125. doi: 10.1007/s11440-007-0033-0. URL http://dx.doi.org/10.1007/s11440-007-0033-0.

MJ Jiang, S Leroueil, and JM Konrad. Insight into shear strength functions of unsaturated granulates by dem analyses. *Computers and Geotechnics*, 31(6):473–489, 2004.

L Jing, C-F Tsang, and O Stephansson. DecovalexâĂŤan international co-operative research project on mathematical models of coupled thm processes for safety analysis of radioactive waste repositories. 32(5):389–398, 1995.

Ali Karrech, Thomas Poulet, and Klaus Regenauer-Lieb. Poromechanics of saturated media based on the logarithmic finite strain. *Mechanics of Materials*, 51(0):118 – 136, 2012. ISSN 0167-6636.

Ghonwa Khaddour, Amid Hashemi, Simon Salager, Jacques Desrues, Thierry Jacques Massart, and Bertrand Francois. Phase segmentation in 3d x-ray images of unsaturated granular materials. In *XVI French-Polish Colloquium of Soil and Rock Mechanics*, 2013.

N Khalili, F Geiser, and GE Blight. Effective stress in unsaturated soils: review with new evidence. *International Journal of Geomechanics*, 4(2):115–126, 2004.

Jaehong Kim, Wei Wang, and Richard A Regueiro. Hybrid time integration and coupled solution methods for nonlinear finite element analysis of partially saturated deformable porous media at small strain. *International Journal for Numerical and Analytical Methods in Geomechanics*, 2015.

Miyuki Koiso and Bennett Palmer. Anisotropic capillary surfaces with wetting energy. *Calculus of Variations and Partial Differential Equations*, 29(3):295–345, 2007.

Olaf Kolditz, S Bauer, L Bilke, N Böttcher, JO Delfs, T Fischer, UJ Görke, T Kalbacher, G Kosakowski, CI McDermott, et al. Opengeosys: an open-source initiative for numerical simulation of thermo-hydro-mechanical/chemical (thm/c) processes in porous media. *Environmental Earth Sciences*, 67(2):589–599, 2012.

NP Kruyt and L Rothenburg. Micromechanical definition of the strain tensor for granular materials. *Journal of applied mechanics*, 63(3):706–711, 1996.

Matthew R Kuhn, Hannah E Renken, Austin D Mixsell, and Steven L Kramer. Investigation of cyclic liquefaction with discrete element simulations. *Journal of Geotechnical and Geoenvironmental Engineering*, 140 (12):04014075, 2014.

Matthew R Kuhn, WaiChing Sun, and Qi Wang. Stress-induced anisotropy in granular materials: fabric, stiffness, and permeability. *Acta Geotechnica*, 10(4):399–419, 2015.

Poul V Lade and James M Duncan. Elastoplastic stress-strain theory for cohesionless soil. *Journal of the Geotechnical Engineering Division*, 101(10):1037–1053, 1975.

Poul V Lade and Jerry A Yamamuro. Effects of nonplastic fines on static liquefaction of sands. *Canadian Geotechnical Journal*, 34(6):918–928, 1997.

Lyesse Laloui and Mathieu Nuth. On the use of the generalised effective stress in the constitutive modelling of unsaturated soils. *Computers and Geotechnics*, 36(1):20–23, 2009.

David Lasry and Ted Belytschko. Localization limiters in transient problems. *International Journal of Solids and Structures*, 24(6):581–597, 1988.

Nicolas Lenoir, JE Andrade, WC Sun, and JW Rudnicki. In situ permeability measurements inside compaction bands using x-ray ct and lattice boltzmann calculations. *Advances in Computed Tomography for Geomaterials: GeoX2010*, pages 279–286, 2010.

Roland Wynne Lewis and Bernard A Schrefler. *The finite element method in the static and dynamic deformation and consolidation of porous media*. John Wiley, 1998.

RW Lewis, CE Majorana, and BA Schrefler. A coupled finite element model for the consolidation of non-isothermal elastoplastic porous media. *Transport in Porous Media*, 1(2):155–178, 1986.

Chao Li, Ronaldo I Borja, and Richard A Regueiro. Dynamics of porous media at finite strain. *Computer Methods in Applied Mechanics and Engineering*, 193(36):3837–3870, 2004.

Xiang Song Li and Yannis F Dafalias. Anisotropic critical state theory: role of fabric. *Journal of Engineering Mechanics*, 138(3):263–275, 2011.

Xiang Song Li and Yannis F Dafalias. Anisotropic critical state theory: role of fabric. *Journal of Engineering Mechanics*, 138(3):263–275, 2012.

Xikui Li, Zejia Liu, and R. W. Lewis. Mixed finite element method for coupled thermo-hydro-mechanical process in poro-elasto-plastic media at large strains. *International Journal for Numerical Methods in Engineering*, 64(5):667–708, 2005. ISSN 1097-0207.

XS Li and YF Dafalias. Dissipation consistent fabric tensor definition from dem to continuum for granular media. *Journal of the Mechanics and Physics of Solids*, 78:141–153, 2015.

Guoping Lian, Colin Thornton, and Michael J Adams. A theoretical study of the liquid bridge forces between two rigid spherical bodies. *Journal of Colloid and Interface Science*, 161(1):138–147, 1993.

Jia Lin and Wei Wu. A comparative study between dem and micropolar hypoplasticity. *Powder Technology*, 2015.

Jia Lin, Wei Wu, and Ronaldo I Borja. Micropolar hypoplasticity for persistent shear band in heterogeneous granular materials. *Computer Methods in Applied Mechanics and Engineering*, 289:24–43, 2015.

Hoe I Ling, Dongyi Yue, Victor N Kaliakin, and Nickolas J Themelis. Anisotropic elastoplastic bounding surface model for cohesive soils. *Journal of engineering mechanics*, 128(7):748–758, 2002.

R Liu, MF Wheeler, CN Dawson, and R Dean. Modeling of convection-dominated thermoporomechanics problems using incomplete interior penalty galerkin method. *Computer Methods in Applied Mechanics and Engineering*, 198(9):912–919, 2009.

Yang Liu, WaiChing Sun, Zifeng Yuan, and Jacob Fish. A nonlocal multiscale discrete-continuum model for predicting mechanical behavior of granular materials. *International Journal for Numerical Methods in Engineering*, 2015.

Yang Liu, WaiChing Sun, and Jacob Fish. Determining material parameters for critical state plasticity models based on multilevel extended digital database. *Journal of Applied Mechanics*, 88(1), 2016.

Ning Lu and William J Likos. *Unsaturated soil mechanics*. Wiley, 2004.

Ning Lu, Bailin Wu, and Chee P Tan. Tensile strength characteristics of unsaturated sands. *Journal of Geotechnical and Geoenvironmental Engineering*, 133(2):144–154, 2007.

Rolf Mahnken and Erwin Stein. A unified approach for parameter identification of inelastic material models in the frame of the finite element method. *Computer methods in applied mechanics and engineering*, 136(3): 225–258, 1996.

Kalehiwot N Manahiloh and Balasingam Muhunthan. Characterizing liquid phase fabric of unsaturated specimens from x-ray computed tomography images. In *Unsaturated Soils: Research and Applications*, pages 71–80. Springer, 2012.

Mouloud Mansouri, J-Y Delenne, Moulay Saïd El Youssoufi, and Ahcene Séridi. A 3d dem-lbm approach for the assessment of the quick condition for sands. *Comptes Rendus Mécanique*, 337(9):675–681, 2009.

Majid T Manzari and Yannis F Dafalias. A critical state two-surface plasticity model for sands. *Geotechnique*, 47(2):255–272, 1997.

B Markert, Y Heider, and W Ehlers. Comparison of monolithic and splitting solution schemes for dynamic porous media problems. *International journal for numerical methods in engineering*, 82(11):1341–1383, 2010.

Mario J Martinez, Pania Newell, Joseph E Bishop, and DZ Turner. Coupled multiphase flow and geomechanics model for analysis of joint reactivation during co 2 sequestration operations. *International Journal of Greenhouse Gas Control*, 17:148–160, 2013.

Gérard A Maugin and Andrei V Metrikine. Mechanics of generalized continua. *Advances in mechanics and mathematics*, 21, 2010.

DF McTigue. Thermoelastic response of fluid-saturated porous rock. *Journal of Geophysical Research*, 91 (B9):9533–9542, 1986.

C Miehe, J Dettmar, and D Zäh. Homogenization and two-scale simulations of granular materials for different microstructural constraints. *International Journal for Numerical Methods in Engineering*, 83(8-9):1206–1236, 2010.

Christian Miehe and Joachim Dettmar. A framework for micro–macro transitions in periodic particle aggregates of granular materials. *Computer Methods in Applied Mechanics and Engineering*, 193(3):225–256, 2004.

Raymond David Mindlin. Micro-structure in linear elasticity. *Archive for Rational Mechanics and Analysis*, 16 (1):51–78, 1964.

P Mira, M Pastor, T Li, and X Liu. A new stabilized enhanced strain element with equal order of interpolation for soil consolidation problems. *Computer methods in applied mechanics and engineering*, 192(37):4257–4277, 2003.

F Molenkamp. Limits to the jaumann stress rate. *International journal for numerical and analytical methods in geomechanics*, 10(2):151–176, 1986.

B Moran, M Ortiz, and CF Shih. Formulation of implicit finite element methods for multiplicative finite deformation plasticity. *International Journal for Numerical Methods in Engineering*, 29(3):483–514, 1990.

SeonHong Na and WaiChing Sun. Wave propagation and strain localization in a fully saturated softening porous medium under the non-isothermal conditions. *International Journal for Numerical and Analytical Methods in Geomechanics*, 2016.

A Needleman. Material rate dependence and mesh sensitivity in localization problems. *Computer methods in applied mechanics and engineering*, 67(1):69–85, 1988.

DM Newitt and JM Conway-Jones. A contribution to the theory and practice of granulation. *Trans. Inst. Chem. Eng*, 36(s 422), 1958.

Tang-Tat Ng. Input parameters of discrete element methods. *Journal of Engineering Mechanics*, 132(7):723–729, 2006.

Trung Kien Nguyen, Gaël Combe, Denis Caillerie, and Jacques Desrues. Fem$\times$ dem modelling of cohesive granular materials: Numerical homogenisation and multi-scale simulations. *Acta Geophysica*, 62(5):1109–1126, 2014.

T.S Nguyen and A.P.S Selvadurai. Coupled thermal-mechanical-hydrological behaviour of sparsely fractured rock: Implications for nuclear fuel waste disposal. *International Journal of Rock Mechanics and Mining Sciences and Geomechanics Abstracts*, 32(5):465 – 479, 1995. ISSN 0148-9062.

Michał Nitka, Gaël Combe, Cristian Dascalu, and Jacques Desrues. Two-scale modeling of granular materials: a dem-fem approach. *Granular Matter*, 13(3):277–281, 2011.

Patrick K Notz, Roger P Pawlowski, and James C Sutherland. Graph-based software design for managing complexity and enabling concurrency in multiphysics pde software. *ACM Transactions on Mathematical Software (TOMS)*, 39(1):1, 2012.

Amos Nur and JD Byerlee. An exact effective stress law for elastic deformation of rock with fluids. *Journal of Geophysical Research*, 76(26):6414–6419, 1971a.

Amos Nur and JD Byerlee. An exact effective stress law for elastic deformation of rock with fluids. *Journal of Geophysical Research*, 76(26):6414–6419, 1971b.

Masanobu Oda and Kazuyoshi Iwashita. Study on couple stress and shear band development in granular media based on numerical simulation analyses. *International journal of engineering science*, 38(15):1713–1740, 2000.

E Onate and J Rojek. Combination of discrete element and finite element methods for dynamic analysis of geomechanics problems. *Computer methods in applied mechanics and engineering*, 193(27):3087–3128, 2004.

Michael Ortiz, Yves Leroy, and Alan Needleman. A finite element method for localized failure analysis. *Computer methods in applied mechanics and engineering*, 61(2):189–214, 1987.

Catherine O'Sullivan. *Particulate discrete element modelling*. Taylor & Francis, 2011.

Daniel Pantuso and Klaus-Jürgen Bathe. On the stability of mixed finite elements in large strain analysis of incompressible solids. *Finite elements in analysis and design*, 28(2):83–104, 1997.

Roger P Pawlowski, Eric T Phipps, and Andrew G Salinger. Automating embedded analysis capabilities and managing software complexity in multiphysics simulation, part i: Template-based generic programming. *Scientific Programming*, 20(2):197–219, 2012a.

Roger P Pawlowski, Eric T Phipps, and Andrew G Salinger. Automating embedded analysis capabilities and managing software complexity in multiphysics simulation, part i: Template-based generic programming. *Scientific Programming*, 20(2):197–219, 2012b.

Roger P Pawlowski, Eric T Phipps, Andrew G Salinger, Steven J Owen, Christopher M Siefert, and Matthew L Staten. Automating embedded analysis capabilities and managing software complexity in multiphysics simulation, part ii: Application to partial differential equations. *Scientific Programming*, 20(3):327–345, 2012c.

Juan M Pestana and Andrew J Whittle. Formulation of a unified constitutive model for clays and sands. *International Journal for Numerical and Analytical Methods in Geomechanics*, 23(12):1215–1243, 1999.

Adrian Postelnicu. Influence of a magnetic field on heat and mass transfer by natural convection from vertical surfaces in porous media considering soret and dufour effects. *International Journal of Heat and Mass Transfer*, 47(6):1467–1472, 2004.

Matthias Preisig and Jean H. Prévost. Coupled multi-phase thermo-poromechanical effects. case study: Co2 injection at in salah, algeria. *International Journal of Greenhouse Gas Control*, 5(4):1055 – 1064, 2011. ISSN 1750-5836. doi: 10.1016/j.ijggc.2010.12.006.

J. H. Prevost. Nonlinear transient phenomena in saturated porous media. *Computer Methods in Applied Mechanics and Engineering*, 30(1):3 – 18, 1982. ISSN 0045-7825.

Jean H Prevost. Implicit-explicit schemes for nonlinear consolidation. *Computer Methods in Applied Mechanics and Engineering*, 39(2):225–239, 1983.

Raul Radovitzky and Michael Ortiz. Error estimation and adaptive meshing in strongly nonlinear dynamic problems. *Computer Methods in Applied Mechanics and Engineering*, 172(1):203–240, 1999.

Kumbakonam Ramamani Rajagopal and Lu Tao. *Mechanics of mixtures*, volume 754. World scientific Singapore, 1995.

Amy L Rechenmacher. Grain-scale processes governing shear band initiation and evolution in sands. *Journal of the Mechanics and Physics of Solids*, 54(1):22–45, 2006.

RA Regueiro and D Ebrahimi. Implicit dynamic three-dimensional finite element analysis of an inelastic biphasic mixture at finite strain: part 1: application to a simple geomaterial. *Computer Methods in Applied Mechanics and Engineering*, 199(29):2024–2049, 2010.

James R Rice and Michael P Cleary. Some basic stress diffusion solutions for fluid-saturated elastic porous media with compressible constituents. *Reviews of Geophysics*, 14(2):227–241, 1976a.

J.R. Rice and M.P Cleary. Some basic stress diffusion solutions for fluid-saturated elastic porous media with compressible constituents. *Rev. Geophys.*, 14(2):227–241, 1976b. ISSN 8755-1209. doi: 10.1029/RG014i002p00227.

Vincent Richefeu, Moulay Saïd El Youssoufi, and Farhang Radjai. Shear strength properties of wet granular materials. *Physical Review E*, 73(5):051304, 2006.

Martin Robinson, Marco Ramaioli, and Stefan Luding. Fluid–particle flow simulations using two-way-coupled mesoscale sph–dem and validation. *International journal of multiphase flow*, 59:121–134, 2014.

K H_ Roscoe, ANn Schofield, and CP Wroth. On the yielding of soils. *Geotechnique*, 8(1):22–53, 1958.

John Walter Rudnicki and JR Rice. Conditions for the localization of deformation in pressure-sensitive dilatant materials. *Journal of the Mechanics and Physics of Solids*, 23(6):371–394, 1975.

Jonny Rutqvist. Status of the tough-flac simulator and recent applications related to coupled fluid flow and crustal deformations. *Computers and Geosciences*, 37(6):739 – 750, 2011.

Tarek Sadek, Martin Lings, Luiza Dihoru, and D Muir Wood. Wave transmission in hostun sand: multiaxial experiments. *Rivista Italiana Geotecnica*, 41(2):69–84, 2007.

Simon Salager, Frederic Jamin, Moulay Said El Yussoufi, and Christian Saix. Influence of temperature on the water retention curve of porous media. *COMPTES RENDUS MECANIQUE*, 334(6):393–398, 2006.

Andrew G Salinger, Roger P Pawlowski, Eric T Phipps, Roscoe A Bartlett, Glen A Hansen, Irina Kalashnikova, Jakob T Ostien, Waiching Sun, Quishi Chen, Alejandro Mota, Richard P Muller, Erick Nielsen, and Xujiao Gao. Albany: A component-based partial differential equation code built on trilinos. *ACM. Transactions on Mathematical Software*, 2013.

Lorenzo Sanavia, BA Schrefler, and P Steinmann. A formulation for an unsaturated porous medium undergoing large inelastic strains. *Computational Mechanics*, 28(2):137–151, 2002.

M Satake. New formulation of graph-theoretical approach in the mechanics of granular materials. *Mechanics of materials*, 16(1):65–72, 1993.

M Satake. Tensorial form definitions of discrete-mechanical quantities for granular assemblies. *International journal of solids and structures*, 41(21):5775–5791, 2004.

Andrew Schofield and Peter Wroth. Critical state soil mechanics. 1968.

Luc Scholtès, P-Y Hicher, François Nicot, Bruno Chareyre, and Félix Darve. On the capillary stress tensor in wet granular materials. *International journal for numerical and analytical methods in geomechanics*, 33 (10):1289–1313, 2009.

BA Schrefler. Fe in environmental engineering: coupled thermo-hydro-mechanical processes in porous media including pollutant transport. *Archives of Computational Methods in Engineering*, 2(3):1–54, 1995.

BA Schrefler, L Simoni, and E Turska. Standard staggered and staggered newton schemes in thermo-hydro-mechanical problems. *Computer methods in applied mechanics and engineering*, 144(1):93–109, 1997.

APS Selvadurai and TS Nguyen. Scoping analyses of the coupled thermal-hydrological-mechanical behaviour of the rock mass around a nuclear fuel waste repository. *Engineering Geology*, 47(4):379–400, 1997.

APS Selvadurai and AP Suvorov. Boundary heating of poro-elastic and poro-elasto-plastic spheres. *Proceedings of the Royal Society A: Mathematical, Physical and Engineering Science*, 468(2145):2779–2806, 2012.

S Shapiro. *The effects of nonplastic fines on the three-dimensional behavior of sand*. PhD thesis, MS thesis, Clarkson University, New York, NY, USA, 2000.

Daichao Sheng, SW Sloan, and A Gens. A constitutive model for unsaturated soils: thermomechanical and computational aspects. *Computational Mechanics*, 33(6):453–465, 2004.

JC Simo and Ch Miehe. Associative coupled thermoplasticity at finite strains: Formulation, numerical analysis and implementation. *Computer Methods in Applied Mechanics and Engineering*, 98(1):41–104, 1992.

JC Simo, RL Taylor, and KS Pister. Variational and projection methods for the volume constraint in finite deformation elasto-plasticity. *Computer Methods in Applied Mechanics and Engineering*, 51(1):177–208, 1985.

B.R. Simon, J.S.-S. Wu, O.C. Zienkiewicz, and D.K. Paul. Evaluation of u âĂŞ w and u âĂŞ π finite element methods for the dynamic response of saturated porous media using one-dimensional models. *International Journal for Numerical and Analytical Methods in Geomechanics*, 10(5):461–482, 1986. ISSN 1096-9853.

L Simoni, S Secchi, and BA Schrefler. Numerical difficulties and computational procedures for thermo-hydro-mechanical coupled problems of saturated porous media. *Computational Mechanics*, 43(1):179–189, 2008.

A Skempton. Effective stress in soils, concrete, and rocks. *Selected papers on soil mechanics*, pages 4–16, 1984.

V Šmilauer, E Catalano, B Chareyre, S Dorofeenko, J Duriez, A Gladky, J Kozicki, C Modenese, L Scholtès, L Sibille, et al. Yade documentation. *The Yade Project.(http://yade-dem. org/doc/)*, 2010.

Jeong-Hoon Song, Pedro MA Areias, and Ted Belytschko. A method for dynamic crack and shear band propagation with phantom nodes. *International Journal for Numerical Methods in Engineering*, 67(6):868–893, 2006.

Fabien Soulie, Moulay Said El Youssoufi, Fabien Cherblanc, and C Saix. Capillary cohesion and mechanical strength of polydisperse granular materials. *The European Physical Journal E: Soft Matter and Biological Physics*, 21(4):349–357, 2006.

G Subhash, S Nemat-Nasser, MM Mehrabadi, and HM Shodj. Experimental investigation of fabric-stress relations in granular materials. *Mechanics of Materials*, 11(2):87–106, 1991.

W. Sun, J.T. Ostien, and A. Salinger. A stabilized assumed deformation gradient finite element formulation for strongly coupled poromechanical simulations at finite strain. *International Journal for Numerical and Analytical Methods in Geomechanics*, 2013a. doi: 10.1002/nag.2161.

WaiChing Sun. A unified method to predict diffuse and localized instabilities in sands. *Geomechanics and Geoengineering*, 8(2):65–75, 2013.

WaiChing Sun. A stabilized finite element formulation for monolithic thermo-hydro-mechanical simulations at finite strain. *International Journal for Numerical Methods in Engineering*, 2015a. ISSN 1097-0207. doi: 10.1002/nme.4910.

WaiChing Sun. A stabilized finite element formulation for monolithic thermo-hydro-mechanical simulations at finite strain. *International Journal for Numerical Methods in Engineering*, 2015b.

WaiChing Sun and Alejandro Mota. A multiscale overlapped coupling formulation for large-deformation strain localization. *Computational Mechanics*, pages 1–18, 2014.

WaiChing Sun, José E. Andrade, and John W. Rudnicki. Multiscale method for characterization of porous microstructures and their impact on macroscopic effective permeability. *International Journal for Numerical Methods in Engineering*, 88(12):1260–1279, 2011a.

WaiChing Sun, José E Andrade, John W Rudnicki, and Peter Eichhubl. Connecting microstructural attributes and permeability from 3d tomographic images of in situ shear-enhanced compaction bands using multiscale computations. *Geophysical Research Letters*, 38(10):L10302, 2011b.

WaiChing Sun, José E Andrade, John W Rudnicki, and Peter Eichhubl. Connecting microstructural attributes and permeability from 3d tomographic images of in situ shear-enhanced compaction bands using multiscale computations. *Geophysical Research Letters*, 38(10), 2011c.

WaiChing Sun, Qiushi Chen, and Jakob T Ostien. Modeling the hydro-mechanical responses of strip and circular punch loadings on water-saturated collapsible geomaterials. *Acta Geotechnica*, 2013b.

WaiChing Sun, Matthew R. Kuhn, and John W. Rudnicki. A multiscale dem-lbm analysis on permeability evolutions inside a dilatant shear band. *Acta Geotechnica*, pages 1–16, 2013c.

WaiChing Sun, Jakob T. Ostien, and Andrew G. Salinger. A stabilized assumed deformation gradient finite element formulation for strongly coupled poromechanical simulations at finite strain. *International Journal for Numerical and Analytical Methods in Geomechanics*, 2013d. ISSN 1096-9853. doi: 10.1002/nag.2161. URL http://dx.doi.org/10.1002/nag.2161.

WaiChing Sun, Jakob T. Ostien, and Andrew G. Salinger. A stabilized assumed deformation gradient finite element formulation for strongly coupled poromechanical simulations at finite strain. *International Journal for Numerical and Analytical Methods in Geomechanics*, 37(16):2755–2788, 2013e.

WC Sun, JE Andrade, and JW Rudnicki. Multiscale method for characterization of porous microstructures and their impact on macroscopic effective permeability. *International Journal for Numerical Methods in Engineering*, 88(12):1260–1279, 2011d.

WC Sun, Q Chen, and JT Ostien. Modeling the hydro-mechanical responses of strip and circular punch loadings on water-saturated collapsible geomaterials. *Acta Geotechnica*, pages 1–32, 2013f. ISSN 1861-1125. doi: 10.1007/s11440-013-0276-x.

J Tejchman and A Niemunis. Fe-studies on shear localization in an anistropic micro-polar hypoplastic granular material. *Granular matter*, 8(3-4):205–220, 2006.

K von Terzaghi and L Rendulic. Die wirksame flachenporositat des betons. *Z. Ó st. Ing.-u. ArchitVer*, 86(1):2, 1934.

Karl Terzaghi. *Soil mechanics in engineering practice*. John Wiley & Sons, 1996.

Karl Terzaghi, Karl Terzaghi, Civil Engineer, Austria Czechoslowakia, Karl Terzaghi, Ingénieur Civil, Autriche Tchécoslovaquie, and Etats Unis. *Theoretical soil mechanics*, volume 18. Wiley New York, 1943.

von K Terzaghi. The shearing resistance of saturated soils and the angle between the planes of shear. In *Proceedings of the 1st International Conference on Soil Mechanics and Foundation Engineering*, volume 1, pages 54–56. Harvard University Press Cambridge, MA, 1936.

Tayfun E Tezduyar and Yasuo Osawa. Finite element stabilization parameters computed from element matrices and vectors. *Computer Methods in Applied Mechanics and Engineering*, 190(3):411–430, 2000.

S Thevanayagam. Effect of fines and confining stress on undrained shear strength of silty sands. *Journal of Geotechnical and Geoenvironmental Engineering*, 124(6):479–491, 1998.

N Kartal Toker, John T Germaine, and Patricia J Culligan. Effective stress and shear strength of moist uniform spheres. *Vadose Zone Journal*, 13(5), 2014.

Antoinette Tordesillas, David M Walker, and Qun Lin. Force cycles and force chains. *Physical Review E*, 81 (1):011302, 2010.

Clifford Truesdell and Richard Toupin. *The classical field theories*. Springer, 1960.

Andrzej Truty and Thomas Zimmermann. Stabilized mixed finite element formulations for materially nonlinear partially saturated two-phase media. *Computer methods in applied mechanics and engineering*, 195(13): 1517–1546, 2006a.

Andrzej Truty and Thomas Zimmermann. Stabilized mixed finite element formulations for materially nonlinear partially saturated two-phase media. *Computer methods in applied mechanics and engineering*, 195(13): 1517–1546, 2006b.

David M Walker, Antoinette Tordesillas, and Matthew R Kuhn. Spatial connectivity of force chains in a simple shear 3d simulation exhibiting shear bands. *Journal of Engineering Mechanics*, page C4016009, 2016.

Jing Wan. *Stabilized finite element methods for coupled geomechanics and multiphase flow*. PhD thesis, Citeseer, 2002.

R Wan, S Khosravani, and M Pouragha. Micromechanical analysis of force transport in wet granular soils. *Vadose Zone Journal*, 13(5), 2014.

Kun Wang and WaiChing Sun. Anisotropy of a tensorial bishopâĂŹs coefficient for wetted granular materials. *Journal of Engineering Mechanics*, page B4015004, 2015.

Kun Wang and WaiChing Sun. A semi-implicit micropolar discrete-to-continuum method for granular materials. In *VII European Congress on Computational Methods in Applied Science and Engineering*, 2016a.

Kun Wang and WaiChing Sun. A semi-implicit discrete-continuum coupling method for porous media based on the effective stress principle at finite strain. *Computer Methods in Applied Mechanics and Engineering*, 304:546–583, 2016b.

C Wellmann, C Lillie, and P Wriggers. Homogenization of granular material modeled by a three-dimensional discrete element method. *Computers and Geotechnics*, 35(3):394–405, 2008.

SJ Wheeler, D Gallipoli, and M Karstunen. Comments on use of the barcelona basic model for unsaturated soils. *International journal for numerical and analytical methods in Geomechanics*, 26(15):1561–1571, 2002.

Joshua A White and Ronaldo I Borja. Stabilized low-order finite elements for coupled solid-deformation/fluid-diffusion and their application to fault zone transients. *Computer Methods in Applied Mechanics and Engineering*, 197(49):4353–4366, 2008a.

Joshua A White and Ronaldo I Borja. Stabilized low-order finite elements for coupled solid-deformation/fluid-diffusion and their application to fault zone transients. *Computer Methods in Applied Mechanics and Engineering*, 197(49):4353–4366, 2008b.

David Muir Wood. *Soil behaviour and critical state soil mechanics*. Cambridge university press, 1990.

P Wriggers and S Reese. A note on enhanced strain methods for large deformations. *Computer Methods in Applied Mechanics and Engineering*, 135(3):201–209, 1996.

Wei Wu, Erich Bauer, and Dimitrios Kolymbas. Hypoplastic constitutive model with critical state for granular materials. *Mechanics of materials*, 23(1):45–69, 1996.

Nicolay Nicolayevich Yanenko. *The method of fractional steps*. Springer, 1971.

Q Yang, A Mota, and M Ortiz. A class of variational strain-localization finite elements. *International Journal for Numerical Methods in Engineering*, 62(8):1013–1037, 2005.

Mitsutoshi Yoshimine, Kenji Ishihara, and William Vargas. Effects of principal stress direction on intermediate principal stress on undrained shear behavior of sand. *Soils and Founcations*, 38(3):179–188, 1998. doi: 10.3208/sandf.38.3_179.

HW Zhang, L Sanavia, and BA Schrefler. An internal length scale in dynamic strain localization of multiphase porous media. *Mechanics of Cohesive-frictional Materials*, 4(5):443–460, 1999a.

HW Zhang, L Sanavia, and BA Schrefler. An interal length scale in dynamic strain localization of multiphase porous media. *Mechanics of Cohesive-frictional Materials*, 4(5):443–460, 1999b.

Jidong Zhao and Ning Guo. Unique critical state characteristics in granular media considering fabric anisotropy. *Géotechnique*, 63(8):695–704, 2013.

Zheyuan Zheng, WaiChing Sun, and Jacob Fish. Micropolar effect on the cataclastic flow and brittle-ductile transition in high-porosity rocks. *Journal of Geophysical Research: Solid Earth*, 2016. ISSN 2169-9356.

HP Zhu, ZY Zhou, RY Yang, and AB Yu. Discrete particle simulation of particulate systems: theoretical developments. *Chemical Engineering Science*, 62(13):3378–3396, 2007.

Olgierd C Zienkiewicz, AHC Chan, M Pastor, BA Schrefler, and T Shiomi. *Computational geomechanics*. Wiley Chichester, 1999a.

Olgierd Cecil Zienkiewicz, AHC Chan, M Pastor, BA Schrefler, and T Shiomi. *Computational geomechanics with special reference to earthquake engineering*. Wiley Chichester, UK, 1999b.